THESIS FOR THE DEGREE OF DOCTOR OF PHILOSOPHY

$YBa_2Cu_3O_{7-\delta}$ nanowires to study nanoscale ordering in High-T_C Superconductors

RICCARDO ARPAIA

Department of Microtechnology and Nanoscience
Quantum Device Physics Laboratory
CHALMERS UNIVERSITY OF TECHNOLOGY
Göteborg, Sweden 2016

$YBa_2Cu_3O_{7-\delta}$ nanowires to study nanoscale ordering in High-T_C Superconductors
RICCARDO ARPAIA
ISBN 978-91-7597-370-8

Author email: `riccardo.arpaia@chalmers.se`

Doktorsavhandlingar vid Chalmers tekniska högskola
Ny serie nr 4051
ISSN 0346-718X

Chalmers University of Technology
Department of Microtechnology and Nanoscience (MC2)
Quantum Device Physics Laboratory
SE-412 96 Göteborg, Sweden
Telephone +46 (0)31-772 1000

ISSN 1652-0769
Technical Report MC2-335

Printed by Chalmers Reproservice, Chalmers University of Technology
Göteborg, Sweden, April 2016

$YBa_2Cu_3O_{7-\delta}$ nanowires to study nanoscale ordering in High-T_C Superconductors
RICCARDO ARPAIA
Department of Microtechnology and Nanoscience, MC2
Chalmers University of Technology, 2016

Abstract

We present the realization of $YBa_2Cu_3O_{7-\delta}$ (YBCO) nanowires for both basic physics studies, which could help to elucidate the microscopic mechanisms of High critical Temperature Superconductors (HTS), and for novel applications.

The first part of the thesis describes an improved nanopatterning procedure, based on e-beam lithography in combination with an amorphous carbon mask and a very gentle Ar^+ ion etching. By using this procedure, nanowires preserving pristine superconducting properties, characterized by critical current densities very close to the theoretical depairing limit, have been achieved. These structures represent model systems for the study of HTS: their superconducting properties are very close to the as grown films.

We have grown YBCO thin films covering a broad oxygen doping range going from the slightly overdoped regime down to the strongly underdoped region of the phase diagram. We have been able to trace the entire underdoped part of the phase diagram, and to show that the most peculiar features encountered in single crystals are well reproduced in our thin films.

The core of the thesis describes an experiment done to study the effect of the nanoscale ordering on the superconducting properties of our nanowires. The presence of a local charge density wave (CDW) order has been recently demonstrated to be ubiquitous among all the cuprate families; if associated to a local modulations of Cooper pair density, CDWs might affect the absolute value of the critical current density of nanowires patterned at different in plane angles. We have used YBCO nanowires, fabricated on untwinned films, as a function of the oxygen doping and with dimensions of the same order as the CDW correlation length. By measuring the current voltage characteristic (IVC) of nanowires with the same width, patterned at different angles with respect to a fixed in plane direction of the substrate, we have revealed a cosinusoidal modulation of the critical current density for the narrowest width w (of the order of 65 nm). This dependence, that smears out for wider nanowire dimensions, can represent one of the first evidence of the existence of a pair density wave in YBCO.

In the second part of the thesis we have focused on applications. YBCO nanoSQUIDs, employing very short nanowires in the so-called Dayem bridge configuration, have been fabricated and characterized. These devices, working in the whole temperature range from 300 mK up to the critical temperature T_C (close to 85 K), have revealed an ultra low-white noise, below 1 $\mu\Phi_0/\sqrt{\mathrm{Hz}}$ above 10 kHz, corresponding to a predicted spin sensitivity of 50 μ_B per $\sqrt{\mathrm{Hz}}$.

The homogeneity of the nanowires has also given a boost to the realization of devices, aimed at the detection of single photons. We have shown that in ultrathin (7-8 unit cell thick) YBCO nanowires a hot spot is formed within the wire: as a consequence, the nanowires are driven from the superconducting directly to the normal state, analogously to NbN nanowires commonly used as single photon detectors.

Keywords: High-T_C superconductors, nanowires, oxygen doping, nanoscale ordering, nanoSQUIDs, ultrathin films, nanowire-based single photon detectors

A nonna Mima

List of Publications

This thesis is based on the work obtained in the following papers:

- **Improved nanopatterning for YBCO nanowires approaching the depairing current**
  R. Arpaia, S. Nawaz, F. Lombardi, and T. Bauch
  IEEE Trans. Appl. Supercond., **23**, 1101505 (2013)

- **Microwave response of superconducting $YBa_2Cu_3O_{7-\delta}$ nanowire bridges sustaining the critical depairing current: evidence of Josephson-like behavior**
  S. Nawaz, **R. Arpaia**, F. Lombardi, and T. Bauch
  Phys. Rev. Lett., **110**, 167004 (2013)

- **Approaching the theoretical depairing current in $YBa_2Cu_3O_{7-x}$ nanowires**
  S. Nawaz, **R. Arpaia**, T. Bauch, and F. Lombardi
  Physica C, **495**, 33 (2013)

- **Resistive state triggered by vortex entry in $YBa_2Cu_3O_{7-\delta}$ nanostructures**
  R. Arpaia, D. Golubev, R. Baghdadi, M. Arzeo, G. Kunakova, S. Charpentier, S. Nawaz, F. Lombardi, and T. Bauch
  Physica C, **506**, 165 (2014)

- **Ultra low noise $YBa_2Cu_3O_{7-\delta}$ nano superconducting quantum interference devices implementing nanowires**
  R. Arpaia, M. Arzeo, S. Nawaz, S. Charpentier, F. Lombardi, and T. Bauch
  Appl. Phys. Lett., **104**, 072603 (2014)

- **$YBa_2Cu_3O_{7-\delta}$ nanorings to probe fluxoid quantization in High Critical Temperature Superconductors**
  R. Arpaia, S. Charpentier, R. Toskovic, T. Bauch, and F. Lombardi
  Physica C, **506**, 184 (2014)

- **Highly homogeneous YBCO/LSMO nanowires for photoresponse experiments**
  R. Arpaia, M. Ejrnaes, L. Parlato, R. Cristiano, M. Arzeo, T. Bauch, S. Nawaz, F. Tafuri, G. P. Pepe, and F. Lombardi
  Supercond. Sci. Technol., **27**, 044027 (2014)

- **High-temperature superconducting nanowires for photon detection**
  R. Arpaia, M. Ejrnaes, L. Parlato, F. Tafuri, R. Cristiano, D. Golubev, R. Sobolewski, T. Bauch, F. Lombardi, and G.P. Pepe
  Physica C, **509**, 16 (2015)

- **Ultrathin $YBa_2Cu_3O_{7-\delta}$ nanowires for single photon detection**
  R. Arpaia, R. Baghdadi, R. Ciancio, D. Golubev, E. Trabaldo, T. Bauch, and F. Lombardi
  manuscript to be submitted (2016)

Papers that are outside the scope of this thesis

- **Investigation into the growth and structure of thin-film solid solutions of iron-based superconductors in the $FeSe_{0.92}$-$FeSe_{0.5}Te_{0.5}$ system**
  E.A. Stepantsov, S.M. Kazakov, V.V. Belikov, I.P. Makarova, **R. Arpaia**, R. Gunnarsson, and F. Lombardi
  Cristallogr. Rep., **58**, 735 (2013)

- **Phase transition of bismuth telluride thin films grown by MBE**
  A. Fülöp, Y. Song, S. Charpentier, P. Shi, M. Ekström, L. Galletti, **R. Arpaia**, T. Bauch, F. Lombardi, and S. Wang
  Appl. Phys. Express, **7**, 045503 (2014)

- **Influence of topological edge states on the properties of $Al/Bi_2Se_3/Al$ hybrid Josephson devices**
  L. Galletti, S. Charpentier, M. Iavarone, P. Lucignano, D. Massarotti, **R. Arpaia**, K. Kadowaki, T. Bauch, A. Tagliacozzo, F. Tafuri, and F. Lombardi
  Phys. Rev. B, **89**, 134512 (2014)

- **Josephson effect in Al/Bi_2Se_3/Al coplanar hybrid devices**
  L. Galletti, S. Charpentier, P. Lucignano, D. Massarotti, **R. Arpaia**, F. Tafuri, T. Bauch, Y. Suzuki, A. Tagliacozzo, K. Kadowaki, and F. Lombardi
  Physica C, **503**, 162 (2014)

- **Ablation replacement of iron with Co, Mn, Ni, and Cu during growth of iron-based superconductor films in the $Fe_{0.9}M_{0.1}Se_{0.92}$ system**
  E.A. Stepantsov, S.M. Kazakov, V.V. Belikov, I.P. Makarova, **R. Arpaia**, R. Gunnarsson, and F. Lombardi
  Cristallogr. Rep., **59**, 739 (2014)

- **Toward $YBa_2Cu_3O_{7-\delta}$ Nanoscale Structures for Hybrid Devices**
  R. Baghdadi, **R. Arpaia**, T. Bauch, and F. Lombardi
  IEEE Trans. Appl. Supercond., **25**, 1 (2015)

- **Fabricating Nanogaps in $YBa_2Cu_3O_{7-\delta}$ for Hybrid Proximity-Based Josephson Junctions**
  R. Baghdadi, **R. Arpaia**, S. Charpentier, D. Golubev, T. Bauch, and F. Lombardi
  Phys. Rev. Applied, **4**, 014022 (2015)

- **Y-Ba-Cu-O nanostripes for optical photon detection**
  G.P. Pepe, L. Parlato, M. Ejrnaes, R. Cristiano, **R. Arpaia**, F. Tafuri, D. Golubev, T. Bauch, F. Lombardi, and R. Sobolewski
  SPIE Optics+ Optoelectronics, 950406 (2015)

- **Growth of twin-free b-oriented $YBa_2Cu_3O_{7-x}$ films**
  E.A. Stepantsov, **R. Arpaia**, and F. Lombardi
  Cristallogr. Rep., **60**, 393 (2015)

- **The Role of Quantum Interference Effects in Normal-State Transport Properties of Electron-Doped Cuprates**
  P. Orgiani, A. Galdi, C. Sacco, **R. Arpaia**, S. Charpentier, F. Lombardi, C. Barone, S. Pagano, D.G. Schlom, and L. Maritato
  J. Supercond. Novel Magn., **28**, 3481 (2015)

List of symbols and abbreviations

Definitions of symbols

α_V	Vicinal angle
$\vec{A}$	Magnetic vector potential
A_{eff}	Effective area
A_g	Geometrical area
A_w	Nanowire cross section, $w \cdot t$
β_L	Screening inductance factor, $I_C^{max} L_{loop}/\Phi_0$
B_C^0	Thermodynamical critical field
δ	Doping parameter, $0 \leq 7 - n \leq 1$
δ^m	Film/substrate lattice mismatch
Δ	Superconducting gap
ΔI_C	Critical current modulation depth
ΔR	Amplitude of resistance oscillations
d_{T-S}	Target to substrate distance
e	Electronic elementary charge
F	Free energy
F_n	Free energy of the normal phase
F/S	Ferromagnetic/Superconducting
γ	In-plane angle with respect to the YBCO b-axis
h	Plank constant
H_c	Magnetic critical field
I_b	Bias current
I_C	Critical current
I_C^{max}	Maximum critical current (within a population of nanowires)
I_{exc}	Excess current
I_r	Retrapping current
J_C	Critical current density, I_C/A_w
$\bar{J}_C$	Average critical current density
J_d	Depairing critical current density
J_s	Superconducting current density

J_v	Vortex entry critical current density
κ	Thermal conductivity
k_B	Boltzmann constant
λ_L	London penetration depth
λ_0	Zero temperature London penetration depth
λ_P	Pearl length, $\lambda_L^2/2t$
l	Nanowire length
ℓ	Electronic mean free path
L_g	Geometrical inductance
L_k	Kinetic inductance
L_{loop}	Total loop inductance
μ_B	Bohr magneton
n_s	Superfluid density
n	Oxygen content
ξ	Coherence length
ξ_0	Zero temperature coherence length
p	Hole doping
p_{ann}	Oxygen post-annealing pressure
p_{dep}	Deposition pressure
$R_\square$	Sheet resistance
R_0	Residual resistance
R_L	Load resistance
R_{Little}	Wire resistance due to phase slips (Little model)
R_N	Normal resistance
R_{sh}	Shunt resistance
R_v	Wire resistance due to vortex entry
$S_v^{1/2}$	Voltage noise density
$S_\Phi^{1/2}$	Flux noise density, $S_v^{1/2}/V_\Phi$
t	Film/nanowire thickness
t_{preann}	Preannealing time
T_C	Critical Temperature
$\overline{T_C}$	Mean Critical Temperature
T_C^0	Zero Resistance Critical Temperature
T_{coh}	Coherence Temperature
T_{Curie}	Curie Temperature
T_{dep}	Deposition Temperature
T_N	Néel Temperature
T^{onset}	Temperature onset of the superconducting transition
v_s	Superfluid velocity
V_r	Retrapping voltage
V_Φ	Voltage-to-flux transfer function
w	Nanowire width
Φ	Magnetic Flux
Φ_0	Magnetic Flux Quantum, $h/2e$
ϕ	Phase

$\Psi(\vec{r})$	Order Parameter, $\|\Psi(\vec{r})\|e^{i\phi(\vec{r})}$
Ψ_∞	Equilibrium Order Parameter

List of abbreviations

AF	Antiferromagnetic
AFM	Atomic Force Microscopy
BKT	Berezinskii-Kosterlitz-Thouless
CPR	Current Phase Relation
dc	Direct Current
FWHM	Full width at half maximum
GL	Ginzburg-Landau
HTS	High Critical Temperature Superconductors
IVC	Current-Voltage Characteristic
LAO	$LaAlO_3$
LBCO	$La_{2-x}Ba_xCuO_4$
LSCO	$La_{2-x}Sr_xCuO_4$
LSMO	$La_{0.7}Sr_{0.3}MnO_3$
LTS	Low Critical Temperature Superconductors
PBCO	$PrBa_2Cu_3O_{7-\delta}$
PLD	Pulsed Laser Deposition
RSJ	Resistively Shunted Junction
SEM	Scanning Electron Microscopy
SC	Superconducting
S-I-S	Superconductor-insulator-superconductor
S-N-S	Superconductor-normal metal-superconductor
SNSPD	Superconducting Nanowire Single Photon Detector
SQUID	Superconducting QUantum Interference Device
S-S'-S	Superconductor-superconducting narrow bridge-superconductor
STO	$SrTiO_3$
TAPS	Thermally activated phase slip
XRD	X-Ray Diffraction
YBCO	$YBa_2Cu_3O_{7-\delta}$

Contents

List of Publications **v**

List of symbols and abbreviations **ix**

1 Introduction **1**

2 Introduction to superconductivity and cuprates **5**
- 2.1 Brief historical review of superconductivity 5
- 2.2 High-T_C superconductors and $YBa_2Cu_3O_{7-\delta}$ 7
  - 2.2.1 Crystal structure 8
  - 2.2.2 Phase diagram 9
  - 2.2.3 Superconducting properties 10
  - 2.2.4 Nanostructures to probe different models for HTS . . . 12
- 2.3 Key properties of superconducting nanostructures 13
  - 2.3.1 Fluxoid quantization 13
  - 2.3.2 Josephson effect 14
  - 2.3.3 Thermal suppression of superconductivity 18
- 2.4 Nanowire-based superconducting sensors 20
  - 2.4.1 Dayem nanobridge Superconducting QUantum Interference Devices 21

3 Growth and characterization of YBCO films **25**
- 3.1 Untwinned and twinned YBCO 25
- 3.2 Choice of the substrates 26
- 3.3 Thin film growth 27
- 3.4 YBCO films on MgO(110) 29
  - 3.4.1 Structural characterization 30
  - 3.4.2 Transport characterization 34
- 3.5 YBCO films on STO(001) with vicinal angle 35
- 3.6 Summary of the film properties 39

4 Ultrathin YBCO films 41
4.1 **Growth and structural characterization** 42
4.2 **Transport characterization** 43
4.2.1 **Determination of the oxygen doping** 44
4.2.2 **Broadening of the superconducting transition** 45

5 Underdoped YBCO films 47
5.1 **Film deposition** 48
5.2 **Study of the temperature dependence of the resistance** 48
5.3 **Structural characterization** 52
5.4 **Doping determination: the thin film phase diagram** 54
5.5 **Summary** 56

6 Fabrication of YBCO nanowires 57
6.1 **The nanopatterning procedure** 58
6.2 **YBCO nanowires** 60

7 Transport characterization of YBCO nanowires 63
7.1 **Current-voltage characteristics** 64
7.1.1 **Critical current density vs wire width** 65
7.1.2 **Critical current density vs temperature** 67
7.2 **Influence of vortex dynamics in YBCO nanostructures** 68
7.2.1 **Resistance vs temperature measurements of nanowires** . 68
7.2.2 **Magnetoresistance measurements of nanorings** 73
7.3 **Ultrathin nanowires** 75
7.4 **Underdoped nanowires** 77

8 YBCO nanoSQUIDs implementing nanowires 81
8.1 **NanoSQUID design** 82
8.2 **Transport characterization** 83
8.3 **Comparison between numerical and experimental results** . . . 84
8.4 **Noise measurements** 86

9 Photoresponse on YBCO nanowires 89
9.1 **Working principles of SNSPDs** 90
9.2 **Nanowire design** 91
9.3 **First approach: 50 nm thick, long nanowires** 92
9.3.1 **Nanowire geometry** 92
9.3.2 **Transport characterization** 93
9.3.3 **Photoresponse measurements** 95
9.4 **Second approach: ultrathin, short nanowires** 99
9.4.1 **Nanowire fabrication** 99
9.4.2 **Transport characterization** 99

10 Transport anisotropy in untwinned YBCO nanowires 105

11 Summary and outlook 111

Appendices **115**

A Recipes for sample fabrication **117**
  A.1 **YBCO nanowires on MgO (110)** 117
  A.2 **YBCO nanowires on LAO (001)** 118
  A.3 **YBCO/LSMO nanowires on LAO (001)** 119

B The measurement setups **121**
  B.1 **280 mK system - Heliox** 121
  B.2 **4.2 K system with optical access** 122

Acknowledgments **125**

Bibliography **127**

1

Introduction

The thesis focuses on the realization of superconducting $YBa_2Cu_3O_{7-\delta}$ (YBCO) nanowires for both basic physics studies and novel applications.

YBCO is a cuprate which belongs to the family of High Critical Temperature Superconductors (HTS). HTS materials are characterized by a rich and complex phenomenology, whose microscopic origin - after exactly 30 years from their discovery - still remains one of the grand challenges in solid state physics.

Much of the well-understood quantum theory of the electronic properties of solids, successfully used for conventional metals and superconductors, has entirely failed to address the basic features of this class of materials. Already 10 years ago it was clear that the mechanism of superconductivity ≪[...] cannot be found by merely thinking hard [...]. It requires experiments to give away the clue≫[1]. Hence, new experiments have to be designed and performed, to scrutinize among the novel theoretical models which have been proposed.

- *HTS at the nanoscale: why?*

The phase diagram of HTS is shaped by the spontaneous emergence of various ordered states, tuned by doping and driven by the many competing degree of freedom, where not only charge and spin are of relevance, but also lattice and orbitals have an active role in building up the ground state. The identification of all ordered states is crucial for the understanding of high critical temperature superconductivity. In strongly correlated systems, the tendency of the valence electrons to segregate in periodically modulated structures can lead to the formation of a peculiar charge order. The evidences for a new charge state, ubiquitous in all cuprate families [2, 3, 4] and with translational/rotational symmetry breaking, have recently come from neutron scattering [5], scanning tunnel microscopy [6] and resonant elastic/inelastic x-ray scattering [7] experiments. This discovery has added considerable credibility to the suggestion that local order is an important bridge between the Mott insulator, representing the starting cuprate material at very low doping, and the more metallic state at heavy doping. The charge density modulation, named Charge Density Wave (CDW), is biaxial and incommensurate with the lattice period, and more importantly it competes with superconductivity. There are still many open questions regarding the newly discovered CDW. Are they dynamical and possibly relevant for high critical temperature superconductivity [8] or are we dealing with a merely static local order? How is this charge order spatially distributed [9], and what is the local symmetry of the resulting state? What is the role of chemical and structural disorder in the stabilization and detectability of charge order [10]?

In underdoped YBCO, CDWs are particularly strong around the $p = 1/8$ doping, with a correlation length which strongly increases, up to 10 nm, when reducing the temperature T toward the superconducting critical temperature T_C ($T > T_C$). Considering that the coherence length and the London penetration depth are also in the order of nanometers, it becomes evident that most of the fundamental lengths in HTS materials are on such a scale. *Therefore, we believe that the experimental investigation of structures on the nanoscale - made it possible by the huge advances of nanotechnologies applied to HTS compounds in recent years - could help to elucidate the microscopic mechanism for High critical Temperature Superconductivity (HTS).*

Superconductivity in structures with reduced dimensionality is very intriguing and still unsettled, even for Low Critical Temperature Superconductors (LTSs), touching interesting topics as the suppression of superconductivity via phase-slips due to quantum or thermal fluctuations [11, 12, 13], and the enhancement of the superconducting properties in nanowires and nanodots [14, 15, 16, 17].

From an application point of view, HTS nanostructures can be potentially employed in single photon detectors [18, 19] and in nanoSQUIDs [20, 21], where they have been predicted to behave as weak links [22, 23].

- *HTS at the nanoscale: how?*

The investigation of HTS at the nanoscale requires the realization of homogeneous nanostructures preserving pristine superconducting properties: the structure, the morphology and the stoichiometry need to be as close as possible to the bulk ones. In this way novel phenomena can be directly attributed to intrinsic properties of the superconductor, rather than to inhomogeneities and defects possibly introduced by the nanopatterning procedure.

While the reliable fabrication of nanostructures is nowadays feasible for conventional superconductors, it still represents a challenging task for cuprate HTS, because of their chemical instability, mostly related to oxygen out-diffusion, and their extreme sensitivity to defects and disorder due to very short coherence length (of the order of 1 nm). The result is that - while for LTS the nanoscale is readily achievable - the properties of HTS nanostructures available in literature up to now present such a spread of values, that it is difficult to draw a clear picture of the physics in play [24, 25, 26, 27, 28, 29].

The realization of HTS nanostructures requires:

- *the ability to deposit homogeneous and epitaxial thin films.* The growth of HTS is problematic in itself, because of the strong dependence of the superconducting properties on the ratios of different elements (in particular the oxygen doping).

  We have succeeded in getting high quality YBCO thin films as a function of the thickness, down to 2-3 unit cells, and of the oxygen doping, from the slightly overdoped down to the strongly underdoped region of the phase diagram. In particular on MgO (110) substrates, we got untwinned films, which imply the presence of aligned CuO chains throughout most of the sample. The films have smooth surfaces, which is of crucial relevance for the patterning of nanostructures, and present transport properties in perfect qualitative agreement with single crystals. This implies that the rich and complex physics, characterizing both the superconducting and the normal state of the underdoped region of the phase diagram, below the pseudogap temperature, is preserved in our films and it can be studied as a function of the dimensionality of the system, down to the nanoscale.

- *the ability to master nanoscale structures.* Since the deposition of HTS materials takes place at high temperature (T ≈ 800°C), traditional lift-off procedures cannot be used. To realize HTS nanostructures the most common top-down approach is based on electron beam lithography in combination with an amorphous hard mask and ion etching. The challenge is therefore to minimize/eliminate the damage to the nanostructures (oxygen losses, disorder) due to the resist baking and to the ion milling etching.

  By using a soft etching procedure and preserving a Au capping layer on top of the nanostructures, we have succeeded in the fabrication of YBCO nanowires with width down to 50 nm^2 and lengths from 100 nm to several microns. These nanostructures exhibit critical temperatures T_C similar to those of the electrodes/unpatterned film and carry critical current densities J_C close to the theoretical depairing limit. This last result, difficult to achieve even for conventional superconductors, gives a measure of the highly uniform superconducting properties of our nanowires, representing model systems to study HTS at the nanoscale.

- *Thesis outline*

In Chapter 2 we give an overview of the basic properties of superconductivity and of cuprates, which are of relevance for the discussion of the experiments, with reference to the current literature on the subject.

In the first part of the thesis, we discuss about the optimization of the thin film growth of YBCO (Chapter 3), focusing on the results achieved on ultrathin films (Chapter 4) and on underdoped films (Chapter 5). In Chapter 6, we present the fabrication of YBCO nanowires. The transport characterization of the nanostructures, used as a benchmark to test their quality, is discussed in Chapter 7.

In the second part of the thesis, we present the employment of YBCO nanowires in devices for the detection of magnetic flux and photons.

The shortest nanowires have been used for the realization of YBCO nanoSQUIDs with loops on the nanometer scale (Chapter 8). The development of such sensors with LTS nanowires has recently gained a lot of attention for the possibility to achieve the necessary flux sensitivity to detect magnetic moment of nanoscaled systems, with the ultimate goal of observing a single spin [30, 31, 32, 33]. In the case of YBCO, several attempts have been made in the mid-'90s, but a proper SQUID behavior has never been observed using the Dayem bridge configuration [34, 35]. On the contrary our devices work in the full temperature range up to T_C, exhibiting critical current modulations as a function of the external magnetic field, never seen before for similar HTS devices. Moreover, they show record values for the white flux noise, making them very attractive for many applications, ranging from nanomagnetism to spintronics and spin-based quantum information processing.

Chapter 9 focuses on the experiments devoted to the detection of single photons with YBCO nanowires. YBCO and HTS materials in general are indeed potentially very interesting for this application because of their fast thermalization dynamics with respect to LTS materials, like NbN, which are currently the preferred for superconducting nanowire single photon detectors (SNSPDs) [18]. We have engineered nanowires, with lengths up to 10 μm and covered by a ferromagnetic $La_{0.7}Sr_{0.3}MnO_3$ capping layer, showing encouraging homogeneity properties. We measured the response of the devices to optical laser pulses as a function of the current bias, of the temperature and of the power, finding that a major contribution to the photoresponse signals has a bolometric nature. To overcome this issue, we have also studied the properties of 7-8 unit cell thick, short, YBCO nanowires. Here, a voltage switch occurs in the current voltage characteristics, driving the nanowire from the superconducting directly to the normal state. This occurrence, in similarity with NbN nanowires, makes our ultrathin nanostructures attractive candidates for SNSPDs.

In Chapter 10 we have described the experiment done to investigate the effect of the nanoscale ordering on the superconducting properties of our nanowires with different oxygen doping. We have studied the in-plane anisotropy of the critical current density, and its evolution with the width of the nanowires, when YBCO is scaled down at dimensions comparable with its fundamental lengths (λ_L, ξ, CDW correlation length). The measured critical current density of the wires shows a cosinusoidal modulation as a function of the angle measured from a reference in plane direction of the substrates. This dependence smears out for wider nanowire dimensions. This unconventional modulation could be linked to a momentum-dependent Cooper pair density, recently predicted to be associated to charge density waves. If confirmed, our observation can represent one of the first evidence of the existence of a pair density wave in YBCO, and more in general in HTS cuprates.

Finally, Chapter 11 gives a summary of the main results, with an outlook for possible future work.

2

Introduction to superconductivity and cuprates

2.1 Brief historical review of superconductivity

In what follows we will give a brief chronological account of the superconductivity phenomenon from its discovery to the understanding of the microscopic mechanism for conventional materials:

- 1911. By measuring the mercury resistance as a function of the temperature, Onnes discovers the first hallmark characterizing the superconductivity: the perfect conductivity. Below a critical temperature T_C, the metal resistance rapidly vanishes [36].

- 1933. Meissner and Ochsenfeld discover the second hallmark of the superconductors: the perfect diamagnetism. A magnetic field less than a critical value, B_C, is excluded from the bulk of a superconductor when the latter is cooled down below T_C (the so-called Meissner effect) [37].

- 1935. Fritz and Heinz London develop two equations, which relate the current to the electromagnetic fields in a superconductor, so describing the two previously observed hallmarks of superconductivity [38]:

$$\partial_t \vec{J}_s = \frac{n_s e^{*2}}{m^*} \vec{E} \tag{2.1}$$

$$\vec{\nabla} \times \vec{J}_s = -\frac{n_s e^{*2}}{m^*} \vec{B} \ , \tag{2.2}$$

  where $\vec{J}_s$ is the superconducting current density, $\vec{E}$ and $\vec{B}$ are respectively the electric and the magnetic fields within the superconductor, n_s is the density of superconducting electrons which flow without dissipation (superfluid density), m^* and e^* are respectively the effective mass and effective electric charge of superconducting electrons (which typically are assumed to take the double value of the mass and the elementary charge in the normal state, i.e. $m^* = 2m$ and $e^* = 2e$, with $e \approx -1.6 \times 10^{-19}$ C). The equation (2.1) describes the perfect conductivity: the electric field accelerates the super-electrons, while it simply sustains the velocity of the electrons in normal metals, described by the Ohm's law. The equation (2.2), combined with the curl of Ampere's law, explains instead the Meissner effect:

$$\nabla^2 \vec{B} = \frac{1}{\lambda_L^2} \vec{B} \; , \qquad \lambda_L \equiv \sqrt{\frac{m^*}{\mu_0 n_s e^{*2}}} \; , \tag{2.3}$$

with μ_0 the vacuum permeability. The magnetic field is screened completely in the bulk of the material due to screening currents flowing in a thin region at the surface of the superconductor. Both the magnetic field and the corresponding screening currents decay exponentially into a superconductor from its surface with a characteristic length scale given by λ_L, known as the *London penetration depth*.

- 1950. Ginzburg and Landau postulate a phenomenological model [39], based on Landau's previously established theory of second-order phase transitions, which extends the London theory, considering the superfluid density $n_s(\vec{r})$ as function of spatial variables, and introduces the order parameter, a complex wavefunction related to the superfluid density, defined as

$$\Psi(\vec{r}) = |\Psi(\vec{r})| e^{i\phi(\vec{r})} \; , \tag{2.4}$$

where $|\Psi(\vec{r})| = \sqrt{n_s(\vec{r})}$ is the amplitude and $\phi(\vec{r})$ is the phase as a function of position.

Their theory is developed at temperature close to the superconducting transition, where the order parameter $\Psi(\vec{r})$ is postulated to be small and slowly varying in the space. As a consequence, the free energy $F = F(\Psi, T)$ of the superconducting system, immersed in a magnetic field B, can be expanded in series of Ψ and $\vec{\nabla}\Psi$, taking the form [40]

$$F = F_n + \alpha|\Psi|^2 + \frac{\beta}{2}|\Psi|^4 + \frac{1}{2m^*}\left|(-i\hbar\vec{\nabla} - e^*\vec{A})\Psi\right|^2 + \frac{\vec{B}^2}{2\mu_0} \; , \tag{2.5}$$

where F_n is the free energy of the normal phase, $\alpha = \partial F/\partial n_s$ and $\beta = \partial^2 F/\partial n_s^2$ are temperature dependent parameters, and $\vec{A}$ is the magnetic vector potential.

The equilibrium wave function can be found minimizing the free energy written in eq. (2.5), integrated on the system volume, with respect to variations both in the order parameter and in the vector potential. The results are the two Ginzburg-Landau (GL) equations:

$$\alpha|\Psi| + \beta|\Psi|^2\Psi + \frac{1}{2m^*}\left(-i\hbar\vec{\nabla} - e^*\vec{A}\right)^2 \Psi = 0 \tag{2.6}$$

$$\vec{J}_s = \frac{\hbar e^*}{2im^*}(\Psi^* \vec{\nabla}\Psi - \Psi\vec{\nabla}\Psi^*) - \frac{e^{*2}}{m^*}\vec{A}|\Psi|^2 \; , \tag{2.7}$$

with the boundary condition $(-i\hbar\nabla - e^*\vec{A})\Psi|_n = 0$, assuring that no current passes through the surface n. Beside the London penetration depth, contained in eq. (2.7), a second characteristic length scale can be extracted, from the first GL equation, representing the distance at which the order parameter can vary without the system undergoing an energy increase. Considering a negligible external magnetic field and a very small but finite value of Ψ at some point in a superconductor just above its transition temperature, eq. (2.6) becomes

$$\nabla^2\Psi = \frac{\Psi}{\xi^2}\,, \qquad \xi \equiv \sqrt{\frac{\hbar^2}{2m^*|\alpha|}}\,. \tag{2.8}$$

This equation describes an exponential decay of Ψ on a characteristic length scale given by the *coherence length* ξ.

- 1950. Maxwell observes the Isotope effect for Hg, which suggested that the electron-phonon coupling is related to the superconductive phenomenon [41].

- 1957. Bardeen, Cooper and Schrieffer (BCS) propose the first microscopic theory of superconductivity [42]. According to their model, electrons of opposite spin and momentum close to the Fermi surface may overcome the Coulomb repulsion at temperatures below the critical one, due to a weak attractive force mediated by the electron-phonon interactions. As a consequence, they pair up into spin singlet pairs, named Cooper pairs, and form a condensate. This superconducting condensate is described by the order parameter $\Psi(\vec{r})$ and $|\Psi(\vec{r})|^2 = n_s(\vec{r})$ is the density of Cooper pairs. The coherence length ξ represents the length scale of the pair interaction. The energy required to break a Cooper pair is 2Δ, where Δ is the gap, predicted by the BCS theory, in the excitation spectrum of the superconductor. However, the BCS theory predicts a theoretical maximum critical temperature of about 25-30 K [43].

2.2 High-T_C superconductors and $YBa_2Cu_3O_{7-\delta}$

The discovery in 1986, by Bednorz and Müller, of a new class of compounds with a $T_C \approx 35$ K [44] was embraced by the scientific community with great enthusiasm. The existence of superconductors overcoming the T_C limit predicted by the BCS theory opened new perspectives in the quest toward room temperature superconductivity. The new compound was $Ba_xLa_{5-x}Cu_5O_{5(3-y)}$, in which the substitution of some La^{3+} ions with Ba^{2+} ions created hole-carriers, giving rise to the superconductivity. Few months later another cuprate, $YBa_2Cu_3O_{7-\delta}$ (YBCO), was discovered [45] with a $T_C = 92$ K. Since then many other HTS materials have been discovered, including both electron- and hole- doped superconductors, with T_C up to 135 K under ambient pressure in mercury compounds [46]. However, YBCO is still one of the most important HTS materials for both fundamental studies and applications, together with $La_{2-x}Sr_xCuO_4$ (LSCO) and $Bi_2Sr_2CaCu_2O_{8+x}$ (BSCCO).

2.2.1 Crystal structure

The HTS cuprates have a quasi-two-dimensional (2D) layered structure in common, containing one or more copper oxide (CuO_2) planes. The crystal structure is based on an alternate stacking of CuO_2 planes separated by other oxide layers or layers containing a single element. These intermediate layers normally act as charge reservoirs [47], which maintain both charge neutrality as well as cohesion of the structure. The interaction between CuO_2 planes and charge reservoirs plays an important role for the control and the change of the carrier concentration. The substitution or insertion of oxygen in the layers separating the CuO_2 planes dopes the material by either electrons or holes [48] (see Fig. 2.1a).

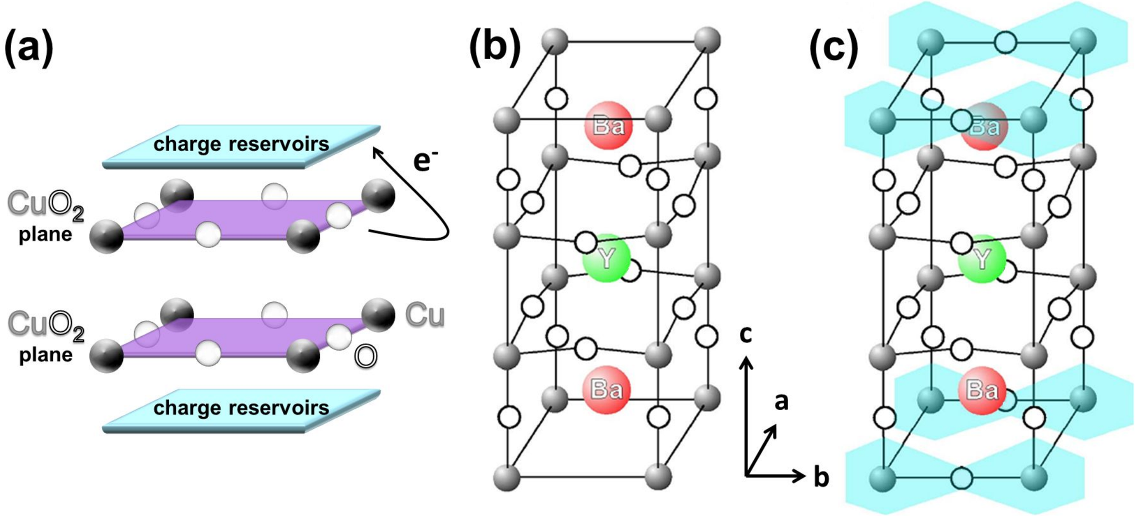

Figure 2.1: (a) The alternate stacking of CuO_2 planes separated by charge reservoir layers. Hole doping is represented by the transfer of electrons from the CuO_2 planes to the charge reservoirs. (b) and (c) represent respectively the $YBa_2Cu_3O_6$ and the $YBa_2Cu_3O_7$ unit cell. The highlighted regions, oriented along the *b*-axis parameter, indicate the presence of the CuO chains. (Adapted from [49])

The $YBa_2Cu_3O_7$ unit cell consists of three perovskite cells on top of each other (see Fig. 2.1c). Each perovskite unit cell contains a Y or Ba atom at the center: Ba in the bottom and in the top unit cells, Y in the middle one. Cu atoms occupy all the corner sites, while oxygens are placed in the middle edge positions. The CuO_2 planes are located right above and below the Y ion. Oxygen atoms at the top and bottom planes of the $YBa_2Cu_3O_7$ cell are instead missing in the [100] direction, giving rise to CuO chains in the [010] direction. These chains act as charge reservoirs, and are extremely sensitive to oxygen doping.

Oxygen vacancies, introduced in the CuO chains, play indeed an important role, varying the oxygen content (indicated as $n = 7-\delta$) from 6 to 7 per formula [50]. When $\delta = 1$, YBCO is an insulator with a tetragonal crystal structure. By adding oxygen into the charge reservoirs, i.e. decreasing δ, one dimensional CuO chains along the b axis are formed, changing the crystal structure to orthorhombic: the CuO_2 planes are hole-doped and the compound becomes superconducting, with a variable T_C depending on the oxygen stoichiometry. At the optimal doping, the lattice parameters of the unit cell are $a = 3.82$ Å, $b = 3.89$ Å and $c = 11.69$ Å [51].

Such a complex chemistry, together with the large diffusion length of oxygen even at moderate temperatures [52], may affect the YBCO properties at the nanoscale. Oxygen out-diffusion, induced by sample overheating and small dimensions, can indeed dramatically change the structural and superconducting properties.

2.2.2 Phase diagram

YBCO can be doped by introducing oxygen in the CuO chains, resulting in a change of the carrier concentration (hole doping) of the CuO_2 planes [53]. The resulting phase diagram, shown in Fig. 2.2 as a function of both the hole doping p per planar Cu atom and the oxygen content n per unit cell, is very rich and complex, and still under discussion.

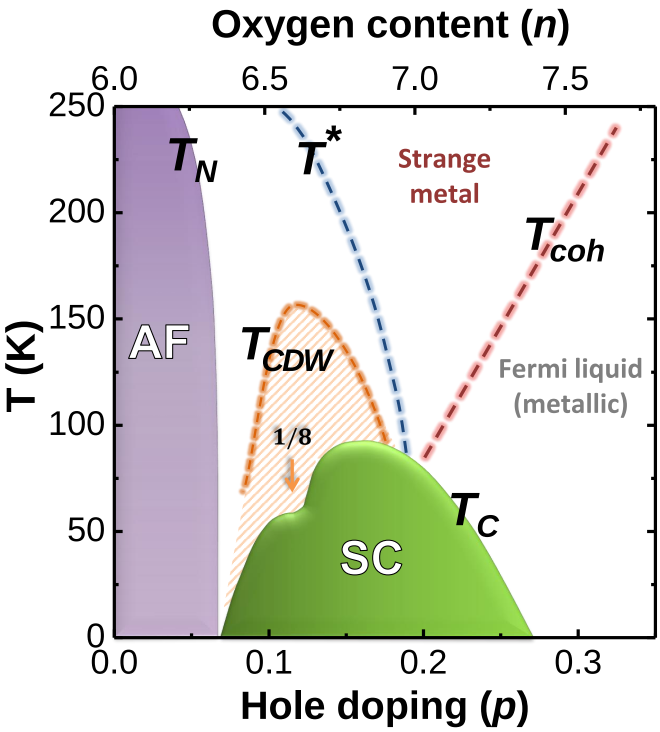

Figure 2.2: Phase diagram of $YBa_2Cu_3O_{7-\delta}$, as a function of both hole doping p per planar copper atom and oxygen content n per unit cell. T_N, T_{coh}, T^* and T_C are respectively the Néel, the coherence, the pseudogap and the critical temperature. T_{CDW} is the onset temperature of the charge density wave (CDW) order.

At zero doping ($p = 0$, $n = 6.0$) YBCO is a Mott-Hubbard insulator with antiferromagnetic (AF) long range order [54]. The AF ordering is easily destroyed by only a small amount of hole doping ($p = 0.05$, $n \approx 6.3$), giving rise to a metallic compound, characterized by superconductivity (SC) with low critical temperatures. By further doping, the superconducting transition temperature increases, reaching its maximum ($T_C = 94$ K for bulk crystals) for an optimal value $p = 0.16$ ($n \approx 6.95$). Upon additional doping, T_C decreases and the superconductivity disappears at $p = 0.27$ ($n \approx 7.4$).

This phase diagram can be divided into three regions, namely the underdoped, optimally doped and overdoped regime:

- the *overdoped* region ($p > 0.16$) is explained in terms of the Fermi liquid theory, which associates the electronic excitations at the Fermi level to an non-interacting gas of renormalized quasiparticles [55]. However, recent studies have proven deviations from this model [56].

- the *optimally doped* region ($p \approx 0.16$) is commonly described as a "strange metal phase". The normal state properties are indeed still not univocally understood. However, the linear temperature dependence of the electrical resistance, observed over the entire accessible temperature range up to 1000 K, can be phenomenologically explained assuming a strangely modified excitation spectrum ("Marginal Fermi Liquid") [57].

- the *underdoped* region ($p < 0.16$) is probably the most intriguing part of the phase diagram. It has been intensively studied by various experimental techniques [58], which all conclude on the existence of a pseudogap region in the normal state phase of the underdoped regime, persisting up to a temperature T^* well above T_C, that disappears moving in the optimally doped region of the phase diagram [59]. The connection between the pseudogap and the superconducting phase is still debated: are they competing orders [60, 61] (pseudogap state is suppressed below T_C) or do they cooperate [62, 63] (the pseudogap phase is a precursor of the superconducting state)? The answer to these questions may have a central role in the comprehension of the microscopic mechanisms of HTS.

The section of the phase diagram which encloses the superconductive phase as a function of doping is commonly known as the superconducting dome. Two plateaux at $T = 90$ K and $T \approx 60$ K are clearly visible. The first one is related to the occurrence of the optimal doping, while the origin of the second one, in the underdoped region, is still unclear [64, 49]. Two main explanations have been proposed. The first one suggests an ordering of the oxygen atoms in the basal planes (the planes where the CuO chains are located) [65, 66]. The second one, recently corroborated by different experiments [2, 7], suggests a purely electronic reason: the superconductivity is weakened at the hole doping of $p = 0.125$ ("1/8 anomaly"), as a consequence of a charge density wave (CDW) state (e.g. the formation of charge stripes or checkerboard) [67, 68] present in the pseudogap region. An enhancement of the T_C reduction at that value of doping would lead to the plateau formation.

2.2.3 Superconducting properties

The poor coupling between CuO$_2$ planes, which are perpendicular to the *c*-axis, results in a weak superconductivity along this direction and in a high anisotropy of the superconducting properties (see Table 2.1).

As a consequence of the orthorhombicity of the YBCO unit cell, anisotropy in the *a* and *b* direction of the CuO$_2$ planes is also present in untwinned single crystals and films. For instance, far-infrared spectroscopy [69] and neutron scattering on flux-line lattices [70] have shown an anisotropy between 20% and 60% in the London penetration depth, and different values of resistivity, critical current and superconducting gap have been measured along the a and the b axes [71, 72, 73].

Material	T_C (K)	Δ (meV)	λ_L^a; λ_L^b; λ_L^c (nm)	ξ_{ab}; ξ_c (nm)	H_{c2}^{ab}; H_{c2}^c (T)
YBCO	94	20-25	150-300; $\lambda_L^a/1.2$; $\approx$1000	1-3; $\approx$0.24	250; 120
Al	1.18	0.2	50	1600	0.01 (*)
Nb	9.25	1.5	44	40	$\approx$3
NbN	16.1	1.5	$\approx$200	$\approx$5	$\approx$20

Table 2.1: Summary of the anisotropic superconducting parameters of optimally doped YBCO in form of single crystal and thin films. For comparison, the same parameters are listed also for some common LTS materials [70, 74, 75]. (*) This value is the H_c of Al.

Compared to LTS, the carrier density of YBCO is lower, which results in an increased λ_L. Because of the very short coherence length ξ, thermal fluctuations become important and defects like impurities and grain boundaries have a large impact on the current transport. YBCO is a superconductor of type II (for more details, see section 2.3.1) and the value of its upper magnetic critical field H_{c2} is much higher than typical values of H_{c2} in type II LTS.

The superconducting order parameter in YBCO is predominantly of the $d_{x^2-y^2}$ type, in contrast to LTS, characterized by an s-wave type order parameter. The energy gap varies in k-space according $\Delta(\vec{k}) = \Delta_0(cos(k_x a) - cos(k_y a))$ [76], which has four lobes in orthogonal directions, corresponding to the a and b directions of the CuO$_2$ planes, and nodal lines at 45° angle with respect to the lobes (see Fig. 2.3). Recent studies showed deviations from a pure $d_{x^2-y^2}$ symmetry, with the appearance of a subdominant complex component is (or id_{xy} at low temperature), resulting in a fully gapped quasiparticle density of states [77].

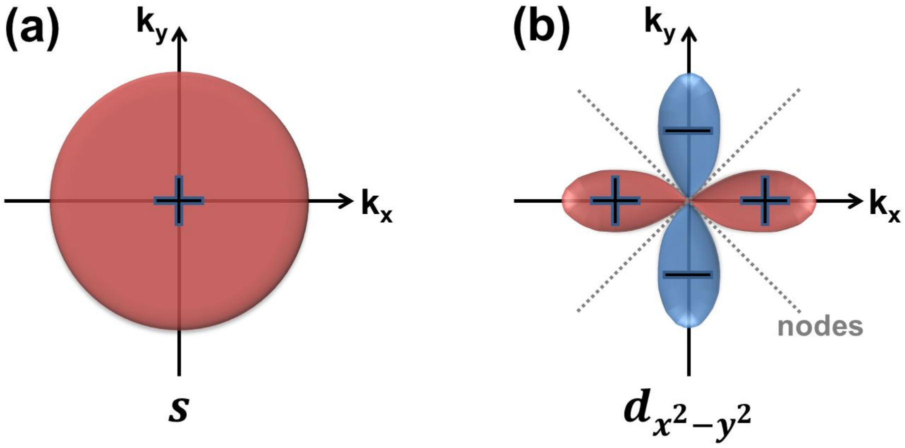

Figure 2.3: Sketch of a pure s-wave (a) and a pure d-wave (b) order parameter.

2.2.4 Nanostructures to probe different models for HTS

A remarkable number of models and theories have been proposed in the last two decades to explain the microscopic mechanism for HTS [78, 1]. Experimental anomalies have been discovered recently with neutron scattering [5] and scanning tunnel microscopy [6]. High energy X-ray diffraction [2, 7] measurements have shown a peculiar charge-ordering in the CuO_2 planes, ubiquitous among the various cuprate HTS. A charge density wave (CDW) is a periodic modulation of conduction electrons, along the crystallographic axes, expressed by a wavevector $\vec{Q}$ in the reciprocal space (see Fig. 2.4). The charge modulations appears in the underdoped region of the cuprate phase diagram, at a temperature $T_C < T_{CDW} < T^*$. The intensity and the correlation length of CDW have a maximum at T_C, while they decrease at temperatures both below and above T_C [7]. A complex intertwining exists between superconductivity and CDW order, as highlighted by the doping dependence of the charge modulations: charge density waves appear in the slightly overdoped regime; their intensity and the correlation length increase decreasing the doping, reaching the maximum in correspondence of the doping $p = 1/8$, where superconductivity is instead suppressed [80].

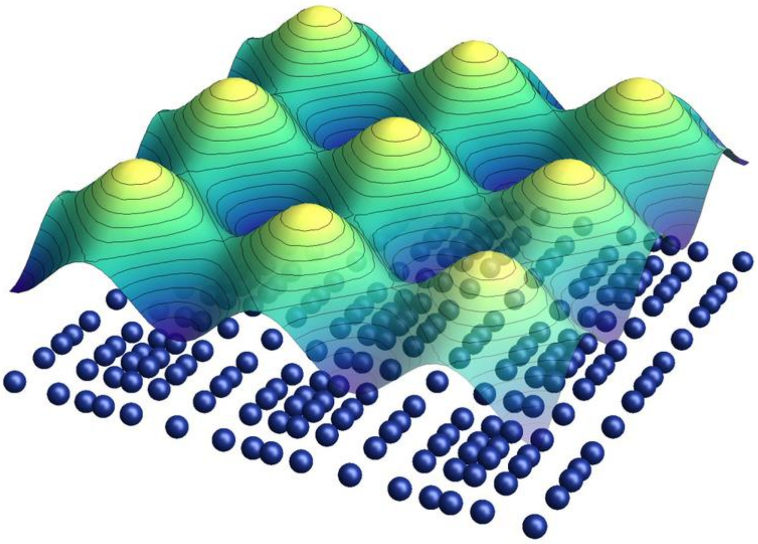

Figure 2.4: Sketch of the charge density waves (CDWs), superimposed to a CuO_2 plane, typical of HTS cuprates: the coupling between the lattice and the charge modulation occurs via electron-phonon coupling. Consequently, CDWs slightly distort the crystal lattice, as indicated in the CuO_2 plane by the irregular distances between the atoms (From [79]).

In YBCO a biaxial incommensurate charge order has been revealed by Resonant X-ray scattering, whose correlation length strongly increases up to 10 nm by reducing the O_2 doping [2, 7]. Differently from La-based cuprates, where holes are confined in one dimension and separated by antiferromagnetic regions, forming peculiar stripe domains, the local properties of the CDWs in YBCO have not yet been resolved. Both unidirectional charge stripes (in the presence of 90° rotated domains) and a bidirectional checkerboard pattern are consistent with Resonant X-ray scattering measurements, which reveal CDW characterized by wave vectors along both the a- and b axes, at $\vec{Q}_a = (Q, 0)$ and $\vec{Q}_b = (0, Q)$ respectively [9].

By fabricating structures with mesoscopic dimensions, HTS materials can be explored on the same scale of their characteristic lengths (ξ, λ_L, CDW correlation length) and interesting and potentially important findings could be revealed.

Moreover, unusual phases have been predicted and associated to the CDW order, the most exotic of which is a charge-$4e$ superconducting state [81], with a corresponding associated fractional flux $h/4e$. By measuring flux quantization in a variety of geometries, as in SQUID and ring loops, the existence of these novel superconducting states could be confirmed.

2.3 Key properties of superconducting nanostructures

2.3.1 Fluxoid quantization

The most important phenomenon which shows evidence of the macroscopic quantum behavior of superconductivity is the fluxoid quantization, deriving from the uniqueness of the wave function.

Inserting the expression for order parameter (eq. 2.4) into eq. (2.7), and considering the London limit in which the modulus of the wave function is not function of the spatial variables, the second Ginzburg-Landau equation writes as:

$$\vec{A} + \mu_0 \lambda_L^2 \vec{J}_s = \frac{\hbar}{e^*} \vec{\nabla} \phi \ . \tag{2.9}$$

The integration of eq. (2.9) on a closed line path around a hole in the superconductor, as depicted in Fig. 2.5a, yields to

$$\Phi + \mu_0 \oint \lambda_L^2 \vec{J}_s \, d\vec{r} = \frac{\hbar}{e^*} \oint \vec{\nabla} \phi \, d\vec{r} \ , \tag{2.10}$$

where Φ is the magnetic flux enclosed in the area surrounded by the closed path, while the sum of the two terms on the left side is called the fluxoid. To keep the order parameter single valued, the integral on the right side of eq. (2.10) over the full path must be an integer multiple of 2π:

$$\oint \vec{\nabla} \phi \, d\vec{r} = 2\pi n \ , \qquad n = 0, \pm 1, \pm 2, \dots \ . \tag{2.11}$$

As a consequence, eq. (2.10) writes as

$$\Phi + \mu_0 \oint \lambda_L^2 \vec{J}_s \, d\vec{r} = n \Phi_0 \ , \tag{2.12}$$

where $\Phi_0 = h/e^*$ is the flux quantum. The equation (2.12) describes the fluxoid quantization. In particular, considering an integration path where the screening currents are negligible, the second term on the left side of eq. (2.12) can be dropped ($\vec{J}_s = 0$); the total magnetic flux through a superconducting loop is quantized in units of Φ_0.

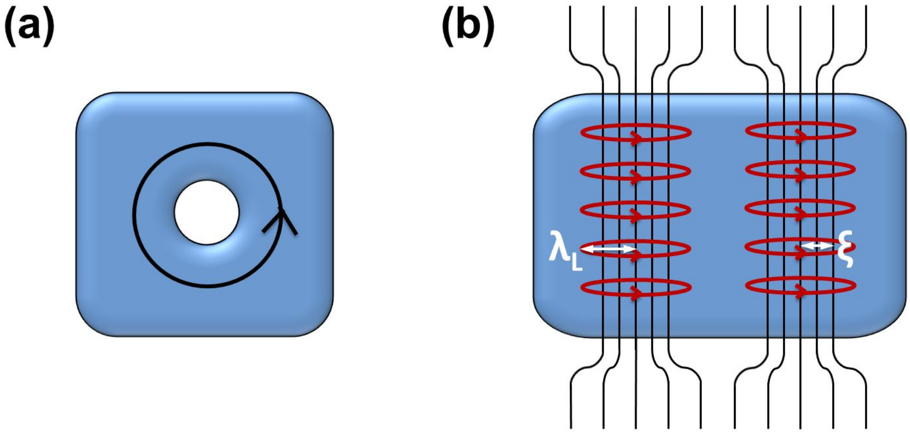

Figure 2.5: (a) Sketch of a superconducting loop. The black line shows a closed line path. (b) Sketch of Abrikosov vortices in a type II superconductor.

The first experiments on flux quantization [82, 83] showed a value of the superconducting flux quantum of $\approx 2 \cdot 10^{-15}$ Tm^2, that is compatible with $e^* = 2e$. Thence, the fluxoid quantization confirmed one of the main assumption of the BCS theory, namely that the superconducting fluid is composed by couples of electrons and not by single electrons.

The ratio between the London penetration depth and the coherence length $k = \lambda_L/\xi$, known as the GL parameter, identify univocally if a superconductor is of type I or of type II. In particular, Abrikosov showed that the breakpoint is at $k = 1/\sqrt{2}$, based on considerations of the energy at the interface between a superconductor and a normal conductor [84]. If $k > 1/\sqrt{2}$, a superconductor is of type II, allowing the entering of magnetic field through Abrikosov vortices. An Abrikosov vortex, also called a fluxon, consists of a normal core with radius approximately given by ξ, around which a supercurrent circulates on a length scale given by λ_L. Each vortex carries a flux quantum Φ_0 (see Fig.2.5b). On the contrary, if $k < 1/\sqrt{2}$, a superconductor is of type I, where Abrikosov vortices cannot exist.

2.3.2 Josephson effect

In 1962 Josephson published a theoretical paper [85] predicting the existence of two remarkably effects. The basic idea of the DC-Josephson effect is that S-I-S junctions, made by two superconducting electrodes separated by a thin insulating barrier, may sustain a non-dissipative (zero-voltage) superconducting current I_S:

$$I_S = I_C \sin\phi \ . \tag{2.13}$$

Here, $\phi = \phi_2 - \phi_1$ is the phase difference between the wavefunctions describing the order parameter in the two electrodes and I_C is the critical current, which is the maximum supercurrent the junction can sustain without dissipation. The AC-Josephson equation tells instead that the phase varies linearly with time, if a fixed voltage V is applied across the junction:

$$\frac{d\phi}{dt} = \frac{2e}{\hbar} V \ . \tag{2.14}$$

Both effects have been verified by experiments shortly after Josephson prediction [86]. Moreover, it soon became clear that the Josephson effects exist not only in S-I-S junctions, but also in other kinds of the so-called weak links, that is, short sections of superconducting circuits where the critical current is substantially suppressed (see Fig. 2.6).

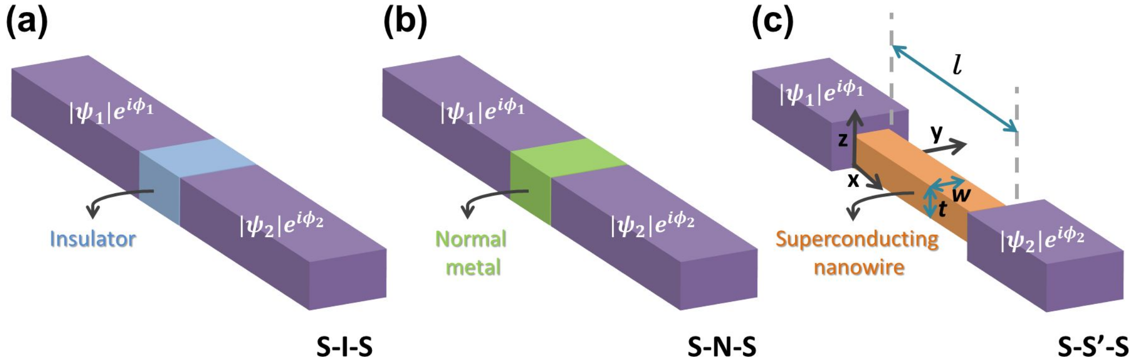

Figure 2.6: Different types of weak links: (a) superconductor-insulator-superconductor (S-I-S); (b) superconductor-normal metal-superconductor (S-N-S); (c) superconductor-superconducting narrow bridge-superconductor (S-S'-S).

Among the different types of weak links, we will focus on superconducting narrow bridges with thickness t, width w and length l connecting two bulk electrodes of the same material (see Fig. 2.6c).

- In the limit of short ($l \ll \xi$) and one dimensional ($w, t \ll \xi$) bridge, the current-phase relation (CPR) between the wide electrodes, derived by Aslamazov and Larkin from the GL equation (2.7), has the following expression:

  $$J_s^{AL} = \frac{\Phi_0}{2\pi\mu_0\lambda_L^2 l} \sin\phi \ . \tag{2.15}$$

  As a consequence of this equation, all the weak links are characterized by a sinusoidal CPR near T_C, where ξ diverges, similarly to superconducting tunnel junction (eq. 2.13).

- Increasing the bridge length, the current-phase relation close to T_C evolves from sinusoidal to saw tooth-like (see Fig. 2.7), as predicted by Likharev and Yakobson [87]. In particular, if $l \leq 3.49\xi$ an ideal Josephson behavior, described by a single valued CPR, is expected. If $l > 3.49\xi$, a multivalued CPR, strongly connected to depairing effects, characterizes the bridge. The maximum current saturates in fact for $l > 10\xi$ at a value given by the depairing current density, above which the order parameter (pair density) is locally suppressed, i.e. due to the nucleation of phase slip centers. Such unstable states are described by the lower reverse branch of the current-phase relation. As regards to the stable branch, instead, it can be derived from the GL equations, considering that in the limit of long ($l \gg \xi$) and one-dimensional ($w, t \ll \xi$ and $wt \ll \lambda^2$) bridge the free energy writes as [40]

$$F = F_n + \alpha|\Psi|^2 + \frac{\beta}{2}|\Psi|^4 + |\Psi|^2 \frac{1}{2} m^* v_s^2 \, , \tag{2.16}$$

where v_s is the superfluid velocity, defined from the relation $\vec{J_s} = e^*|\Psi|^2 \vec{v_s}$. Indeed in this particular case, the condition $w, t \ll \xi$ ensures that $\Psi(\vec{r}) = |\Psi| e^{i\phi(\vec{r})}$ is constant across the cross section of the superconductor; the limit $wt \ll \lambda^2$ ensures both a uniform current density and that the kinetic energy of the superconducting charge flow dominates over the magnetic energy produced by the same current by roughly a factor λ^2/wt, so allowing to neglect the magnetic self-field terms in eq. (2.5). Defining the following order parameter inside the wire:

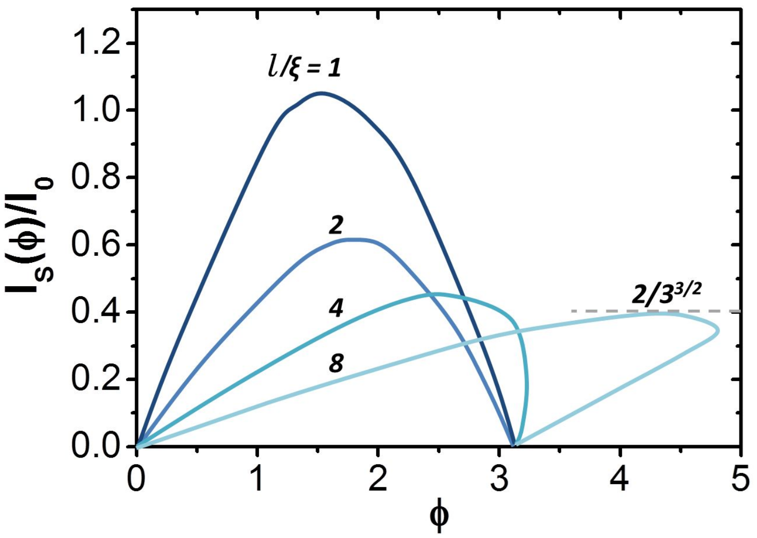

Figure 2.7: Current phase relation for different bridge lengths. The currents are normalized to the value $I_0 = \Phi_0/2\pi\mu_0\lambda_L^2\xi$. (Adapted from [87])

$$\Psi^{LY}(x) = |\Psi^{LY}| \, e^{ix\phi/l} \, , \tag{2.17}$$

the modulus of the wave function can be derived, minimizing the eq. (2.16) for a given v_s:

$$|\Psi^{LY}|^2 = |\Psi_\infty^{LY}|^2 \left[1 - \left(\frac{\phi\xi}{l}\right)^2\right] \, , \tag{2.18}$$

where $|\Psi_\infty^{LY}|^2$ is the modulus of the wave function at zero phase difference. Finally the current-phase relation for a long one-dimentional bridge can be determined, inserting eq. (2.17) and eq. (2.18) into eq. (2.7):

$$J_s^{LY} = \frac{\Phi_0}{2\pi\mu_0\xi{\lambda_L}^2} \left[\left(\frac{\xi}{l}\right)\phi - \left(\frac{\xi}{l}\right)^3 \phi^3\right] \, . \tag{2.19}$$

Maximizing the previous equation with respect to ϕ/l, we determine the maximum value ϕ_d of the phase gradient

$$\phi_d = l/\sqrt{3}\xi \ , \tag{2.20}$$

corresponding to the depairing critical current density J_d given by:

$$J_d = \frac{\Phi_0}{3\sqrt{3}\pi\mu_0\lambda_L^2\xi} \ . \tag{2.21}$$

It is worth noticing that, since $l \gg \xi$, this CPR is defined in a range $-l/\sqrt{3}\xi < \phi < l/\sqrt{3}\xi$, which is much larger than that of an ideal Josephson junction (2π).

- The effect of increasing the width of the bridge on the current-phase relation, studied by Likharev [88], is shown in Fig. 2.8. In particular, a different regime is expected for bridges wider $w > 4.44\xi$, if $l > 3.49\xi$, due to the coherent motion of Abrikosov vortices inside the structure. However, the current can be considered homogeneous in the limit $t < \lambda_L$ and $w < \lambda_P$, with $\lambda_P = \lambda_L^2/t$ the Pearl length, allowing to reduce the GL equations to the 1-dimensional form[89]. As a consequence, the stable branch of the CPR writes again as eq. (2.19), with the only difference that the maximum critical current density is not given by depairing effects, i.e. phase slips, but by Abrikosov vortices, driven by the Lorentz force, overcoming the bridge edge barrier. According to Bulaevskii et al. [90], this occurs for a phase difference $\phi_v = l/2.718\xi \simeq 0.64\phi_d$. As a consequence,

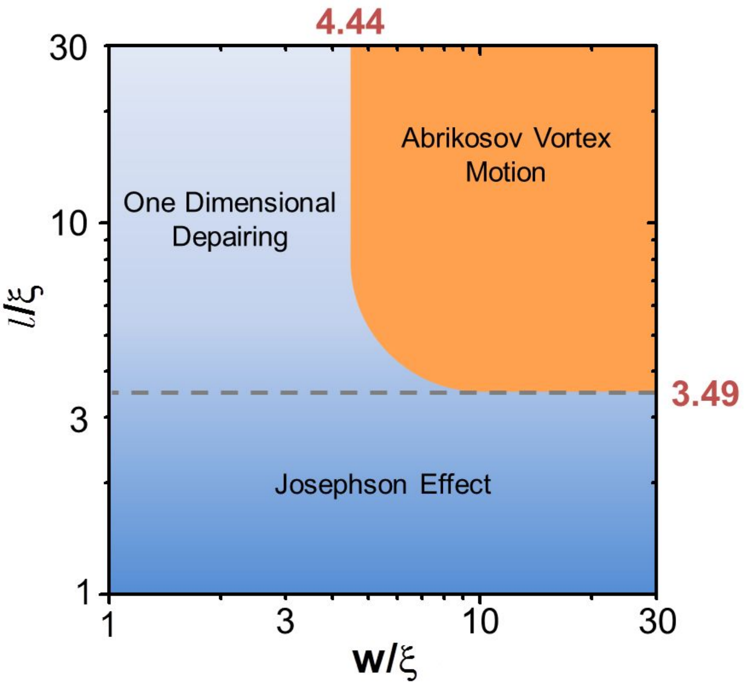

Figure 2.8: Likharev criteria for the origin of the current phase relation in SS'S weak links, for different bridge dimensions. (Adapted from [88])

the critical current density J_v due to vortex entry is smaller than the depairing critical current:

$$J_v \simeq 0.826 J_d \; . \tag{2.22}$$

For $|\phi| < \phi_v$ the expression of the CPR (eq. 2.19) can be reasonably approximated by the linear term:

$$I = \frac{\Phi_0}{2\pi L_k}\phi \; , \tag{2.23}$$

where $I = J_v \cdot wt$ is the supercurrent passing through the bridge and L_k is the kinetic inductance of the bridge, given by $(\mu_0 \lambda^2 l)/(wt)$. Indeed, the inductance of a bridge with cross section $wt \ll \lambda^2$ is dominated by the kinetic inductance with a negligible contribution of the geometric inductance $L_g \simeq \mu_0 l$.

2.3.3 Thermal suppression of superconductivity

In systems with reduced dimensionality it can be observed that the superconducting phase transition is frequently not sharp and the measured dependence of the sample resistance $R(T)$ in the vicinity of the critical temperature T_C may have a finite width, even in absence of any sample inhomogeneity. This broadening is due to thermal fluctuations. In 1D wires $(w, t \ll \xi)$ such fluctuations, called thermally activated phase slips (TAPS), with spacial extensions of the order of the coherence length, hence of the wire diameter, disrupt locally the flow of supercurrent, thereby imparting a non-zero resistance to the wire [91, 92, 93]. In 3D wires instead the resistive state is triggered by vortices crossing the wire, appearing below T_C even at low bias currents [90, 94].

Eventually, in 1D wires the broadening in the transition may even lead to a non-vanishing resistivity down to $T = 0$: the physical reason behind such smearing of the transition has been attributed to temperature-independent quantum phase slip events (QPS) [95]. However, we will not focus on them since they've been observed only in LTS nanostructures so far [96].

Phase slips

Little in 1967 introduced the concept of TAPS to explain the presence of a finite resistance below T_C in one dimensional superconducting nanowires, with width w, thickness t and length l [91]. Thermal fluctuations cause a deviation of the superconducting order parameter from its steady state, which is represented in the Argand plane by an helix of pitch $2\pi/q$ (with $q = \phi/l$ the phase gradient) and radius $|\Psi|$ (see Fig. 2.9a). In particular, the modulus can be suppressed temporally down to zero at some point

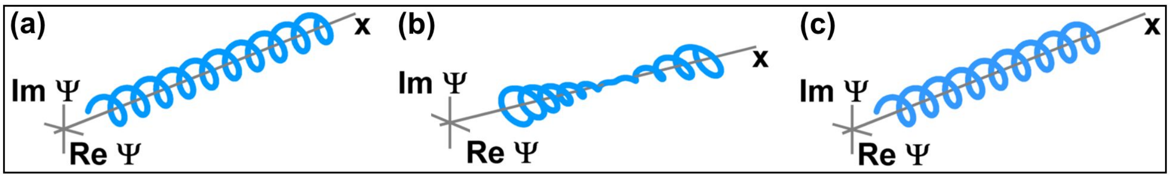

Figure 2.9: Polar plot of the complex GL wave function (a) before, (b) during and (c) after a phase slip event. (Adapted from [40])

inside the wire. As a consequence the phase, becoming unrestricted, can “slip”, but only by 2π or integer multiples of it, since the order parameter in the macroscopic leads is defined modulo 2π. At the end of this process the system returns in its initial steady state, accumulating a net phase shift 2π (provided phase slips are sufficiently rare, we can ignore fluctuations with $|n| \geq 2$, restricting $n = \pm 1$). Schematically, this process can be mimicked in the Argand plane, considering that the helix tightens up until its radius reaches zero at some point (see Fig. 2.9b), a phase slip occurs and the radius returns to $|\Psi|$.

According to eq. (2.14), each phase slip event determines a voltage drop V across the wire. However, if a bias current is not applied, the net voltage drop is zero, since the number of positive ($n = +1$) and negative ($n = -1$) phase slips is stochastically the same. Vice versa, if a current $I \propto |\Psi|^2 \Delta\phi$ is applied, a phase gradient is created along the wire, favoring positive phase slips: thence, a non-zero voltage drop is present due to TAPS, causing the appearance in the wire of a resistance $R = V/I$, different than zero even below T_C [97]. Quantitative theories predict that this resistance R is determined by the activation exponent

$$R(T) \propto \exp\left(-\frac{\Delta F(T)}{k_B T}\right) , \tag{2.24}$$

where k_B is the Boltzmann constant and $\Delta F(T)$ is the energy barrier for phase slips, depending on temperature and going to zero at $T = T_C$, which is proportional to the product of the condensation energy density and the cross section volume $\xi(T)wt$ in which superconductivity can be destroyed by thermal fluctuation [92, 93]:

$$\Delta F(T) \propto \frac{\mu_0 H_C^2(T)}{2} \xi(T)wt . \tag{2.25}$$

In particular, according to Langer-Ambegaokar-McCumber-Halperin (LAMH), who developed this theory, eq. (2.24) writes as [92, 93]

$$R_{LAMH}(T) = \left(\frac{h}{4e^2}\right)\left(\frac{\hbar\Omega_D}{k_B T}\right) \exp\left(-\frac{\Delta F(T)}{k_B T}\right) , \tag{2.26}$$

where $\Omega_D = (l/\xi)\sqrt{(\Delta F/k_B T)}\tau_{GL}^{-1}$ is the attempt frequency of phase slip events, and $\tau_{GL} = \pi\hbar/8k_B(T_C - T)$ is the GL relaxation time. The total resistance of the wire close to the transition can be expressed as the parallel combination of the resistance due to phase slip events and the normal resistance of the wire R_N:

$$R(T) = \left(R_{LAMH}^{-1}(T) + R_N^{-1}\right)^{-1} . \tag{2.27}$$

However, the prefactor (i.e. the attempt frequency) in the LAMH expression (eq. 2.26) has been recently shown to be incorrect [98]. As a consequence, the resistance of the wire (eq. 2.24) can be better approximated with the “Little fit” [96], where the normal resistance of the wire is explicitly included in the prefactor:

$$R_{Little}(T) = R_N \exp\left(-\frac{\Delta F(T)}{k_B T}\right) \ . \tag{2.28}$$

Vortex slips

In case of 3D wires ($w > 4.44\xi$, $l > 3.49\xi$), the resistance below the transition can be still written according to the form of eq. (2.24), but the energy barrier for phase slips ΔF has to be substituted with that for vortex entry, which can be written as a function of position y (parallel to the width) in presence of a uniform bias current as follows [90]:

$$\Delta U(y, I_b, T) = \mu^2 \epsilon_0 \left[\ln\left(\frac{2w}{\pi\xi}\sin\frac{y\pi}{w}\right) - \frac{I_b}{\mu^2 I_0}\frac{y\pi}{w}\right] \ , \tag{2.29}$$

with $I_0 = \Phi_0 t/4\mu_0\lambda_L^2$ and $\epsilon_0 = \Phi_0^2 t/4\pi\mu_0\lambda_L^2$ the characteristic energy of a vortex in thin films. μ^2 describes the order parameter suppression due to the bias current:

$$\mu^2 = \frac{|\Psi|^2}{|\Psi_\infty|^2} = 1 - \left(\frac{\phi\xi}{l}\right)^2 \ . \tag{2.30}$$

In the limit of zero bias, the resistance of the wire affected by vortex tunneling below T_C writes as [99]

$$R_v(T) = R_\square \sqrt{2\pi}(1+\pi)\frac{l\xi}{w^2}\left(\frac{\mu^2}{k_B T}\frac{\Phi_0^2 t}{4\pi\mu_0\lambda_L^2}\right)^{3/2}\exp\left(-\frac{\mu^2}{k_B T}\frac{\Phi_0^2 t}{4\pi\mu_0\lambda_L^2}\ln\frac{w}{\pi\xi}\right) \ , \tag{2.31}$$

where $R_\square$ is the sheet resistance of the wire and μ^2 is equal to 1 in the zero bias limit.

2.4 Nanowire-based superconducting sensors

In recent years, superconducting nanowires have been employed in nanosized quantum limited sensors, allowing the detection of magnetic field and photons with unprecedented resolution [21, 18].

In particular, nanowires are substituting traditional tunnel Josephson junctions in superconducting quantum interference devices (SQUIDs), which are extremely sensitive sensors of magnetic flux. The development of nanosized devices is boosted by the possibility to achieve performances in terms of sensitivity and low noise, which could allow the investigation of few atomic spins (for more details, see Chapter 8).

On the other hand, superconducting nanowires for single photon detection (SNSPDs) have gained great interest during the last decade [18, 100]. Indeed the theoretical performances of these devices in terms of detection efficiencies (close to 100% up to the near infrared wavelength region), together with the extremely low dark counts (< 1 s^{-1}), fast time response (few ps) and low time jitters (< 30 ps) [18], are very attractive for fast detector applications (for more details, see Chapter 9).

In what follows, we will briefly summarize the basics of the SQUIDs, either when they employ standard Josephson junctions with sinusoidal CPR, and when Josephson junctions are substituted by nanowires.

2.4.1 Dayem nanobridge Superconducting QUantum Interference Devices

The dc-SQUID consists of two Josephson junctions in a superconducting loop (see Fig. 2.10a).

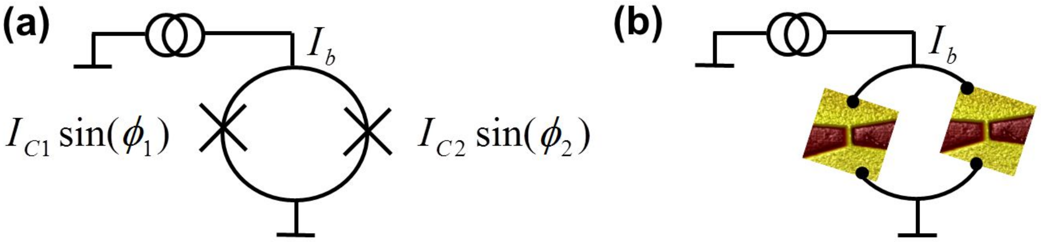

Figure 2.10: (a) Sketch of a typical SQUID, implementing tunnel Josephson junctions. (b) Sketch of a Dayem bridge nanoSQUID, where the Josephson junctions are substituted by nanowires.

The total current through the SQUID is given by adding the currents flowing through each junction, according to eq. (2.13):

$$I_{SQUID} = I_{C1}\sin\phi_1 + I_{C2}\sin\phi_2 \ . \tag{2.32}$$

In a magnetic field, and neglecting the contribution of the inductance of the SQUID arms, ϕ_1 and ϕ_2 are related to each other by the flux through the loop area. In the closed path of eq. (2.10) each junction contributes with a phase difference across the junction. Thence, we obtain

$$2\pi n = \phi_1 - \phi_2 + 2\pi\frac{\Phi}{\Phi_0} \ , \tag{2.33}$$

where Φ is the external magnetic flux. From eqs. (2.32-2.33), then using simple algebraic relations, it follows that the maximum SQUID supercurrent modulates as a function of the magnetic flux through the loop according to (see blue curve in Fig. 2.11a):

$$I_{SQUID} = 2I_C \left|\cos\pi\frac{\Phi}{\Phi_0}\right| \ , \tag{2.34}$$

where we have assumed the SQUID to be symmetric, i.e. both junctions carrying the same critical current $I_{C1} = I_{C2} = I_C$.

If we now consider also the contribution of the inductances L_1 and L_2 of the two SQUID arms, the resulting magnetic field pattern will be modified. The total supercurrent through the SQUID loop is still given by eq. (2.32), while the equation (2.33), in its more general form, writes as

$$2\pi n = \phi_1 - \phi_2 + 2\pi\frac{\Phi}{\Phi_0} + 2\pi\beta_{L,1}\sin\phi_1 + 2\pi\beta_{L,2}\sin\phi_2 \ , \tag{2.35}$$

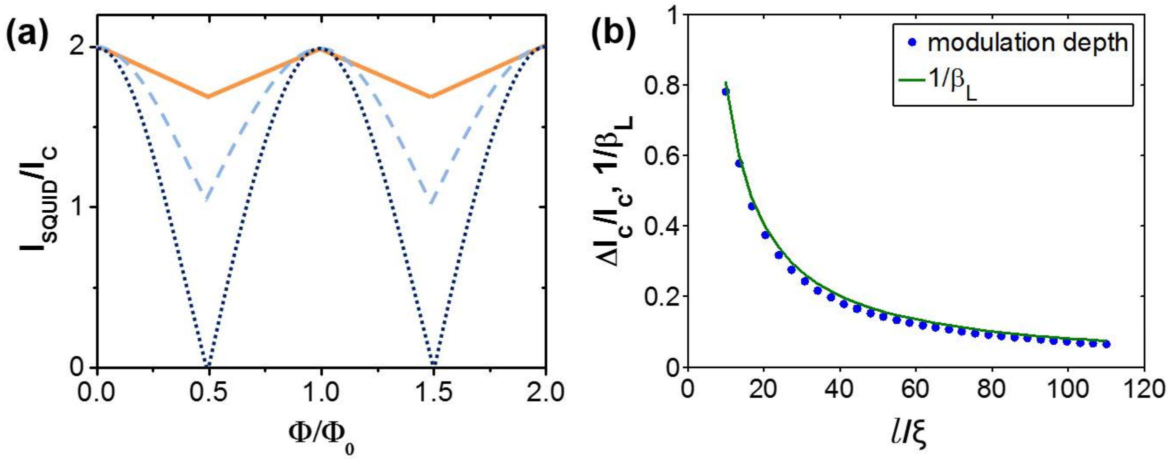

Figure 2.11: (a) Modulation of the critical current as a function of the applied magnetic flux for a standard SQUID, whether the contribution of the inductance is negligible (*dotted line*, $\beta_L = 0$) or it has to be considered (*dashed line* and *solid line*, $\beta_L = 1$ and 5, respectively). (Adapted from [101]) (b) Calculated relative modulation depth of a Dayem bridge nanoSQUID as a function of the wire length.

with $\beta_{L,1} = L_1 I_{C1}/\Phi_0$ and $\beta_{L,2} = L_2 I_{C2}/\Phi_0$ expressing the effect of the self-induced field. To determine the modulation of the critical current as a function of the applied magnetic field, one value for Φ/Φ_0 and one of the junction phase difference (either ϕ_1 or ϕ_2) have to be assumed, then the phase of the second junction has to be varied until eq. (2.35) is satisfied. The values for ϕ_1 and ϕ_2 are substituted in eq. (2.32) to find the total current. The maximum value for I, after repeating this procedure for all initial values of ϕ_1 and ϕ_2, is the critical current for the value of Φ/Φ_0 previously chosen. By iterating this procedure for different values of Φ/Φ_0, the final $I_{SQUID}(\Phi)$ characteristic is achieved (see light blue and orange curves in Fig. 2.11a) [102]. The modulation depth of the magnetic pattern is reduced, according to the value of the screening inductance factor $\beta_L = L_{loop} I_{SQUID}^{max}/\Phi_0$. In particular, Tesche and Clarke [103] proved that, in the limit $L_{loop} I_{SQUID}^{max} \gg \Phi_0$, with L_{loop} total inductance of the SQUID loop, the scaling behavior of the modulation depth ΔI_C on β_L is the following:

$$\frac{\Delta I_C}{I_{SQUID}^{max}} = \frac{1}{\beta_L} \; . \tag{2.36}$$

In Dayem bridge nanoSQUIDs, the two Josephson junctions are substituted by two nanowires (see Fig. 2.10b). Depending on the nanowire dimensions, the CPR may change from sinusoidal single valued to "sawtooth" like multivalued (see Fig. 2.7) and the magnetic pattern may consequently be nonstandard. In particular, if YBCO nanowires are used ($w, t \gg \xi$), the current-phase relation of each wire inside the loop assumes the form of eq. (2.23), and the inductance contribution cannot be ignored. The $I_{SQUID}(\Phi)$ characteristic can be numerically calculated, following the aforementioned procedure, but substituting the sinusoidal CPR of the Josephson junctions in eq. (2.35) with the CPR of the nanowires (eq. 2.23). In Fig. 2.11b we show the calculated relative modulation depth as a function of the wire length. Here, for simplicity we neglected the contribution of the SQUID arms on the total inductance. The solid line is the expression for $1/\beta_L$, assuming that the total loop inductance is given by the kinetic inductance of the wires. Indeed, as it can be seen from Fig. 2.11b, the scaling behavior of the modulation depth ΔI_C on β_L is still given with good approximation by eq. (2.36).

3

Growth and characterization of YBCO films

The possibility to nanostructure oxide superconductors strongly relates to the crystalline structure and surface morphology of thin films, which are a direct result of deposition conditions and substrate properties.

In this chapter we will discuss the work done to optimize the thin film growth of YBCO on various substrates.

3.1 Untwinned and twinned YBCO

Highly textured YBCO thin films are generally deposited by sputtering or by pulsed laser deposition (PLD) at temperatures in the range 700 - 900 °C. Due to these high temperatures, YBCO films grow in the oxygen depleted tetragonal phase ($0.6 \leq \delta \leq 1$). During the subsequent cool down, in highly-pressurized oxygen atmosphere, the oxygen atoms diffuse into the film, causing a phase transition from tetragonal to orthorhombic. Four different twin orientations are formed at this step: to accommodate the strain energy, the diagonals of the *a*-*b* planes of the emerging orthorhombic phase adopt the directions of the diagonals of the *a*-*b* planes of the tetragonal phase [104, 105] (see Fig. 3.1). Two twin orientations, named S_1^+ and S_2^-, align along the [110] diagonal of the tetragonal *a*-*b* planes, while a second pair, formed by the two orientations S_1^- and S_2^+, align along the $[\bar{1}\bar{1}0]$ diagonal of the tetragonal *a*-*b* planes. S_1^+ and S_2^-, as well as S_1^- and S_2^+ can be transferred into each other by a reflection in a $\{110\}$ plane, while S_1^+ and S_2^+, as well as S_1^- and S_2^- can be transferred into each other by a 90° rotation. The orientation angle between S_1^+ and S_1^- and between S_2^+ and S_2^- is $2\eta = 2[\arctan(b/a) - 45°] = 1.04°$, using the lattice parameters of sec. (2.2.1).

The final twinning state in the *a*-*b* planes of the YBCO film is strongly dependent on the in-plane symmetry of the substrate, since the in-plane lattice parameters of the film are subject to a strain induced by the substrate.

In most of the cases, none or only one twin pair is suppressed; consequently the YBCO films are *twinned*. For instance, substrates with a cubic symmetry, as the (001) oriented MgO, $SrTiO_3$ and $LaAlO_3$, have the in-plane lattice which can be transformed into itself both by a 90° rotation and by a reflection in a $\{110\}$ plane: as a consequence, all the four twinning orientations S_1^+, S_1^-, S_2^+, S_2^- are equivalent and will be present in

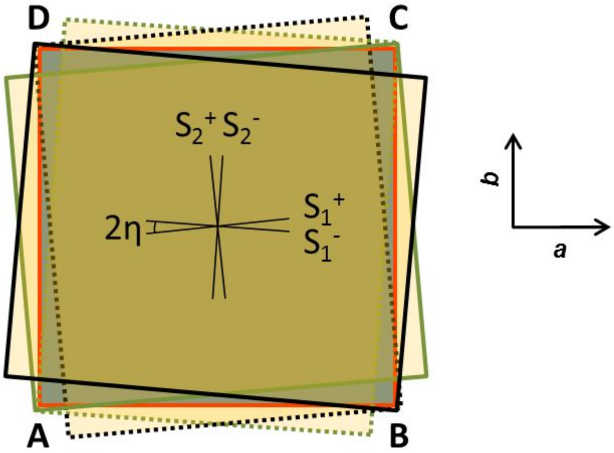

Figure 3.1: Epitaxial relationship between the tetragonal phase (the ABCD square, highlighted by a red outline) and the orthorhombic phase of YBCO (the twin orientations S_1^+ and S_2^- have been outlined in green, with solid and dotted line respectively, while the twin orientations S_1^- and S_2^+ have been outlined in black, with solid and dotted line respectively).

the YBCO films [105]. In twinned YBCO films, a random exchange of the a and b axis is present, and the in-plane anisotropy of the electronic structure, mentioned in sec. 2.2.3, is completely lost. All the physical properties, i.e. the cell dimensions, the critical current densities, measured in the two orthogonal in-plane directions will be equal, corresponding to an average of the a and b axes. Moreover twin planes, separating domains in which a and b directions interchange, act as defects (pinning centers), which weaken locally the superconductivity and can become preferential channels for magnetic-flux penetration [106].

The YBCO films are instead *untwinned* if they grow on substrates with an in-plane symmetry able to suppress both the twin pairs. In this case, the random exchange of the a and the b axes is eliminated: the crystal structure and the superconducting properties, related to the presence of CuO chains along the b direction, are preserved [72]. The removal of twinning domains, up to now, has been obtained with substrates with a vicinal angle [72, 107].

3.2 Choice of the substrates

The achievement of homogeneous and epitaxial YBCO films and the definition of their epitaxial orientation are strongly related to the initial choice of the substrate. As already discussed in sec. (3.1), the crystallographic structure of YBCO, and its superconducting properties, may differ from that of the parent bulk, when it is prepared in epitaxial thin film form. This is due to the biaxial stress determined by the substrate that results in a strained film structure. A relevant parameter, quantifying such stress, is the film/substrate lattice mismatch δ^m, defined as

$$\delta^m = \frac{a_{substrate} - a_{film}}{a_{substrate}} , \tag{3.1}$$

where $a_{substrate}$ and a_{film} are respectively the in-plane lattice parameters of the substrate and the film.

To minimize defects, the use of substrates with lattice parameters very close to those of YBCO should in principle be considered. For this reason substrates as $SrTiO_3$ (STO) and $LaAlO_3$ (LAO) are commonly used, which results in a very small tensile ($\delta^m = +2.2\%$ for STO) and compressive ($\delta^m = -0.7\%$ for LAO) stress of the YBCO cell. However, STO cannot be used in devices where a good coupling with the microwave radiation is required, because of its high dielectric constant and loss tangent, especially at low temperature; LAO instead is affected by twin boundaries that have been reported to cause inhomogeneities in the YBCO films [108], negatively affecting for example their microwave properties [109]. Moreover, both these crystals have a cubic cell, favoring the growth of twinned YBCO films.

MgO crystals, instead, although presenting a large lattice misfit with YBCO (9% in case of (001) orientation), are free from twinning and strain defects. They have a thermal expansion coefficient ($\approx 1 \cdot 10^{-5}$ K^{-1} at 273 K) similar to that of YBCO, and are characterized by low dielectric constant (≈ 10) and microwave losses (loss tangent $\approx 10^{-5}$ at 10 GHz and 90 K) [110]. Moreover, the usage of (110) oriented MgO substrates, with even larger lattice misfit with the two in-plane directions, introduces a strong in-plane anisotropy.

We have chosen MgO (110) as the main substrate to deposit high quality YBCO thin films. We have also optimized the growth of YBCO on MgO (001), STO (001), both with and without a vicinal angle, and LAO (001) substrates. These films have been used both for comparison and, as it will be clarified during the next sections, for specific experiments.

3.3 Thin film growth

YBCO thin film growth is a rather complicated process, as a consequence of the strong dependence of the compound properties on the ratios of different elements (in particular the oxygen doping) and of the difficulty to keep the correct stoichiometry in the films. The homogeneity and smoothness of YBCO thin films are crucial requirements to get reliable transport properties at the nanoscale. They depend on the deposition technique employed for the growth and on the deposition conditions of thin films.

High quality thin films of YBCO have been fabricated during the years by various methods such as rf magneton sputtering, high-pressure dc sputtering, thermal co-evaporation, chemical vapor deposition and pulsed laser deposition (PLD). Among these techniques, high-pressure dc sputtering and PLD (each of them with its pros and cons) are regarded as the most effective methods to produce stoichiometric films.

We have deposited YBCO thin films by PLD on different substrates. A sketch of the used system is in Fig. (3.2). The working principle of this technique is the following: a pulsed high-energetic laser beam is focused on a target, resulting in the ablation of some material. This mixture of atoms, molecules, ions and clusters forms the so-called *plasma plume*, which emerges from the target and condenses on a heated substrate placed in front of the target.

For each substrate, different parameters have to be considered to get films with

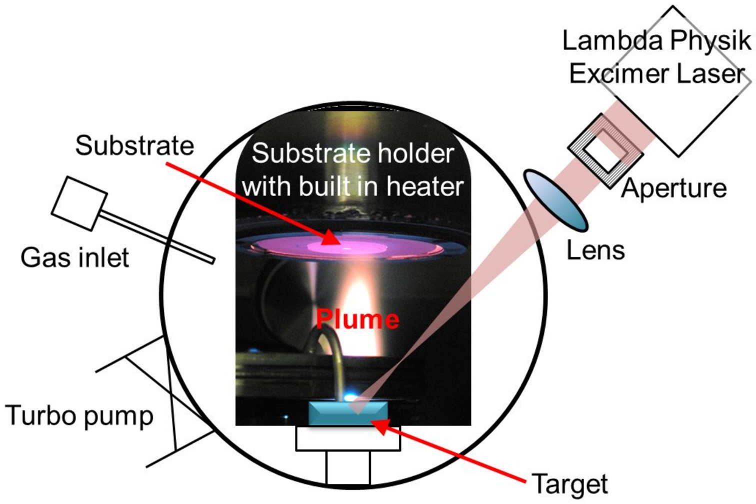

Figure 3.2: Sketch of the PLD system used in this thesis.

the required properties. The parameters influencing the size and shape of the plume and that control the surface kinetics of the deposited atoms, are the fluence and pulse repetition rate of the laser, the oxygen pressure (p_{dep}) and substrate temperature (T_{dep}) during the deposition, the distance between target and substrate (d_{T-S}). As already mentioned in sec. (3.1), the oxygen diffusing into the film during the cool down to ambient temperature is responsible of the doping level of YBCO films. The post-annealing conditions (oxygen pressure p_{ann} and cooling rate) are therefore extremely important.

We have optimized the growth conditions for 50 nm thick YBCO films on four different substrates. Some parameters, like the laser fluence (2 J/cm^2) and the laser pulse repetition rate (4-6 Hz) have been fixed independently of the substrate. The other parameters are listed in Table (3.1) for different substrates.

Parameter	MgO(110)	MgO(001)	LAO(001)	STO(001)
T_{dep} (°C)	760	770	810	770
p_{dep} (mbar)	0.7	0.7	0.6	0.6
d_{T-S} (mm)	54	53.5	53.5	54
p_{ann} (mbar)	900	900	900	900
cooling rate (°C/min)	5	5	5 (*)	5 (*)

Table 3.1: Parameters used to deposit YBCO thin films by PLD on different substrates. The symbol (*) in the cooling rate raw refers to films that have been annealed one hour at 550 °C after the deposition.

The deposition parameters have been chosen to get the right compromise between surface smoothness and critical temperature T_C of the film. In particular, an increase of T_{dep} leads to a high superconducting critical temperature at the expense of the surface morphology; a reduced T_{dep} leads to smooth surfaces at the expense of the critical temperature and sharpness of the superconducting transition.

Depending on the substrates, the YBCO thin films are characterized by different structural and transport properties. In the next sections, we will focus on the morphological and electrical characterization of YBCO films deposited on MgO (110), and STO (001) and LAO (001), representing two of the main substrates used in my thesis work.

3.4 YBCO films on MgO(110)

The surface of a (110) oriented MgO substrate is rectangular ($[0,0,1] = 4.21$ Å, $[1,-1,0] = 5.96$ Å).

In principle, a rectangular lattice cannot be transformed into itself by a 90° rotation, or by a reflection with respect to one of the two in-plane diagonal. Hence both the twin pairs should be suppressed and the YBCO film grown on top is expected to be untwinned. However, this is the case only for substrates having in-plane lattice parameters close to those of YBCO, as in strained STO substrates, having a vicinal angle. For MgO substrates the stress induced by the MgO to the YBCO crystal structure is peculiar and very small, as a consequence of the large mismatch between the in plane lattice parameters (δ^m is $\approx 9\%$ and $\approx 35\%$ along the [0,0,1] and [1,-1,0] MgO directions respectively).

To induce an anisotropic strain to the YBCO thin film, and suppress both the twin orientations, we have nanostructured the MgO surface, with a heat treatment which emulates the effect usually obtained with a vicinal angle (see next section). The MgO substrates have been annealed for 12 hours in the PLD deposition chamber, at the same oxygen pressure used for the deposition of the YBCO films and at a temperature slightly higher than T_{dep}. Prior to the annealing, no polishing or chemical etching treatment of the surface have been made. The as delivered substrate surface is reasonably flat without indication of nanoscale facets (see Fig. 3.3a). Surface reconstruction occurs

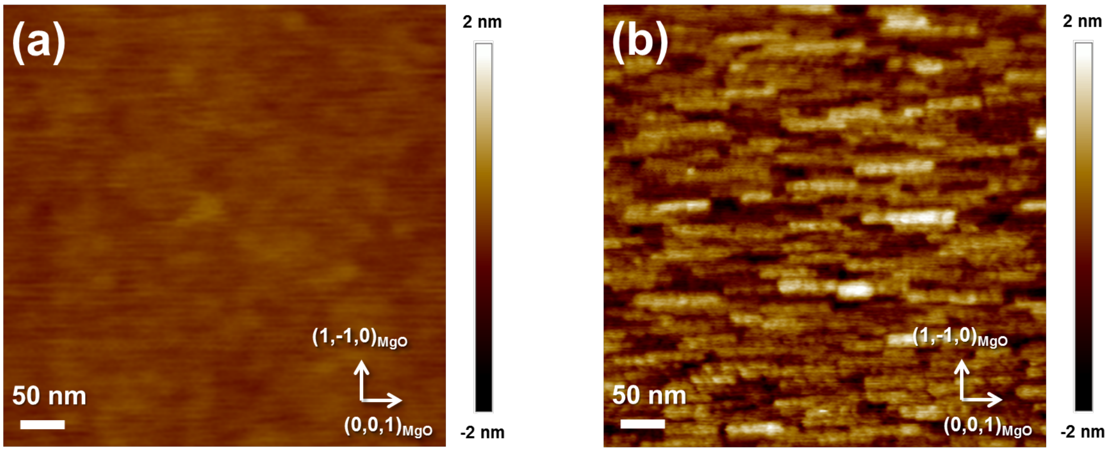

Figure 3.3: AFM images of the surface of a (110) oriented MgO substrate (a) before and (b) after a 5 h long annealing done in the PLD deposition chamber at a pressure $p = p_{dep} = 0.7$ mbar and at a temperature $T = 790°$C.

instead after the annealing (see Fig. 3.3b): elongated islands, running along the [0,0,1] in-plane direction, with average length, width and height of ≈ 80 nm, ≈ 15 nm, and ≈ 1.5 nm respectively, are formed. The occurrence of facets upon annealing on the surface of (110) MgO substrates is a well known phenomenon. However, the dimensions and orientation of the facets seem to be very dependent on the experimental conditions (i.e. annealing temperature and pre-treatment of the substrate) [111, 112, 113]. Nanometer-sized facets as those shown in Fig. 3.3b have never been previously reported.

YBCO films with a thickness of 50 nm have been deposited on (110) MgO substrates in two different conditions: soon after the YBCO deposition temperature is reached (no preannealing), and after the substrate is preannealed between 1 and 12 h.

3.4.1 Structural characterization

The surface morphology of the films has been studied by Atomic Force Microscopy (AFM) and Scanning Electron Microscopy (SEM) (see Fig. 3.4).

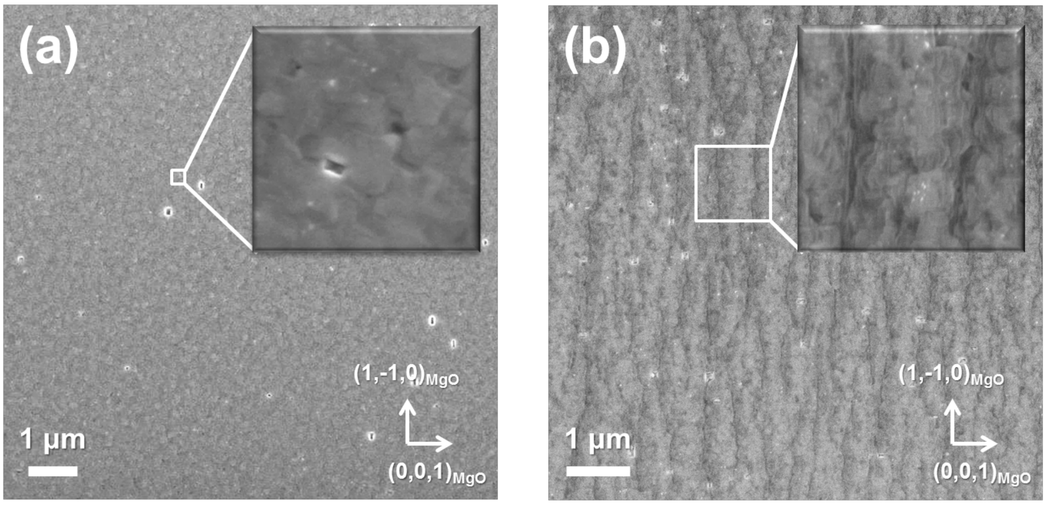

Figure 3.4: (a) SEM picture of a YBCO film, deposited on MgO (110) soon after T_{dep} has been reached (no preannealing). The inset shows *c*-axis spiral domains, randomly oriented, with an average size of about 50-100 nm. (b) SEM picture of a YBCO film, which has been deposited after a substrate preannealing of 1 h at $T = 790°C$. In the inset, elongated domains made of *c*-axis spirals are oriented along the MgO [1,-1,0] direction.

The films present smooth surfaces, characterized by the typical *c*-axis domains with a tridimensional spiral-like growth, few holes and an average roughness of 1.5-2 nm. The film morphology is strongly dependent on the preannealing time of the substrate. Without preannealing, the *c*-axis spiral domains are randomly oriented, and no preferential directions, within the film, are visible (Fig. 3.4a); on the contrary, a preannealing time of 1 hour is already enough to significantly modify the YBCO growth: here, we observe elongated domains where incomplete coalescence lead to the formation of channels 10-20 Å deep in the direction [1,-1,0], perpendicular to the long side of the facets which are formed on the surface of the substrate because of the annealing (Fig. 3.4b). This indicates an additional degree of anisotropy induced by the substrate reconstruction.

The structural properties have been determined by X-Ray Diffraction (XRD) analysis. Symmetric $2\theta - \omega$ scans confirm that the films are highly crystalline and c-axis oriented (see Fig. 3.5). From the angular position of the (0,0,n) peaks the length of the c-axis parameter can be estimated. Without preannealing, the c-axis is 11.73 Å long: such elongation, with respect to the bulk value, can be attributed to a compressive in-plane strain induced by the substrate, which is not expected simply judging by the length of the in-plane lattice parameters of substrate and thin film. However the extracted length of the c-axis parameter decreases when the MgO preannealing time is increased: after 12 h of preannealing, the c-axis length is 11.707 Å, a value much closer to the relaxed one of bulk crystals (see inset of Fig. 3.5). For preannealing times longer than 2 h, the extracted value of the c-axis saturates, which indicates the complete reconstruction of the MgO surface.

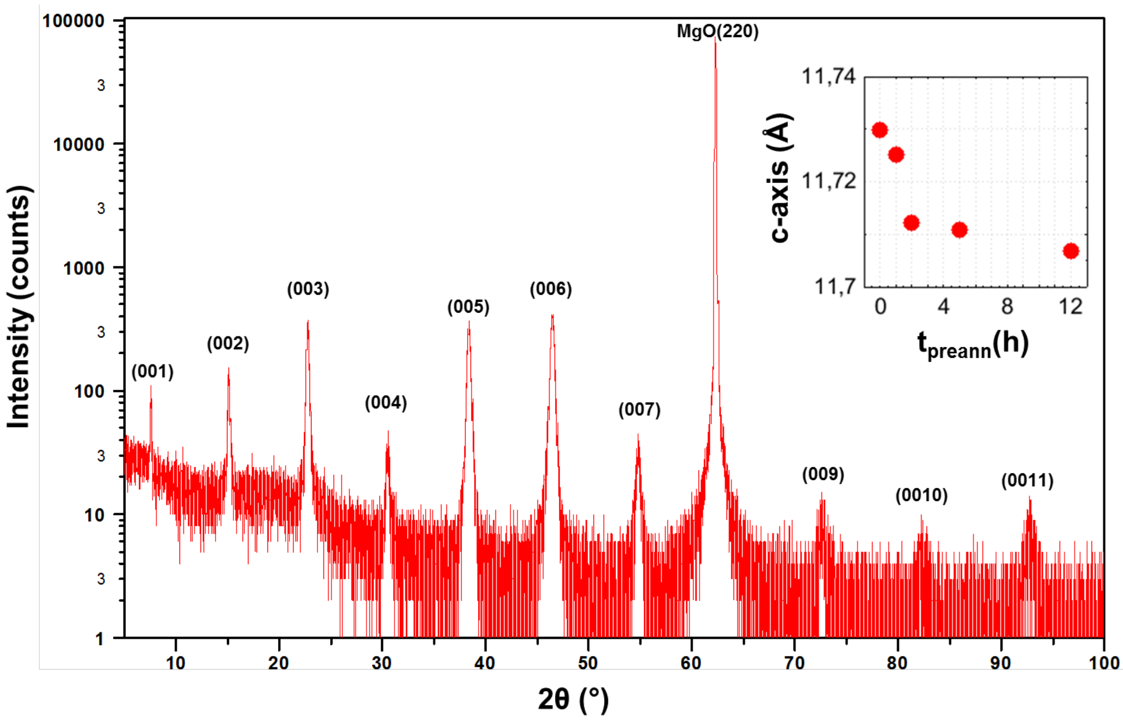

Figure 3.5: XRD $2\theta - \omega$ scan of a 50 nm thick YBCO film on MgO (110). Only (00n) YBCO reflections are observed. In the inset, the c-axis peak extracted by the (00n) reflections is shown, and plotted as a function of the preannealing time of the substrate.

The smoothness of the films is confirmed by the presence of the interference fringes which are visible at both sides of the lowest diffraction order (0 0 n) YBCO Bragg-peaks (see Fig. 3.6a). The position of the maximum of the fringes allow to extract the thickness of the films.

Figure 3.6b shows the rocking curve for a typical film. We get a full width at half maximum (FWHM) $\Delta\omega \approx 1°$, which supports highly textured thin films.

To determine the twinning state of these films as a function of the MgO preanneal-

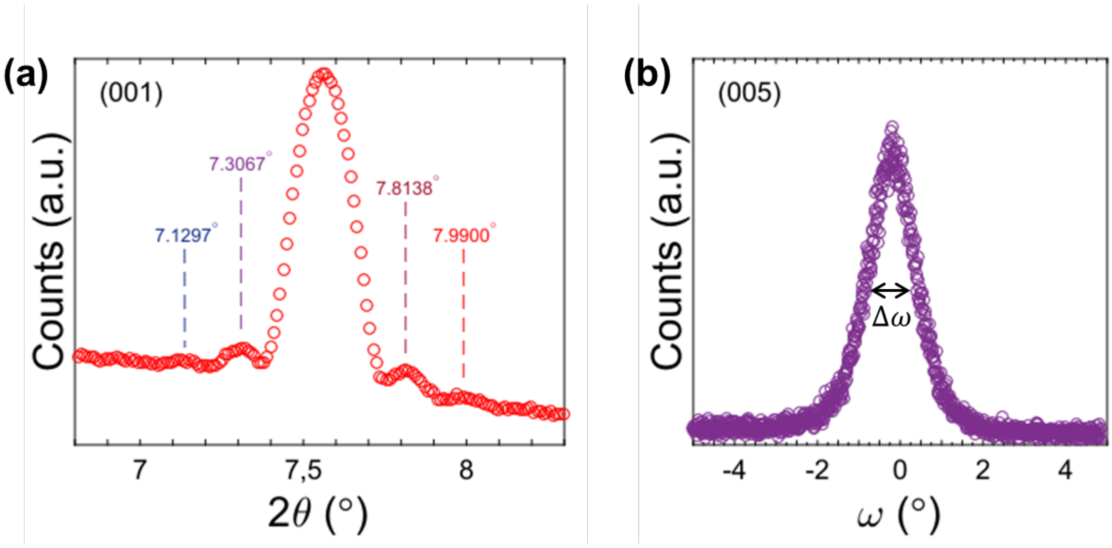

Figure 3.6: (a) $2\theta-\omega$ XRD scan of the (001) reflection for a YBCO film on MgO (110). Interference fringes at both sides of the peak are clearly visible. From the maxima of the four more evident fringes - the corresponding angles $\omega_n = 2\theta_n/2$, $n = 1,2,3,4$, have been highlighted in the picture -, we can calculate the thickness t of the film by using the expression $t = \lambda_{Cu} \cdot [2 \cdot (\sin\omega_n - \sin\omega_{n-1})]^{-1}$, where $\lambda_{Cu} = 1.540598$ Å is the wavelength of the incident X-ray wave. The average thickness of this film, calculated from two couples of adjacent maxima, is 501 ± 1 Å. (b) Rocking curve of the (005) YBCO reflection (FWHM ≈ 1°).

ing time, and the film-substrate orientation relations, the asymmetrical $(l0n)/(0ln)$ reflections of YBCO have been explored. To resolve the splitting of the reflections associated to a and b, we have performed $2\theta-\omega$ maps around the (038)-(308) reflections, which in relaxed films should be at $2\theta = 105.31°$ and $2\theta = 106.80°$ respectively. For each film the maps have been taken at $\phi = 0°$ (ϕ is the rotation angle around the sample surface normal direction) and at $\phi = 90°$, that are along the [0,0,1] and [1,-1,0] MgO directions respectively (see Fig. 3.7).

The acquired asymmetrical maps on films deposited without annealing of the substrate are shown in Fig. 3.7a and 3.7c. Both the (038) and (308) reflections are present, with almost the same intensity, in each of the two maps. The film is strained, as seen by the remarkable elongation of the c-axis parameter, and twinned: random exchange of the a-axis (represented by the presence of the (308) reflection) and b-axis (represented by the presence of the (038) reflection) is present. From the tiny difference of intensity between the two peaks in each map we can estimate an untwinning degree (percentage of the most frequent YBCO in-plane parameter along each MgO in-plane orientation) of 57%. It is worth noticing that the splitting in ω of both the (308) and (038) reflections at $\phi = 90°$ is not related to the twinning state. It is instead associated to a one directional waving of the c-axis parameter, which could be associated to the peculiar growth of the YBCO layer on a substrate with large mismatch. The origin and the characteristic parameters (i.e. amplitude, period) of this waving need a deeper analysis, which will be object of future investigation.

The $2\theta-\omega$ maps relative to films deposited on substrate annealed 12 h are sig-

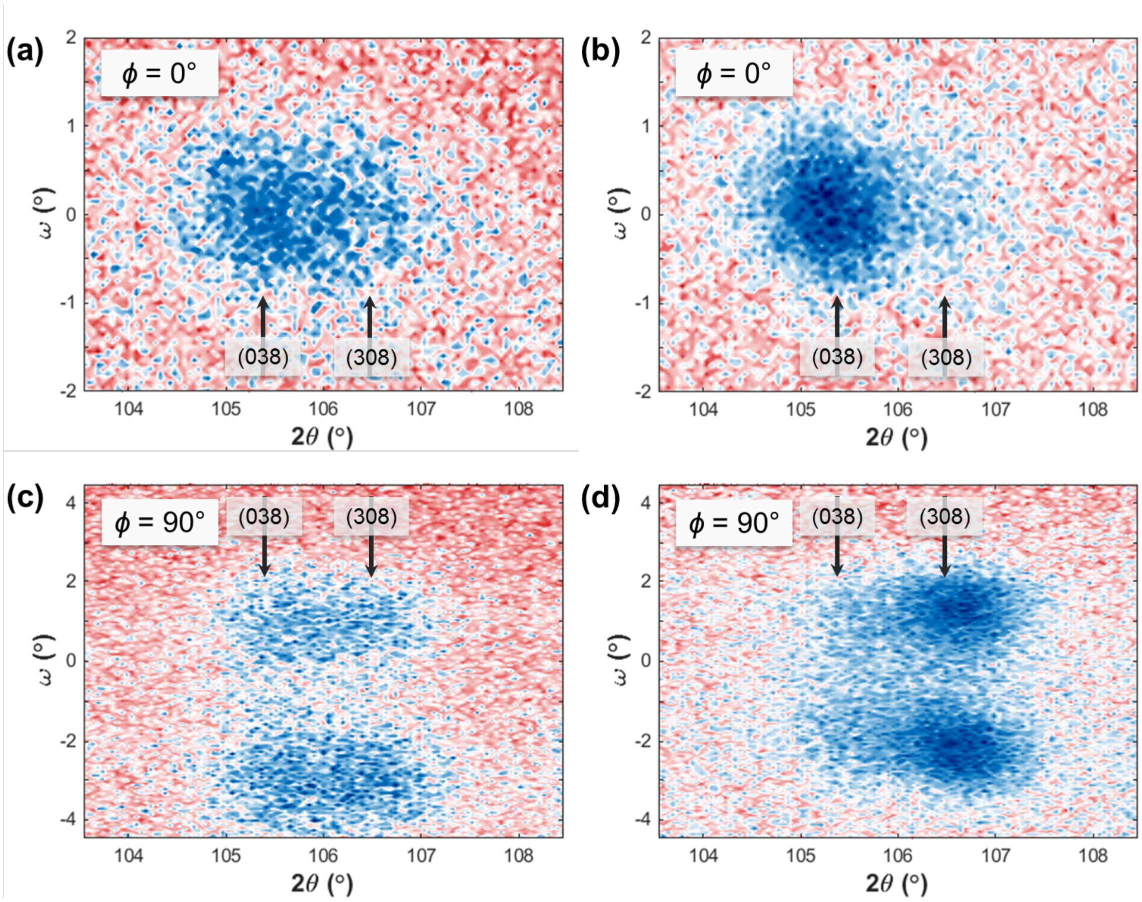

Figure 3.7: XRD $2\theta - \omega$ maps around the (308)/(038) reflections of YBCO (a) fixing $\phi = 0°$, for a film without preannealing; (a) fixing $\phi = 0°$, for a film with $t_{preann} = 12$ h; (c) fixing $\phi = 90°$, for a film without preannealing; (d) fixing $\phi = 90°$, for a film with $t_{preann} = 12$ h.

nificantly different (see Fig. 3.7b and 3.7d). At $\phi = 0°$ the (038) peak (*b*-axis) is predominant, while at $\phi = 90°$ the opposite situation is present, and the (308) reflection (*a*-axis) is much stronger than the (038) one. The presence of the elongated facets on the surface of the MgO substrate after the annealing favors the growth of almost untwinned YBCO films. The ratio of the intensities of the two reflections is the same in both maps: from this value we can estimate an untwinning degree of 82%, close to the values achieved in YBCO films deposited on substrates with vicinal angle. Moreover, from the 2θ position of the (308) and (038) reflections, and considering the value of *c*-axis extracted by the (0,0,*n*) symmetrical reflections, we can derive the length of the *a*-axis and *b*-axis parameters, which are respectively equal to $a = 3.82$ Å and $b = 3.88$ Å. With regards to the film-substrate orientation relationship, the (038)/(308) maps show that the *b* axis is aligned along the [0,0,1] MgO direction ($\phi = 0°$), while the *a* axis is aligned along the [1,-1,0] MgO direction ($\phi = 90°$).

3.4.2 Transport characterization

Transport properties of the YBCO films on (110) MgO substrates have been studied through resistance vs temperature $R(T)$ measurements (see Fig. 3.8). The critical temperature T_C (defined at the onset of the superconducting transition) is $\approx$ 86 K, well below the T_C of the bulk, but still among the highest values reported in literature so far for MgO substrates [114]. The homogeneity of the films is proven by a rather sharp transition of about 1 K.

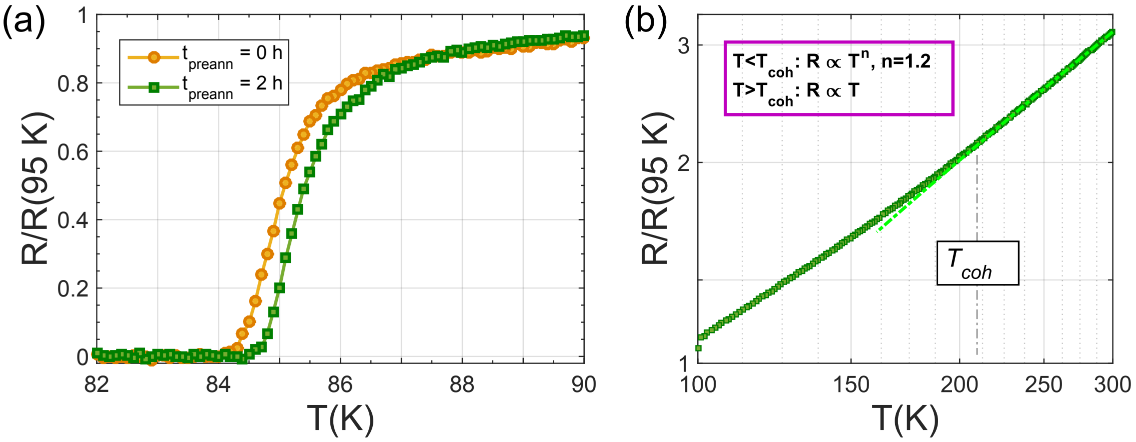

Figure 3.8: (a) $R(T)$ measurements, normalized to the value of the resistance at 95 K, of a film deposited soon after the T_{dep} is reached (*squares*) and of a film whose substrate has been preannealed 2 hours (*squares*). (b) Normalized resistance of the same YBCO film, characterized by a long substrate preannealing, as in panel (a), in the temperature range between 100 and 300 K (the plot is in log-log scale for a better visualization of the data). The dashed line represents the linear fit to the data at temperatures close to 300 K. There is a good agreement between the data and the linear dependence down to $T_{coh} \approx 210$ K. Below T_{coh}, the data have been fitted assuming a power low dependence $R = a + b \cdot T^n$, where a and b are free parameters, and $n = 1.2$.

From the normal state properties of the films we can also extract additional information about the oxygen doping. Fully oxygenated YBCO films ($\delta \approx 0$) lie on the slightly overdoped side of the superconducting dome [115, 116]. To promote the full oxygenation of the YBCO layer, the films have been slowly cooled down after the deposition in oxygen pressure at 900 mbar [117]. The $R(T)$ measurement is linear only at high temperature, while it exhibits a power low dependence below $T \approx 210$ K (see Fig. 3.8b). This behavior is typical for YBCO films in the overdoped side of the phase diagram, characterized by the so-called coherence temperature T_{coh}, which increases as the oxygen doping increases: below T_{coh} the dependence of the resistance with the temperature is not linear any longer and it becomes a power low like, $T \propto T^n$. The exponent n varies from 1 at the optimal doping to 2 at the oxygen doping corresponding to the disappearance of the superconducting phase [118, 119, 120].

3.5 YBCO films on STO(001) with vicinal angle

Our nearly untwinned films on (110) oriented MgO substrates have been compared with those deposited on (001) oriented STO substrates, with nominal vicinal angles $\alpha_V = 1.0°$ and $1.5°$. For both the investigated α_V, the vicinal cuts are towards the [010] STO direction.

The surface of STO substrates, having a vicinal angle α_V towards the [010] (or the [100]) direction exhibits a periodic sequence of steps, with very straight edges and a height h_T, spaced by (001) terraces, whose width w_T decreases with increasing α_V (see Fig. 3.9a). When a YBCO thin film is grown on top of these terraces, a strain

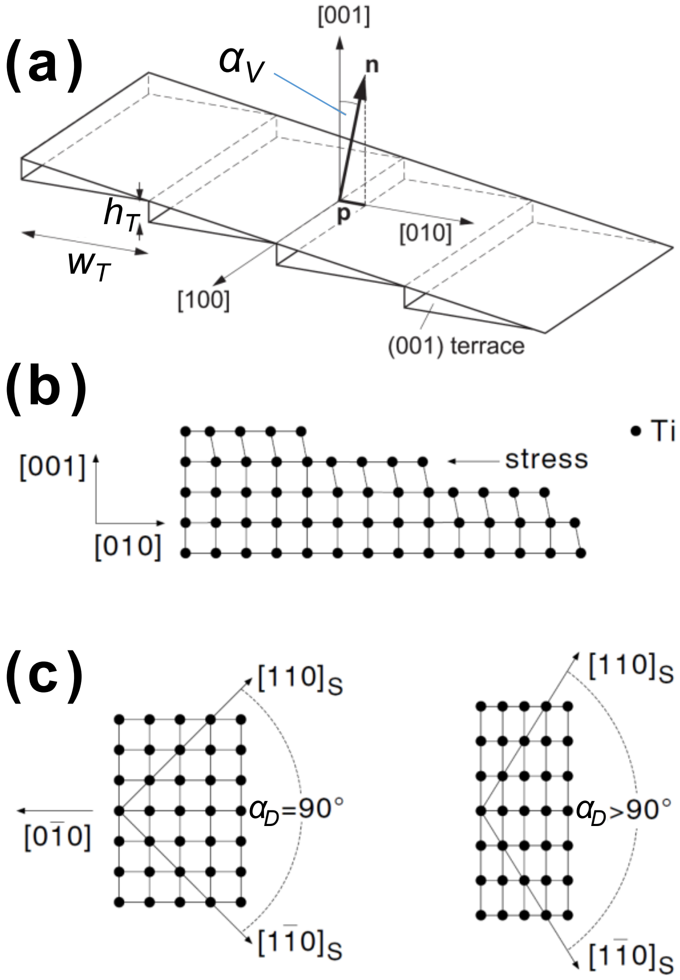

Figure 3.9: a) A vicinal angle α_V towards the [010] STO direction leads to (001) terraces with width w_T and height h_T. The vectors $\vec{n}$ and $\vec{p}$ represent respectively the surface normal and its projection to the (001) terrace. b) Cross section of the (001) terraces on the STO surface. When a YBCO film is deposited, a compressive strain, perpendicular to the step edge, occurs on the STO terraces. c) Top view of a (001) terrace of the STO surface, both in its unstrained condition (*left*) and after a YBCO thin film is deposited on top (*right*). Due to the lattice mismatch, the substrate surface is distorted and transforms to a rectangular lattice, with the angle α_D between the two in-plane diagonals becoming larger than 90°. These three panels are adapted from [121].

occurs at the interface, because of the small lattice mismatch between the cubic STO substrate ($a = 3.905$ Å) and the unit cell of the YBCO film (which transforms from tetragonal to orthorhombic during the postannealing). The in-plane lattice parameters of the YBCO unit cell are stretched, while the (001) terraces of the STO substrate are compressed. However the strain of the substrate is strongly anisotropic, since the STO lattice parameter shrinks more easily perpendicular to the step edges, where the atoms are under-coordinated (see Fig. 3.9b). As a consequence, a distortion of the substrate surface occurs: the unstrained square lattice of the (001) terraces transforms into a strained rectangular lattice (see Fig. 3.9c). This distortion has a strong influence on the twinning domains of the YBCO thin films: if $\alpha_V < 10°$ the longer b-axis parameter of YBCO tends to align preferentially along the step edges, where the STO lattice parameter is longer [121, 122].

The surface of the vicinal (001) STO substrates is more compressed by the YBCO films toward the direction of the vicinal angle. Increased α_V are associated to smaller terrace width. Since the surface lattice can be strained more easily toward the direction of α_V, reducing the terrace width enables a tailoring of the anisotropic strain, therefore of the twinning state of YBCO. By changing the vicinal angle and its orientation, as well as the termination of the STO substrates, different twinning states have been explored in YBCO. In particular, an untwinning exceeding 95% has been reported, using a STO substrate having a vicinal angle $\alpha_V = 1.1°$ towards the [010] direction [107].

We have optimized the growth conditions so to achieve 50 nm thick films with a T_C of ≈ 87.5, and a rather sharp transition (< 1.5 K).

The films present very smooth surfaces, characterized by evident c-axis spirals giving a clear indication of a 3D growth (see Fig. 3.10).

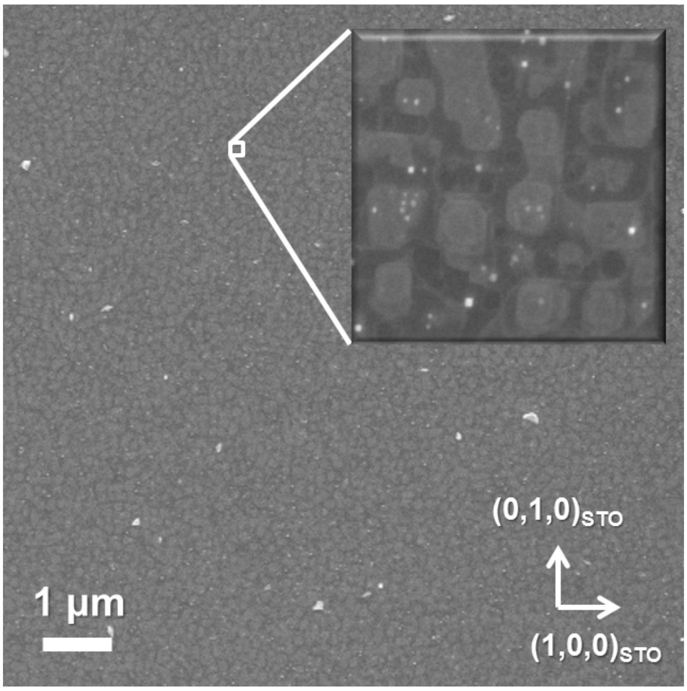

Figure 3.10: SEM image of a YBCO film on a STO (001) substrate with $\alpha_V = 1.0°$.

Symmetric $2\theta - \omega$ maps have been performed, to determine not only the structural properties of the films, but also their relative orientation with respect to the STO substrate (see Fig. 3.11). The films are highly crystalline and c-axis oriented. From the angular position of the (0,0,n) peaks the length of the c-axis parameter can be estimated. The determined value, c = 11.67 Å, is lower than the relaxed, bulk one: such c-axis compression is expected since the in-plane STO parameters ($a = b = 3.905$ Å) are larger than those of the YBCO, therefore inducing an in-plane tensile strain to the film. In addition we can see in Fig. 3.11, which refers to a film grown on a substrate with $\alpha_V = 1.0°$, that a tilt $\Delta\omega \approx 1°$ is present between the (0,0,n) reflections of YBCO and those of STO. The c-axis has an inclination with respect to the crystallographic surface normal of STO, and consequently the film is tilted toward the optical surface normal. This phenomenon has been seen in literature, and associated to a regime where the YBCO diffusion length during the PLD growth ($\approx$ 20 nm [123]) is smaller than the substrate terrace length [107].

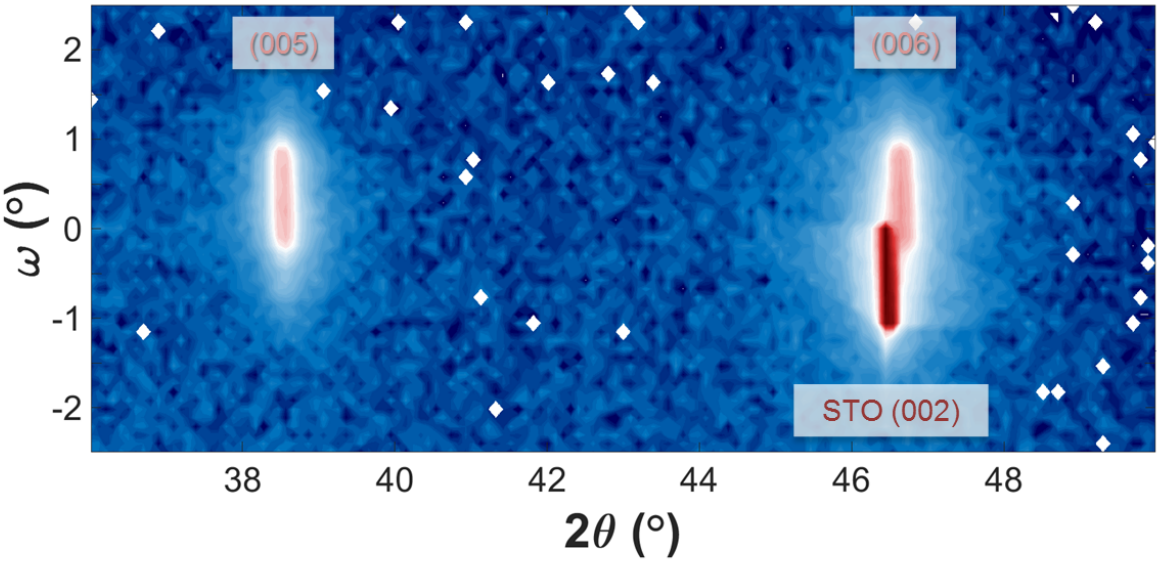

Figure 3.11: XRD symmetrical $2\theta - \omega$ map in the range $2\theta = [36, 50]$ of a 50 nm thick YBCO film on (001) STO substrate with $\alpha_V = 1.0°$. The (005) and (006) YBCO reflections are visible, as well as the (002) STO reflection. The elongation of the peaks in ω is an artifact of the diffractometer.

Fig. 3.12 shows the (038)-(308) maps of a film grown on a substrate with $\alpha_V = 1.0°$. They have been taken at $\phi = 0°$ and at $\phi = 90°$, corresponding to the directions parallel and perpendicular to the step edges, respectively. At $\phi = 0°$ the (038) reflection (b-axis) is much stronger than the (308) reflection. The opposite situation, with an inverted intensity ratio, is present at $\phi = 90°$. As expected, these films are untwinned. From the ratio of the intensities of the two reflections we can estimate an untwinning degree of 88.5% for the film shown in Fig. 3.12. However, when using substrates with $\alpha_V = 1.5°$, we have achieved untwinning degrees as high as 91%.

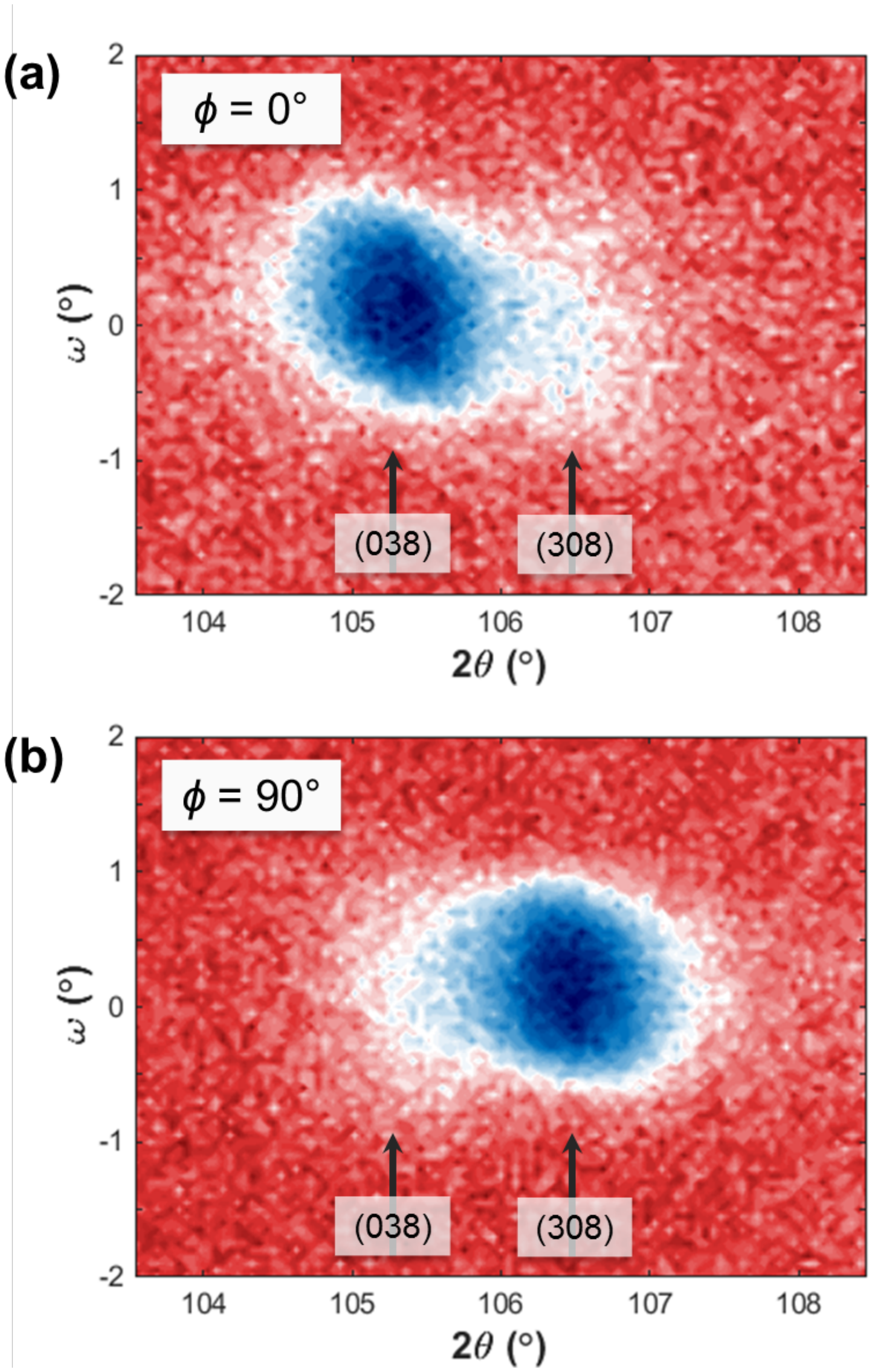

Figure 3.12: XRD $2\theta - \omega$ maps around the (308)/(038) reflections of YBCO (a) fixing $\phi = 0°$; (b) fixing $\phi = 90°$. From the position of the two reflections we can extract the following in-plane parameters: $a = 3.835$ Å, $b = 3.895$ Å.

3.6 Summary of the film properties

Table (3.2) summarizes the results of the transport and morphological characterizations that we have preformed on YBCO films deposited on (001) oriented MgO substrates. In addition, the in-plane epitaxial relations found for the YBCO films grown on the three different substrates (MgO, STO and LAO) are schematized in Fig. 3.13.

Parameter	MgO(110)	MgO(001)	LAO(001)	STO(001) 1.5° off
T_C (K)	≈ 86	≈ 86.5	≈ 89	≈ 87.5
roughness (nm)	≈ 1.5	≈ 2	≈ 0.8	≈ 0.8
a-axis (Å)	3.82	-	3.82	3.835
b-axis (Å)	3.88	-	3.88	3.895
c-axis (Å)	11.71	11.70	11.71	11.67
untwinning	82%	-	60%	91%

Table 3.2: Transport and structural properties of the optimized YBCO films. In case of MgO(110), we have considered the results achieved on YBCO films grown on preannealed (12 h) substrate.

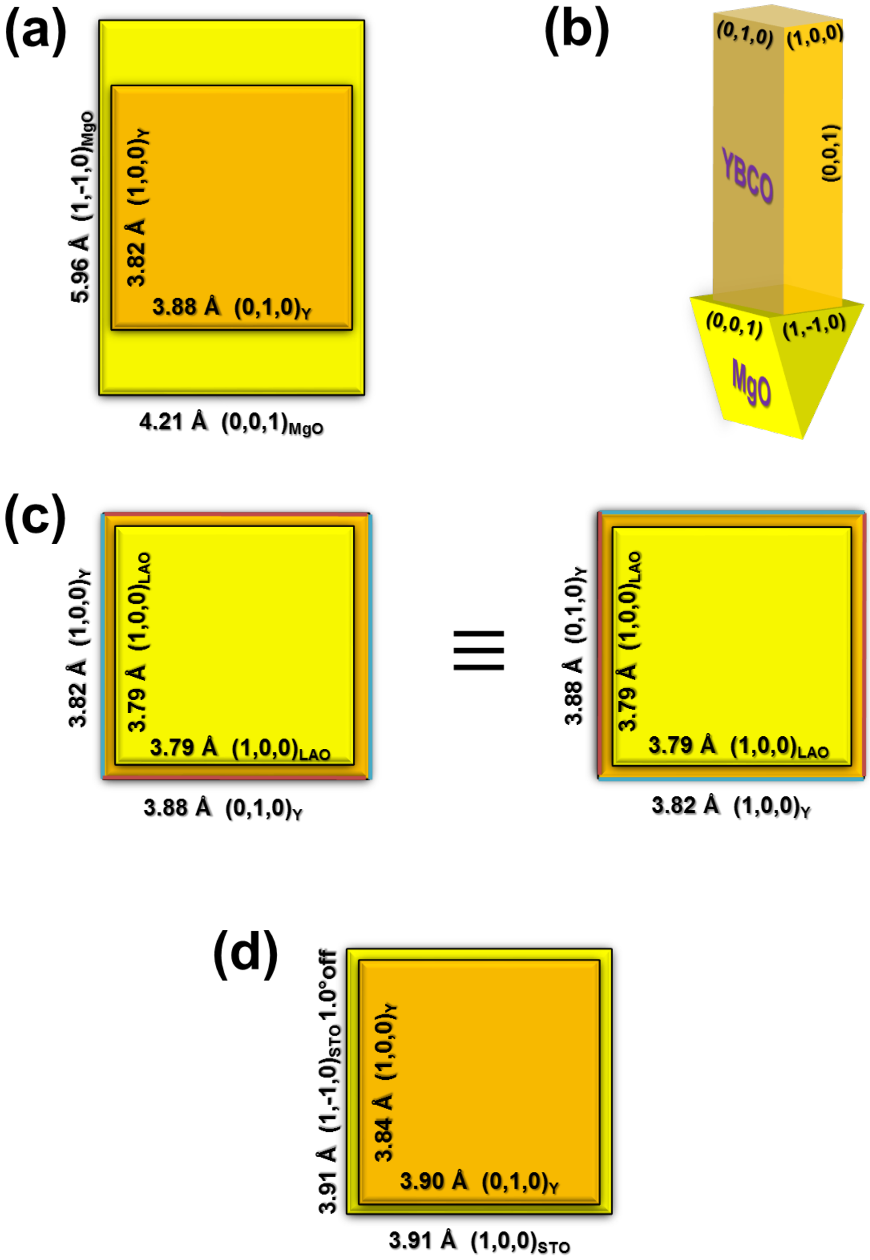

Figure 3.13: (a) Top view and (b) side view sketches of the YBCO/MgO(110) epitaxial relations. After $p_{preann} = 12$ h, the film is almost untwinned, and the 82% of the *a*- and *b*-axis domains is aligned according to these relations. (c) Sketch of the YBCO/LAO(001) epitaxial relations: the film is twinned and a random exchange of the *a*- and *b*-axis occurs. (d) Sketch of the epitaxial relations of YBCO/vicinal angle STO(001). The YBCO film is untwinned and if the vicinal angle is 1.5° the 91% of the *a*- and *b*-axis domains align according to these relations.

4

Ultrathin YBCO films

For some applications, like nanowire based single photon detectors, it is required the nanopatterning of films with a thickness of few atomic layers. In this case, the proper stoichiometry has to be preserved, at thicknesses comparable with ξ.

The realization of ultrathin YBCO films has been object of intense research since the discovery of the cuprate superconductors. In the beginning, the focus was on few (ideally one) unit cell thick YBCO films, embedded between layers of $PrBa_2Cu_3O_{7-\delta}$ (PBCO), and the main systems under investigation were YBCO/PBCO superlattices [124, 125] and PBCO/YBCO/PBCO trilayers structures [126, 127]. These systems, precursors of 2D superconductors [128], were mainly studied with the aim a) to determine if in YBCO, and in HTS in general, the superconducting phenomenon could occur within a single atomic layer, at thicknesses comparable with the size of the superconducting coherence length ξ, and b) to establish the role of the inter-CuO_2-layer coupling in determining the superconducting critical temperature T_C.

The choice of using PBCO in combination with YBCO was initially made because of the peculiar PBCO properties, being not metallic, not superconducting, and with a crystallographic structure and lattice parameters very similar to YBCO. PBCO is often used as a protective layer, since bare ultrathin YBCO films are characterized by degraded superconducting properties, as a consequence of the surface and chemical instability of the compound [126]. However, the deposition at high temperature of a PBCO layer may also lead to some complications, like the interdiffusion at the interface between PBCO and YBCO, which brings to the substitution of Pr atoms in Y sites, with percentages as high as 30% [129]. It is known that a 45% atomic interdiffusion into the first YBCO layer results in a T_C of $\approx$ 30 K for the resulting alloy [128]. Thence, PBCO capped YBCO films cannot be considered the proper structure to realize ultrathin nanowires.

In this chapter, we will show the growth and characterization of ultrathin YBCO films on MgO (110) substrates, which exhibit superconductivity at thicknesses down to 3 nm. They have been obtained by using Au as capping layer.

4.1 Growth and structural characterization

We have deposited YBCO films, with thicknesses from 50 nm down to 3 nm, on MgO (110) substrates by using the same deposition parameters which have been listed in section 3.3, and after the substrate has been preannealed for one hour. For each thickness, we have deposited two YBCO films: the first one is a bare YBCO films, and the second has a 50 nm thick Au layer, in situ sputtered after the YBCO deposition. To sputter the Au layer we have used a low power ($P = 10$ W), to minimize possible damages to the YBCO surface.

A proper estimate of the thickness of the deposited YBCO films has been achieved, with an error of less than 1 atomic layer (≈ 1 nm), using AFM (measuring the height of the step between the film surface and a non-deposited area of the substrate) and XRD (measuring the period of the interference fringes visible at both sides of the lowest order $(00n)$ reflections).

A morphological and structural characterization has been carried out to establish the quality of the YBCO films.

Surface morphology has been studied by AFM and SEM. The films, in agreement with what previously seen in sec. 3.4, present smooth surfaces, characterized by the typical c-axis domains with 3D spirals. With respect to thicker films, we observe that a) the average roughness is lower, being at the order of one atomic cell, and b) the small holes on the surface, previously seen in Fig. 3.4b, and located at the edges of the elongated islands, become larger and deeper (see Fig. 4.1). In particular, for films with thickness $t = 5$ nm or lower the coalescence between the islands is not complete and the voids have the same depth as the film thickness.

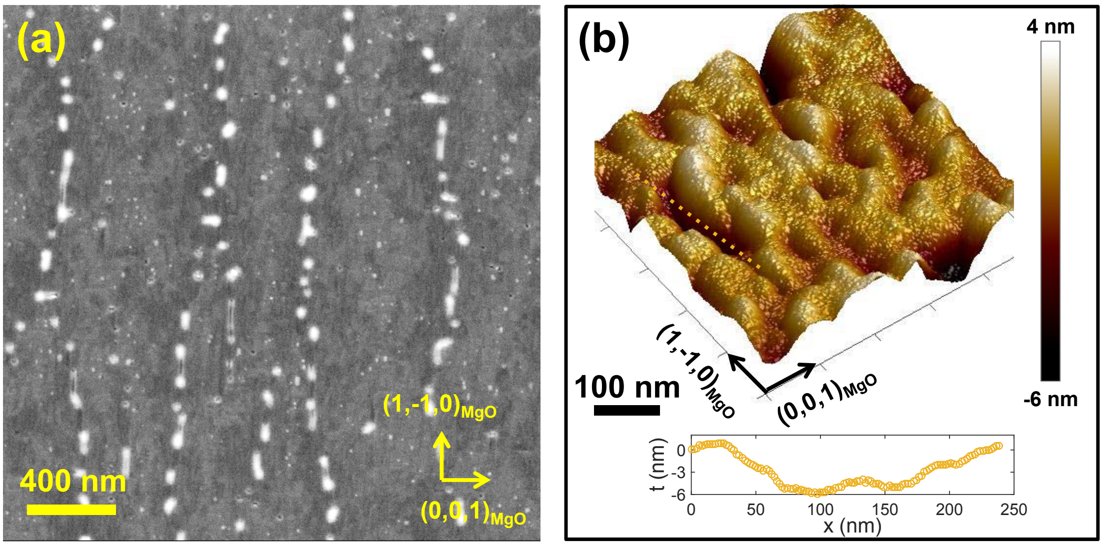

Figure 4.1: (a) SEM picture of a 10 nm thick YBCO film deposited on (110) MgO, after a substrate preannealing of 1 h at $T = 790°$ C. Some regions appear white due to charging induced by the substrate. (b) These regions have been further investigated by AFM: they represent deep voids, at the edge between the islands, where the coalescence is incomplete (see depth profile, corresponding to the dotted line in the 3D AFM picture).

The structural properties have been determined by XRD analysis, performed on films down to thicknesses of 3.5 nm. Symmetric $2\theta - \omega$ scans confirm that also the ultrathin films are highly crystalline and c-axis oriented. From the angular position of the $(00n)$ peaks we can estimate the c-axis length. The ultrathin films are all characterized by a c-axis length, ≈ 11.715 Å, which is approximately the same as that of the 50 nm thick overdoped films deposited on MgO substrates preannealed for 1 h (see Fig. 4.2a).

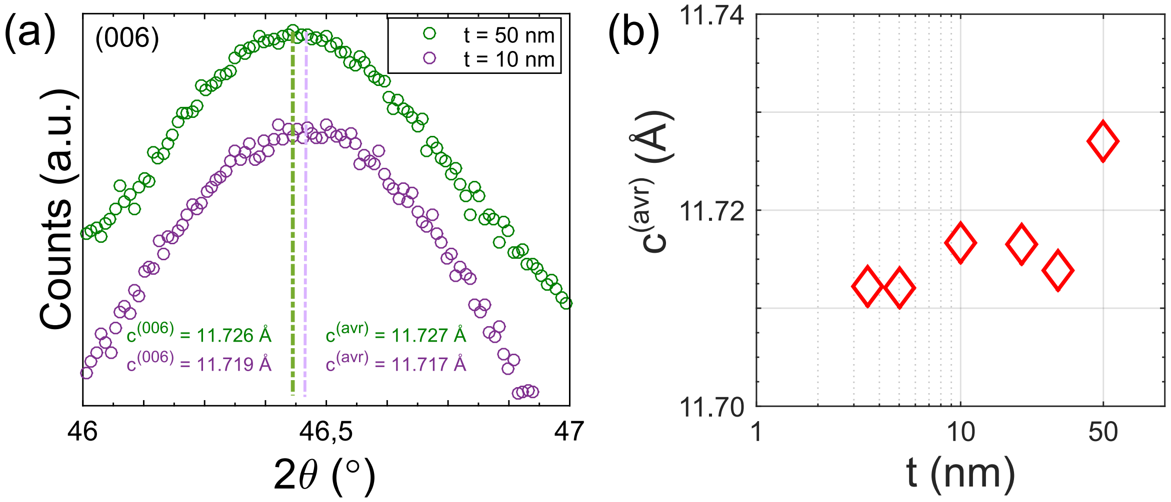

Figure 4.2: a) $2\theta - \omega$ XRD scans of the (006) reflection of a 10 nm thick film (violet circles) and of a 50 nm thick slightly overdoped film (green circles). The maximum of each peak is highlighted by the dashed line. The c-axis values extracted from these two peaks, $c^{(006)}$, are reported, together with the average values $c^{(avr)}$, extracted considering all the $(00n)$ reflections. b) The c-axis average value $c^{(avr)}$ is plotted as a function of the film thickness.

In ultrathin YBCO films, especially when grown on substrates with a large mismatch, a c-axis expansion has been observed in literature [130], and attributed to a large number of misfit dislocations caused by the extreme strain induced by the substrate on the whole film thickness. Instead our films, as a consequence of their peculiar strain when grown on MgO (110) substrates (widely discussed in the previous chapter), do not show this c-axis expansion. Therefore, they seem not to be affected by a large number of misfit dislocations.

Films with thicknesses below 30 nm have the c-axis which is even a bit shorter (0.01 Å) than the reference 50 nm thick films (see Fig. 4.2b). This small c-axis reduction could be attributed to a different oxygen doping. In particular, the high postannealing pressure we use to reach the right oxygen stoichiometry can be even more effective when the films are only few unit cell thick: as a consequence, this small c-axis compression indicates that ultrathin YBCO films could be even more overdoped than the 50 nm thick one.

4.2 Transport characterization

Transport properties of the ultrathin YBCO films have been studied by $R(T)$ measurements. The aim was to check how the superconducting properties are modified by the reduction in thickness. For ultrathin YBCO films, when grown on substrates with a large mismatch (without a PBCO seed layer), a strong reduction of the temperature corresponding to the zero resistance, T_C^0, has been reported [131]. Here we show instead that the T_C^0 of our films is higher than the liquid nitrogen temperature down to thicknesses of 10 nm. In addition, from the onset of the superconducting transition and from the normal state properties of the ultrathin films we are able to extract additional information about the oxygen doping.

4.2.1 Determination of the oxygen doping

In Fig. 4.3a and 4.3b the $R(T)$ measurements of the bare 10 and 20 nm thick films are compared with those of the bare 50 nm thick film.

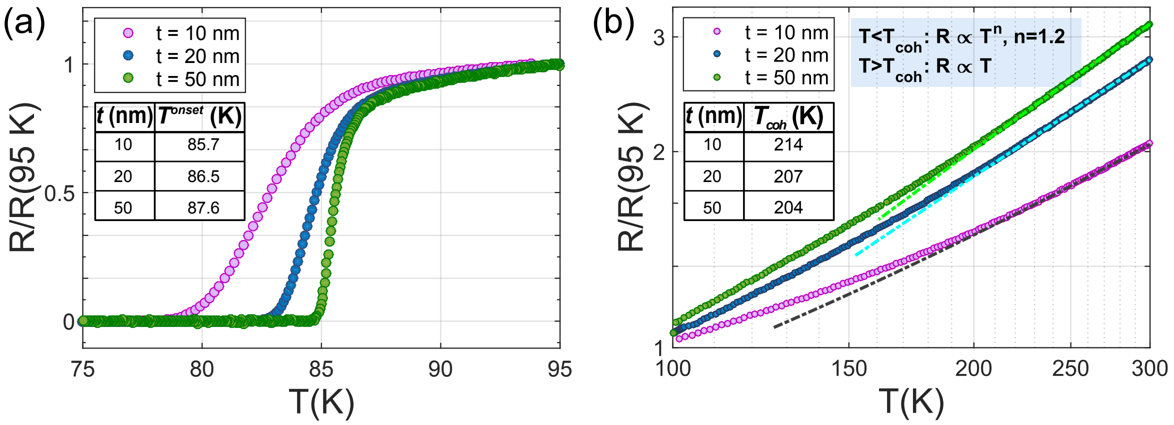

Figure 4.3: a) $R(T)$ curves, normalized to the value of the resistance at 95 K, of bare YBCO films with thicknesses $t = 10, 20$ and 50 nm. The T^{onset} of these three films, calculated as the temperature where the resistance $R = 0.9 \cdot R_N$ (with R_N being the normal resistance and corresponding to the change in $\mathrm{d}R/\mathrm{d}T$), is listed in the inset table: this value slightly decreases when decreasing the thickness, as a possible consequence of the better oxygenation of ultrathin films. b) Normalized resistance of the same three films presented in panel a), in the temperature range between 100 and 300 K (the plot is in log-log scale for a better visualization of the data). The dashed lines represent the linear fit to the data at temperatures close to 300 K. The linear dependence is in good agreement with the data down to T_{coh}. Below T_{coh}, the $R(T)$ data can be fitted assuming a power low dependence $R = a + b \cdot T^n$, where a and b are free parameters, and $n = 1.2$ for the three films. The resulting T_{coh} of the three films is listed in the inset table: the value slightly increases when decreasing the thickness, indicating the better oxygenation of ultrathin films.

The onset temperature of the superconducting transition, T^{onset}, slightly changes with the film thickness (see inset table in Fig. 4.3a), while T_C^0 substantially decreases by reducing the thickness (due to the significant broadening of the superconducting transition, see Fig. 4.3a).

In principle a lower T^{onset} could be associated both to an increase or to a reduction of the oxygen doping within the film. However, in this case, we can attribute the T^{onset} reduction to the better oxygenation of ultrathin films.

The 10 nm and 20 nm thick films behave similarly to the 50 nm thick film, shown in sec. 3.4: the $R(T)$ are linear only at high temperature, while they exhibit a power low dependence, characterized by the same exponent $n = 1.2$, below T_{coh} (see Fig. 4.3b).

As shown in the inset table of Fig. 4.3b, the T_{coh} slightly increases by 10 K, when reducing the film thickness to 10 nm, signifying an oxygen content comparable with 50 nm thick films, if not slightly higher than that.

4.2.2 Broadening of the superconducting transition

In Fig. 4.4 we have plotted (*circles*) the T_C^0 extracted by our YBCO films - bare films above $t = 10$ nm and Au capped films below $t = 10$ nm - as a function of the thickness. As discussed earlier the T_C^0 slightly decreases down to 5 nm, which corresponds approximately to 4 unit cells. For lower thicknesses, it abruptly drops. Films below 3 nm, where only two complete atomic layers are present, are still superconducting with a $T_C^0 = 14.5$ K. At even lower thicknesses the films are not superconducting down to 4.2 K.

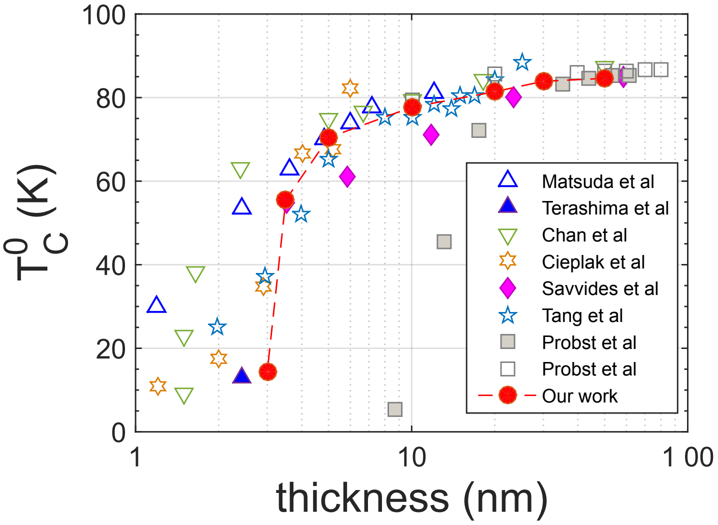

Figure 4.4: Zero resistance critical temperature T_C^0 of our capped and bare YBCO films versus their thickness (*circles*). Our results have been compared to those previously achieved in literature. In particular, open symbols show results achieved on YBCO films sandwiched between two PBCO layers by Matsuda et al [126, 132], Chan et al [129], Cieplak et al [127], Tang et al [133], and Probst et al [134]. Filled symbols show instead results achieved on YBCO films, not embedded between two PBCO layers, by Terashima et al [126], Savvides et al [130], and Probst et al [131].

We have compared our results with those published in literature starting from the beginning of the '90s up to now.

As previously mentioned, most of the works have focused on YBCO films sandwiched between two PBCO layers [126, 132, 129, 127, 133, 134]. The T_C^0 values as a function of the YBCO thickness, collected from these papers, have been shown as open symbols in Fig. 4.4. In all the previous works, T_C^0 gradually decreases down to 4 unit cell thick ($t \approx 5$ nm) YBCO films, while it presents a sudden drop at lower thicknesses. The same behavior can be also seen in multilattices, when the YBCO layers are interchanged either with PBCO layers [135] or $SrTiO_3$ layers [136]. Below 5 nm thick films, the spread of T_C^0 values, which have been measured in different works, becomes wider. The origin of this spread can have at least two possible reasons. On one side, on such extremely thin YBCO films the error which can be done in the determination of the thickness becomes significant; on the other, a small difference, between different samples, in the interdiffusion rate between Pr and Y atoms at the interfaces or in the PBCO stoichiometry and/or the presence of crystalline defects, can be the origin of such huge variation of T_C^0 in these thickness range [137].

The best result, whose validity has been object of debates for years [138, 139], is the one achieved by Terashima et al [126, 132], reporting a $T_C^0 = 30.1$ K in a one unit cell thick YBCO film.

The origin of such a wide broadening of the superconducting transition, significantly suppressing the T_C^0 of thin films, has been commonly attributed to an intrinsic size effect of the material, and explained in terms of the Berezinskii-Kosterlitz-Thouless (BKT) transition related to vortex-antivortex pair dissociation in 2-dimensional systems [140, 132, 137]. However, such interpretation has not achieved a general consensus [127, 141], and other mechanisms, mainly implicating transfer of charge carriers from the YBCO to the PBCO layer as well as the presence of structural defects at the PBCO/YBCO interfaces cannot be ruled out [137].

The T_C^0 versus thickness results have been shown with filled symbols in Fig. 4.4 for YBCO films not embedded between two PBCO layers [126, 130, 131]. In this case a more pronounced depression of T_C^0, with respect to the sandwiched structures, appears at thicknesses lower than 20 nm. Moreover, in some cases films with thicknesses below 10 nm are not anymore superconducting [131]. The best result has been achieved by Terashima et al [126], showing a 2 unit cell thick bare YBCO film with a $T_C^0 \approx 13$ K.

Our films (*filled circles* in Fig. 4.4), capped by using only a Au layer, are characterized by T_C^0 values which are comparable, down to 5 nm, with the best results of PBCO/YBCO/PBCO multilayers (*open triangles*). Below 5 nm, the drop of T_C^0 is faster. However, the T_C^0 of our 3 nm thick film is very close to the value achieved on the two-unit-cell thick bare film by Terashima et al [126].

In summary:

- very thin films on large mismatched substrates have generally shown a large increase of the *c*-axis compared to bulk, due to a large number of misfit dislocations. Our films instead show a *c*-axis, close to the reference 50 nm thick films, which still corresponds to a slightly overdoped regime, signifying a high crystallinity down to 2 -3 unit cells.

- the T_C^0 of our thinnest films, obtained by only using a Au capping, is comparable, down to 4 unit cells, with the best value obtained by sandwiching YBCO films with PBCO. Since the presence of the PBCO capping and buffering induces substitutions and/or chemical modifications, our results can be considered a first step toward the realization of few unit cell structures with properties representative of the YBCO bulk.

5

Underdoped YBCO films

The understanding of the electronic phase diagram of the HTS cuprates is an important experimental step towards the comprehension of high-T$_C$ superconductivity. The recent observation of local charge ordered states ubiquitous among the various HTS cuprates - by nuclear magnetic resonance, scanning tunnel microscopy and X-ray scattering techniques - emphasizes the need to understand the competition between local ordering and superconductivity. This is particularly important in the underdoped region of the phase diagram, where local orders are more pronounced.

Despite the extensive reports present in literature on underdoped HTS cuprates, the doping dependence of the electronic and transport properties is well established only for single crystals. A typical $T(p)$ phase diagram for a hole doped HTS cuprate is presented in sec. 2.2.2 [142, 143, 144] (see also Fig. 5.5b at the end of this chapter). For thin films the strain induced by the substrate may affect the doping dependence of the electronic properties, in particular the critical temperature T_C. For instance, for the LSCO and $La_{2-x}Ba_xCuO_4$ (LBCO) cuprates under compressive strain it has been observed the complete disappearance of the 1/8 anomaly, corresponding to the T_C suppression around the doping $p = 0.125$, together with an enhancement of the T_C with respect to the bulk in the whole doping range [145, 146]. Both these phenomena arise from the c-axis expansion caused by the mismatch δ^m between film and substrate [147]. At $p = 1/8$ not only T_C, but also the temperature dependence of the resistance above T_C differs from that of the bulk. Under tensile strain, instead, LSCO and LBCO films show only traces of the 1/8 anomaly, together with a strong reduction of T_C with respect to single crystals in the whole doping range [147]. Similarly, in YBCO thin films the peculiar depression of T_C at $p = 1/8$ has never been observed (see Fig. 5.5a at the end of this chapter) [148, 149, 150]. The disappearance of this peculiar feature from the underdoped region of the phase diagram of thin films can be crucial, since it is believed to be strictly connected to the presence of charge density waves.

In this chapter we will present the transport characterization of YBCO thin films grown on MgO (110), for the whole underdoped region of the $T(p)$ phase diagram.

5.1 Film deposition

We have deposited by PLD 30 nm thick YBCO films on (110) oriented MgO substrates, using the same deposition parameters listed in sec. 3.3. To explore the underdoped region of the superconducting dome, after the deposition each film has been cooled down at a lower post-annealing pressure, with respect to the one used to achieve slightly overdoped samples. To ensure the stability of the pressure during the post-annealing, which favor the reproducibility of the results, we have cooled down the films at a constant and continuous oxygen flow: with this procedure we may use pressures down to $1 \cdot 10^{-5}$ mbar, with a stability which is guaranteed within $2 \cdot 10^{-6}$ mbar (see Table 5.1 for a list of the postannealing pressures we have used).

Similar experiments are reported in literature, by using as starting point optimally doped films: a subsequent annealing in a reduced oxygen pressure is done ex-situ to reduce the oxygen content [148, 149, 150, 151]. In our case, we have chosen an in-situ annealing to achieve a better degree of homogeneity and reproducible results.

On (110) oriented MgO substrates YBCO films cannot grow fully strained, as a consequence of the large mismatch between the in plane lattice parameters. In this way the typical compressive or tensile stresses, which are responsible for the change in the doping dependence of the electronic properties of HTS cuprates, should be avoided.

The thickness t has been chosen to be 30 nm. As we have discussed in sec. 4.1, the postannealing becomes more effective at thicknesses $\leq$ 30 nm, favoring homogeneous films, with the same oxygen content throughout the thickness.

5.2 Study of the temperature dependence of the resistance

The resistance vs temperature of underdoped films has been measured in the range between 5 and 300 K. By decreasing the postannealing pressure, we have observed a progressive reduction of T_C^0, as expected for underdoped films, achieving superconducting films with T_C^0 down to $\approx$ 15 K (see Fig. 5.1a, and Table 5.1).

The good homogeneity of the films is proven by a rather narrow - lower than 5 K in most of the cases - transition broadening (see Table 5.1).

In Fig. 5.1b the resistance of several films at different oxygen doping is shown as a function of the temperature. As a consequence of the oxygen reduction the underdoped films present a remarkable increase of the sheet resistance $R_\square$. Even though there is some uncertainty about the absolute values of $R_\square$ (the $R(T)$ measurements have been done on unpatterned films, and the current and voltage probes of our 4-point measurement setup are not always located exactly at the same positions for different films), the trend is clear. When decreasing the oxygen content, $R_\square$ increases smoothly at first; then it increases much faster for samples with $T_C^0 \lessapprox 50$ K. This feature has been previously seen both in YBCO single crystals and thin films [64, 151], and the threshold, at which such abrupt change appears, has been associated to a sudden change in carrier concentration, which - according to different calculations - is associated to a doping level $p = 0.1$ [152].

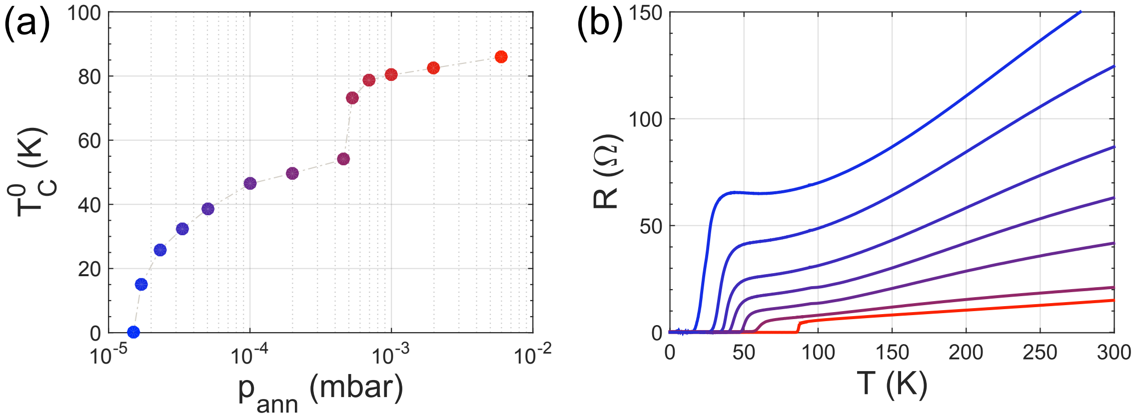

Figure 5.1: (a) Zero resistance critical temperature T_C^0 of the 30 nm thick YBCO films on MgO (110) as a function of the post-annealing pressure. (b) The resistance $R = R_\square$ vs temperature of the YBCO films, covering a region of the phase diagram going from $T_C^0 = 85.9$ K down to $T_C^0 = 14.9$ K.

In addition, a clear change in the temperature dependence of the resistance is visible, as a function of the doping. Indeed the resistance of the films, showing the highest T_C^0, show the linear temperature dependence, typical of optimally doped films, from 300 K down to ≈ 100 K (see red curve in Figs. 5.1b and 5.2a). When decreasing the oxygen content, the temperature interval in which $R_\square$ is linear decreases, shifts to higher temperatures, and a downward bending develops at lower temperatures. In the more de-oxygenated samples, this downward bending is followed, at even lower temperatures, by an upward bending. Finally, in non-superconducting samples this upward bending is even more pronounced, giving rise to a clear metal-insulator transition (data not shown) [153].

All these features are a clear sign of the rich and complex physics which is present in the underdoped region of the YBCO phase diagram. Indeed, in underdoped HTS cuprate single crystals, at least four different characteristic temperatures $T^* > T^{**} > T' > T_C$ can be extracted from each $R(T)$ curve, acting as crossover lines between different regimes and phases (see Fig. 5.5b at the end of this chapter) [143]:

- *the pseudogap temperature* T^*. It represents the crossover line between the pseudogap region and the still poorly understood strange metal phase (see sec. 2.2.2). Since the latter one is characterized by a linear dependence of the resistance on the temperature, T^* can be inferred by the downward deviation from the T-linear behavior.

- *the temperature* T^{**}. A crossover from a linear to a purely quadratic resistive behavior can be observed in underdoped films. The temperature T^{**} represents the onset of this $R \propto T^2$ regime. This temperature linearly decreases when increasing the doping p. It is also close to the characteristic temperatures relative to the maximum of the thermoelectric power [154] and the onset of the Kerr rotation signal [155]. Moreover, below $p = 0.1$, this temperature has been recently associated to the onset of the nematicity, an in-plane anisotropy in the transport properties of HTS cuprates, appearing in addition to the anisotropy due to the CuO chains, and whose origin is still debated [156].

- *the temperature* T'. It can be inferred from the $R(T)$ characteristic as the termination of the quadratic resistive dependence in temperature. Above $p = 0.1$, it can be associated with the appearance of superconducting fluctuations, affecting the dc conductivity close to T_C, in agreement with microwave absorption measurements [157]: the region of superconducting fluctuations is very narrow, though it expands at low doping, where it can extent to more than 20 K above the superconducting transition. Below $p = 0.1$ it is instead strictly connected with the metal-insulator crossover temperature [153].
- *the critical temperature* T_C. It represents the crossover line in the $T(p)$ phase diagram below which a superconducting phase appears. Because of the finite broadening of the superconducting transition, a mean critical temperature $\overline{T_C}$ can be extracted from the maximum of the first derivative of the $R(T)$ characteristic.

The extrapolation of the high-temperature linear behavior of the resistance to zero temperature gives the value of the residual resistance R_0. A low value of R_0 is the signature of a very clean metallic system, with low disorder. In single crystals it is almost negligible at the optimal doping, while it increases when decreasing the doping [149, 143].

The resistance of our films present the same dependence on the temperature as observed in single crystals, at all oxygen doping. Thence, we can extract the values of T^*, T^{**}, T' and $\overline{T_C}$ for our thin films. From the fitting of the high-temperature linear behavior of the resistance we have extracted the pseudogap temperature T^* and, by extrapolation to zero temperature, the residual resistance R_0 (see Figs. 5.2a and 5.2b). While R_0 increases by reducing the doping, the pseudogap temperature T^* increases. Nearly optimal doped films present a linear dependence of the resistance on the temperature almost down to the critical temperature ($T^* = 99$ K); for underdoped films the interval of linearity decreases. In particular, in films having a T_C^0 lower than 46.4 K we do not observe a wide-enough temperature range where the T-linear behavior can be unambiguously determined below 300 K, so T^* and R_0 cannot be extracted. Underdoped films present instead a purely quadratic resistive behavior at lower temperatures (see Fig. 5.2c). This Fermi liquid-like dependence of the resistance holds between the two temperatures T' and T^{**} (see Fig. 5.2d). The dependence of the temperature T^{**} with the oxygen doping is similar to that of the pseudogap temperature, since T^{**} increases in films with lower $\overline{T_C}$. Regarding T', it is only few kelvin higher than $\overline{T_C}$ at all oxygen doping, except for the strongly underdoped films, where it increases significantly by reducing the doping. A summary of all the parameters extracted in the most significant samples is listed in Table (5.1).

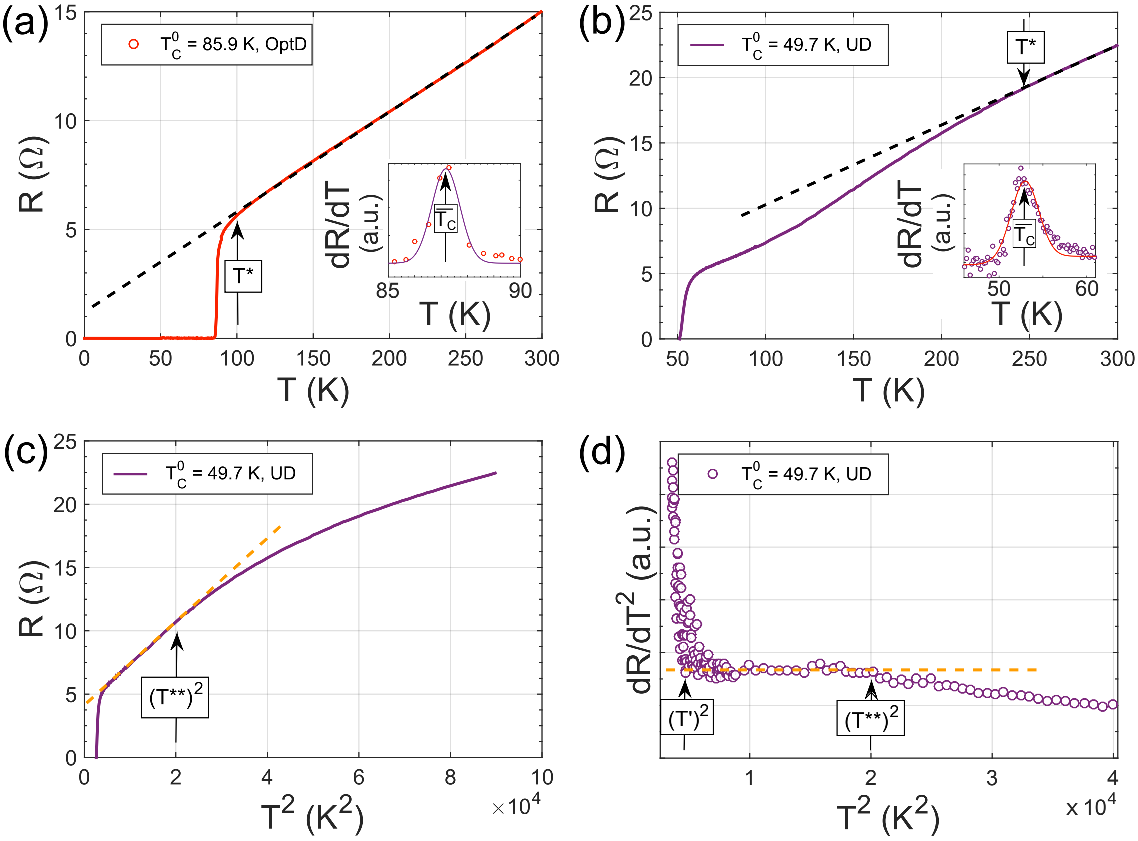

Figure 5.2: The $R(T)$ of a nearly optimal doped film, having a $T_C^0 = 85.9$ K (panel a) and of an underdoped film, having a $T_C^0 = 49.7$ K (panel b), are analyzed and compared. The high temperature resistive behavior has been fitted with the equation $R = R_0 + \epsilon \cdot T$ (dashed line), where the intercept R_0 and the slope ϵ are free parameters. In the nearly optimal doped films, the agreement between the data and the linear fit is very good from 300 K down to 99 K, representing the pseudogap temperature T^*. The intercept, $R_0 = 1.1\ \Omega$, is the residual resistance. For underdoped films, the linear resistive regime is much narrower (in panel b, $T^* = 246$ K) and a quadratic resistive behavior appears at lower temperatures. The residual resistance increases (in panel b, $R_0 = 4.5\ \Omega$), while the slope ϵ is almost independent on the oxygen doping. In strongly underdoped films the linear resistive regime below 300 K is absent, or it is too narrow to be fitted properly, so to unambiguously determine T^* and R_0. In the inset of both panels the $\overline{T_C}$ is extracted as the maximum of the first derivative of the $R(T)$ curve. (c) The resistance of the film shown in panel b is plotted as a function of T^2: the linear behavior at low temperature confirms that the dependence of the $R(T)$ at low temperatures is purely quadratic. (d) First derivative of the $R(T^2)$ data presented in panel c: the temperatures $T' \approx 64$ K and $T^{**} = 142$ K have been extracted respectively from the lower and upper temperatures where dR/dT^2 is constant.

p_{ann} (mbar)	T_C^0 (K)	$\overline{T_C}$ (K)	T' (K)	T^{**} (K)	T^* (K)	R_0 (Ω)	ΔT_C (K)
$1.5 \cdot 10^{-5}$	0	0	140	197	-	-	-
$1.7 \cdot 10^{-5}$	14.9	23.7	115	183	-	-	8.0
$2.3 \cdot 10^{-5}$	25.8	33.1	102	176	-	-	6.0
$3.3 \cdot 10^{-5}$	32.3	37.7	88	167	-	-	4.5
$5.0 \cdot 10^{-5}$	38.5	42.5	63	156	-	-	5.0
$1.0 \cdot 10^{-4}$	46.4	49.9	64	143	250	7.6	3.4
$2.0 \cdot 10^{-4}$	49.7	52.5	64	142	246	4.5	3.1
$4.6 \cdot 10^{-4}$	54	60.1	69	125	216	4.2	6.0
$7.0 \cdot 10^{-4}$	78.8	80.6	-	108	165	2.9	3.7
$2.0 \cdot 10^{-3}$	82.5	85.9	-	112	140	2.7	2.9
$6.0 \cdot 10^{-3}$	85.9	86.9	-	-	99	1.1	2.0
$9.0 \cdot 10^{2}$	84.5	85.4	-	-	-	0.8	1.7

Table 5.1: The four temperatures $\overline{T_C}$, T', T^{**}, T^* and the residual resistance R_0, extracted for films with different doping as illustrated in Fig. 5.2, are listed together with T_C^0 (plotted in Fig. 5.1a). These films have been grown by changing the postannealing oxygen pressure from 15 nbar up to 6 μbar. To achieve nearly optimally doped films, the postannealing pressure has been decreased from 900 mbar down to 6 μbar. The transition broadening of the films, ΔT_C, defined as the difference between the temperatures T_1 and T_2 where the resistance has 90% and 10% respectively of the normal state value, is also listed.

5.3 Structural characterization

The structural properties of the underdoped films have been investigated by SEM and XRD.

The surface morphology has been determined by SEM images. The surface of all the underdoped YBCO films looks identical to that we have observed on slightly overdoped films grown on MgO (110) (see SEM images in Fig. 3.4).

Additional structural properties have been obtained by XRD analysis. Symmetric $2\theta - \omega$ scans confirm that the films are highly crystalline and *c*-axis oriented (see Fig. 5.3a and insets therein). We also observe the interference fringes (like those observed in slightly overdoped films, see Fig. 3.6a) which are visible at both sides of the (001) reflection, even for the most strongly underdoped sample, and despite the films are only 30 nm thick. The presence of interference fringes is an indication of very smooth surfaces.

In the whole range of doping the (0,0,n) rocking curves have the same FWHM (see Fig. 5.3b). This indicates that the broadening ΔT_C of the transition to the superconducting state we observe in the underdoped films is not due to structural dishomogeneities. In our case ΔT_C is larger for the more underdoped films, and for films having a $\overline{T_C} \approx 60$ K (see Table 5.1). This occurrence could be therefore related to intrinsic properties of the YBCO compound at these doping levels, when various local orders are simultaneously at play.

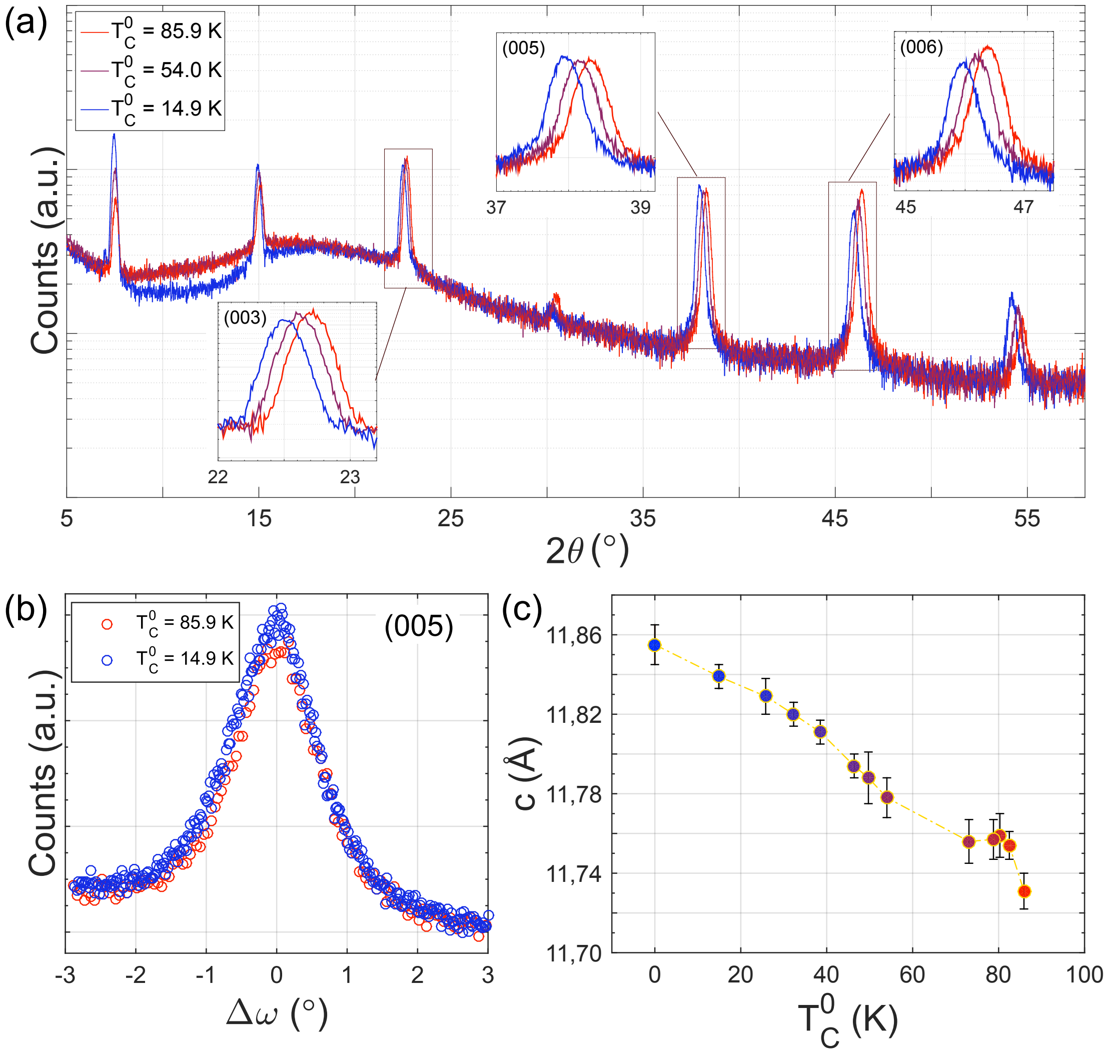

Figure 5.3: (a) XRD $2\theta-\omega$ scans of a nearly optimally doped YBCO film (red line), of an underdoped film with $T_C^0 = 54.0$ K (purple line), and of a strongly underdoped film with the lowest critical temperature, $T_C^0 = 14.9$ K, which we have been able to grow (blue line). All the $(00n)$ reflections shift toward lower angles when the oxygen content in the films (the T_C^0) decreases, as highlighted by the three insets relative to the (003), (005) and (006) reflections. (b) Rocking curves of the (005) reflection of the nearly optimal doped sample (red circles) and of a strongly underdoped film (blue circles). The curves are both characterized by the same FWHM of $\approx 1.4°$, despite the huge difference in T_C^0 (of about 70 K) of the thin films. (c) The c-axis parameter of the films, extracted considering all the $(00n)$ Bragg peaks of the XRD $2\theta-\omega$ scans, is shown as a function of T_C^0.

A very significant difference is present in the $2\theta-\omega$ scans measured on films with different T_C^0. The reduction of oxygen doping in YBCO is associated to an elongation of the c-axis length, which has been been observed both in single crystals and in thin films [158, 159]. In agreement with that, we have observed that the symmetric $(00n)$ Bragg peaks in the XRD $2\theta-\omega$ scans appreciably shift toward lower diffraction angles (see Fig. 5.3a). The extracted c-axis lattice parameters of YBCO are shown as a function of the T_C^0 of the films in Fig. 5.3c.

5.4 Doping determination: the thin film phase diagram

To construct the doping $p(T)$ phase diagram, we have to determine for each film the doping p, representing the number of holes per planar copper atom.

The experimental determination of p in thin films of HTS cuprates is extremely difficult, since it requires the knowledge of the oxygen content n, which can be accurately determined only in single crystals. Indeed, in bulk crystals chemical and thermogravimetric analyses, implying the possibility of measuring the mass of the oxygen atoms and its variation as a function of the temperature, bring to a precise estimate of n [65].

However, for the specific case of the YBCO compound, the measurement of p in very difficult also for single crystals. As a consequence of the crystal structure (see sec. 2.2.1), one needs to know how holes are arranged between Cu atoms in the CuO_2 planes and Cu atoms in the CuO chains, which depends not only on the oxygen content n, but also on the degree of oxygen ordering in the chains.

Because of the difficulty in determining p, the hole doping is commonly calculated in YBCO single crystals from the critical temperature $\overline{T_C}$ by using the empirical parabolic relationship

$$1 - \overline{T_C}/\overline{T_C^{max}} = 82.6 \cdot (p - 0.16)^2 \ , \tag{5.1}$$

where $\overline{T_C^{max}}$ is the critical temperature at the optimal doping. This equation has been found working well in LSCO, with the exclusion of the data around $p = 1/8$ [160, 161]. Consequently, it is inaccurate for determining hole doping around $p = 1/8$, and it is not applicable for strongly underdoped, not superconducting, samples.

In single crystals the knowledge of the c-axis length, in combination with the approximate estimation of p given by eq. 5.1, has allowed to establish a unique relation between the values of p and c [162].

We have applied the same analysis, for the first time to our knowledge, to YBCO thin films. In Fig. 5.3c we have previously shown the relation between the c-axis parameter and T_C^0. To determine the relation between the c-axis parameter and p, we can substitute in this plot each T_C^0 value with the corresponding $\overline{T_C}$ value (see Table 5.1). For every $\overline{T_C}$, the corresponding doping p can be estimated from eq. 5.1, considering $\overline{T_C^{max}} = 88.5$ K, the value of our nearly optimal doped film. The extracted p as a function of the c-axis lattice parameter is shown in Fig. 5.4a.

In the interval between $p = 0.05$ and $p = 0.08$, corresponding to YBCO films with $0\text{ K} < \overline{T_C} < 40\text{ K}$, the dependence of the doping p on the c-axis parameter is linear. The linearity can be extrapolated down to $p = 0$, in the strongly underdoped regime.

At intermediate doping, in the interval between $p = 0.08$ and $p = 0.13$, corresponding to YBCO films with $40\text{ K} < \overline{T_C} < 80$ K,the data fall below the low doping linear dependence on the c-axis value. A possible reason for this deviation at intermediate doping ($p \approx 1/8$) is the depression of the critical temperature, associated to the presence of charge density wave instability [2, 7].

From the fit of the data at $p < 0.08$ and $p > 0.13$ (dashed line in Fig. 5.4a) we can determine the following relationship between p and c, which is valid in the entire

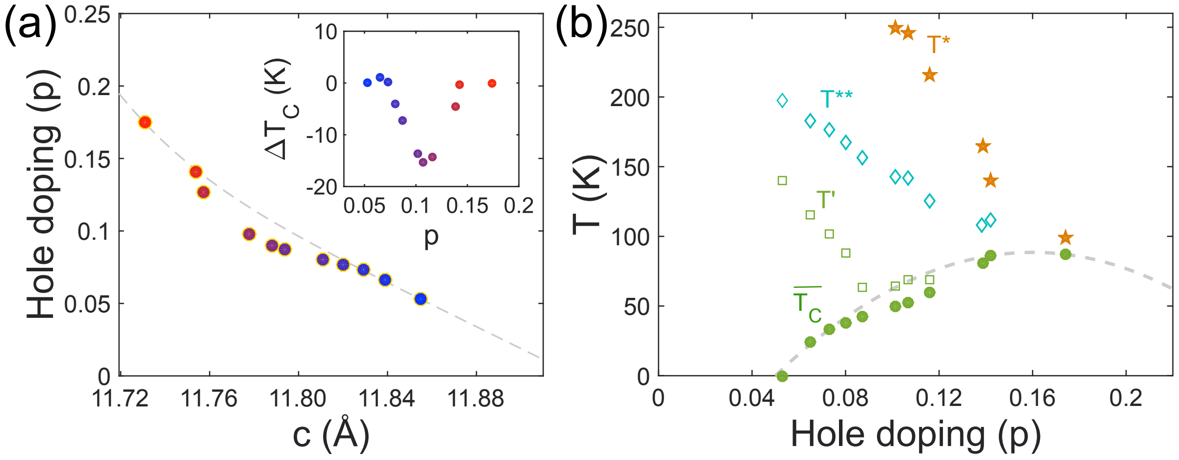

Figure 5.4: (a) Doping p as a function of the c-axis parameter (circles). The dashed line represents the fit to the data at $p < 0.08$ and $p > 0.13$. The inset shows the difference ΔT_C between the measured $\overline{T_C}$ values and the parabolic relation (eq. 5.1). The maximum ($\approx 18\%$) of the $\overline{T_C}$ suppression can be observed in correspondence of $p = 0.11$. (b) The four temperatures $\overline{T_C}$, T', T^{**}, T^{*} extracted from the $R(T)$ measurements are plotted as a function of p. The resulting phase diagram is very similar to that of YBCO single crystals [143]. The dashed line is the parabolic relationship (eq. 5.1), with $\overline{T_C^{max}} = 88.5$ K.

oxygen content range:

$$p = 9y + 1.5 \times 10^9 y^6 \ , \tag{5.2}$$

where $y = 1 - c/c_0$, and $c_0 = 11.925$ Å is the c-axis parameter at zero doping.

The empirical formula 5.2 is very similar to that, found for YBCO single crystals [162]. However, in our case the goal of the analysis is only to prove that our data (the independent measurements of $\overline{T_C}$ and c-axis) deviate, similarly to YBCO single crystals, from the parabolic dependence which is instead typical for YBCO thin films (see Fig. 5.5a) [148]. It is worth pointing out that the p values we have extracted from equation 5.2 only represent a rough estimate of the actual hole doping in our films. The origin of this inaccuracy is mainly related to the lower $\overline{T_C}$ and longer c-axis parameter (possibly due to the YBCO-MgO mismatch) that we measure in our films with respect to what one would obtain at the same doping in a single crystal.

The measured $\overline{T_C}$ values can be plotted as a function of the hole doping p, obtained using equation 5.2, and compared with those calculated via the parabolic equation 5.1. The difference ΔT_C between the measured and calculated critical temperatures is negligible, except around $p = 0.11$, where a 16 K ($\approx 18\%$) suppression of critical temperature is observed (see inset of Fig. 5.4a). The maximum of the $\overline{T_C}$ suppression is very similar to the $\approx 20\%$ occurring in LSCO and YBCO single crystals at $p = 0.125$ [160, 162].

Finally, one can plot the four temperatures $\overline{T_C}$, T', T^{**}, T^{*} extracted from the $R(T)$ measurements as a function of the hole doping p, so to get the $p(T)$ phase diagram of our underdoped YBCO films (see Fig. 5.4b).

5.5 Summary

In this chapter we have demonstrated that with our YBCO thin films we can have access to the whole underdoped region of the YBCO phase diagram. Moreover, from the comparison of this phase diagram with that of YBCO single crystals (see Fig. 5.5b), we can conclude that the transport properties of our underdoped films are strictly entangled to a wide range of other physical properties (as discussed in sec. 5.2), like charge density waves, similarly to what has been observed for YBCO single crystals. Even though the values of the four temperatures extracted from the $R(T)$ measurements may slightly differ with respect to the bulk values (e.g. as a consequence of the YBCO-MgO mismatch), their behavior as a function of the hole doping p is in perfect agreement with what observed in single crystals. As a consequence, the rich and complex physics characterizing the underdoped region of the YBCO phase diagram is preserved in our thin films, and it can be studied as a function of the dimensionality of the system, down to the nanoscale, when thin films are patterned into nanostructures.

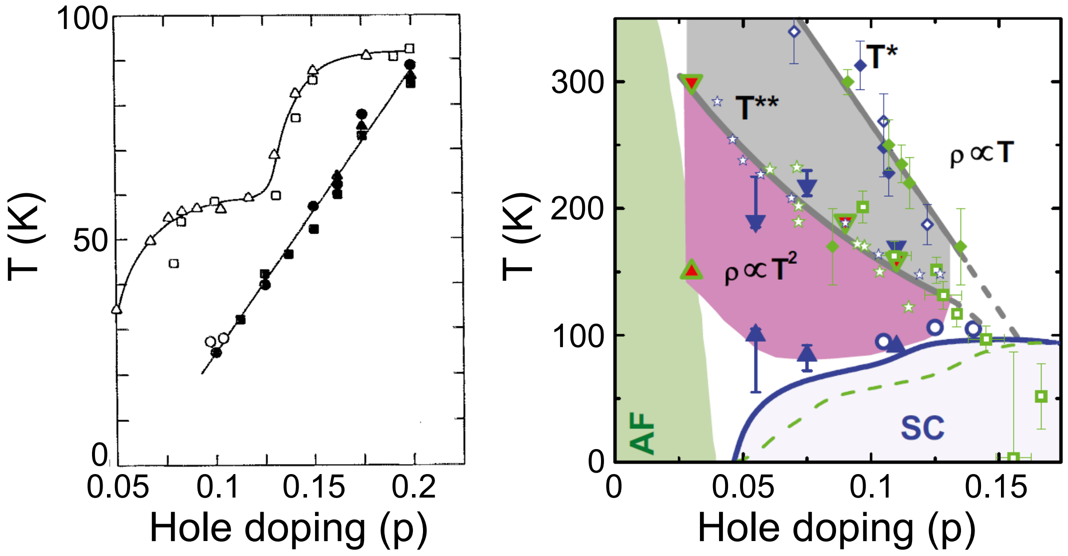

Figure 5.5: (a) YBCO phase diagram, adapted from Ref. [148], where the T_C of different thin films deposited on MgO (100) substrates (filled symbols) is compared, as a function of the hole doping, with that of single crystals (empty symbols). The disappearance of the “1/8 plateau” in thin films is evident. The full lines are guides to the eye. (b) Phase diagram of $HgBa_2CuO_{4+\delta}$ (blue symbols and lines) and YBCO (green symbols and lines) single crystals, adapted from Ref. [143]. The dependence of the temperatures T_C, T', T^{**}, T^*, extracted from the $R(T)$ measurements, on the hole doping is shown. T^{**} is in fairly good agreement with the characteristic temperatures determined by other experiments: the maximum of the thermoelectric power [154] (*stars*) and the onset of the Kerr rotation signal [155] (*squares*).

6

Fabrication of YBCO nanowires

The realization of homogeneous nanostructures preserving pristine superconducting properties represents a challenge for HTS cuprates. The chemical instability of these materials, mostly related to oxygen-out-diffusion, and the extreme sensitivity to defects and disorder due to the very short ξ (of the order of 1 nm), do represent real issues in establishing reliable nanofabrication routines.

For these reasons, different approaches have been followed in the last two decades to achieve YBCO sub micron wires:

- Focused ion beam (FIB) milling and ion implantation have been used to pattern YBCO nanowires in configurations suitable for the detection of magnetic flux [163] and photons [164].

- Arrays of YBCO superconducting nanowires with lengths of several micrometers have been grown in porous alumina acting as morphology-directing hard template [165]. Similarly, porous insulating thin film templates of STO have been deposited between two *c*-axis oriented YBCO thin films and used to achieve *c*-axis YBCO nanowires, with widths smaller than 100 nm [166]. Amorphous STO templates have been also used to fabricate submicron YBCO wires avoiding both chemical and physical etchings [167].

- AFM has been used, in contact mode, as a lithographic tool achieving YBCO nanobridges with widths down to 500 nm [168].

- A special superlattice-nanowire-pattern-transfer technique has been employed to fabricate YBCO nanowires with widths down to 10 nm and lengths of the order of micrometers [169].

- Besides all these different techniques, the patterning of YBCO nanowires is more commonly realized by electron beam lithography and ion beam etching in combination with an hard mask [27, 26, 25, 24, 170, 171]. In particular, the best performances in terms of critical current density, which represents a measure of the highly uniform superconducting properties of these structures, have been recently reported for YBCO nanowires fabricated using this procedure [28].

In this work we have used e-beam lithography, in combination with an amorphous carbon mask and a soft Ar^+ ion etching to achieve nanowires with cross sections as small as 40×50 nm^2 and lengths spanning in a wide range from 100 nm to several microns [172, 173, 174]. A 50 nm Au capping layer is also kept on top of the nanostructures.

6.1 The nanopatterning procedure

In the following, we will show step by step our improved nanopatterning procedure for the realization of YBCO nanowires. The superconducting properties of the patterned nanostructures are strongly affected by the choice of the masking materials and of the parameters for the patterning, in particular the resist baking temperature and the ion milling etching parameters. For more details, we refer to the Appendix A. In what follows we briefly summarize the main steps (see legend in Fig. 6.1):

Figure 6.1: Legend of the colors, which are used in the schematic representations of the nanofabrication steps in the following pages.

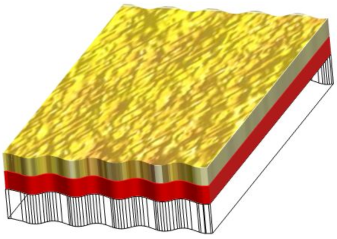

- The YBCO film is covered ex-situ, soon after its deposition, by a 50 nm thick Au film acting as a protective capping layer, so as to prevent any oxygen loss and to avoid any possible contaminations.

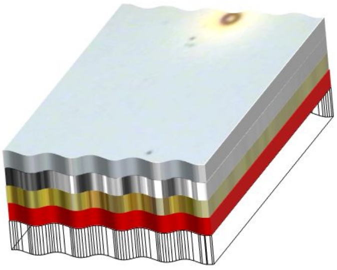

- A carbon (C) layer is used as a mask. The choice of this material is due to its robustness to Ar^+ ion milling (2-3 times harder than YBCO) and to its property to be removed by oxygen plasma (e.g. differently than titanium [171]). After carbon deposition, a double layer resist is spun.

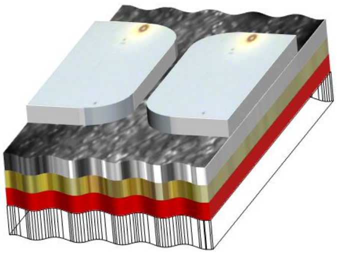

- The nanowire geometry is defined by electron beam lithography at 100 kV. The exposed areas of the resists are than removed during the resist development.

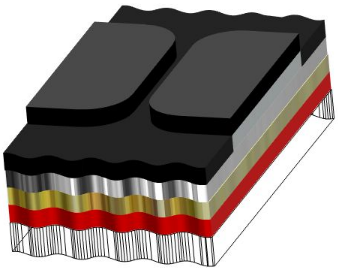

- A thin layer of chromium (Cr), acting as a mask for the carbon, is evaporated on top of the exposed double layer resist.

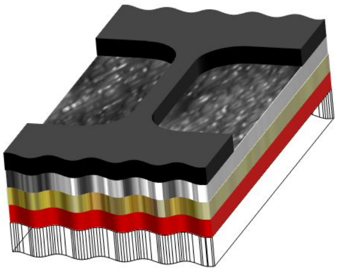

- The mask is defined after the Cr layer is lifted-off.

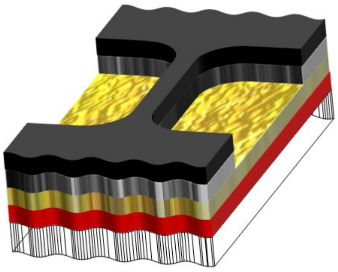

- The carbon layer not covered by chromium is removed by low power oxygen plasma etching.

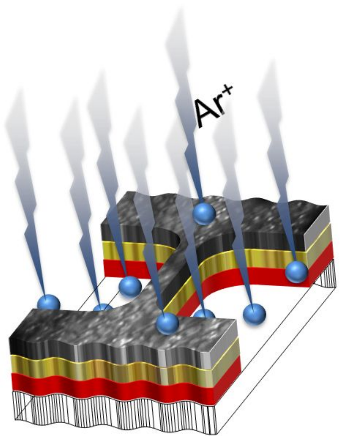

- The Cr layer, the Au and YBCO which are not covered by C, are etched by Ar^+ ion-beam milling. The etching parameters (beam voltage and current, time) have been carefully calibrated in order to minimize the interaction of the ions with the nanostructures. In particular, we have chosen to work close to the etching voltage threshold for YBCO. The overheating of the YBCO has been also reduced by means of the presence of the Au capping.

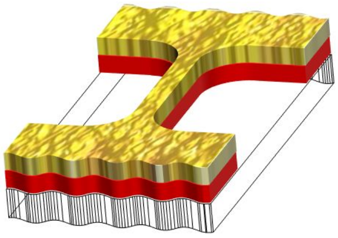

- The C layer is removed by plasma etching, while the Au capping is kept, so to avoid any interaction between the Ar^+ ions and the surface of the YBCO wires.

Pristine structures and reproducible results at the nanoscale are intimately related to a good control of the etching process. For this reason, we have engineered an extremely gentle and slow ion milling procedure. Indeed, the interaction of Ar^+ ions with YBCO can strongly affect the transport properties because of severe changes in film stoichiometry and disorder. As it will be clarified in Chapter 7, big differences can be observed in the transport properties, in particular the value of the critical current density and its temperature dependence, by tiny changes of the etching parameters. Moreover, to prevent any redeposition of etched YBCO in the vicinity of the final nanowires, which may cause unwanted parallel shorts along the lateral sides, we overetch 50 nm into the substrate[1].

As regards the Au capping layer, it protects YBCO during all the nanopatterning steps, it favors the thermalization inside YBCO during the ion etching and it minimizes the interaction of the milling species with the YBCO nanostructures. Its thickness is also a crucial parameter. By doing a systematic characterization of the nanowires as a function of the Au thickness, we have noticed that the superconducting properties of the wires (i.e. the current densities, see Chapter 7) strongly degrade by reducing the Au thickness to 30 nm. On the other side, a thicker Au coverage, of the order of 100 nm, limits the minimum achievable lateral size of the nanowires to 80-100 nm, because of the erosion of the C mask caused by longer etching times.

6.2 YBCO nanowires

Following the procedure described in sec. (6.1), we have achieved YBCO nanowires with widths down to 40 nm and lengths from 200 nm to several microns (see Fig. 6.2).

A combination of AFM and SEM has been used for the determination of the cross sections of the nanostructures. The YBCO bridge thickness is known from our calibration of the PLD deposition rate for YBCO films. From the AFM images we obtain the total thickness of the patterned structure, which is typically 150 nm. It consists (from top to bottom) of 50 nm Au, 50 nm YBCO and 50 nm substrate (see Fig. 6.3a). Moreover, from AFM we can extract the minimum angle between the substrate surface and nanobridge sidewalls ($\approx 75°$), which is only limited by the shape of the AFM tip. The SEM images give instead a very good "direct" measure of the width of the bridge on the top (w_{min}, interface of gold capping layer with vacuum) and bottom (w_{max}, interface of YBCO film with substrate) (see Fig. 6.3b). The determinations of the width of the bridge side walls using SEM, given by $w_{sw} = (w_{max} - w_{min})/2$, is very similar to the one extracted from AFM and they do indeed coincide within few nanometers. Therefore the absolute error of the bridge width w determination is less than 5 nm.

---

[1] The unavoidable redeposited substrate material should not have any influence on the superconducting properties.

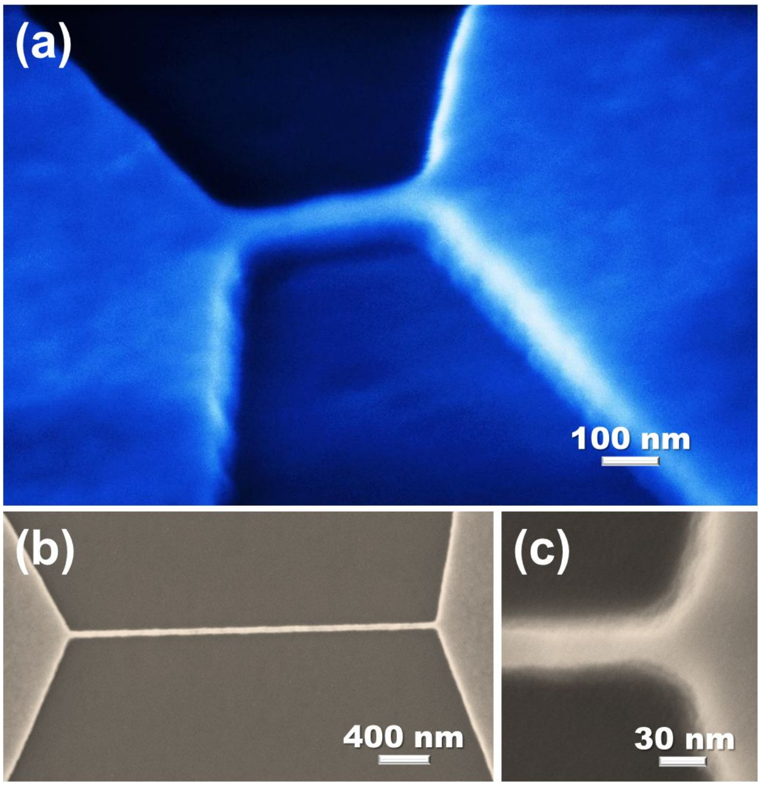

Figure 6.2: (a) Tilted angle SEM image of a 40 nm wide and 200 nm long YBCO nanowire. (b) SEM image of a 40 nm wide and 3 μm long YBCO nanowire, whose enlargement, confirming the uniformity of the nanostructure, is shown in panel (c).

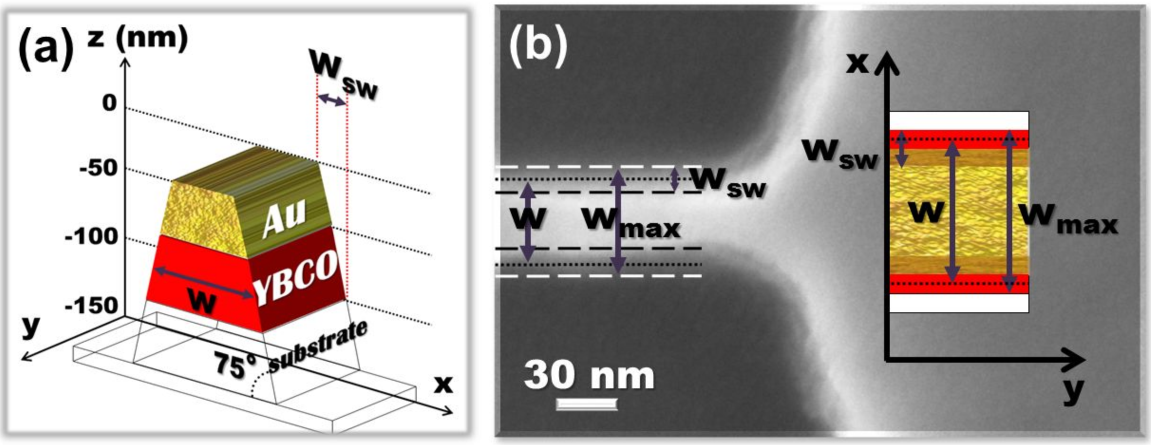

Figure 6.3: (a) Schematics of a typical AFM line scan along the cross section of a nanobridge. (b) a SEM picture of a nanowire is combined to the schematics of the top view of the AFM cross section, showing the wire from the SEM perspective. The w can be calculated as $w = w_{max} - w_{sw}$.

7

Transport characterization of YBCO nanowires

As already pointed out in Chapter 6, HTS nanostructures may undergo a strong degradation during the patterning. As a consequence, their superconducting properties are seriously affected. To assess the homogeneity of these structures, a valuable test is the measurement of the critical current density J_C (defined as the ratio between the measured critical current and the wire cross section), which is very sensitive to any local non-uniformity and damage inside the wire [175].

Theoretically, an infinite long wire with width smaller than the Pearl length $\lambda_P = \lambda_L^2/t$ (which is ≈ 800 nm in case of a 50 nm thick wire) and much larger than ξ (which is the case for YBCO nanowires) is characterized by a uniform current distribution, with a J_C value, only limited by entry of Abrikosov vortices. Indeed, as already stated in sec. (2.3.2), when ramping up the bias current applied to a bridge, the critical supercurrent is reached once the local current density at the edges of the bridge equals a value close to the depairing current density [89]. At this point vortices can enter the bridge, causing a transition from the zero voltage state to the finite voltage state. The expression for the depairing limit is equal to $J_d = \Phi_0/(3\sqrt{3}\pi\mu_0\lambda_L^2\xi)$ according to the Ginzburg-Landau theory (see eq. 2.21), and its value for YBCO at 4.2 K is equal to $\approx 1.3 \times 10^8$ A/cm^2 (with $\xi = 1.5$ nm and $\lambda_L = 230$ nm).

The J_C values of HTS nanowires available in literature present a huge spread of values, together with an unexpected reduction by reducing the width, which has been mainly attributed to damages occurring during the patterning (see Fig. 7.1). In Ref. [24] the authors find a steady reduction of the J_C from $w \approx 1$ μm till 200 nm with values never exceeding 10^7 A/cm^2 at 4.2 K. An almost constant J_C for nanowires in the range 50 nm $< w <$ 150 nm has been obtained in Ref. [26]. However in this case the maximum achieved J_C is of the order of 2×10^7 A/cm^2. Xu et al. [169], with their parallel arrays of hundreds of YBCO nanowires, have reached the ultimate lateral size, at the expenses of the superconductivity, which is strongly affected by the nanopatterning procedure, with average J_C for a single 15 nm wide wire as low as 10^5 A/cm^2 and a transition temperature below 20 K. In the attempt to improve the superconducting properties of YBCO nanowires, Papari et al. [28] have made preliminary studies of the role of a protecting layer of Au. They have obtained substantial improvement in the performances for nanowires widths ≈ 150 nm with J_C as high as 7×10^7 A/cm^2.

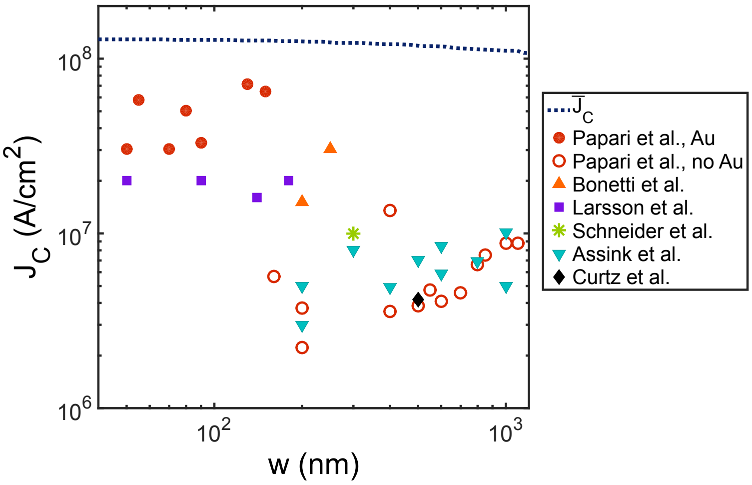

Figure 7.1: Critical current density J_C measured at 4.2 K as a function of the width w for different YBCO nanowires, available in literature [28, 27, 26, 25, 24, 164] (adapted from [28]). The dotted line represents the numerically calculated critical current density $\bar{J}_C$ for an infinite long (type II) wire, with thickness $t < \lambda_P$, as a function of the width w. If $w < \lambda_P$, which is $\approx$ 800 nm for $t = 50$ nm, such a value saturates to the depairing limit.

However for narrower wires they still observe a decreasing J_C by reducing the wire's width with values not exceeding 3×10^7 A/cm^2 for 50 nm wide wires. More importantly in their work the narrower nanowires showed a transition temperature several degrees lower compared to the larger one. This indicates significant damages at the smallest nanowire widths, possibly due to a too thin Au protecting layer of only 20 nm and to non-optimal Ar$^+$ ion etching parameters for very narrow wires.

In this chapter we will show the transport characterization of our YBCO nanowires. As a consequence of the soft ion milling procedure we have performed and of the presence of the Au capping layer on top, our nanostructures demonstrate that the superconducting properties, close to the as grown films, are preserved. Thence, they represent model systems, which may open new directions in engineering novel HTS devices at the nanoscale for both fundamental and applied purposes. In particular, the wide range of lengths and thicknesses we have been able to achieve allows their integration in magnetometers for the shortest, 50 nm thick, wires and in devices for photodetection experiments for the longest, 50 nm thick, ones and for the short, ultrathin ones.

7.1 Current-voltage characteristics

The electrical transport properties of the nanowires have been measured in a ^{3}He cryostat (for more details, see Appendix B) using a four point probe configuration. Fig. 7.2a shows a current-voltage characteristic (IVC): it is flux-flow like at high bias voltages, with the presence of a small switch from the zero voltage state to a finite voltage state at I_C (see inset of Fig. 7.2a). Differently from LTS materials, the high value of the thermal conductivity in YBCO (≈ 2 Wm^{-1}K^{-1}) [176] prevents self-heating

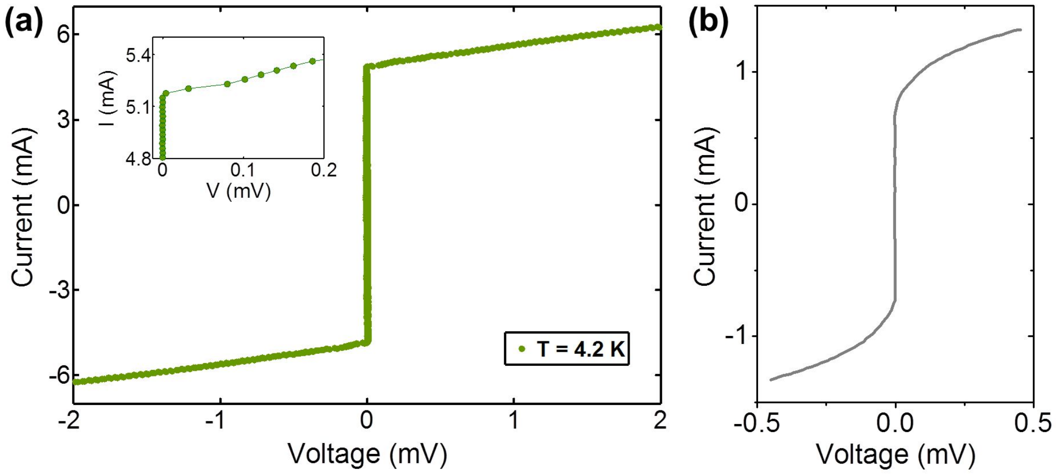

Figure 7.2: (a) IVC measured at 4.2 K for a 90 nm wide and 200 nm long YBCO nanowire. In the inset, the small voltage step driving the superconducting channel to the resistive state is highlighted. This step represents the most significative deviation of our IVC from typical flux-flow behavior (shown in (b) for comparison. Adapted from [35]).

effects, which could bring the whole device to the normal state just above the critical current.

Similarly to the J_C values, also the IVCs of YBCO nanowires, available in literature, present a large spread of behaviors. Several authors have reported the presence of very large voltage switches/steps ($\Delta V = 50 - 150$ mV) above I_C in the IVC of YBCO nanowires, at high bias voltages [28, 177]. These switches, which are accompanied by a large hysteresis (exceeding 30% of the total current) have been explained in terms of the appearance of phase slip centers and hot spots, triggering the nanostructures from the superconducting to the resistive and normal state. In Ref. [178] flux-flow like IVCs have been reported, characterized by a series of small voltage steps ($\Delta V \leq 1$ mV) in the resistive branch. These voltage steps have been attributed to an incoherent motion of vortices across the nanowire at currents above I_C. None of these mentioned features is present in our case. The origin of the small voltage switch we measure above I_C is still under investigation.

7.1.1 Critical current density vs wire width

Once the cross sections A_w have been accurately determined with SEM and AFM, we have extracted from the IVC the critical current density $J_C = I_C/A_w$ of more than 200 nanowires, with fixed thickness of 50 nm, varying in width from 40 nm to 2 μm and length from 100 nm to 3 μm.

In Fig. 7.3a (*filled circles*), the J_C at 4.2 K of our YBCO nanowires with a fixed length of 200 nm and belonging to the same chip, are reported as a function of the width. We have observed two important features:

- The decrease of J_C with decreasing wire width w, observed several times in literature (see Fig. 7.1), is not present in our case.

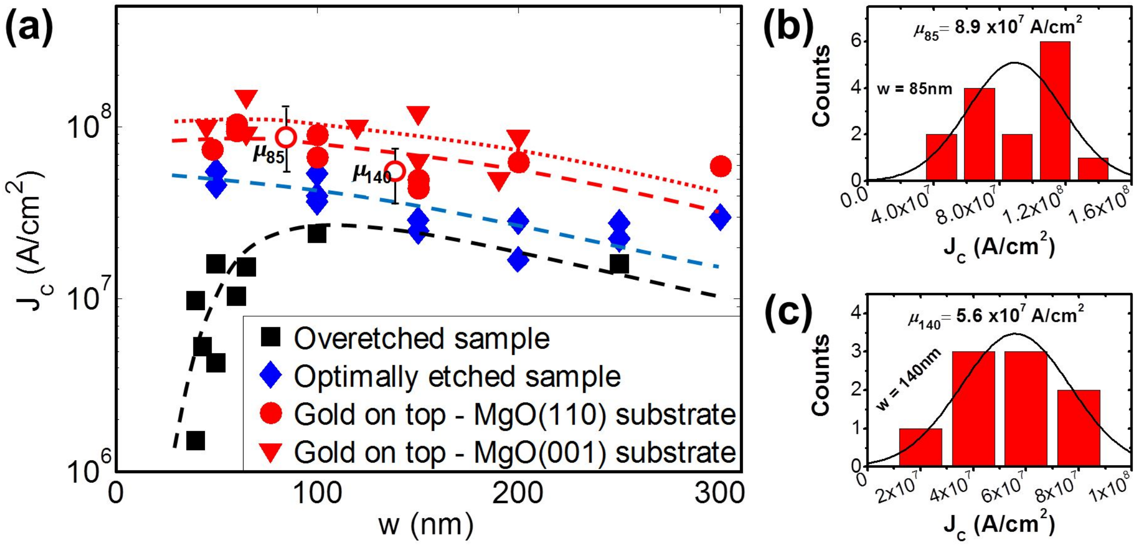

Figure 7.3: Critical current density J_C measured at 4.2 K as a function of the width w for 200 nm long YBCO wires with and without a Au capping layer. The dashed lines are guides for the eyes. The two open circles represent the mean values of the two sets of nanowires with fixed width $w = 85$ nm (panel b) and $w = 140$ nm (panel c).

- The narrowest wires have a J_C larger than 10^8 A/cm^2, approaching the Ginzburg-Landau depairing limit. Such a value is about $1 - 3 \times 10^8$ A/cm^2, (eq. (2.21)[1], for (001) YBCO films with T_C of 85 K, characterized at low temperature by a coherence length and a London penetration depth given respectively by $\xi_0 = 1.4 - 2$ nm and $\lambda_0 = 150 - 250$ nm [28, 180]).

To strengthen these findings, we have added in Fig. 7.3a the results of two more chips, fabricated with the same nanopatterning procedure. The first one was prepared with the idea to acquire large statistics of the distribution of the J_C values for a specific width and it includes only nanowires with fixed width of 85 nm and 140 nm. The J_C distributions for the two widths are reported Figs. 7.3b and 7.3c: the two mean values μ_{85} and μ_{140}, shown as open circles in Fig. 7.3a together with the standard deviations, agree extremely well with the expected J_C for those widths. The second chip is made by nanowires fabricated on a commercial (001) YBCO film grown on a (001) MgO substrate, provided by Theva GmbH [181], characterized by a slightly higher T_C of ≈ 1 K compared with our YBCO films on MgO (110) and comparable structural and morphological properties. The J_C values measured on these wires as a function of their width are reported in Fig. 7.3a as triangles: also in this case we have the same $J_C(w)$ behavior already observed for YBCO grown on MgO (110), with values even a little higher.

Moreover, in Fig. 7.4 the critical current densities measured at 4.2 K for 100 nm wide bridges, all belonging to the same chip, are shown as a function of the bridge

---

[1] Here it is important to note that this equation is strictly valid only at temperatures close to the critical one. However, calculations for the depairing critical current density in the clean and dirty limit at $T = 0$ K predict a deviation from the GL limit by a maximum factor of 1.5 [179].

length. The independence on length of the critical current density values rules out any kind of artifact in the determination of our very high values of J_C, due to redeposition of YBCO in the vicinity of the wires or to a non-correct estimate of the widths of the narrowest wires.

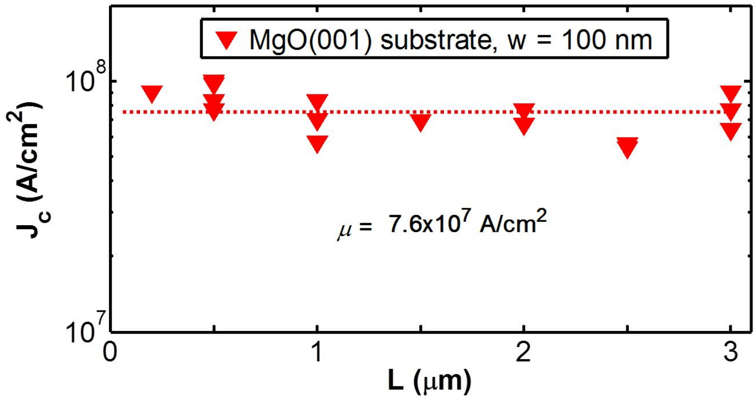

Figure 7.4: Critical current density J_C measured at 4.2 K as a function of the length l for 100 nm wide YBCO wires. The dashed line is the mean value of the J_C distribution for these nanowires.

We have fabricated a sample in which the Au layer has been completely removed from the top of the wires. To minimize the damages on the superconducting nanostructures, the gold has been “optimally etched” with the help of an end point detector installed in our milling system together with a careful inspection of the sample under optical microscope and AFM every 1-2 minutes for the latest part of the Au etching. The resulting J_C, represented as diamonds in Fig. 7.3a, does not decrease with decreasing width, differently to what previously reported in literature. On the contrary, the J_C exhibits the same behavior as a function of the width we already observed for Au capped nanowires, although with slightly lower values.

To further prove that the reduced Ar$^+$ ion bombardment of YBCO nanostructures was the turning point in our research, we have fabricated different samples slightly overetching the YBCO nanowires. The squares in Fig. 7.3a, which all refer to the same sample, show that the J_C decreases with decreasing the nanowire width below 100 nm, in agreement with what has been published in literature during the past years.

All these results prove that we have engineered pristine YBCO nanowires, preserving the properties of the as-grown films. By means of the soft etching procedure and keeping the gold on top, i.e. minimizing the interaction of the Ar$^+$ ions with the nanowires, we may conclude that the damage of the sides is so minimal that it does affect neither the global nor the local superconductive properties of the nanowires.

7.1.2 Critical current density vs temperature

To further demonstrate the excellent quality of the 50 nm thick nanowires, in terms of uniformity of the transport properties, we have measured their critical current density as a function of the temperature up to the critical temperature T_C.

The result is that the critical current density data of nanowires (even the narrowest ones) with a Au capping layer can be very well fitted (see Fig. 7.5a) by the Bardeen expression [179], valid in the dirty limit[2] ($\ell < \xi$) and commonly used to describe LTS nanowires [183, 184]:

$$J_C(T) \propto \left[1 - \left(\frac{T}{T_C}\right)^2\right]^{\frac{3}{2}}. \tag{7.1}$$

On the contrary, deviations from the Bardeen expression are observed for wires whose Au capping layer has been etched (see Fig. 7.5b). Only few nanowires, probably less affected by damages induced by the nanopatterning, have a $J_C(T)$ following the Bardeen expression in the full temperature range.

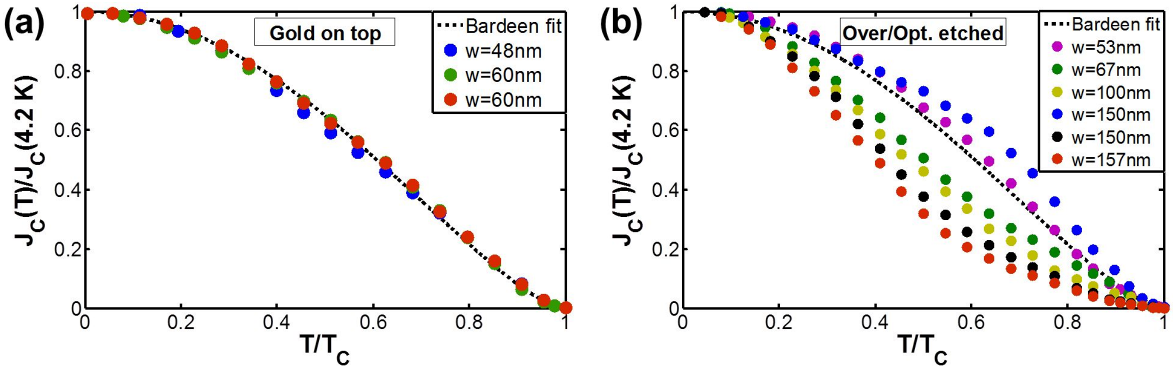

Figure 7.5: Normalized critical current density $J_C(T)/J_C(4.2\text{ K})$ measured in the whole range of temperature below T_C for nanowires capped with gold (panel (a)) and for those whose Au capping layer has been removed (panel (b)).

7.2 Influence of vortex dynamics in YBCO nanostructures

7.2.1 Resistance vs temperature measurements of nanowires

We have measured the resistance of the 50 nm thick YBCO nanowires with various lengths and widths as a function of the temperature, in a temperature range around T_C (see Fig. 7.6). The current and voltage probes of our 4-point measurement setup are situated at the far ends of the two wide and long electrodes, with widths $w > 10^4$ nm and $l > 10^5$ nm, connected to the nanowires. Therefore the first transitions at higher temperatures are related to the electrodes and the second broader transitions are instead related to the nanowires. Differently from what previously reported in literature [28], the onset temperature of the wire transition is typically only 1 K (or less) below the one of the wide electrodes, even for the narrowest wires [99].

It is important to note that the measured onset temperature of the wide electrodes, and consequently that of the wire, is 1-2 K lower than the expected one, corresponding to the value of the bare YBCO films. However this is only due to the additional resistive

---

[2] The equivalent expression, derived for the clean limit ($\ell > \xi$) [182], should be more correct in our case. However, the agreement of our data with such expression is rather poor.

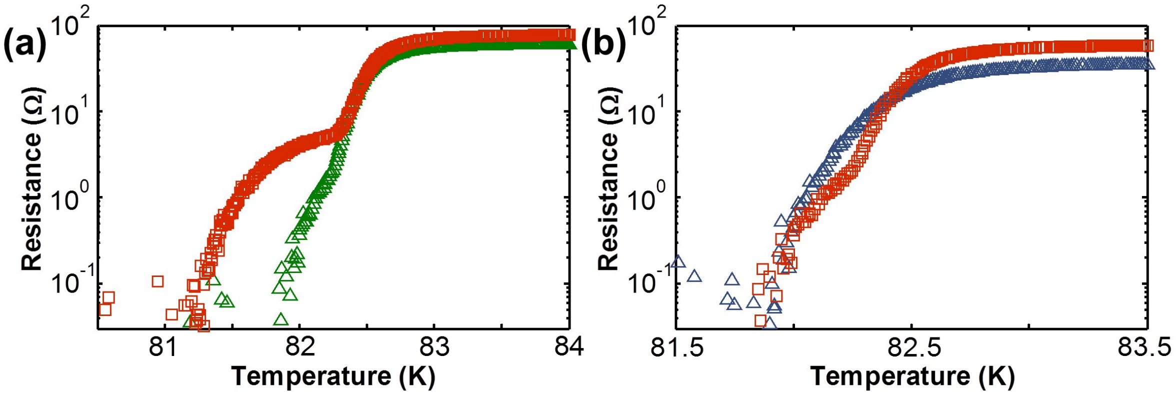

Figure 7.6: $R(T)$ measurements of Au capped YBCO nanowires with different lengths and widths grown on MgO (110). (a) $R(T)$ measurements of a 50 nm (squares) and 150 nm (triangles) wide wires. The length of both these wires is 200 nm. (b) $R(T)$ measurements of a 200 nm (squares) and 1000 nm (triangles) long wires, whose width is 150 nm in both the cases.

shunt of the Au film and not to a change of the superconducting transition temperature of the film. To clarify this point, we have to consider that the resistance $R(T)$ we measure is a parallel combination between the resistance of the YBCO nanowire $R_w(T)$ and the resistance of the gold film on top of the nanowire structures R_{sh}, i.e. $R^{-1}(T) = R_w^{-1}(T) + R_{sh}^{-1}$. The resistance R_{sh} becomes dominant at temperatures close to T_C, where it is much smaller than the resistance of the YBCO wire, $R_w(T_C) \approx R_N$. In particular, as we can clearly see in Fig. 7.7a, where we have studied with numerical calculations the influence of different values of R_{sh} on the total resistance $R(T)$ of a YBCO wire with fixed geometry, the onset temperature T^{onset}, at which the resistive transition becomes observable, decreases with decreasing the value of the shunt resistance. Thence, a discrepancy will be present between the T_C of the bare film and the T^{onset} we measure for our capped nanostructures.

In our case, the R_{sh} can be roughly approximated by the resistance R^w_{Au} of the gold strip of length $l_{Au} = l_{wire}$ and width $w_{Au} = w_{wire}$, on top of the YBCO wire (see Fig. 7.7b).[3]

The temperature broadening in the $R(T)$ of the wires (see Fig. 7.6) can be analyzed according to the models discussed in sec. (2.3.3), considering thermally activated phase slip events or vortices crossing the wires as the dominating source of resistance during the superconducting transition. Both these models predict that the resistive transition gets broader in temperature for decreasing wire width, in complete agreement with what we observe in our nanowires (see Fig. 7.6). For the same reason we have ruled out the BKT theory [140], related to vortex-antivortex pair dissociation in 2-dimensional systems with lateral extensions smaller than λ_P, which does not predict

---

[3] A more precise estimation has been derived from simulations of the current distributions in our structures using typical values for the resistivity of Au and YBCO, and the contact resistivity between Au and YBCO. The result is that the shunt resistance R_{sh} can be approximated by the series combination of the Au resistance on the top of the wire, R^w_{Au}, and the resistance associated to the current redistribution from the gold capping layer into the superconducting/low ohmic YBCO electrodes, R_{el}, which is independent on the YBCO wire resistivity. Typical values we have obtained for $R_{el} \approx 2\ \Omega$, are of the same order as R^w_{Au}.

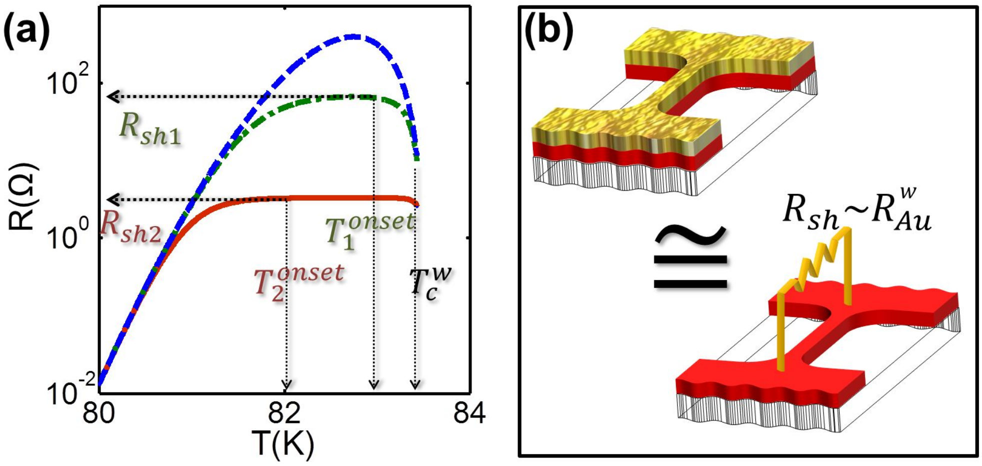

Figure 7.7: (a) Numerically calculated total resistance $R(T)$ for three different values of R_{sh}: $R_{sh,\infty} = \infty$ (dashed line), $R_{sh,1} = 80\ \Omega$ (dash dotted line) and $R_{sh,2} = 4\ \Omega$ (solid line). The difference between the observable onset temperature and the critical temperature T_C^w increases as the shunt resistance is decreased. (b) Equivalent circuit, describing the role of the Au layer: the value of R_{sh} in our capped nanowires can be approximated by the resistance of a gold strip of length $l_{Au} = l_{wire}$ and width $w_{Au} = w_{wire}$, R_{Au}^w, on the top of a YBCO wire.

any size dependence in the $R(T)$ broadening.

Our wires are three-dimensional systems and in principle only vortex slips should be considered [185, 186]. However, phase slip theories, although developed for one-dimensional systems, have been demonstrated to give reasonable results also in case of two-dimensional systems [94]. Thence, we have applied both the phase slip and the vortex slip theories to our experimental $R(T)$ data, and compared the extracted parameters [99].

In regards to the phase slip theories, we have considered the Little model to describe our $R(T)$ curves close to the transition, avoiding the intrinsic limitations of the LAMH model (see sec. 2.3.3) [98]. According to the Little model, the resistance of our YBCO wire is given by equation (2.28), $R_w(T) = R_{Little}(T)$. The energy barrier for phase slip nucleation $\Delta F(T)$writes analytically as:

$$\Delta F(T) = \left(\frac{8\sqrt{2}}{3}\right)\left(\frac{B_C^2(T)}{2\mu_0}\right) wt\xi(T)\,, \tag{7.2}$$

where w and t are respectively the width and the thickness of the wire. Moreover, close to T_C, the coherence length $\xi(T)$ and the critical field $B_C(T)$ can be expressed as $\xi(T) = \xi_0[2(1-T/T_C)]^{-1/2}$ and $B_C(T) = B_C^0(1-T/T_C)$, where $B_C^0 = h(2e\sqrt{2}\pi\lambda_0\xi_0)^{-1}$, λ_0 and ξ_0 are the thermodynamical critical field, the London penetration depth and the coherence length at $T = 0$, respectively.

Since our wires are covered by a gold capping layer acting as a shunt, the final resistance can be expressed as:

$$R(T) = \left[R_{Little}^{-1}(T) + R_{sh}^{-1}\right]^{-1}. \tag{7.3}$$

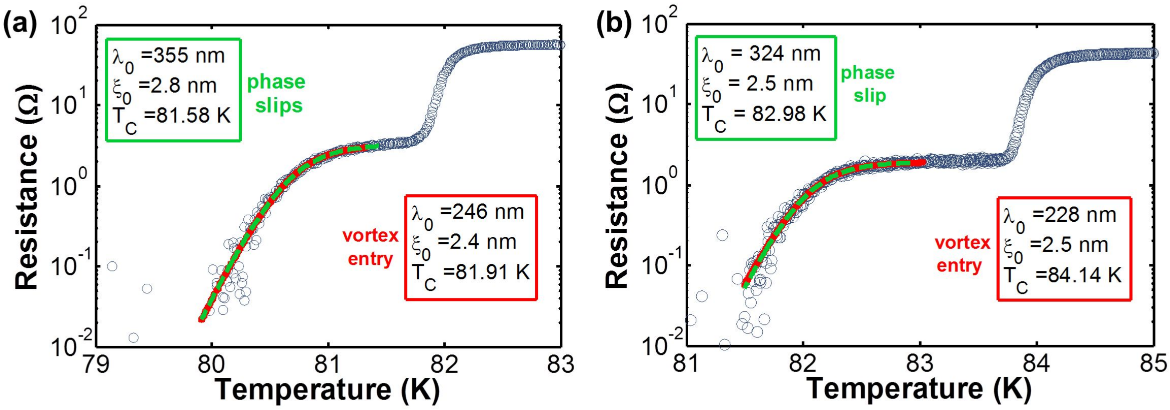

Figure 7.8: We have fitted both with the Little fit (dashed line) and with the vortex slip model (solid line) (a) a 85 nm wide wire grown on MgO (110); (b) a 67 nm wide wire grown on MgO (001).

In order to describe the broadening of the resistive transition in terms of vortex slips, we have considered the energy barrier for vortex entry expressed by eq. (2.29) [90]. As a consequence, the resistance of a YBCO wire is given by eq. (2.31), $R_w(T) = R_v(T)$. The gold shunt has to be accounted to derive the expression of the total resistance:

$$R(T) = \left[R_v^{-1}(T) + R_{sh}^{-1}\right]^{-1}. \tag{7.4}$$

We have fitted the $R(T)$ of the wires, both grown on MgO (110) and MgO (001), with eqs. (7.3) and (7.4), inserting the dimensions determined with AFM/SEM and extracting λ_0, ξ_0 and T_C as fitting parameters (see Fig. 7.8).

From a comparison between the parameters extracted with the two models, we can observe that the values of London penetration depth we obtain by fitting with the Little expression are more than 20% higher than those extracted from the vortex slip fit. A summary of the parameters extracted by the fits on different wires grown both on MgO (110) and MgO (001) is shown in Table 7.1.

Substrate	λ_0^{Little} (nm)	ξ_0^{Little} (nm)	J_d^{Little} (A/cm^2)	λ_0^v (nm)	ξ_0^v (nm)	J_d^v (A/cm^2)
MgO(110)	340-370	2-3	$\approx$ 3.2e7	235-265	2-3	$\approx$ 6.5e7
MgO(001)	315-340	2-3	$\approx$ 3.8e7	210-240	2-3	$\approx$ 8e7

Table 7.1: Summary of the parameters extracted from the fits of the $R(T)$, considering phase slip and vortex slip models. The values of J_d^{Little} and J_d^v have been derived using eq. (2.21).

To obtain a confirmation on the validity of the used models, we have calculated the expected depairing current density of the nanowires through eq. (2.21), using the values of ξ_0 and λ_0 extracted from both the fits, which are typical for YBCO thin films [180]. In particular if one is considering vortex slips as the main source of resistance, the expected values of J_d so calculated, J_d^v, are rather consistent with those extracted from the IV curves at 4.2 K (see Fig. 7.3). Moreover, comparing nanowires grown on MgO (110) and MgO (001), the difference between the extracted J_d is consistent both with the difference between the measured J_C at 4.2 K (e.g. see in Fig. 7.3 the shift between circles and triangles) and with the lower T_C measured on films grown on MgO (110), as a consequence of the large mismatch between the film/substrate in-plane lattice parameters. On the contrary, the discrepancy with the measured J_C values significantly increases when calculating the expected Ginzburg-Landau depairing current density of the nanowires with the ξ_0 and λ_0 values extracted from the Little fit.

These results give a confirmation of the validity of the vortex slip fitting procedure to extract physical quantities, as ξ_0 and λ_0, representing the nanowire. Thence, the possibility to explain the broadening in the resistive transition only in terms of the dissipation due to vortices crossing the wire, proves once more the high quality of our nanostructures, preserving pristine superconducting properties because of the presence of the gold capping layer.

To assess the effect of the capping layer on the superconducting properties, we have measured and analyzed the $R(T)$ of a 50 nm thick nanowire before and after the removal ("overetching") of the Au layer (see Fig. 7.9). The results are as follows:

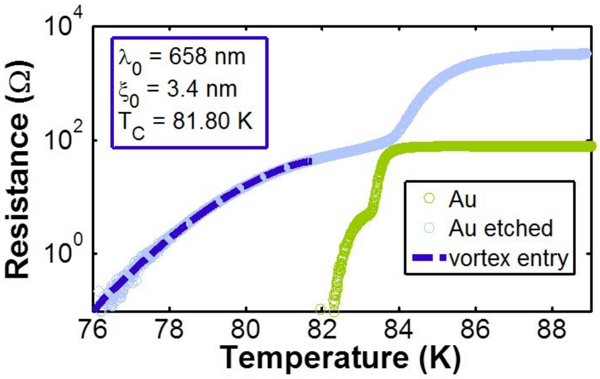

Figure 7.9: $R(T)$ of a 200 nm long and 50 nm thick YBCO wire grown on MgO (001) before (green circles) and after (blue circles) the eching of the Au capping layer. The blue dashed line is the fit to the vortex slip theory (eq. 2.31).

- As already mentioned previously, without the gold layer acting as a shunt, the onset temperatures of the wide electrodes and of the wire shift to higher values (in particular, the T^{onset} of the electrodes corresponds to the T_C of the bare film.

- The broadening of the superconducting transition of the wire is much bigger after the removal of gold. While the $R(T)$ before the Au etching can be fitted with the vortex slip model, extracting parameters in the ranges listed in Table 7.1, when fitting with the same model the $R(T)$ of the uncapped wire completely unfeasible parameters are extracted (see fitting parameters in Fig. 7.9). Therefore we have to conclude that the very broad superconducting transition is not caused by the motion of vortices across the wire, rather by local damages of the YBCO wire occurred during the last etching step.

7.2.2 Magnetoresistance measurements of nanorings

To confirm how vortex dynamics permeates the physics of 3D wires and nanostructures made of type II superconductors, we have used our slightly overdoped YBCO nanowires as building blocks to realize nanorings [187].

Nanorings are the basic structures for studying the fluxoid quantization and other coherent quantum phenomena. Indeed, the analysis of the magnetoresistance $R(B)$ oscillations, which can be observed in nanorings at temperatures close to T_C, allows the identification of the responsible charge carrier in superconductors, shedding light on different issues on HTS pairing mechanisms. Magnetoresistance measurements made on HTS nanorings [188], and in particular on YBCO submicron rings [189], have shown up to now that in the optimally doped/slightly overdoped regime the conventional periodicity $h/2e$ is present[4].

Our devices have been realized patterning 30 nm thick YBCO films, provided by Theva GmbH [181], grown on MgO (001) substrates and with a T_C of 85 K. Typical ring geometries we have realized are shown in Fig. 7.10a: the rings have an internal radius r_{int} in the range 120-200 nm, and arm width w in the range 50-80 nm. The four wide electrodes, used as current and voltage probes during the measurements, are situated very close to the nanostructures.

$R(T)$ and $R(B)$ measurements of different nanorings have been carried out in a Physical Property Measurement System (PPMS) of Quantum Design, using a 4-point measurement scheme. In the following, we will focus on the nanoring shown in Fig. 7.10a, having a cross section of 50×30 nm^2.

The $R(T)$ has been obtained by biasing the ring with a current of 500 nA. Since the electrodes are closely attached to the nanostructure, only the transition related to the nanoring is observed in the $R(T)$ (see Fig. 7.10b). The broadening of the resistive transition can be modeled in terms of a vortex slip model (eq. 2.31), considering the actual dimensions measured by AFM: feasible values for λ_0 and ξ_0 have been extracted ($\lambda_0 \approx 340$ nm and $\xi_0 \approx 2.5$ nm), only slightly higher than those listed in Table (7.1), probably as a consequence of the thinner YBCO layer [180].

We have measured the magnetoresistance of the ring at different temperatures within the resistive transition (see open squares in Fig. 7.10b). Large oscillations appear as a function of the flux enclosed by the ring (see Fig. 7.10c). Considering the geometrical area of the ring $A = \pi r_{avr}^2$, with $r_{avr} = 175$ nm, and the magnetic field periodicity $B_0 = 22$ mT, we have that the flux periodicity: $\Phi = B_0 \pi r_{avr}^2$ is equal to Φ_0, in agreement with a conventional $h/2e$ quantization.

Oscillations of the resistance as a function of the externally applied magnetic field are observed in the range $78 - 82$ K. The temperature dependence of the amplitude of these oscillations, ΔR, is shown in Fig. 7.10d (*filled circles*).

The most straightforward interpretation for these oscillations in LTS nanorings is

---

[4] HTS nanorings have attracted a lot of interest during last years, after theoretical studies have predicted the appearance of an additional component in the magnetoresistance with flux periodicity h/e, attributed to the d-wave order parameter [190, 191, 192, 193, 194]. At the same time, theories utilizing striped order to explain the mechanism of HTS have predicted the appearance of a periodicity $h/4e$ (corresponding to half a quantum of flux), replacing/coexisting with the usual periodicity of $h/2e$, in rings made with HTS materials [81].

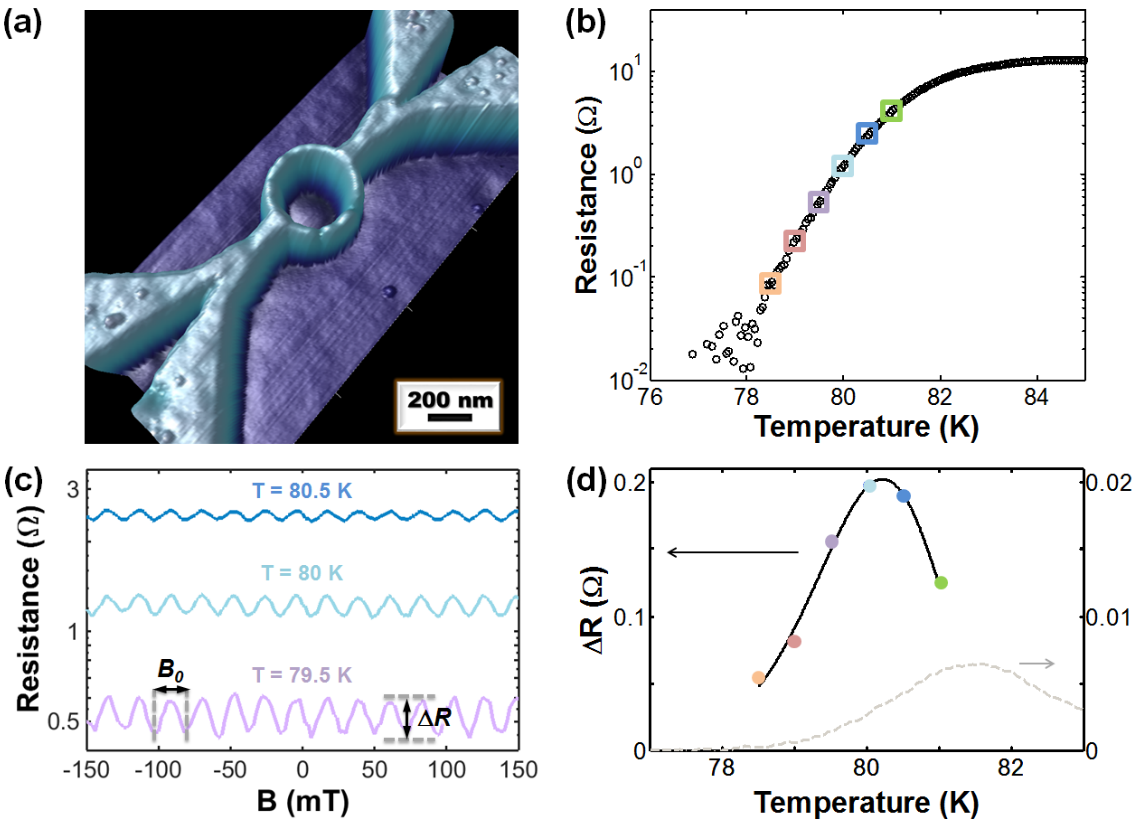

Figure 7.10: (a) AFM picture of a typical 30 nm thick nanoring, with internal radius of 150 nm and a linewidth of 50 nm. (b) $R(T)$ curve of the ring shown in panel (a). (c) On the $R(T)$ transition, at fixed values of the temperature, we have applied an external magnetic field, observing large magnetoresistance oscillations (which are reported here for three different temperatures). (d) Amplitude ΔR of the R(B) oscillations, at different temperatures (circles). The solid line represents the fit of the data by using eq. (7.5), accounting for the interaction between thermally excited moving vortices and oscillating screening currents circulating in the two arms of the ring. The dashed line represents instead an upper limit for the amplitude of the resistance oscillations as predicted by the Little-Park effect (its scale, on the right, is expanded by a factor 10).

the Little-Parks effect [195, 196]. According to this model, the expected temperature oscillations should have an amplitude $\Delta T_C = 0.14 T_C (\xi_0 / r_{avr})^2 \approx 1.5$ mK, with $T_C \approx 82$ K, defined at the onset of the superconducting transition, and $\xi_0 \approx 2$ nm. Since in the actual experiments one measures the resistance oscillations as a function of B rather than ΔT_C, it is possible to calculate the upper limit of the resistance amplitude predicted by the Little-Parks effect via the expression $\Delta R = \Delta T_C (\mathrm{d}R/\mathrm{d}T)$. The grey dashed line in Fig. 7.10d shows the expected Little-Parks ΔR. The discrepancy between the measured resistance amplitudes ΔR and those predicted by the Little-Parks effect is more than a factor 10.

These large magnetoresistance oscillations, which cannot be ascribed to classic Little-Parks oscillations, have been already observed in HTS nanoloops [188] and explained in terms of the vortex dynamics, triggering the resistive state in 3-dimensional nanowires (as we have also confirmed through the analysis of the $R(T)$ curve of the ring). In particular, according to this interpretation, the energy barrier for vortex entry, defined in eq. (2.29), becomes oscillatory, as a consequence of the interaction of the thermally excited moving vortices with the screening current circulating in the two arms of the ring, which - as we have previously observed in nanoSQUIDs - is a periodic function of the externally applied magnetic field. The equation describing the temperature dependent amplitude of the magnetoresistance oscillations is [188]:

$$\Delta R \approx R_0 \left(\frac{\epsilon_0^r}{2k_B T} \right)^2 \frac{K_1(\gamma)}{(K_0(\gamma))^3} \ , \tag{7.5}$$

where $\epsilon_0^r = \Phi_0^2 w/(4\pi\sqrt{\pi} r_{avr} \mu_0 \lambda_P(T))$ is the characteristic energy of a vortex in a nanoring, R_0 the resistance at the onset of the superconducting transition, K_0 and K_1 the zero-order and first-order modified Bessel functions of the first kind respectively and $\gamma = (E_\nu + \epsilon_0^r/4)/(2k_B T)$, with $E_\nu = \Phi_0^2/(4\pi\mu_0\lambda_P(T))\ln(2w/(\pi\xi(T)))$ the energy barrier for vortex entry, in the limit of zero bias. We have fitted our measured $\Delta R(T)$ with eq. (7.5), by using λ_0 and ξ_0 as fitting parameters. As shown by the solid line in Fig. 7.10d, the agreement between the data and the model is excellent, and the values of $\lambda_0 \approx 360$ nm and $\xi_0 \approx 3$ nm, which we extract, are in agreement with those extracted from the fitting of the $R(T)$.

In general, magnetoresistance oscillations originate both from the vortex dynamics and from the Little-Parks effect. In our case, the contribution of the vortex dynamics is dominant, as a consequence of the strong thermal fluctuations; at the same time, the contribution of the Little-Parks effect is very small, because of short coherence length in YBCO.

7.3 Ultrathin nanowires

Ultrathin nanowires, from Au capped 10, 20 nm thick YBCO films (described in Chapter 4), have been realized. 100 nm long and 65 nm wide nanowires have been fabricated (see Fig. 7.11). The edges between the wires and the wider electrodes have been designed with a rounded shape, to minimize current crowding effects, which could be a source of reduction of the critical current density J_C [197, 173].

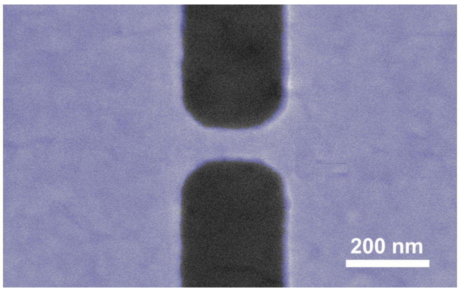

Figure 7.11: SEM picture of a Au capped 10 nm thick and 65 nm wide YBCO nanowire.

The nanodevices have been characterized via current-voltage characteristics IVCs and resistance versus temperature $R(T)$ measurements. We have compared the results with those obtained on nanowires with the same geometry, starting from a 50 nm thick YBCO film.

All the measured nanowires were superconducting. The IVCs of the nanowires, measured at $T = 4.2$ K, exhibit a typical flux flow like behavior, as shown in sec. 7.1.

To test the reproducibility of our nanostructures, we have measured for each sample a large number of identical wires. In Fig. 7.12a we have plotted the distribution of the extracted J_C values as a function of the film thickness. For each curve, we can extract an average critical current density $\bar{J}_C$. The J_C distributions become broader for thinner nanowires, possibly due to a most prominent role of defects at such reduced dimensions. However $\bar{J}_C$ is the same as the 50 nm thick nanowires, and the highest J_C within each distribution $\approx 8 \cdot 10^7$ A/cm^2, a value very close to the depairing limit.

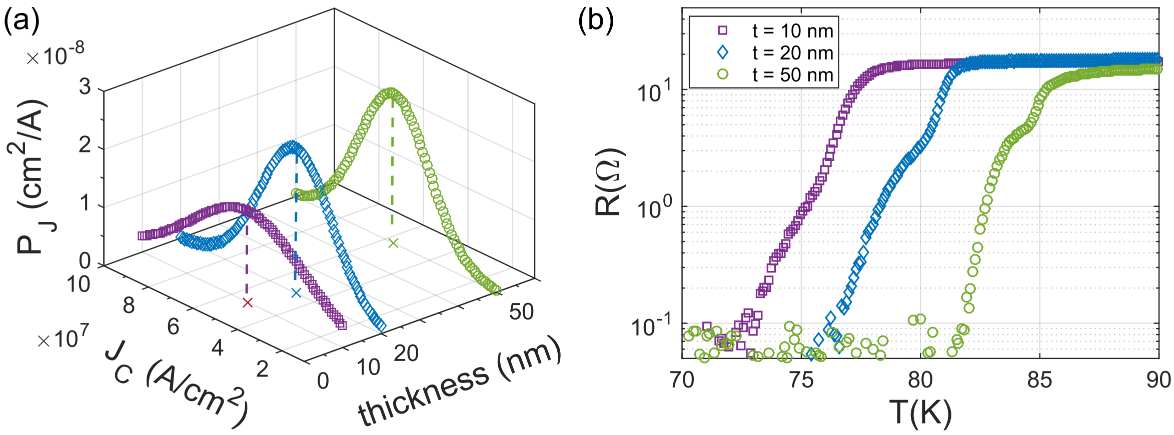

Figure 7.12: a) Distribution P_J of the critical current densities J_C of the population Π of 65 nm wide Au capped nanowires, as a function of the wire thickness ($\Pi_{10} = 12$, $\Pi_{20} = 59$ and $\Pi_{50} = 18$). The $\bar{J}_C$ values of the three distributions, highlighted by the dashed lines, are almost identical ($\bar{J}_{C\,10} = 5.3 \cdot 10^7$ A/cm^2, $\bar{J}_{C\,20} = 4.8 \cdot 10^7$ A/cm^2 and $\bar{J}_{C\,50} = 5.6 \cdot 10^7$ A/cm^2). b) $R(T)$ of three 65 nm wide Au capped nanowires, at different thicknesses.

The resistance as a function of the temperature, in a temperature range around T_C, is shown in Fig. 7.12b for two nanowires, with thicknesses $t = 10, 20$ nm. They have been compared with a typical dependence obtained for 50 nm thick nanowires. For each device, as described in sec. 7.2.1, the first transition in the $R(T)$, at higher temperature, is related to the wide electrodes connected to the nanowire: the temperature range of this transition corresponds to that of the unpatterned film (previously seen in Fig. 4.3a), though the onset is lower because of the shunt effect of the Au layer. The second, broader, transition in the $R(T)$, at lower temperature, is instead associated to the nanowire: what is more remarkable of this transition is that the onset temperature is typically only 1-2 K lower than the one of the wide electrodes, independently of the thickness.

The broadening of the superconducting transition of the thinnest nanowires is not much wider than that of the 50 nm thick nanowires. However, this broadening cannot be only ascribed to the dissipation induced by Abrikosov vortices crossing the nanowires, as it has been been previously shown for the 50 nm thick nanodevices (see sec. 7.2.1). Indeed, on ultrathin nanowires the picture is more complicated, since the broadening is both caused by the confinement of the width, which can be explained in terms of the vortex entry model, and by the confinement of the thickness, which - as previously mentioned - is not unambiguously associated to the BKT model, valid for 2D superconductors (see sec. 4.2.2). Thence, a quantitative analysis of the superconducting transition of ultrathin nanowires requires further investigations, which go beyond the scope of this thesis.

In summary, we have shown that ultrathin Au capped YBCO nanowires, with thicknesses down to 10 nm behave similarly to the 50 nm thick nanowires, and are characterized by superconducting properties not touched by the nanopatterning procedure up to their T_C^0, which is very close to the T_C^0 of the unpatterned films.

7.4 Underdoped nanowires

Despite the extensive research present in literature on underdoped HTS thin films, only few works are devoted on the fabrication of underdoped nanostructures, with not very encouraging results.

Bonetti et al [27] report about the fabrication of underdoped YBCO nanowires, with widths down to 200 nm. The T_C of the nanowires is 5-10 K lower than that of the unpatterned films, which is already a sign of the degradation of the superconducting properties. Moreover nanowires, patterned on underdoped films having T_C lower than 75 K, are not superconducting.

Carillo et al [198] show the realization of $\mathrm{Nd_{1.2}Ba_{1.8}Cu_3O_z}$ nanodevices, starting from films having T_C gradually changing from the maximum of 65 K down to the non-superconducting state. The T_C of sub-micron wires decreases dramatically - by tens of Kelvin - when reducing the width. Structures narrower than 200 nm are not anymore superconducting.

Even though charge density waves are stronger in the underdoped regime, so far underdoped HTS cuprates have never been studied at the nanoscale, on dimensions comparable with the CDW correlation length.

To realize underdoped nanowires, we have patterned two 50 nm thick Au capped YBCO films, one slightly underdoped, with $T_C^0 = 81.4$ K, and the second one, having a doping close to the 1/8 plateau, with $T_C^0 = 60.5$ K. More details about these films have been described in Chapter 5.

On both films, we have fabricated 100 nm long nanowires, with widths of 65 and 140 nm, having the same geometry as the nanowires shown in Fig. 7.11.

At any doping, all the measured nanowires are superconducting. The IVCs measured at $T = 4.2$ K, exhibit a typical flux flow like behavior, as shown in sec. 7.1.

We have measured for each sample a large number of identical 65 nm wide wires. In Fig. 7.13a we have plotted the distribution of the J_C values extracted within each sample as a function of the T_C^0 of the parent bare film.

As it is evident in Fig. 7.13a, the $\bar{J}_C$ values decrease by almost one order of magnitude going from overdoped nanowires to "1/8" underdoped nanowires. Such a reduction can be attributed to the change of the λ_0 and ξ_0 values, occurring in the

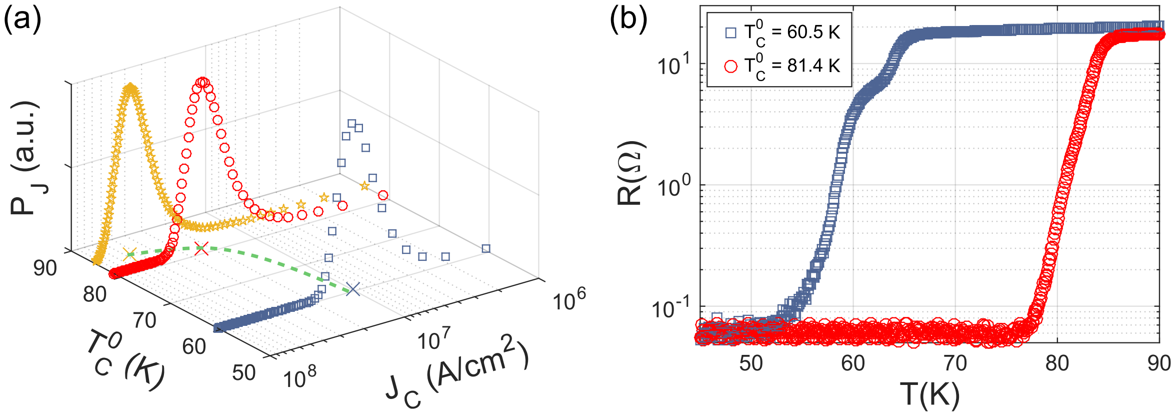

Figure 7.13: a) Distribution P_J, normalized to the maximum, of the critical current densities J_C extracted by the population Π of 65 nm wide Au capped nanowires, as a function of the T_C^0 of the films before to be patterned ($\Pi_{60.5} = 24$, $\Pi_{81.4} = 24$ and $\Pi_{85} = 18$). The $\bar{J}_C$ values of the three distributions, highlighted by crosses, decrease as the oxygen doping decreases, consequently to the increase of λ_0 and ξ_0 occurring at low doping ($\bar{J}_{C\,60.5} = 9.9 \cdot 10^6$ A/cm^2, $\bar{J}_{C\,81.4} = 2.2 \cdot 10^7$ A/cm^2 and $\bar{J}_{C\,85} = 5.6 \cdot 10^7$ A/cm^2). The dashed line is a guide for the eye. b) $R(T)$ of two 140 nm wide Au capped nanowires, having different doping (the T_C^0 is the zero resistance critical temperature of the films, before the patterning).

underdoped regime. However these two values cannot be extracted from the $R(T)$ of the underdoped nanowires, shown in Fig. 7.13b, as we have done on slightly overdoped nanowires, for reasons which will be clarified in the end of this section.

In single crystals, the dependence of the London penetration depth and of the coherence length on the oxygen doping has been determined by electron-spin resonance measurements and by the values of the upper critical magnetic field respectively [199, 200]. In single crystals having the same T_C of our slightly underdoped film, λ_0 and ξ_0 increase, with respect to the values at the optimally doped regime, by $\approx 20\%$ and $\approx 65\%$ respectively; such increase is even larger in single crystals at the 1/8 doping, reaching $\approx 50\%$ and $\approx 110\%$ for λ_0 and ξ_0 respectively.

Thence, assuming that the dependence of the London penetration depth and of the coherence length on the oxygen doping is the same in single crystals and thin films, we can determine λ_0 and ξ_0 in our two patterned underdoped films. To do so, we assume that the values of λ_0 and ξ_0 at the optimally doped regime are those we have extracted from the fits of the $R(T)$ of our slightly overdoped nanowires, considering vortex slip model (see sec. 7.2.1 and Table 7.1).

By knowing λ_0 and ξ_0, for each underdoped film we can calculate, using eq. (2.22), the maximum critical current density that the YBCO nanowires can carry because of vortex entry, J_v, and compare this value with the measured $\bar{J}_C$. A summary of all the measured and calculated parameters for the different films is enclosed in Table 7.2: at any doping, the agreement between J_v and $\bar{J}_C$ is fairly good. Such occurrence shows that, similarly to our slightly overdoped nanostructures, the underdoped nanowires are not affected by the patterning.

In the previous analysis, we have considered the same λ_0 and ξ_0 values for the thin

doping	T_C^0 (K)	λ_0 (nm)	ξ_0 (nm)	J_v (A/cm^2)	$\bar{J}_C$ (A/cm^2)
UD	60.5	375	5.2	$1.1 \cdot 10^7$	$9.9 \cdot 10^6$
UD	81.4	300	4.1	$2.3 \cdot 10^7$	$2.2 \cdot 10^7$
OD	85	250	2.5	$5.3 \cdot 10^7$	$5.6 \cdot 10^7$

Table 7.2: The parameters extracted from underdoped (UD) YBCO nanowires are summarized and compared with those of slightly overdoped (OD) nanowires. For the OD sample, λ_0 and ξ_0 have been extracted from the fits of the $R(T)$, considering vortex slip model (see Table 7.1). From these values, we have extrapolated λ_0 and ξ_0 of UD nanowires, considering the typical doping dependence of these two parameters in single crystals [200]. Given these two parameters, for each sample we have calculated J_v, maximum critical current density YBCO nanowires can carry because of vortex entry, using eq. (2.22). The J_v value has been compared with $\bar{J}_C$, average of the measured J_C values extracted within the wire population. The agreement between the two values is fairly good, at any doping.

film and for the patterned nanowires. This is supported by the $R(T)$ of the nanowires with different doping, shown in Fig. 7.13b. It is evident that the onset temperature of the transition related to the nanowire is only 1-2 K lower than the one of the wide electrodes, independently of the oxygen doping. This circumstance never occurred in previous works on underdoped HTS nanostructures.

The broadening of the superconducting transition associated to the nanowire increases at lower doping, as expected considering dissipation induced by Abrikosov vortices crossing the nanowires (eq. 2.31), as a consequence of the larger values of λ_0 and ξ_0. However, at the moment a quantitative analysis of this transition is still missing. Indeed, the broadening of the transition of the bare underdoped films, which could be related to intrinsic properties of the YBCO compound at specific doping levels, influences the transition broadening of the nanowires, though it is not taken into account by eq. 2.31.

8

YBCO nanoSQUIDs implementing nanowires

With the progress in nanotechnologies the development of quantum limited sensors, allowing the measurement of the physical properties of nano-objects with unprecedented resolution, has become crucial. In particular, Josephson junction based nanodevices, such as Superconducting Quantum Interference Devices (nanoSQUIDs), have recently gained a lot of attention for their extreme magnetic flux sensitivity [30, 31]. Within this field, a real challenge is to what extend the flux sensitivity can be improved to be able to detect a single spin, a holy grail for physical measurements [32]: a SQUID loop on the nanometer scale is indeed a crucial requirement for such detection [33].

However, the downscaling of tunnel junction based SQUIDs is an extremely challenging task. In particular, scaling down the dimensions of a conventional tunnel junction to nanometer size implies several drawbacks such as the deterioration of the tunnel barrier, with increased critical current/resistance noise [201], and small critical current values, limiting the working operation range of the SQUIDs far below the transition temperature of the superconducting material used. For these reasons during the recent years a lot of effort has been put into the development of nanoSQUIDs implementing superconducting nanowires in a Dayem bridge configuration [202, 203]. At the moment, the realization of such nanoSQUIDs is well established for Low critical Temperature Superconductors (LTS) [204]. However, nanoSQUIDs made of High critical Temperature Superconductors (HTS) might extend the operational working temperature (from mK to above 77 K) and the range of magnetic field that can be applied compared to Nb based nanoSQUIDs, making them even more attractive for applications ranging from fundamental studies of nano-magnetism in molecules and magnetic nanoclusters to low field magnetic resonance imaging.

Several attempts to achieve HTS nanoSQUIDs, implementing YBCO Dayem bridges, have been done during the last few decades [34, 35, 205, 163]. However a proper SQUID behavior, with a periodic modulation of the critical current in the full temperature range below T_C has never been observed. These results suggest a severe degradation of the YBCO nanostructures during fabrication, highlighted by critical current densities J_C never above 10^6 A/cm^2 at 4.2 K.

In this chapter, we will show the fabrication and transport characterization of our nanoSQUIDs, realized in the Dayem bridge configuration by using the nanowires previously presented [206]. For the first time, critical current modulations have been

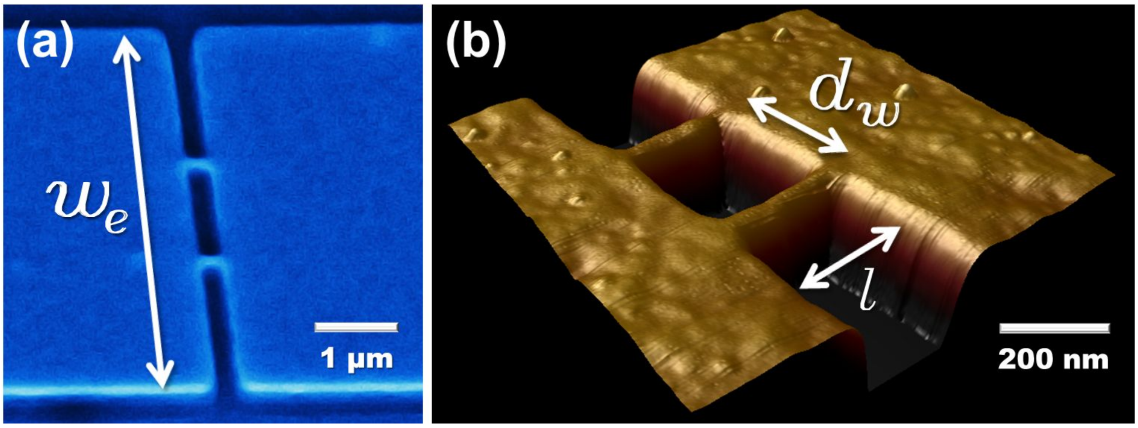

Figure 8.1: (a) SEM and (b) AFM images of two nanoSQUIDs in the Dayem bridge configuration. The loop areas, respectively of 200×970 nm^2 and 200×150 nm^2 are realized with two parallel YBCO nanowires, capped with Au and placed to a distance d_w, connecting two wider electrodes (whose width is w_e).

observed as a function of an externally applied magnetic flux in the full temperature range below the transition temperature T_C of the devices. Both the modulation depth and the period in magnetic field are in good quantitative agreement with numerical computations. The high values of the critical current density we have achieved, demonstrating superconducting properties close to the as grown film, make these devices model systems to study the intrinsic properties of HTS, such as the fluxoid quantization in superconducting loops [188, 189]. Moreover, the record white flux noise below 1 $\mu\Phi_0/\mathrm{Hz}^{1/2}$ we have measured above 10 kHz makes these devices also appealing for the investigation of small spin systems.

8.1 NanoSQUID design

The devices have been realized by patterning both untwinned YBCO films grown on MgO (110) substrates, and twinned YBCO films, provided by Theva GmbH [181], grown on MgO (001) substrates. The nanopatterning procedure is the one described in detail in Chapter 6. As a only difference, to better define square-shaped loop geometries even for very small areas, we have exposed the wider electrodes and the narrower wires in two different e-beam lithographic steps. Typical geometries we have realized for the nanoSQUIDs are shown in Fig. 8.1: two nanowires in parallel, whose length l is in the range 100 - 200 nm, connect two wide electrodes with widths w_e in the range 4-16 μm. Different loop areas have been achieved, by varying the distance d_w between the wires in the range 100 - 1000 nm. All the dimensions have been confirmed by scanning electron microscopy (SEM).

8.2 Transport characterization

Electrical transport properties of the devices have been performed in a ^{3}He cryostat. $R(T)$ measurements and IVCs in the whole temperature range from 300 mK up to the T_C of the devices, have been carried out using a 4-point measurement scheme. The nanoSQUIDs have the onset of the superconducting transition very close to the T_C of the bare films (differing not more than 1 K). Moreover, they have very high critical current densities J_C at 300 mK: on the devices patterned on (001) MgO the average J_C values per wire are in the range $7-9\times10^7$ A/cm^2, close to the GL depairing limit; on devices on (110) MgO they are of the same order of magnitude, although slightly lower. This small reduction of J_C could be related to a greater sensitivity of the YBCO films grown on (110) MgO to the double e-beam resist baking treatment, involved in the nanoSQUID patterning process.

In Fig. 8.2 we show the critical current of two nanoSQUIDs as a function of an externally applied magnetic field. Modulations of the critical current have been observed in the whole temperature range, up to the critical temperature of the devices. Here, the critical current has been measured by ramping the current and detecting when the voltage exceeded a voltage criterion, the latter being determined by the noise level and the shape of the IVC (usually a value of $\sim 2\ \mu$V has been considered). From the critical current modulation we have extracted the modulation period ΔB and the relative critical current modulation depth $\Delta I_C/I_C^{max}$, with ΔI_C being the difference between the maximum I_C^{max} and the minimum I_C^{min} values of the critical current (see Fig. 8.2a). The small difference between I_C^{max} values belonging to different lobes within the same modulation (see Fig. 8.2b) is caused by the response of the single junction, which is not point contact-like as supposed in sec. (2.4.1): as a consequence, each nanoSQUID modulation is superimposed to the $I_C(B)$ modulation of the single nanowire. More-

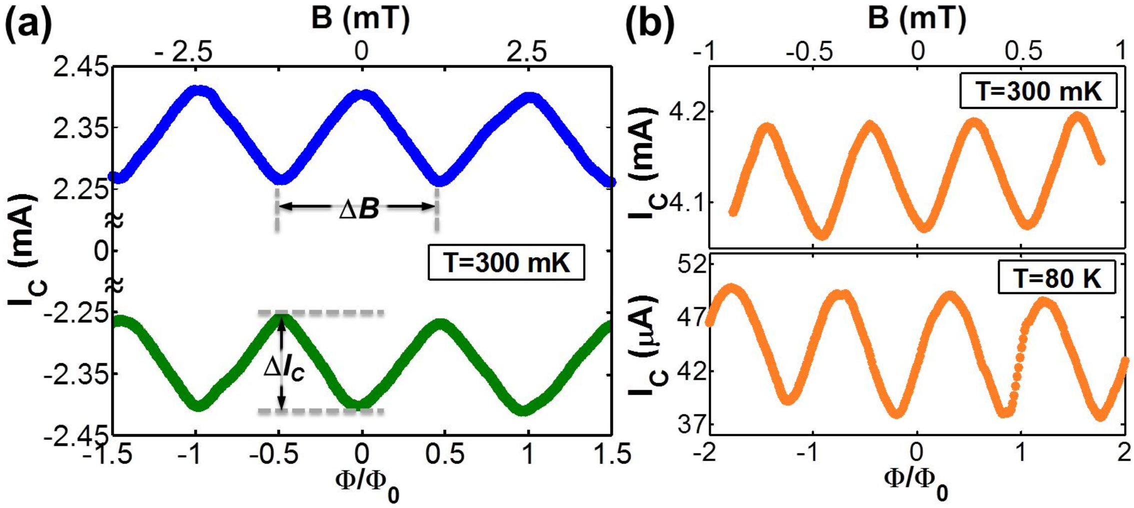

Figure 8.2: Critical current as a function of the applied magnetic field measured (a) at 300 mK, on a device patterned on MgO(110) with a loop area of 130×150 nm^2; (b) at $T = 300$ mK (*upper panel*) and close to T_C (*lower panel*), on a device patterned on MgO(001) with a loop area of 130×1000 nm^2.

over, the distortion of the critical current oscillations, which is most notable in the shift of the maxima and minima along the flux axis, is due to an asymmetry of the critical currents and/or inductances carried by the two nanowires [207].

8.3 Comparison between numerical and experimental results

To calculate numerically the expected ΔI_C, we have followed the approach by Tesche and Clarke [103]. For this purpose, the knowledge of the current-phase relation (CPR) of the bridges and the inductance of the electrodes is required. Concerning the CPR, our bridges are long ($l \gg \xi$) and wide ($w > 4.4\xi$) nanowires, with cross section $wt \ll \lambda^2$. In this limit, as already discussed in sec. (2.3.2), the CPR is given by the linear approximation of the Likharev and Yakobson expression [87], eq. (2.23). Each nanowire inside the nanoSQUID loop is therefore represented by an arm inductance, where the phase difference between the two ends grows linearly with the bias current. As a consequence, the critical current modulation depth will strongly depend on the value of the nanowire inductance: in particular, it decreases as the inductance increases. From numerical calculations, which have been shown in sec. (2.4.1), we have that

$$\frac{\Delta I_C}{I_C^{max}} \approx \frac{1}{\beta_L} \ , \tag{8.1}$$

where β_L is the screening inductance factor, given by

$$\beta_L = \frac{I_C^{max} L_{loop}}{\Phi_0} \ . \tag{8.2}$$

Here, L_{loop} is the total inductance of the SQUID loop, that includes both the contributions of the wires and of the electrodes. Thence, the experimentally measured ΔI_C is directly connected to the inductance of the nanoSQUID, through the β_L parameter.

In our case, we haven't directly measured the nanoSQUID inductance. Instead, we have calculated it by solving the Maxwell and London equations describing the Meissner state on our SQUID geometry [208]. As expected from their dimensions [102], the main contribution to L_{loop} comes from the kinetic inductance $L_k(T)$ of the nanowires (~ 15 pH at 300 mK), which is one order of magnitude higher than the geometrical value already at 4 K. For the temperature dependence of the loop inductance we have used the two-fluid model for the London penetration depth [40], on which L_k is strongly dependent:

$$\lambda_L(T) = \lambda_0 \frac{1}{\sqrt{1 - \left(\frac{T}{T_C}\right)^2}} \ , \tag{8.3}$$

The numerically calculated loop inductance $L_{loop}^{num}(T)$ allows to determine a numerical

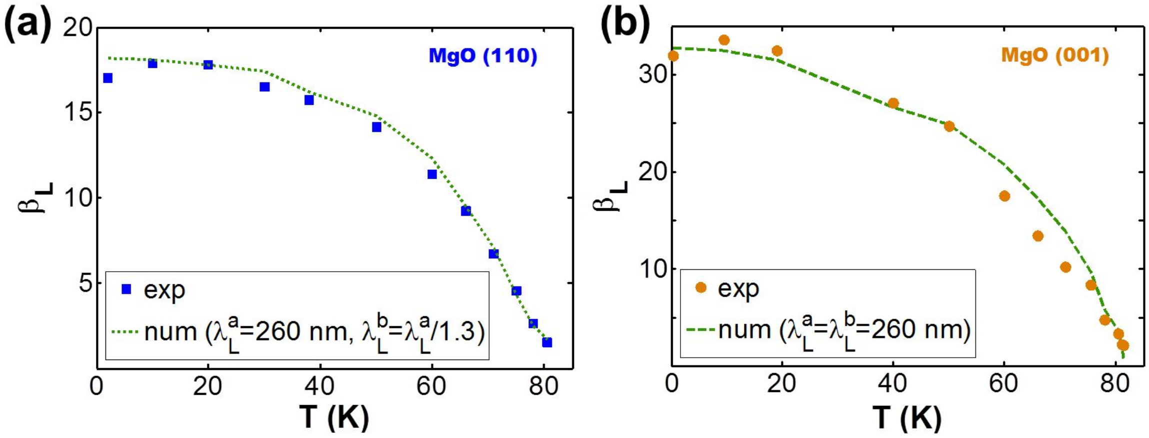

Figure 8.3: Comparison between the experimental (dots) and the theoretical (lines) values of the screening inductance factor β_L as a function of the temperature for nanoSQUIDs patterned on (a) a MgO (110) substrate, considering for the fit a λ_0^a value of 260 nm and the in-plane anisotropy of the London penetration depth; (b) a MgO (001) substrate, considering for the fit a λ_0^a value of 260 nm and assuming the in-plane isotropy of the London penetration depth.

β_L (see lines in Fig.8.3) through eq.(8.2), as[1]

$$\beta_L^{num}(T) = \frac{I_C^{max}(T) L_{loop}^{num}(T)}{\Phi_0} \; . \tag{8.4}$$

We can now fit the numerical temperature dependence of β_L^{num} with an experimentally determined parameter, β_L^{exp} (see solid symbols in Fig. 8.3), defined through eq.(8.1) as

$$\beta_L^{exp}(T) = \frac{I_C^{max}(T)}{\Delta I_C(T)} \; , \tag{8.5}$$

by using λ_0 as the only fitting parameter.

As shown in Fig. 8.3a, for all the measured YBCO nanoSQUIDs fabricated on MgO (110) the agreement between data and numerical calculations is very good in the whole temperature range, using $\lambda_0^a = 260$ nm and considering the in-plane anisotropy of the London penetration depth, which is consequence of the YBCO films, being untwinned on MgO (110) (as highlighted in sec. 3.4). For the fit, an anisotropy factor of 1.3 has been considered ($\lambda_0^b = \lambda_0^a/1.3$) [69, 70]. Moreover, the λ_0^a value extracted by the fit is very close to that extracted from $R(T)$ measurements, assuming vortex slips as sources of the broadening of the resistive transition around T_C (see sec. 7.2.1 and table 7.1).

For the YBCO nanoSQUIDs fabricated on MgO (001), as shown in Fig. 8.3b, the agreement between data and numerical calculations is very good, using a $\lambda_0^a = 260$ nm, which is rather close to the value extracted by vortex slip fitting of the $R(T)$ measurements ($\lambda_0^v = 240$ nm), and considering the in-plane isotropy of the London penetration depth (the films on MgO (001) are twinned, so $\lambda_0^a = \lambda_0^b$).

We now focus on the periodicity ΔB of the critical current modulations. In Fig. 8.4

---

[1] In this expression, we have extracted the $I_C^{max}(T)$ values from the measurements.

we show the experimentally determined effective area $A_{eff}^{exp} = \Phi_0/\Delta B$ of nanoSQUIDs having different distances d_w between the nanowires. These effective areas A_{eff}^{exp} are far larger than the geometrical areas $A_g = d_w \cdot l$, defined by the distance and the length of the two wires. This can be understood considering that the superconducting phase gradient induced in the wide electrodes by the screening currents contributes to the total phase difference between the two wires resulting in an effective area which is larger than the geometric loop area [209, 202]. These experimentally determined values of A_{eff}^{exp} have been compared with those, calculated numerically, following Ref. [210], $A_{eff}^{num} = m/I_{cir}$. Here, $m = \frac{1}{2}\int \vec{r} \times \vec{j} d\vec{r}$ is the magnetic moment generated by a circulating current I_{cir} around the SQUID loop. The result shows a good agreement between theoretically and experimentally determined values of the effective area (see Fig. 8.4). In particular, our calculations show that the effective area is proportional to the product of the wire distance d_w and the electrode width w_e, $A_{eff} \propto w_e \cdot d_w$. A similar dependency has been analytically found for the effective area in Ref. [202], in the limit $d_w \ll w_e$ and $w_e \ll \lambda^2/t$, with a proportionality constant equal to $8G/\pi^2$ (where G is the Catalan number, defined as $G = \sum_{n=0}^{\infty}(-1)^n/(2n+1)^2 \approx 0.916$). Within these limits, we found a good agreement with such a value, with a discrepancy of about 5%.

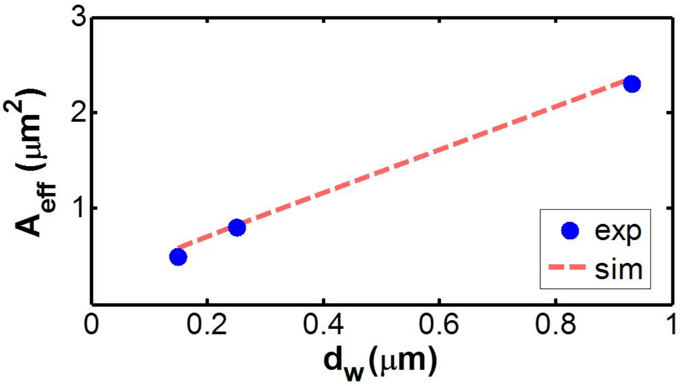

Figure 8.4: Comparison between the experimental (dots) and the calculated (lines) values of the effective area A_{eff} for several devices patterned on MgO (110), with same electrodes width (4 μm) and wire length (150 nm) but different edge to edge distance d_w between the wires. From the plot it could be deduced that $A_{eff} \neq 0$ even if $d_w = 0$: this is simply an artifact caused by the convention to define d_w between the two wire edges rather than between the two wire centers.

8.4 Noise measurements

We have also measured the flux noise of a nanoSQUID (see Fig. 8.5) at a bias current slightly above the critical current and at a magnetic flux bias where the slope of the voltage modulations $V(\Phi)$ (see Fig. 8.6a) is maximized, $V_\Phi = \max(|\partial V/\partial \Phi|)$.

Using a cross correlation measurement scheme (see Fig. 8.6b) [211] we have achieved an amplifier input white noise level of $\simeq 0.7$ nV/$\sqrt{\text{Hz}}$. From the measured voltage noise

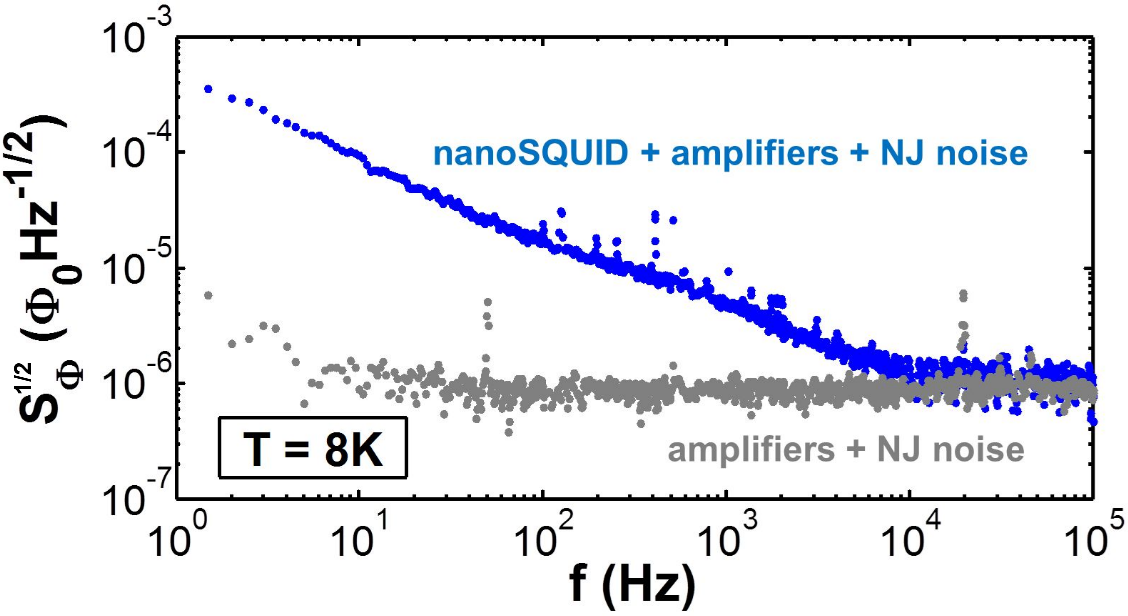

Figure 8.5: Flux noise spectral density $S_\Phi^{1/2}$ vs frequency f, measured at $T = 8$ K on a nanoSQUID grown on (110) MgO and with a geometrical loop area $A_g = 0.1$ μm^2.

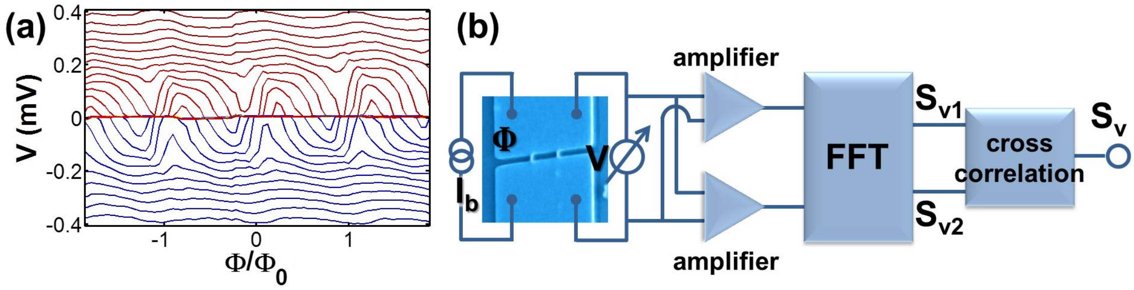

Figure 8.6: (a) Voltage modulations of the nanoSQUID mentioned in Fig. 8.5. $V(\Phi)$ are shown for $I = [-2.5, 2.5]$ mA (in 26 μA steps), among which a voltage modulation of 0.2 mV (peak-to-peak) is present, corresponding to a transfer function $V_\Phi = 1.5$ mV$/\Phi_0$. (b) Basic scheme of the setup used for our noise measurements. The nanoSQUID is biased in current and in magnetic flux. The voltage signal from the device is fed to two independent input amplifiers operating in parallel, followed by a two-channels FFT dynamic system analyzer operated in cross correlation mode. The voltage noise from the nanoSQUID is coherent and correlated in both channels and averages to a finite value. The frequency components of the noises of the two input amplifiers are uncorrelated and they can be reduced by a proper averaging.

density $S_v^{1/2}$ we can calculate the flux noise density $S_\Phi^{1/2} = S_v^{1/2}/V_\Phi$. In Fig. 8.5, the flux noise of a nanoSQUID, recorded at a magnetic flux bias corresponding to the max($|\partial V/\partial\Phi|$) displayed in Fig. 8.6a, is shown. Above 10 kHz the measured white flux noise is $(S_\Phi^w)^{1/2} = 1.2\ \mu\Phi_0/\sqrt{\mathrm{Hz}}$, which is the sum of the intrinsic nanoSQUID flux noise and the noise added from the amplifier. From the measured value of the amplifier noise, including the Nyquist Johnson (NJ) noise of the measurement leads (grey dots in Fig. 8.5), $S_a^{1/2} \simeq 1\ \mu\Phi_0/\sqrt{\mathrm{Hz}}$, we can determine the upper limit for the intrinsic white flux noise of the nanoSQUID: $(S_\Phi^{nS})^{1/2} = \sqrt{S_v - S_a} \simeq 0.7\ \mu\Phi_0/\sqrt{\mathrm{Hz}}$. This is among the lowest values for YBCO nanoSQUIDs reported in literature [212], corresponding to a predicted spin sensitivity of only 50 μ_B per $\sqrt{\mathrm{Hz}}$, where μ_B is the Bohr magneton [213].

At frequencies below 10 kHz the noise spectrum is dominated by $1/f$ noise. Since the measured $1/f$ voltage noise spectra do not depend on the flux bias, we attribute the $1/f$ spectrum to critical current noise. A further characterization is currently in progress, mainly aimed at establishing the ultimate flux noise sensitivity at low frequencies: by performing the measurements in bias reversal mode [214] with a custom made electronics, we should be able to remove the noise due to current fluctuations. Here it is worth mentioning that available electronics for SQUID noise characterization [215] does not allow to characterize devices with very high critical current (in the order of one hundred of μA even close to T_C).

9

Photoresponse on YBCO nanowires

High critical temperature superconductors (HTS), characterized by fast thermalization dynamics, are in principle very interesting for realizing devices for high rate photodetection. In particular, YBCO thin films and micron size wires have been the object of an intense research since the early 90's, based on the investigation of their transient voltage response to laser pulses in the picosecond regime [216, 217, 218]. A slow response, related to thermalization of phonons (bolometric effect), with times down to 1 ns, was observed, together with faster response times, down to the femtosecond regime, attributed to several mechanisms, such as Josephson effect [219], kinetic inductance variations in the superconducting state [220], motion of vortices [221], or electron heating [222]. However the single photon response, requiring a degree of homogeneity of the patterned material, together with very small cross sections, well above that of all the previously mentioned works, has never been observed. As a consequence, despite all the efforts, the focus on nanowire-based single photon detectors (see sec. 2.4) has involved only low temperature superconductors such as NbN, NbTiN, and more recently WSi to fabricate these devices [100, 223, 224].

Since our YBCO nanostructures show superconducting properties close to the as grown films, our aim was to fabricate devices suitable for the single photon response. Basically, what is required for such detection are wires, with very thin thickness, long and not covered by gold. We have followed two different approaches.

As a first approach, we have fabricated 50 nm thick nanowires in a series-parallel configurations, covering areas up to $30 \times 10\ \mu\text{m}^2$ with nanowires widths down to 100 nm, and with a protective layer of $\text{La}_{0.7}\text{Sr}_{0.3}\text{MnO}_3$ (LSMO), which is transparent to optical photons [225]. Transport measurements have shown that, despite the very complex pattern, the superconducting properties are not so much affected by the nanopatterning if an LSMO capping is present. We have illuminated the devices with optical laser pulses, measuring a photoresponse, which has been analyzed as a function of the current bias, of the temperature and of the laser power. With a first approximation, we find that the main origin of such a response is bolometric, being strictly related to the raise of temperature induced by the laser in the YBCO nanowires.

As a second approach, we have patterned and characterized the transport properties of 10 nm thick bare nanowires. Despite the absence of any capping layer, the J_C values are not much depressed, with respect to Au capped thin nanowires. Contrary to 50 nm thick devices, the IV characteristics are hysteretic: self-heating effects drive the nanowires directly from the superconducting to the normal state just above the critical current I_C. This occurrence makes our ultrathin YBCO nanowires very similar to NbN nanowires: they appear therefore to be the fundamental step for the development of HTS single photon detectors. First photoresponse measurements on these devices are currently on progress.

9.1 Working principles of SNSPDs

The working principles of the LTS superconducting nanowire single photon detectors (SNSPDs) will be highlighted to clarify the requirements, which have to be fulfilled by the patterned nanostructures.

Although the microscopic mechanism of photon detection in SNSPDs is still under debate, a supercurrent-assisted, hot spot-formation is considered the main ingredient [100]. The superconducting stripe, biased close to its critical current, is hit by a photon (see Fig. 9.1a). The energy of the absorbed photon E_{ph} is usually much larger than the superconducting energy gap Δ (for optical photons $E_{ph} > 1$ eV, while typically $\Delta \approx 1 - 2$ meV for LTS materials): as a consequence, some Cooper pairs break into quasiparticles of high energy, leading to a region of depressed superconductivity around the absorption site, i.e. the *hot spot* (see Fig. 9.1b). Since the nanowire is biased close to I_C, the hot spot can expand (see Fig. 9.1c). When the whole cross-sectional area of the nanowire becomes normal, the bias current is deviated onto the external load R_L of the read-out circuit, generating the output voltage pulse V on nanosecond time scales (see Fig. 9.1d). By measuring the voltage pulses, the radiation can be detected and counted.

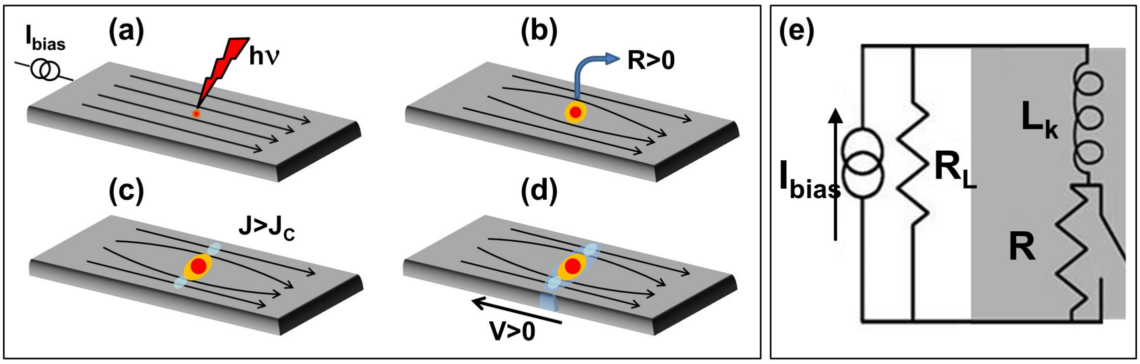

Figure 9.1: (a)-(d) Sketch of the hot spot mechanism. (e) Equivalent circuit of a SNSPD: the wire is represented as a series of a kinetic inductance L_k and a variable resistance R, in parallel with an external load R_L.

On first approximation, the detector can be modeled as an inductor L_k in series with a parallel connection of a current controlled switch and a resistor R. The whole device is in parallel with the external load $R_L \approx 50\ \Omega$. When the wire is superconducting, the whole applied bias current goes into the detector. As soon as the hot-spot generates a normal belt inside the wire, $R \gg R_L$ and the whole current is redirected into the readout line, where a signal $\propto I_b R_L$ will appear (see Fig. 9.1e).

9.2 Nanowire design

The fabrication of YBCO nanowires presents additional technological difficulties if the goal is to reach the single photon limit. First of all, the sensitivity of a SNSPD is strictly related to the capability to trigger a normal conducting cross section, whose propagation is determined by the electro-thermal properties of the wire [226]: thence, a homogeneous current distribution is a crucial requirement. A nanowire for single photon detection is biased close to I_C: only if all the regions within the wire are characterized by the same value of critical current, the hot spot locally generated can expand to a whole cross section. However, three other conditions have to be fulfilled at the same time:

- *The cross section of the wire has to be extremely small.* The hot spot generated by the photon must cause a significant reduction of Cooper pairs compared to the unperturbed state. This has consequences both on the choice of the material, which has to be characterized by a low density of states at the Fermi level (to have a high relative change of Cooper pairs due to the radiation), and of the geometry. A small volume implies that a small photon energy is required to create the normal conducting zone causing the count event (voltage pulse). In this respect, SNSPDs made of low critical temperature superconductors, as those made of NbN, have thicknesses of only few nanometers[1] [224, 227].
- *The wire has to be extremely long.* The normal resistance R_N of the wire needs to be much higher than R_L to guarantee the total redistribution of the whole bias current from the wire to the readout line, after the device becomes normal. In order to use the nanowires for photodetection experiments, there is the need for a large area coverage for many applications. As a consequence, in NbN several microns long nanowires have been employed as detector units [228].
- *Gold capping is not a good choice for single photon detectors applications.* Its high conductivity leads to a high reflection of the light. At the same time, the Au capping layer works as an electrical shunt for the photoresponse and could also represent thermal shunt for the perturbed area inside the detector [229]. In the case of NbN SNSPDs, an enhancement of the critical current density has been observed by using ferromagnetic materials as NiCu (transparent to optical photons) as capping layers [230].

For LTS materials few nanometers thick and several microns long nanowires can be achieved without observing a severe degradation of the superconducting properties. For HTS materials, instead, the realization of nanowires with highly homogeneous superconducting properties fulfilling these requirements, becomes extremely challenging.

---

[1] In principle the cross section could be reduced shrinking either the width or the thickness of the wire. However, squeezing the width down to 5-10 nm, without undergoing a degradation of the wire homogeneity, is a technological issue even for LTS.

9.3 First approach: 50 nm thick, long nanowires

9.3.1 Nanowire geometry

To cover large area devices with narrow wires, we have chosen the *parallel configuration*, first proposed in [227] for realizing a *cascade switch mechanism* in NbN SNSPD. It consists of a serial connection of blocks, each formed by nanowires in parallel (see Fig. 9.2). This configuration has demonstrated to simultaneously allow large signal amplitudes and fast response. The drawback is that the degree of homogeneity of the stripes is even more essential, because the photoresponse is most effective when all the stripes, having the same critical current, are biased around I_C. If few nanostripes have superconducting properties strongly degraded, they can switch to the normal state while all the other stripes inside the block are well below their I_C, so preventing the occurrence of the cascade switch mechanism.

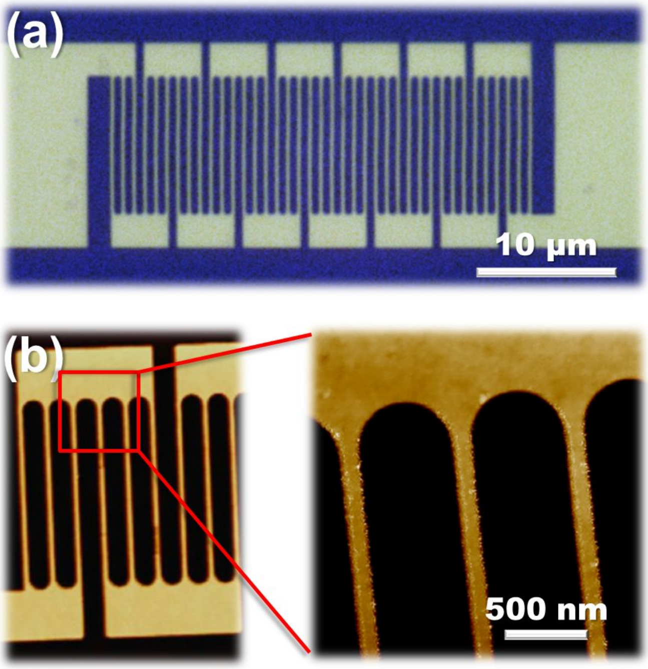

Figure 9.2: (a) Optical picture of a typical device realized for photoresponse experiments, composed by serial connections of 300 nm wide parallel YBCO nanowires. (b) AFM picture of several 130 nm wide YBCO nanowires. The rounded corners between the wires and the wider electrodes are aimed to avoid the reduction of the critical current due to current crowding effect.

To get the same degree of homogeneity in all the stripes of the parallel configuration, we have patterned 50 nm thick nanowires. As we have shown in sec. 7.3, the J_C distribution of an ensemble of many wires becomes broader as the thickness is reduced.

As regards the capping layer, some devices have been fabricated removing completely the Au layer from the top of YBCO by a further Ar^+ etching at the end of the nanopatterning procedure, even though we have demonstrated this is detrimental in achieving “pristine” superconducting properties. In addition, we have investigated a new protective material, the ferromagnetic LSMO, which has been reported to be compatible with YBCO both chemically and structurally [231]. Moreover, it has important functionalities in the context of photodetectors, by reducing the electronic relaxation times when compared to bare YBCO films, as demonstrated in nonequilibrium pump-probe experiments [232]. By patterning YBCO/LSMO films, LSMO acts as a cap layer for YBCO during the last Au etching step, preventing the milling species from vertically impinging on the top surface of the nanowires, causing a degradation of the superconducting properties.

In conclusion, using the same nanopatterning procedure described in detail in Chapter 6, we have fabricated 50 nm thick YBCO and YBCO/LSMO nanowires on LAO substrates, embedded in 7, 9, 11 and 13 blocks of 3 parallel wires (see Fig. 9.2). The nanowires widths are in the range 90-500 nm, while the lengths - which increase proportionally to the widths - are up to 10 μm. The distance between wires is always fixed to 500 nm. We have been able to achieve devices covering areas up to 30 × 10 μm^2, with a filling factor of 50%.

9.3.2 Transport characterization

To probe the quality and the degree of homogeneity of the YBCO and YBCO/LSMO nanowires, we have extracted their critical current densities J_C from current-voltage characteristics, measured down to $T \approx 5$ K both before and after the final etching of the Au capping layer (see Fig. 9.3a).

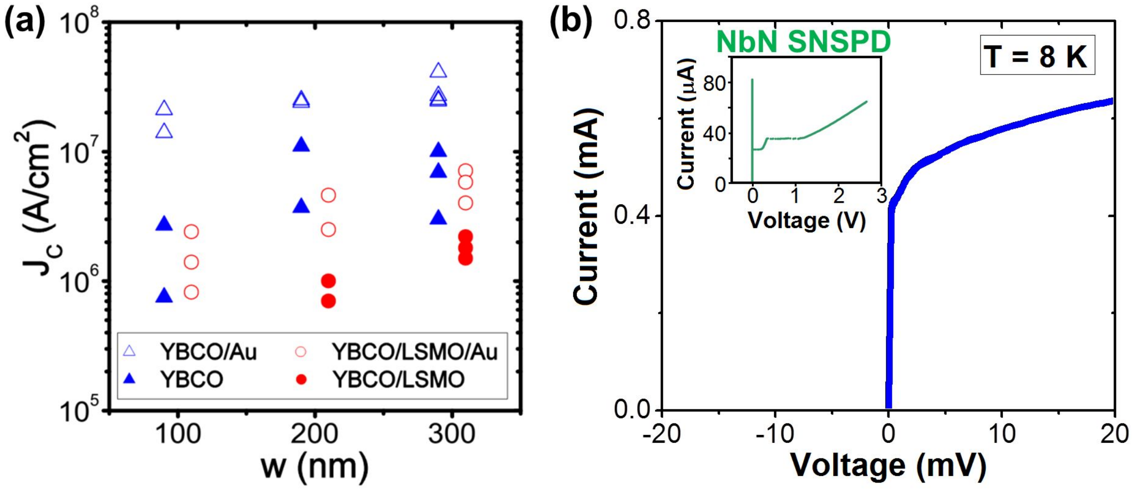

Figure 9.3: (a) The critical current densities of the YBCO/LSMO (*circles*) and YBCO (*triangles*) nanowires, extracted from from the IVC at $T \approx 5$ K of different devices, are shown for three different widths (100, 200 and 300 nm), both before (*open symbols*) and after (*filled symbols*) the Au removal. The data sets belonging to YBCO (YBCO/LSMO) have been shifted to the left (right). (b) Typical flux-flow like IV characteristics of a device made of 130 nm wide YBCO nanowires, after the removal of the Au capping. In the inset, typical IVC of a NbN SNSPD, where a clear switch, of the order of volts, triggering the whole device to the normal state, is present (adapted from [227]).

When the gold is still present, the IVCs, taken in a ^{3}He cryostat using a four point probe configuration, show that YBCO nanowires have J_C of $2 - 5 \cdot 10^7$ A/cm^2 at 4.2 K, independently of the wire width. The small discrepancy with the higher values reported in other YBCO nanostructures (see Chapters 7-8) can be understood considering that these wires are much longer and that they are grown on LAO substrates, where twin boundaries have been reported to affect the superconducting properties of YBCO [108]. The extracted critical current densities of YBCO/LSMO nanowires are one order of magnitude lower than YBCO/Au nanowires. This reduction could instead be associated to the F/S proximity effect (probably reducing the effective thickness of the superconducting layer) or to the Sr contamination of the superconducting layer [233, 234], possibly enhanced by the reduced dimensions of the YBCO nanowires. However, for wires 200 and 300 nm wide, the measured critical current densities are almost width independent and the spread of values among devices with the same geometry is quite limited.

After the Au capping is completely etched, the fundamental role of the LSMO layer becomes clear. In the case of bare YBCO nanowires the critical current densities are severely reduced, almost by a factor of 10, for all widths, as already discussed in sec. (7.1.1), and a spread of J_C values bigger than 75% is present in devices with the same geometry. This spread implies the presence of local damages randomly distributed, affecting the degree of homogeneity of the nanostripes. By considering instead YBCO/LSMO nanowires, we can notice that the wire homogeneity is preserved. We have measured a J_C spread that is always lower than 50% while the J_C values are reduced maximum by a factor of 4 (after removal of the Au layer on LSMO).

In Fig. (9.3b), a typical flux-flow like IVC of a YBCO nanodevice after the Au etching is shown (the behavior is the same for YBCO/LSMO nanowires). The measured resistive branch represents an intermediate state where the device is only “locally” normal: the high value of the thermal conductivity in YBCO ($\kappa \sim 15$ Wm^{-1}K^{-1}) [235] prevents self-heating effects that could bring the whole device to the normal state just above the critical current I_C. This is what happens, for instance, in NbN single nanowires [236] and SNSPDs [227] (see inset in Fig. 9.3b), where the thermal conductivity is almost two orders of magnitude lower [237]. In this case the IVCs are highly hysteretic, with a difference up to the 70% between the critical and the retrapping currents, and a very large voltage switch (of the order of several volts) occurring just above the critical current, which brings all the nanowires into the normal state. The different current-voltage characteristics (related to different intrinsic physical mechanisms), imposes severe limitations for the usage of YBCO nanowires as single photon detectors. Considering the equivalent circuit in Fig. (9.1e), in the case of NbN nanowires, the device switches instantly from $R = 0$ to $R = R_N \gg R_L$, so favoring the redistribution of all the bias current to the readout line, where the signal appears. In the case of YBCO nanowires, the hot spot is not able to drive a whole nanowire “belt” into the normal state, but only triggers the device to the resistive state ($0 < R \ll R_N$), where most probably fluxon dynamics plays a fundamental role [90]. In this case the cascade flow of I_b to the external load cannot happen.

9.3.3 Photoresponse measurements

Photoresponse experiments have been carried out mounting the devices in a liquid helium flow cryostat with optical access. Electrical connections are given by wire bonds to high bandwidth and low bandwidth cables going to room temperature. The low bandwidth connections are used to dc bias the devices, while the output signals are carried by the high bandwidth connection to two cascaded 1 GHz bandwidth amplifiers[2] with an overall voltage gain of 400 (for more details, see Appendix B).

We have recorded IVCs of devices with and without a dc 1550 nm laser illumination as shown in Fig. (9.4). The IVCs with and without radiation differ, mostly around the critical current, where under illumination the I_C decreases down to 85 – 95 % of its unperturbed value.

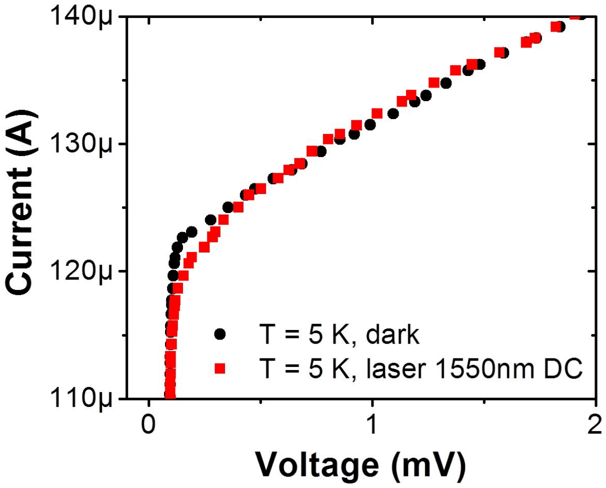

Figure 9.4: IVC of a device made of 100 nm wide YBCO nanowires, measured at 5 K with (*squares*) and without (*circles*) a dc 1550 nm laser illumination. The difference is remarkable around the critical current.

A voltage response is measured when the devices are illuminated with optical laser pulses with 1550 nm wavelength, with a rise and fall time of 3 ns, a duration of 10-500 ns, an intensity of about 50 nW/μm^2 and at a repetition rate of 1 MHz (see Fig. 9.5a). As a first step, we have studied at $T = 5$ K the evolution of the voltage response as a function of the applied bias current. When the devices are biased far below the critical current, no photo signals can be measured. By biasing the nanowires slightly below and above I_C, a clear voltage response is observed, in correspondence with the laser pulses. In particular, we can distinguish between two different regions in which the photoresponse can be measured. The first one is accessible when biasing the devices from $\approx 0.85 \cdot I_C$, (the I_C value when the photoresponse signal appears) up to the critical current I_C (see Fig. 9.5b and inset). Here the signal pulse amplitude increases exponentially with the bias current for all the devices, reaching its maximum in correspondence of the critical current ($\approx 0.99 \cdot I_C$). The second region instead

---

[2] Using these amplifiers, the detection of non-equilibrium signals on picosecond scale is not allowed.

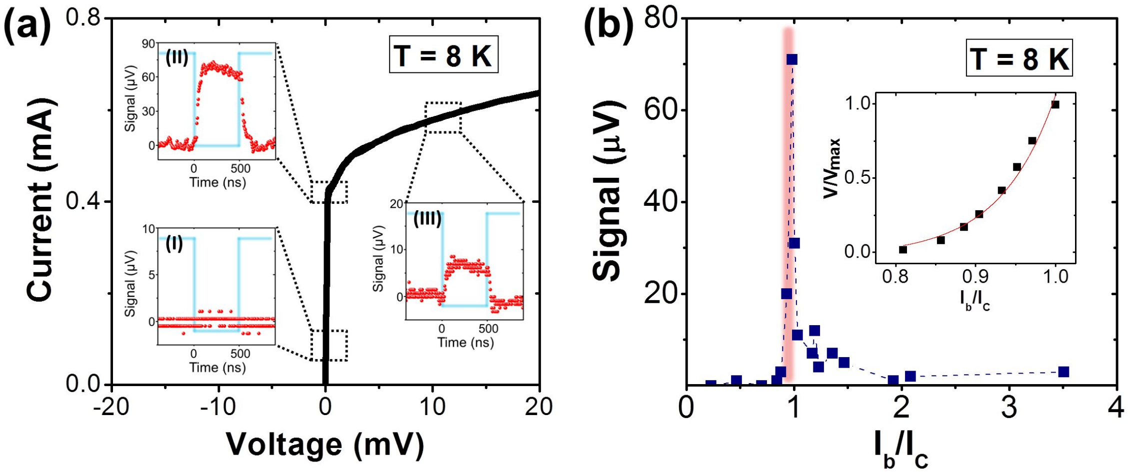

Figure 9.5: (a) IVC measured at $T = 8$ K for a device made of 130 nm wide YBCO nanowires. The three insets show the photoresponse signal (*circles*) measured at three different bias currents, corresponding to different regimes in the IVC: (I) far below the critical current ($I_b/I_C = 0.23$), where no photoresponse is observed; (II) around the critical current ($I_b/I_C = 0.99$), where the maximum voltage signal is measured; (III) on the resistive branch ($I_b/I_C = 1.36$), where the photoresponse has a finite value, though reduced with respect to (II). The signals in the three insets correspond to the inverse light pulses of the ac 1550 nm laser used to illuminate the devices. (b) Photoresponse signal as a function of the applied bias current (normalized to the critical current value), for the device whose IVC is shown in panel (a). In the region below I_C, which has been highlighted, the dependence of the voltage signal on the bias current is exponential (inset).

corresponds to bias currents higher than I_C. In this case, the signal pulse amplitude slowly decreases by increasing the bias (see Fig. 9.5b): at high bias ($> 2 - 3 \cdot I_C$), it vanishes completely or it reaches a very small saturation value ($\approx$ 2-5 μV). The amplitude of the voltage signal around I_C is $\approx$ tens-hundreds of μV: it increases as the nanowire width increases, because more current redistributes into the external load, and - for a fixed geometry - it is higher (20%-50%) if the devices are capped with LSMO.

The photoresponse has been also studied as a function of the temperature (see Fig. 9.6a). Voltage pulses, in correspondence with the laser pulses, are present from 5 K up to T_C, which, depending on the wire width, is in the range 80-85 K. The maximum photoresponse, visible at I_C, decreases as a function of the temperature, with a stronger dependence at lower temperatures (see Fig. 9.6b). Moreover, studying the signal dependence on the bias current at different temperatures, we may notice that the enhancement of the signal around I_C is very strong at lower temperatures, while at T slightly below T_C the photo-signal is almost independent of the bias current.

This behavior suggests that the main contribution, to the photoresponse signals we observe, has a bolometric nature, i.e. it is caused by a raise of temperature δT, induced by the interaction with photons. The IVC changes due to a temperature variation; as a consequence, the voltage changes as $V(I, T + \delta T) - V(I, T)$, possibly giving rise to the signal we measure. To our knowledge, a complete model, describing the effect of the

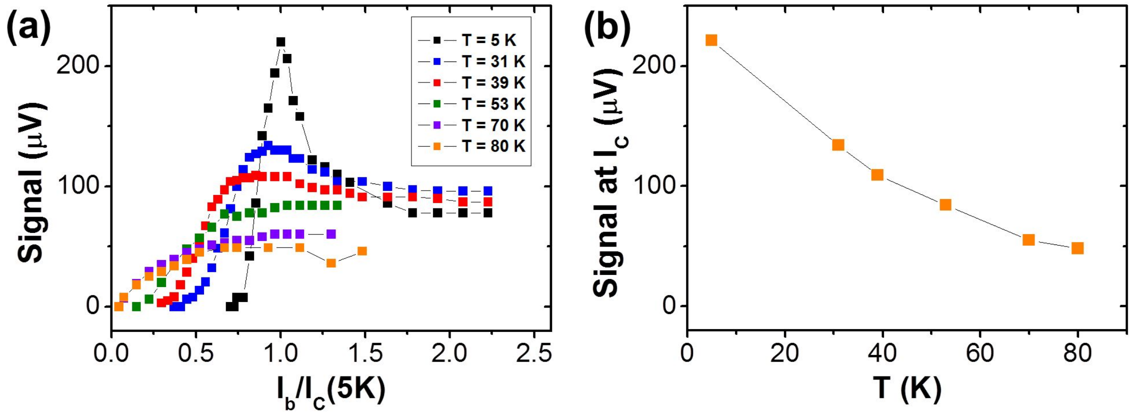

Figure 9.6: (a) Photoresponse signal as a function of the applied bias current measured at different temperature up to the T_C of the device, which is made by 500 nm wide YBCO nanowires. The maximum signal, measured at I_C, is plotted as a function of the temperature in panel (b). In both the panels, the lines are used only to guide the eye.

heating on superconducting nanowires, is still missing. To get a qualitative description of the phenomenon, we can consider the IVCs of a resistively shunted junction (RSJ, see Fig. 9.7a): although this modelization cannot be rigorously used in our case, the overall behavior of the IVCs of the nanowires is similar to that of the RSJ model (see

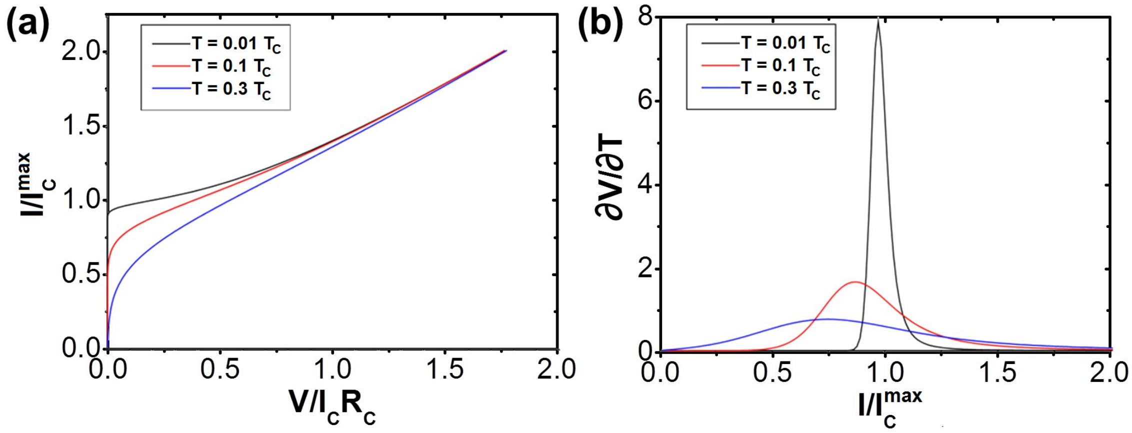

Figure 9.7: (a) RSJ IVCs at three different temperatures. The derivatives $\partial V/\partial T$ as a function of the current, normalized to the I_C of the lowest temperature, are shown in (b). It is worth noticing the similarity with Fig. (9.6a).

Fig. 9.4). The equation describing the dynamics of a Josephson junction in presence of thermal noise, according to the RSJ model [238, 239] , is the following:

$$\frac{1}{R}\frac{\hbar}{2e}\frac{d\phi}{dt} + I_C \sin\phi = I + \xi(t) \ , \qquad (9.1)$$

with ϕ phase difference across the junction and $\xi(t)$ the noise. For simplicity, we can assume that the noise is white and write its correlator as

$$\langle \xi(t)\xi(t')\rangle = \frac{2k_B T^\star}{R_{qp}(T_1)}\delta(t-t') \ , \tag{9.2}$$

where $T^\star$ is the noise temperature and R_{qp} is the quasiparticle resistance. The exact solution of eq. (9.1) can be found in Ref. [240]: the RSJ IVC in presence of thermal noise, which is plotted in Fig. 9.7, writes as:

$$V(I) = \frac{4\pi e k_B T^\star R_{qp}(T_1)}{\hbar\int_{-\pi}^{\pi} d\phi_1 \int_{-\infty}^{\phi_1} d\phi_2 \exp[-\frac{\hbar I}{2ek_BT^\star}(\phi_1-\phi_2)-\frac{\hbar I_C}{2ek_BT^\star}(\cos\phi_1-\cos\phi_2)]} \ . \tag{9.3}$$

The derivative $\partial V/\partial T$ of the theoretical RSJ IVCs, as a function of the bias current at different temperatures is shown in Fig. 9.7b. It is very similar to the photoresponse in Fig. 9.6a, which we have experimentally measured. The main difference is above I_C: the I-V curve of the RSJ model is linear, corresponding to a resistance $R = R_N$, leading to a $\partial V/\partial T$ which is negligible already at $I_b = 1.5 \cdot I_C$. For our nanowires instead, as already previously discussed, above I_C the system is in a resistive state, where the resistance changes continuously as a function of the bias current, with values $0 < R \ll R_N$. This facts determines the main difference of the photoresponse of our nanowire with respect to the RSJ model in presence of thermal noise.

The hypothesis of a bolometric nature of the photoresponse is also confirmed by the variation of the shape of the IVC when we illuminate the nanowires with the laser (see Fig. 9.4), mostly changing around I_C at low temperatures. A further support to this hypothesis comes from the dependence of the photoresponse signals on the laser power. As it can be seen in Fig. 9.8, the amplitude of the photoresponse signal, measured at $I_b = I_C$, decreases linearly by reducing the power of the laser [241]. In particular, if the laser power is reduced by a factor 10, the photoresponse disappears. In correspondence with such value of power, the IVC of the devices does not change, when illuminated

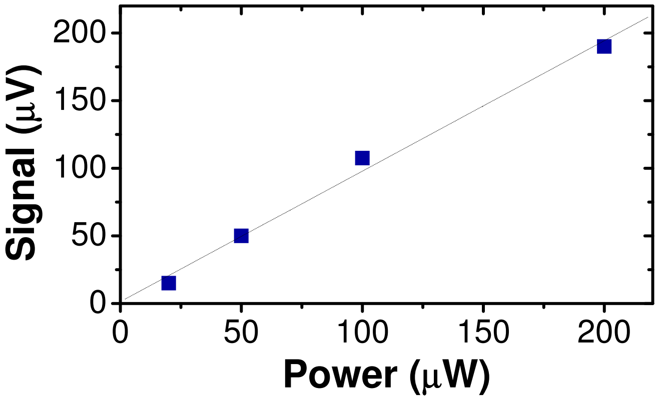

Figure 9.8: Photoresponse signals, measured at $T = 5$ K using a bias current $I_b = I_C$, as a function of the laser power on a device made of 500 nm wide YBCO nanowires (*squares*). The line represents the linear fit to the data, used to determine the responsivity of the nanowire devices.

by the dc laser (differently than in Fig. 9.4). From this power dependence, we can calculate the responsivity, defined as the ratio between the detector output signal and the absorbed radiation power. From the values reported in Fig. 9.8, we can estimate a responsivity of 1 V/W at 5 K. This represents only an approximate value, since we haven't consider the actual radiation power absorbed by the YBCO nanowires. For a better estimate, we should also consider the system coupling efficiency and the actual dimensions of the devices with respect to the laser beam.

Although the heating appears as the dominant mechanism giving rise to the photoresponse, we cannot exclude a possible interaction between the light and the vortices crossing the wires (which have been recently accounted as a possible cause of photon counts in SNSPDs [242, 243]).

9.4 Second approach: ultrathin, short nanowires

9.4.1 Nanowire fabrication

We have patterned different bare ultrathin YBCO films, with thicknesses down to $t = 10$ nm. With respect to the nanofabrication procedure described in Chapter 6, a carbon hard mask - deposited by PLD at room temperature - was the only protecting capping layer for the YBCO film during the patterning. The carbon layer protects YBCO from chemicals and from the direct impact of the Ar^+ ions during the etching. Because of its low thermal conductivity, much lower than for YBCO, it cannot prevent the heating of YBCO during the baking of the resists, and during the ion milling, which causes loss of oxygen atoms from the superconducting layer.

We have patterned short ($l = 100$ nm), 75 nm wide nanowires (see Fig. 9.9a), and long ($l = 1$ μm), 110 nm wide nanowires (see Fig. 9.9b), with the geometry described in sec. 7.3.

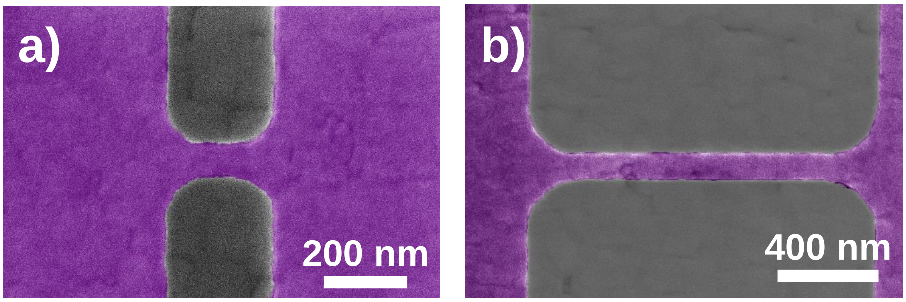

Figure 9.9: a) SEM image of a short ($l = 100$ nm), 75 nm wide nanowire patterned on a 10 nm thick bare YBCO film. b) SEM image of a long ($l = 1$ μm), 110 nm wide nanowire patterned on a 10 nm thick bare YBCO film.

9.4.2 Transport characterization

The nanowires have been characterized by measuring the IV characteristics in the whole temperature range from 4.2 K up to their T_C^0 and the resistance vs temperature.

Nanowires with thicknesses higher than 10 nm are characterized by non-hysteretic IVCs, like those measured on 50 nm thick bare YBCO nanowires, shown in the previous section.

Because of the absence of the Au capping layer, not all the wires - in particular the long ones - are superconducting; the J_C values extracted from the IVCs are lower than those of capped nanowires, shown in sec. 7.3, and their spread of values is higher.

The 10 nm thick nanowires are even more affected by the lack of Au capping: the maximum J_C value we have measured on the 100 nm long wires is $J_C^{max} \approx 2 \cdot 10^7$ A/cm^2, while on the 1 μm long wires it is $J_C^{max} \approx 7 \cdot 10^6$ A/cm^2. In both cases the spread of the J_C values extracted by a wide distribution of identical wires is about one order of magnitude.

The IV curves of 10 nm thick nanowires having J_C lower than $\approx 5 \cdot 10^6$ A/cm^2, are flux flow like. The shape of the IV curve abruptly changes for nanowires with J_C higher than this threshold. A large voltage switch, of the order of several mV, appears above I_C. It drives the device to a state characterized by a constant differential resistance, $dV/dI \approx 10^2\,\Omega$, when applying a bias current $I_b > I_C$ (see Fig. 9.10a). The small difference between the switching (I_C) and the retrapping (I_r) current is in the order of several μA. The fact that we observe the voltage switch only in nanowires with the highest J_C is an indication that the switching is not caused by the presence of local grain boundaries or defects.

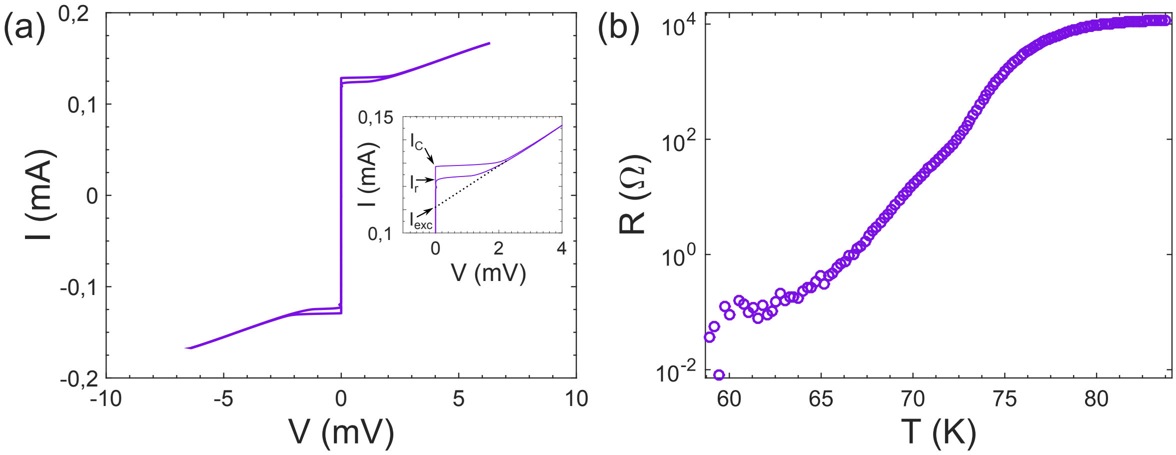

Figure 9.10: a) IVC measured at 4.2 K of a 100 nm long bare nanowire, having a $J_C = 8.6 \cdot 10^6$ A/cm^2. Above I_C, a 2 mV wide voltage switch drives the system to the normal state, corresponding to a differential resistance $dV/dI = 112\ \Omega$ (see inset). b) $R(T)$ measurement of the same nanowire whose IVC is presented in panel a. The R_N of the nanowire, value of the resistance corresponding to the T^{onset} of the nanowire is $\approx 100\ \Omega$, a value very close to the dV/dI measured in the IVC at 4.2 K on the same device.

The T^{onset} of the nanowires, we have measured from the $R(T)$ curves, is very close to that of Au capped nanodevices. The broadening of the superconducting transition depends on how significantly the superconducting properties of the nanowires are degraded: devices with very low J_C present extremely wide superconducting transitions, of the order of tens of Kelvin; devices having the highest J_C values, and the voltage switch in the IVC above I_C, are instead characterized by a superconducting transition (see Fig. 9.10b), comparable with that of Au capped nanowires (see for comparison Fig. 7.12b). In particular, since our IVCs present an excess current I_{exc} deriving from Andreev reflections, we can compare the normal resistance R_N (value of the resistance corresponding to the onset of the superconducting transition) of the nanowires with the highest J_C values, with the differential resistance dV/dI measured in the IVC at 4.2 K. The two values are very similar in all the investigated samples. This occurrence supports the hypothesis that the voltage switch above I_C can be the sign of a hot spot, induced inside the ultrathin wire, which drives the system directly from the superconducting to the normal state.

The presence of a voltage switch and of an hysteresis has been often observed in superconducting nanostructures. In bulk samples it is usually caused by the motion of the vortex lattice [244]. In S-N-S Josephson junctions the Joule heating in the normal part leads to a bi-stability of the IVC [245]. Short superconducting nanowires, like the ones we have patterned, are somewhere between these two limiting cases.

The origin of the thermal hysteresis can be understood as follows. When a bias current $I_b < I_C$ is applied, the wire is superconducting and the temperature of the quasiparticles inside the wire is equal to the temperature of the substrate, T_0. As soon as the critical current I_C is reached, and in case its value is not limited by defects or local damages, the voltage drop across the nanowire generates a hot spot caused by Joule heating. At sufficiently high bias, the hot spot drives the whole wire to the normal state. When I_b is reduced from high values, the normal part of the wire gradually shrinks. Switching back to the superconducting state occurs at the retrapping current, I_r, which is lower than the critical one, $I_r < I_C(T_0)$, since the Joule heating increases the temperature of the wire. I_r is therefore equal to $I_C(T_{NS})$, where $T_{NS} > T_0$ is the minimal temperature, at the boundary between the normal and the superconducting part of the wire, at which the normal hot spot in the middle of the wire still exists. This mechanism is well known for LTS [246].

To make the analysis more quantitative, we have used a model which has been recently proposed for electron-doped $Pr_{2-x}Ce_xCuO_{4-\delta}$ (PCCO) nanowires [247]. We consider a short wire, of length l, width w and thickness t, whose top view is sketched in Fig. 9.11. The leads, to which the nanowire is coupled, are modeled as semi-circles of radius R_{max} and thickness t. The temperature at the outer edges of the leads is

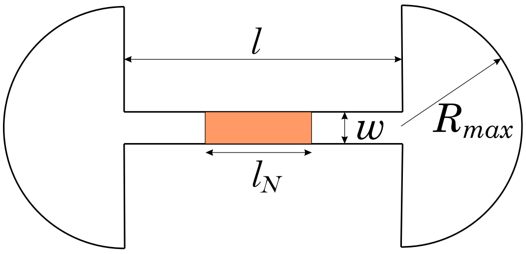

Figure 9.11: Schematic view of the nanowire used for the model. The temperature changes continuously from the normal part, having a length l_N, to the outer limits of the semi-circle, in the lead, where it equals the bath temperature.

supposed to be equal to the bath temperature T_0. The value of R_{max} is determined by the cooling mechanism (via phonons or via substrate).

The central part of the wire, with length l_N, becomes normal due to Joule heating. In the normal state, the resistivity of YBCO can be approximated as linearly dependent on the temperature, $\rho = \beta T$, while the thermal conductivity κ_N is temperature independent. As a consequence, assuming that the cooling through the substrate is weak, a power IV is produced in this section of the nanowire as a consequence of the heating. The heat balance equation in this normal segment of wire writes as

$$\frac{\beta I(I - I_{exc})}{wt} T + wt\kappa_N \frac{d^2T}{dx^2} = 0 \ , \tag{9.4}$$

where I_{exc} is the excess current due to Andreev reflections at the two normal-superconducting (N-S) interfaces. In the measured IVC, this value corresponds to the extrapolation to zero voltage of the normal branch at high bias. In the previous equation, the first term represents the Joule heating, while the second one the electron diffusion.

The power generated in the normal section of the wire is carried away into the leads (half power goes into the left lead, while the other half goes into the right lead) by the quasiparticles. In each superconducting side of the nanowire, a heat current given by $IV/2$ flows, causing a continuous change of the temperature from the N-S interface to the outer limits of the semi-circle, in the lead. Since the heat current can be written as $-wt\kappa(T)dT/dx$, where $\kappa(T)$ is the temperature dependent thermal conductivity of YBCO in the superconducting state, we can write the following equation:

$$\frac{IV}{2} = -wt\kappa(T)\frac{dT}{dx} \ . \tag{9.5}$$

Eq. 9.5 represent the boundary condition at the N-S interface, which together with the heat conservation equation in the S region of the wire,

$$\nabla(\kappa(T)\nabla T) = 0 \ , \tag{9.6}$$

brings to the determination of the temperature profile in the superconducting part of the wire.

Solving Eqs. 9.5 and 9.6, with the approximation of weak hysteresis (which is our case, as it can be seen in Fig. 9.10a), we arrive at the equation which relates the length of the hot spot l_N and the temperature T_{NS} at the N-S interface:

$$\frac{l_N}{l}\left(1 - \frac{l_N}{l} + \frac{2w\ln(2R_{max}/w)}{\pi l}\right) = \frac{4w^2t^2}{I(I - I_{exc})\beta T_{NS} l^2}\int_{T_0}^{T_{NS}} dT'\kappa(T') \ . \tag{9.7}$$

It should be again be supplemented by the equation $I = I_C(T_{NS})$, where $I_C(T)$ is the temperature dependent critical current of the wire. This condition implies that the superconductor becomes normal as soon as the bias current equals the critical one at a given local temperature. The N-S boundary is therefore created. From Eq. 9.7 l_N and T_{NS} can be determined as a function of the bias current. In doing so, one finds that the retrapping current, at which the hot spot abruptly vanishes, occurs at

$$l_N = l_N^{min} = \frac{l}{2}\left(1 + \frac{2w\ln(2R_{max}/w)}{\pi l}\right) . \tag{9.8}$$

This is the shortest possible value for the length of the hot spot. Thus, the two equations for the retrapping current take the form

$$I_r(I_r - I_{exc}) = \frac{16w^2t^2}{\left(1 + \frac{2w\ln(2R_{max}/w)}{\pi l}\right)^2 \beta T_{NS} l^2} \int_{T_0}^{T_{NS}} dT'\kappa(T'), \quad I_r = I_C(T_{NS}), \tag{9.9}$$

and the retrapping voltage reads as

$$V_r = (I_r - I_{exc})R_N . \tag{9.10}$$

To fit our data to the model, we have measured the I_C and I_r as a function of the temperature from 0.3 K up to the T_C of the nanowires (see Fig. 9.12a). In the following, we will focus on the nanowire whose IVC and $R(T)$ has been shown in Fig. 9.10, having a $T_C \approx 72$ K.

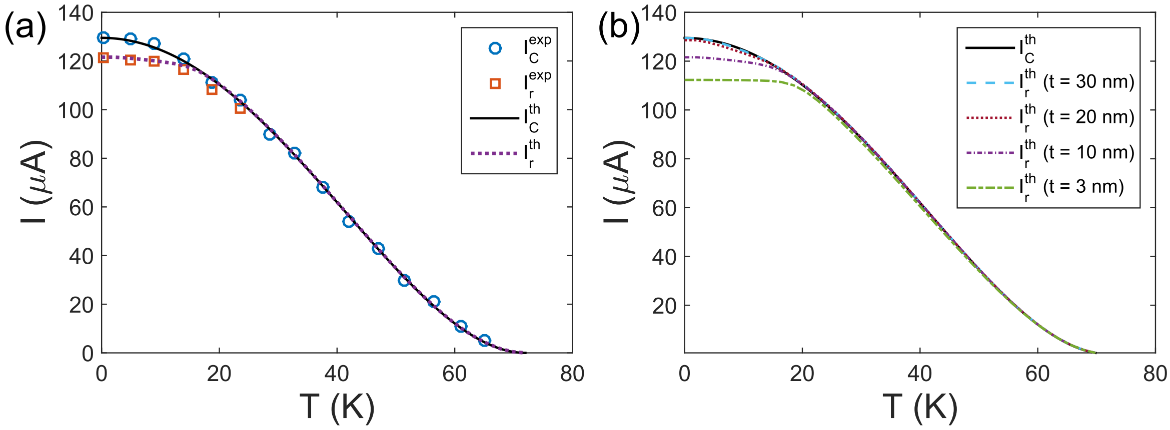

Figure 9.12: a) Experimental critical current I_C^{exp} (*circles*) and retrapping current I_r^{exp} (*squares*) as a function of the temperature, for the nanowire shown in Fig. 9.10. I_C^{exp} can be phenomenologically approximated by the calculated critical current $I_C^{th} \approx I_C(0)(1 - T^2/T_C^2)^2$ (*solid line*). The calculated retrapping current $I_r^{th}(T)$ has been obtained from the numerical solution of Eq. 9.9 (*dotted line*). The parameters of the wire are taken as follows: $l = 100$ nm, $w = 75$ nm, $t = 10$ nm, $R_{max} = 500$ nm, $\beta = 10^{-8}$ Ωm/K, $T_C = 72$ K. For $\kappa(T)$, we have not considered phonon contribution at low temperatures. b) Thickness dependence of the retrapping current $I_r^{th}(T)$, extracted from Eq. 9.9. All the sample parameters, except the thickness t, are the same as in panel (a). The calculated $I_C^{th}(T)$ is shown as reference.

The critical current I_C (*circles* in Fig. 9.12a) can be nicely fitted as a function of the temperature by the expression $I_C^{th} \approx I_C(0)(1 - T^2/T_C^2)^2$ (*solid line* in Fig. 9.12a). The difference between the retrapping and the critical current decreases when increasing the temperature, and it disappears ($T_{NS} - T < 1$ K) at $T \approx 20$ K. To fit the $I_r(T)$ behavior with our model, we have to solve Eq. 9.9, using the dependence of κ on the temperature, valid at $T < T_C$, which has been experimentally found in slightly overdoped YBCO single crystals [235]. In addition, we have taken into account that the phonon system do not contribute to $\kappa(T)$ at low temperatures: indeed in slightly overdoped cuprates an electron-phonon decoupling has been reported at low temperature [248, 249]. With this assumption, the obtained values of $I_r(T)$ (*dotted line* in Fig. 9.12a) show an excellent agreement with the values extracted from the experimental IVC.

It is worth mentioning that in our model the appearance of the hysteresis from Eq. 9.9 is strongly thickness dependent. As we can see in Fig. 9.12b, the difference between I_C and I_r decreases increasing the thickness. In particular, it is almost negligible if $t > 10$ nm.

Another parameter, we can extract from the model and compare with the measurements, is the retrapping voltage. From the IVC of the nanowire (see Fig. 9.10a) we have $(I_r - I_{exc}) \approx 15$ μA and $R_N \approx 100$ Ω. From Eq. 9.10 we extract $V_r = 1.5$ mV, a value in excellent agreement with the measured one (see Fig. 9.10a).

From Eq. 9.4 we can also have a rough estimate of the minimum critical current density J_C^{min} a nanowire can carry, to show a voltage switch and a hysteresis in the IVC. By approximately writing d^2T/dx^2 as $-(T_{NS}-T)/l^2$, neglecting I_{exc} and assuming that $I_b \sim I_C$, Eq. 9.4 can be rewritten as

$$wt\kappa_N \frac{T_{NS}-T}{l^2} \approx \frac{\beta I_C^2 T}{wt} = 0 \; . \tag{9.11}$$

From this equation we estimate the J_C for a given value of the temperature rise $T_{NS}-T$:

$$J_C \approx \sqrt{\frac{\kappa_N(T_{NS}-T)}{\beta T l^2}} \; . \tag{9.12}$$

J_C^{min} can be evaluated from Eq. 9.12, when the temperature rise is the minimum to see the hysteresis, $T_{NS} - T \approx 1$ K. Taking $l = 200$ nm, we find $J_C^{min} \approx 5 \cdot 10^6$ A/cm^2, a value very close to that experimentally determined.

In summary the presence of the voltage switch in the IVC of the short, 10 nm thick YBCO nanowires can be explained in terms of a thermal hysteresis, where a hot spot is created in the wire. In our model, we have calculated how the heat is dissipated, which gives the values of the retrapping current, of the retrapping voltage and of the critical current density J_C^{min}, that have an excellent agreement with the measured ones. The presence of the voltage switch makes ultrathin YBCO nanowires similar to NbN nanowires, commonly used for SNSPDs.

It looks therefore clear that decreasing the thickness of the YBCO nanowires is an essential prerequisite for the development of HTS single photon detectors. For this purpose, the usage of LSMO will be crucial, since we proved it has a beneficial role in preserving the homogeneity of the nanowires. It has been reported that the LSMO layer induces at the interface with YBCO a non-superconducting dead layer [250], reducing even further the effective thickness.

10

Transport anisotropy in untwinned YBCO nanowires

In untwinned YBCO single crystals and thin films, the anisotropy of the superconducting properties in the a and b direction is expected as a consequence of the orthorhombicity of the crystal structure and of the presence of the b-axis oriented CuO chains (see sec. 2.2.3) [69, 71, 73]. In particular a critical current density anisotropy has been measured in YBCO thin films, due to the in-plane anisotropy of the London penetration depth, with J_C values in the b direction up to 1.8 times larger than in the a direction [72].

An additional contribution to the J_C anisotropy in the a-b plane could be caused by the pair density wave (PDW) order, a novel phase, that intertwines with the charge density waves (CDW) and with the superconducting (SC) state. Such emerging order, characterized by Coopers pairs having a finite momentum $\vec{Q}$ and therefore generating states with spatially modulating Cooper pair density [251, 252], has been theoretically predicted in cuprates more than 20 years ago [8], but the first supporting experimental signature has been observed only few months ago [253].

To study the in-plane anisotropy of the critical current density, and its evolution when YBCO is scaled down at dimensions comparable with its fundamental lengths (λ_L, ξ, CDW correlation length), we have patterned untwinned YBCO nanowires at different in-plane angles γ with respect to the substrate (see Fig. 10.1a). The J_C

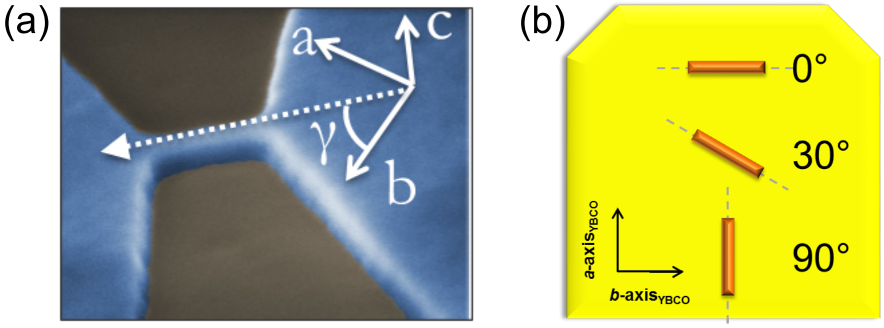

Figure 10.1: (a) SEM image of a nanowire, oriented at an angle γ with respect to the in-plane YBCO axis. (b) Sketch of the nanowires, patterned at different in-plane angles with respect to the substrate. The angle $\gamma = 0°$ is associated to nanowires patterned along the YBCO b-axis parameter (where CuO chains reside), while at $\gamma = 90°$ the nanowires are towards the a-axis direction.

dependence of the nanowires on the angle γ has been studied for different wire widths w and oxygen doping.

The experiment has been performed using MgO (110) substrates annealed 12 h and STO (001) substrates with vicinal angle $\alpha_V = 1.5°$ toward the [010] direction. On these two substrates we have achieved the growth of untwinned YBCO films, where the crystal structure and the superconducting properties, related to the presence of CuO chains along the b direction, are preserved (see Chapter 3). We have used the convention that wires oriented along the CuO chains (b-axis) are at $\gamma = 0°$, while nanowires perpendicular to them (a-axis) are at $\gamma = 90°$ (see Fig. 10.1b).

We have focused on ten different angles, equispaced between $\gamma = 0°$ and $\gamma = 90°$. All the nanowires have the same geometry, thickness $t = 50$ nm and widths spanning in the range from 300/400 nm down to 65/70 nm. The smallest dimensions are close to the CDW correlation length [2].

On each substrate, we have patterned a very large number of YBCO nanowires, the IVCs of which have been measured at 4.2 K. For a given angle and for a given width, we have determined a distribution of the J_C values. For each distribution, with broadening σ_{Jc}, we have extracted an average critical current $\bar{J}_C$.

Figs. 10.2a and 10.2b show the average critical current $\bar{J}_C$ of slightly overdoped YBCO wires patterned respectively on a STO (001) and on a MgO (110) substrate as a function of the angle γ [1]. In both the cases, the $\bar{J}_C(\gamma)$ dependence can be explained considering that, as a consequence of the in-plane anisotropy of the London penetration depth taking place in untwinned YBCO single crystals and thin films, the

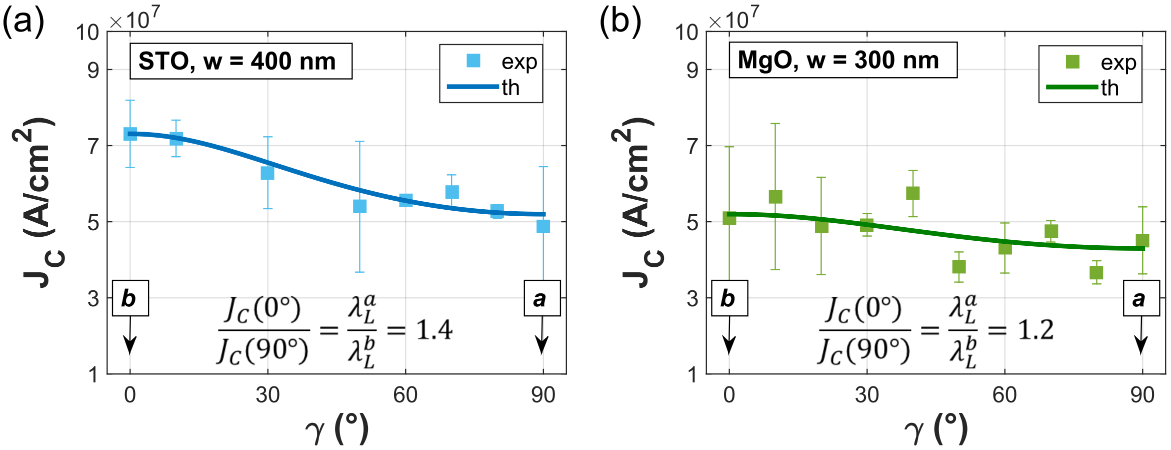

Figure 10.2: (a) Average critical current density $\bar{J}_C$ vs the angle γ (*squares*) for the 400 nm wide, slightly overdoped, YBCO nanowires patterned on a STO (001) substrate with vicinal angle $\alpha_V = 1.5°$ toward the [010] direction. The measured $\bar{J}_C(\gamma)$ dependence can be nicely explained considering the J_C^λ expression (Eq. 10.1) and assuming the London anisotropy $\lambda_L^a/\lambda_L^b = 1.4$ extracted from the periodicity ΔB of the Dayem bridge nanoSQUIDs, patterned on the same sample at $\gamma = 0°$ and $\gamma = 90°$ (*solid line*). (b) $\bar{J}_C$ vs γ for the 300 nm wide, slightly overdoped, YBCO nanowires patterned on a MgO (110) substrate annealed 12 h (*squares*). The measured dependence is in fairly good agreement with J_C^λ, assuming $\lambda_L^a/\lambda_L^b = 1.2$ from the ΔB of the Dayem bridge nanoSQUIDs, patterned at $\gamma = 0°$ and $\gamma = 90°$ (*solid line*).

---

[1] For each angle, the error bar - related to the broadening of the distribution of the J_C values - is equal to $2\sigma_{Jc}$.

J_C, proportional to $\xi^{-1} \cdot \lambda_L^{-2}$ (see Eq. 2.21), is expected to change with the angle γ according to the relation [254]

$$J_C^{\lambda}(\gamma) = \left(\sqrt{k_1 \cos^2(\gamma) + k_2 \sin^2(\gamma)}\right)^{-1} , \tag{10.1}$$

where the ratio of the two parameters k_1 and k_2 corresponds to the in-plane anisotropy of the London penetration depth, $k_2/k_1 = \lambda_L^a/\lambda_L^b$.

The in-plane London anisotropy has been determined for each sample from the measurement of the external magnetic field periodicity ΔB of Dayem bridge YBCO nanoSQUIDs (see Chapter 8). We have patterned nanoSQUIDs, on the same sample as the nanowires at different angles. The two nanobridges forming the nanoSQUID are oriented either along the a-axis or along the b-axis. The corresponding measured periodicities ΔB^a and ΔB^b are different. By solving the Maxwell and London equations describing the Meissner state for both the SQUID geometries [208], we have numerically calculated the periodicities ΔB^a_{num} and ΔB^b_{num}. In particular we have that $\Delta B^b_{num}/\Delta B^a_{num} = \lambda_L^a/\lambda_L^b$, in the range $1 < \lambda_L^a/\lambda_L^b < 2$. Typical λ_L values in YBCO nanodevices are larger than the bulk values, but we have assumed that the ratio λ_L^a/λ_L^b is size independent. With this assumption, we have estimated the in-plane London anisotropy from the measurements of the external magnetic field periodicity as $\Delta B^b/\Delta B^a = \lambda_L^a/\lambda_L^b$.

The knowledge of the in-plane London anisotropy is important to determine - through Eq. 10.1 - the expected dependence J_C^{λ} of the critical current density on the angle γ (*solid line* in Figs. 10.2a and 10.2b). The measured $\bar{J}_C$ vs γ dependence is in fairly good agreement with the theoretical J_C^{λ} for both the samples, even though they are characterized by different London anisotropy. Therefore we conclude that in wide slightly overdoped YBCO wires the dependence of the critical current density on the angle γ is mostly related to the anisotropy of the London penetration depth.

In the following we will focus on the sample on MgO (110) substrate. Here, the dependence of $\bar{J}_C$ on γ dramatically changes when the width of the wires is reduced down to 70 nm (see Fig. 10.3). The average critical current density presents an enhancement at values of γ around $\approx 10°$ and a depression at values of γ around $\approx 60°$, going well beyond the expected anisotropy due to λ_L (see *solid line* in Fig. 10.3a).

After subtraction of the contribution J_C^{λ}, due to the λ_L anisotropy, from the measured $\bar{J}_C$, the resulting critical current density shows a modulation as a function of γ, which phenomenologically can be described by a cosine function, with the maximum shifted by $\delta\gamma \approx 15°$ with respect to the direction of the CuO chains (see Fig. 10.3b).

This peculiar behavior is intimately connected to the twinning state of the YBCO film, i.e. to the presence of aligned CuO chains throughout the sample. Indeed we have patterned nanowires with identical geometries on a YBCO film grown on a MgO (110) substrate without preannealing (twinned film, as shown in Chapter 3). The anisotropy of the London penetration depth is missing: nanoSQUIDs present periodicities $\Delta B^b/\Delta B^a = \lambda_L^a/\lambda_L^b = 1$, while the critical current density of wide nanowires is independent of the angle γ. In addition to the disappearance of the in-plane anisotropy

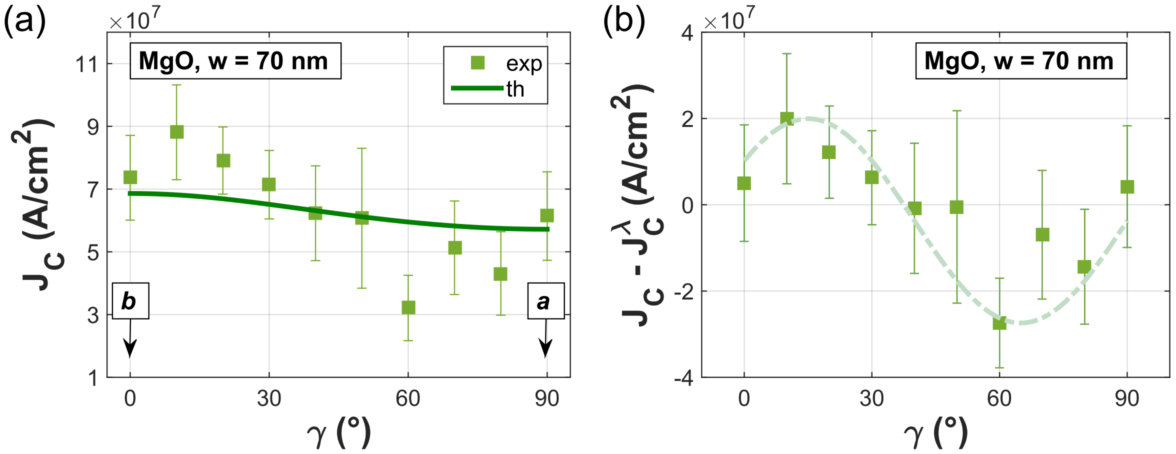

Figure 10.3: (a) Average critical current density $\bar{J}_C$ vs the angle γ for the 70 nm wide, slightly overdoped, YBCO nanowires patterned on a MgO (110) substrate annealed 12 h (*squares*). The measured dependence cannot be explained considering only J_C^λ (Eq. 10.1), related to the anisotropy of the London penetration depth (*solid line*, assuming $\lambda_L^a/\lambda_L^b = 1.2$ as in Fig. 10.2b). $\bar{J}_C$ is enhanced at $\gamma \approx 10°$ and depressed at $\gamma \approx 60°$, resulting in a difference between the minimum and the maximum at almost a factor 3. (b) The measured $\bar{J}_C$ values are plotted as a function of the angle γ after the subtraction of the component J_C^λ to the total anisotropy. The resulting values exhibit a clear modulation as a function of γ, which can be described by a cosine function (*dashed line*).

of λ_L, the cosinusoidal modulation of the critical current density with the angle γ, present in untwinned narrow nanowires, is also missing (see Fig. 10.4).

Finally, we have considered the J_C angular dependence for nanowires with different width, patterned on underdoped YBCO film, having a $T_C^0 = 81.4$ K, grown on a preannealed MgO (110) substrate.

The films are untwinned and the in-plane anisotropy of λ_L has been determined

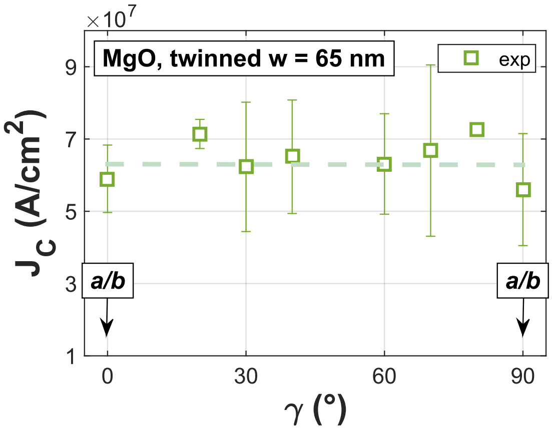

Figure 10.4: Average critical current density $\bar{J}_C$ vs the angle γ for the 65 nm wide, slightly overdoped, YBCO nanowires patterned on a MgO (110) substrate without annealing (*squares*). The film is twinned, therefore we do not expect an anisotropy in λ_L, reflecting in an angular dependent J_C^λ. In addition to this, also the cosinusoidal modulation of $\bar{J}_C(\gamma)$ disappears. As a result, the measured $\bar{J}_C$ is independent of the angle γ, even for the narrowest nanowires. The dashed line, $J_C = \text{const}$, is only a guide for the eye.

from the periodicity of the nanoSQUIDs oriented along the a- and the b-axis. The extracted value, $\lambda_L^a/\lambda_L^b = 1.1$, is smaller than in the slightly overdoped sample on MgO (110), as expected for a film with such oxygen doping [199].

From the knowledge of the in-plane London anisotropy, we have determined - through Eq. 10.1 - the expected dependence J_C^λ of the critical current density on the angle γ. In Fig. 10.5a we see that the measured $\bar{J}_C(\gamma)$ anisotropy is much stronger than $J_C^\lambda(\gamma)$. Moreover, differently from the slightly overdoped sample, here the difference between $\bar{J}_C(\gamma)$ and J_C^λ occurs not only for the narrowest nanowires, but also for those having width $w = 300$ nm.

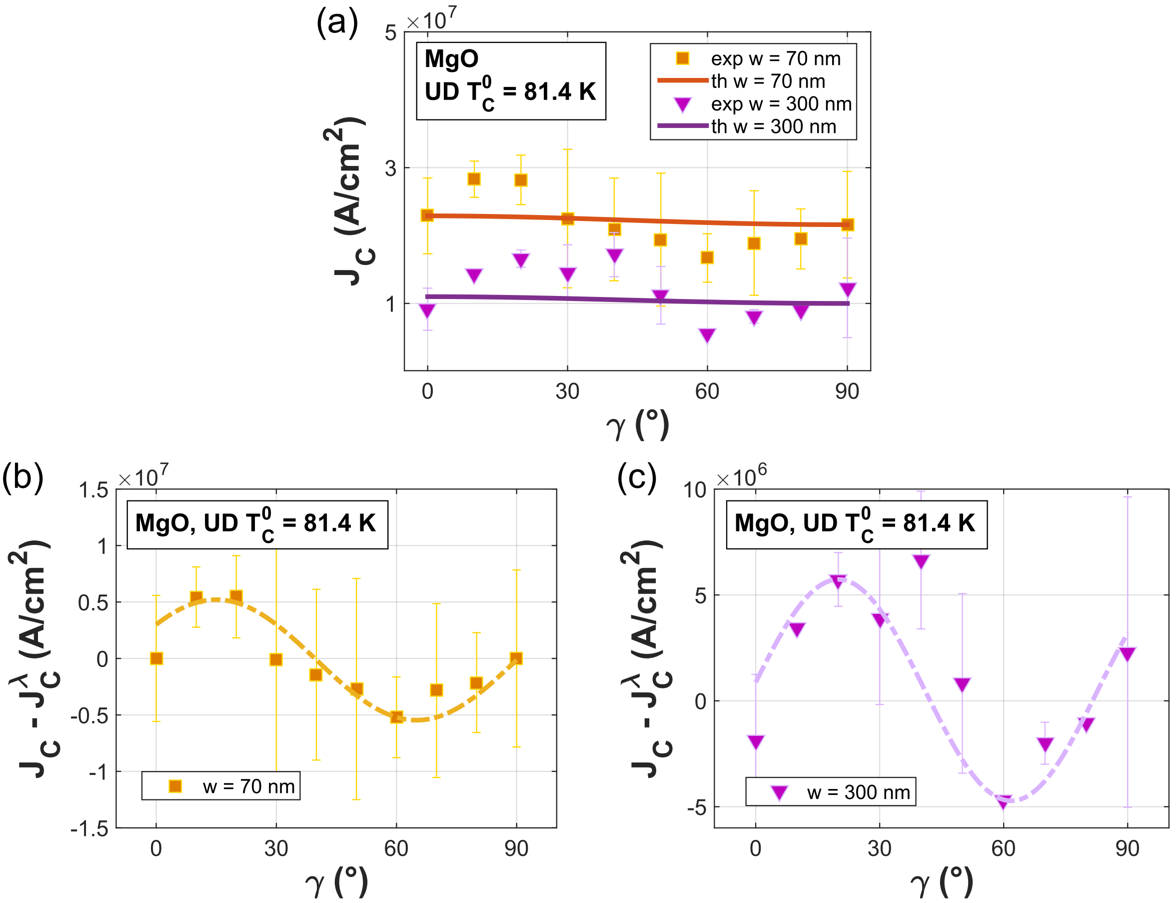

Figure 10.5: (a) Average critical current density $\bar{J}_C$ vs the angle γ for underdoped YBCO nanowires patterned on a film, having $T_C^0 = 81.4$ K, grown on a MgO (110) substrate annealed 5 h. The film is untwinned, characterized by an anisotropy of λ_L, determined by the periodicity of the nanoSQUIDs, $\lambda_L^a/\lambda_L^b = 1.1$. However, the measured $\bar{J}_C(\gamma)$ is stronger than the expected J_C^λ (*solid lines*), both for the narrow wires, with $w = 70$ nm (*squares*), and for the wide wires, with $w = 300$ nm (*triangles*). (b) The measured $\bar{J}_C$ values of the 70 nm wide wires are plotted as a function of the angle γ after the subtraction of the component J_C^λ to the total anisotropy. The resulting values exhibit a clear modulation as a function of γ, which phenomenologically can be described by a cosine function (*dashed line*). (c) The critical current density $\bar{J}_C - J_C^\lambda(\gamma)$ can be phenomenologically described by a cosine function also for the 300 nm wide wires. (*dashed line*).

The values of $\bar{J}_C - J_C^\lambda$ have been plotted as a function of γ both for the 70 nm wide nanowires and for the 300 nm wide nanowires (see Figs. 10.5b and 10.5c). A clear modulation is present is both the cases, with a maximum around $\gamma = 15°$ and a minimum around $\gamma = 65°$. These modulations have been phenomenologically described by using a cosine function, having shift $\delta\gamma$ very close to that used for the slightly overdoped sample (see *dashed lines* in Figs. 10.5b e 10.5c).

The nature of this periodically oscillating critical current density is currently under investigation. The $\bar{J}_C(\gamma)$ modulations are present only in untwinned samples, showing their strong connection to aligned chains throughout the sample. Moreover, they appear only in sub-100 nm wide nanowires in overdoped samples. In underdoped films, instead, they are present in a much broader range of widths. This phenomenology could be connected to the presence of the PDW/CDW order, strictly linked to the presence of CuO chains, and with a correlation length which strongly increases by reducing the O_2 doping. In addition to this, the physics characterizing the underdoped regime is preserved in our YBCO thin films grown on MgO (110), as testified by the presence of the 1/8 plateau (see Chapter 5). Therefore the hypothesis that this additional, unexpected, contribution to the J_C anisotropy comes from PDW associated to CDW has in our sample a strong experimental support. The PDW order, if present, should indeed give rise to a spatially modulating critical current density, as recently observed by scanning Josephson tunnel microscopy [253]. In our measurements, the maximum and the minimum of the modulation should appear in correspondence of the *a*- and *b*-axis parameters, since the PDW state is aligned along the YBCO in-plane axes. A misalignment with respect to the YBCO in-plane axes has been recently predicted [255] and associated to an additional Amperean pairing order [256], a new conceptually different state with a Q dependent pair amplitude. This additional Amperean PDW component, with diagonal momentum (Q, Q), develops in addition to the mixed unidirectional CDW/PDW state aligned along the YBCO in-plane axes: the resulting critical current density modulation will be misaligned with respect to the direction of the CuO chains, in qualitative agreement with the shift $\delta\gamma \approx 15°$ we have measured.

11

Summary and outlook

The optimization of the growth of untwinned YBCO films on MgO (110) substrates, with doping levels covering the full half superconducting dome is certainly one of the main outcomes of this thesis. We have demonstrated that our thin films have electronic properties as a function of doping very similar to single crystals, nicely reproducing the anomalies associated with CDW order at the 1/8 doping. This is the first time such a behavior is found in thin films. Moreover our ultrathin films are free from substitutions and/or chemical modifications, and can be considered a first step toward the realization of few unit cell structures with properties representative of the YBCO bulk. Since the rich and complex physics characterizing the underdoped region of the YBCO phase diagram is preserved in our films, it can be studied as a function of the dimensionality of the system, down to the nanoscale, when thin films are patterned into nanostructures.

Different experiments have been performed with YBCO nanowires:

- We have fabricated and characterized YBCO nanoSQUIDs, employing very short nanowires in the so-called Dayem bridge configuration. These devices, working in the whole temperature range from 300 mK up to the critical temperature ($\approx$ 85 K), have revealed an ultra white low-noise below 1 $\mu\Phi_0/\sqrt{\text{Hz}}$ above 10 kHz, corresponding to a predicted spin sensitivity of only 50 μ_B per $\sqrt{\text{Hz}}$.

  As a consequence, these devices could potentially be used in the next future as magnetic flux sensors, investigating the magnetic moment of small ensembles of spins in a wide range of temperatures and magnetic fields [257]. In particular, it could be very interesting to study magnetic nanoparticles in their transition from their paramagnetic to the ferromagnetic state, which has been limited until now by the critical temperature of Nb-based devices, lower than the typical T_{Curie} of the magnetic nanoparticles [21].

- The homogeneity of the nanowires has given a boost to the realization of devices, aimed at the detection of single photons. We have engineered 50 nm thick YBCO nanowires capped with a ferromagnetic LSMO layer, showing encouraging homogeneity properties. We have measured the photoresponse on these devices, detecting signals whose origin appears to be mostly bolometric.

We have also shown that in ultrathin (7-8 unit cell thick) YBCO nanowires a hot spot is formed within the wire: as a consequence, the nanowires are driven from the superconducting directly to the normal state, analogously to NbN nanowires commonly used as single photon detectors.

Photoresponse measurements on 10 nm thick nanowires are in progress.

- In the last chapter of the thesis we have described an experiment done to study the effect of the nanoscale ordering on the superconducting properties of our nanowires. The presence of a local charge density wave order has been recently demonstrated to be ubiquitous among all the cuprate families; if associated to a local modulations of Cooper pair density, CDWs might affect the absolute value of the critical current density of nanowires patterned at the length scale of the correlation length of this local order. We have used YBCO nanowires, fabricated on untwinned films, as a function of the oxygen doping and with dimensions of the same order as the CDW correlation length. By measuring the IVC of nanowires with the same width, patterned at different angles with respect to a fixed in plane direction of the substrate, we have revealed a cosinusoidal modulation of the critical current density as a function of the angle at the narrowest width w (of the order of 65 nm). This dependence smears out for wider nanowire dimensions. This modulation can represent one of the first evidence of the existence of a pair density wave in YBCO.

- In collaboration with researchers working at the European Synchrotron Radiation Facility (ESRF) in Grenoble, we want to explore by resonant elastic and inelastic X-ray scattering (RXS and RIXS respectively) underdoped (around the 1/8 doping) YBCO nanostructures, in form of nanodots and nanostripes, with geometry analogous to our nanowires.

  Preliminary spectra have been measured on an array of underdoped 65×500 nm^2 nanowires, patterned on a film with $T_C^0 = 60.5$ K (see Fig. 11.1a): as a consequence of the high degree of homogeneity and order, preserved by our nanostructures, both the elastic peak and a low energy contribution compatible with paramagnons can be easily identified with an acquisition time of only 15 minutes (see Fig. 11.1b). The statistical quality is enough for the detection and analysis of the CDW order.

  This experiment will allow to map the evolution of the CDW order with the dimensionality of the system and possibly to get more insight into the anisotropic dependence of the critical current density we have recently found.

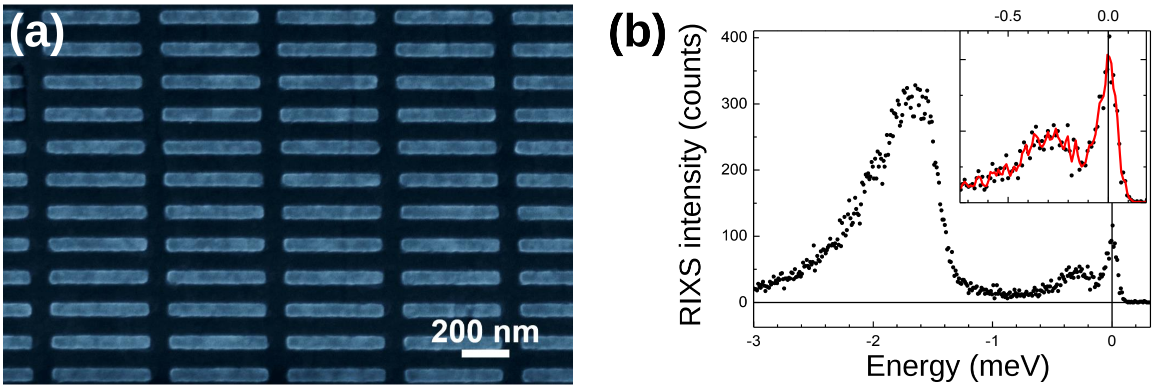

Figure 11.1: (a) SEM image of an array of underdoped ($p \approx 1/8$) 65×500 nm^2 YBCO nanowires. (b) RIXS spectrum measured in 15 min with the spectrometer ERIXS, located at the ID32 station of the ESRF, on the array shown in panel (a) (Courtesy of Giacomo Ghiringhelli).

Appendices

A

Recipes for sample fabrication

The recipes of the nanopatterning procedures presented here are tailored for the Nanofabrication Laboratory at the Department of Microtechnology and Nanoscience, Chalmers. As a consequence, the used parameters are specific of the equipment which are there.

A.1 YBCO nanowires on MgO (110)

1. A 50 nm thick film is deposited by Pulsed Laser deposition (DCA UHV system, tool #1142) on a MgO substrate (110) oriented, according to the parameters that are listed in Table 3.1.

2. A 50 nm thick film of Au is deposited by e-beam evaporation (Lesker#1, tool #451), at a rate of 1-2 Å/sec.

3. An 80 nm thick film of C is deposited by PLD (Carbon System tool #11413), at room temperature and with a deposition rate of 3 Å/sec).

4. The C surface is ashed 5 sec by using a low-power O_2 plasma (BatchTop, tools #418 - #419), to improve adhesion with the upcoming resist.

5. A double layer resist is spun on the chip. Both the bottom resist layer, MMA copolymer, EL4 (4% solid in Ethyl lactate), and the top resist layer, ARP6200.13 1:1, are spin-coated at 6000 RPM for 50 nm, than baked for 5 mins at 92° on a hotplate. Alternatively, a single layer resist can be used. In this case, a layer of ZEP 520A 1:1 is spin-coated at 4000 RPM for 120 nm, than baked for 8 mins at 90° on a hotplate.

6. The desired pattern in CAD file is exposed with e-beam litography at 100 kV. For small structures, a beam current of 2 nA, with a dose of 150 μC/cm^2 and corrections to proximity effects, is used. For big structures (e.g. electrodes, bonding pads), a beam current of 35 nA, with a dose of 250 μC/cm^2 is used.

7. In case of double layer resist: the top layer resist is developed in o-Xylene for 40-45 sec, rinsed in isopropyl alcohol (IPA) and blown dry with N_2, while the

bottom resist is developed in HBIK:IPA 1:3 for 35-40 sec, rinsed in IPA and blown dry with N_2. In case of single layer resist: the ZEP 520A 1:1 is developed in Hexylacetate for 25-30 sec, rinsed in IPA and blown dry with N_2.

8. A fast descum process is carried in an O_2 plasma, e.g. "ash 5s", in the Batchtop (tools #418 - #419).
9. A thin layer (12 - 15 nm) of Cr is evaporated (in Lesker#1, tool #451), at a rate of 1 Å/sec.
10. Lift-off of Cr is done in Removal 1165 at 60°.
11. Unprotected carbon is removed by O_2 plasma etching in the Batchtop (tool #418), for 25 mins at 50 W, and pressure of 100 mTorr.
12. The YBCO and Au not covered by the C mask are very softly and slowly etched in the Ar^+ ion milling system (CAIBE Oxford Ionfab, tool #417). We have chosen to work close to the etching voltage threshold for YBCO: below this value, which is of the order of 300 V, the film is only made amorphous instead of being etched. Moreover we have used the lowest beam current which allows the ignition of the plasma in our milling system. A summary of all the used parameters is reported in the following table:

Parameter	Value
V_{beam}	300 V
I_{beam}	5 mA
Current density	0.06 A/cm^2
Tilt	5°
Base Pressure	1×10^{-7} mbar
Process Pressure	$1.5 - 2.3 \times 10^{-4}$ mbar
Ar^+ flow	3.9 sccm
Stage Rotation	ON
Neutralizer	OFF

With these parameters, the etching rates of the used materials are the following: 5 nm/min for Au, 7 Å/min for YBCO, 1.5 nm/min for MgO (110). As a consequence, ≈ 110 mins are needed to remove 50 nm of Au, 50 nm of YBCO and to overetch 50 nm into the MgO (110) substrate.

13. The remaining carbon is removed by means of a O_2 plasma etching in the Batchtop (tool #418), for 18-22 mins at 50 W, and pressure of 100 mTorr.

A.2 YBCO nanowires on LAO (001)

The procedure is the same as described in sec. (A.1), with the exception of the steps 1, 7 and 12, which are the following:

1. A 50 nm thick film is deposited by Pulsed Laser deposition (DCA UHV system, tool #1142) on a LAO substrate (001) oriented, according to the parameters that are listed in Table 3.1.

7. Both the ARP6200.13 1:1 used as a top layer in the double layer resist and the ZEP 520A 1:1 used as a single layer resist are developed in Hexylacetate for 10-12 sec, rinsed in IPA and blown dry with N_2.

12. With the parameters listed in the table above the etching rate of LAO is $\approx$ 10 nm/min. As a consequence, the etching time required to etch 50 nm of Au, 50 nm of YBCO and 50 nm of LAO (001) substrate is 90 mins.

A.3 YBCO/LSMO nanowires on LAO (001)

The procedure is the same as described in sec. (A.1), with the exception of the steps 1, 7 and 12. Moreover, an additional etching step is required in the end of the process.

1. A 50 nm thick film is deposited by Pulsed Laser deposition (DCA UHV system, tool #1142) on a LAO substrate (001) oriented, with the parameters that are listed in Table 3.1. On the top, a 15 nm thick film of LSMO is deposited ex-situ by Pulsed Laser deposition (Calas System, tool #11411), at 0.2 mbar O_2 pressure and at a temperature of 730°C. Here, the growth conditions have been optimized to get the right compromise between surface smoothness and Curie temperature T_{Curie} of the ferromagnetic LSMO layer. Post-annealing of the bilayers at 800 mbar of O_2 has been employed to promote full oxidation of YBCO through the LSMO capping.

7. Both the ARP6200.13 1:1 used as a top layer in the double layer resist and the ZEP 520A 1:1 used as a single layer resist are developed in Hexylacetate for 10-12 sec, rinsed in IPA and blown dry with N_2.

12. With the parameters listed in the table of sec. (A.1), the etching rate of LSMO is $\approx$ 7 Å/min. As a consequence, the etching time required to etch 50 nm of Au, 15 nm of LSMO, 50 nm of YBCO and 50 nm of LAO (001) substrate is 115 mins.

14. The Au layer on the top of the nanostructures is removed by an additional ion milling step (CAIBE Oxford Ionfab, tool #417). The parameters are again those listed in the table of sec. (A.1), and the time to etch 50 nm of Au is $\approx$ 9 min.

B

The measurement setups

B.1 280 mK system - Heliox

The measurements in Chapters 5 and 6 were all done in an Oxford Heliox VL ^{3}He system, equipped with 44 dc-lines and used to reach temperatures down to 280 mK.

The 5×5 mm^2 chip is glued to a sample holder. Large Au/YBCO pads (250×75 μm^2) are located at the end of the electrodes, connected to the nanodevices. These pads are connected to the contacts of the sample holder by wedge bondings, using a gold wire of 25 μm diameter.

To cool down the nanodevices, the chip is mounted in thermal contact with the ^{3}He pot, located inside a vacuum can of the dip-stick. Then, the dip-stick is inserted in a liquid ^{4}He dewar surrounded by a superconducting magnetic shield. In this way, the chip reaches a temperature of 4.2 K. After this, a temperature of 1 K can be reached by pumping on the liquid ^{4}He contained in the so called 1 K pot. At this point, the charcoal ^{3}He sorb can be heated up with an electrical heater to release ^{3}He, and liquid ^{3}He condenses into the so called ^{3}He pot. Finally, pumping on this liquid with the charcoal absorption pump the cryostat can reach 280 mK.

All the nanodevices are low ohmic, with finite critical currents. As a consequence, measurements were performed in current bias mode. A high ohmic series resistance, R_b, is used to bias the device, while a resistor with lower resistance, R_s, is used to indirectly measure the current. The cryostat and the battery driven voltage preamplifiers are placed in an electromagnetic interference shielded room. All the digital electronics used for the measurements (voltage and current sources, analog to digital converters and the computer) is instead out of the shielded room, so to minimize the digital noise (see Fig. B.1). At the input-output of the matrix box, where the dc-lines are connected to the amplifiers and source, the signal is filtered by simple LC filters. The system is also equipped with a NbTi coil for the application of a magnetic field of around 100 mT. Moreover, a microwave antenna is mounted, close to the chip, to study microwave response of our nanodevices.

In details, the electronics used for the measurements was:

- 2 Stanford Research SR560 voltage preamplifiers.
- 2 HP 34401A multimeters.

- 1 Yokogawa 7651 dc current source, used to bias the NbTi coil.
- 1 Agilent 33220A arbitrary function generator, used for biasing.
- 1 Stanford Research Dynamic Signal analyzer SR785, used for the noise measurements.
- 1 National Instruments PCI-6052E data acquisition card (DAQ).

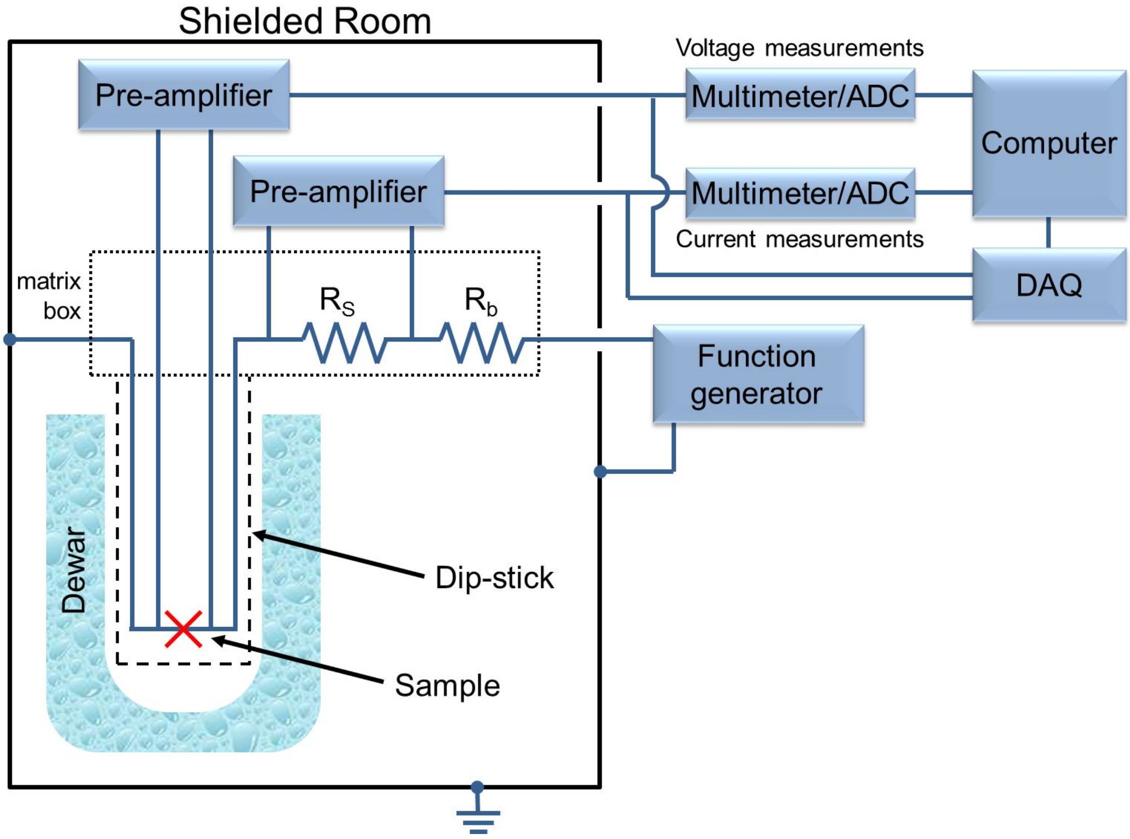

Figure B.1: A schematic diagram of the 300 mK Heliox measurement setup.

B.2 4.2 K system with optical access

The measurements in Chapters 8 were all done in a liquid helium flow cryostat with optical access, reaching temperatures down to 4.2 mK, which allows to perform photoresponse measurements.

The 5×5 mm^2 chip is glued to a sample holder. Large YBCO pads (250×75 μm^2) are located at the end of the electrodes, connected to the nanodevices. These pads are connected to the contacts of the sample holder by aluminum wedge bondings.

The sample holder is cooled down to 4.2 K through its mechanical attachment to a cold finger, which is cooled by using liquid ^{4}He. To cool down the cold finger, a medium vacuum pressure ($p \leq 10^{-6}$ torr), reachable by diffusive pump, is required. Then, the liquid helium is transferred to the cryostat through a transfer tube, insulated at $p \leq 10^{-5}$ torr with respect environment, which is connected to the external liquid ^{4}He dewar. The flow is controlled by a spin valve.

Electric connections to the nanodevices were made through wire bonds to high bandwidth and low bandwidth cables going to room temperature. The low bandwidth connections were used to dc bias the nanodevices, while the output (photo)voltage signals were carried by the high bandwidth connection to two cascaded 1 GHz bandwidth amplifiers with an overall voltage gain of 400. The amplified signal was observed and recorded by using an oscilloscope (see Fig. B.2).

During the photoresponse measurements a diode laser with $\lambda = 1550$ nm characterized by low power (≈ 200 μW) and repetition rate of 10 MHz was used. The optical bench is also equipped with various 3 dB and 6 dB full-band-pass optical filters, used to attenuate the power of the laser before hitting the sample.

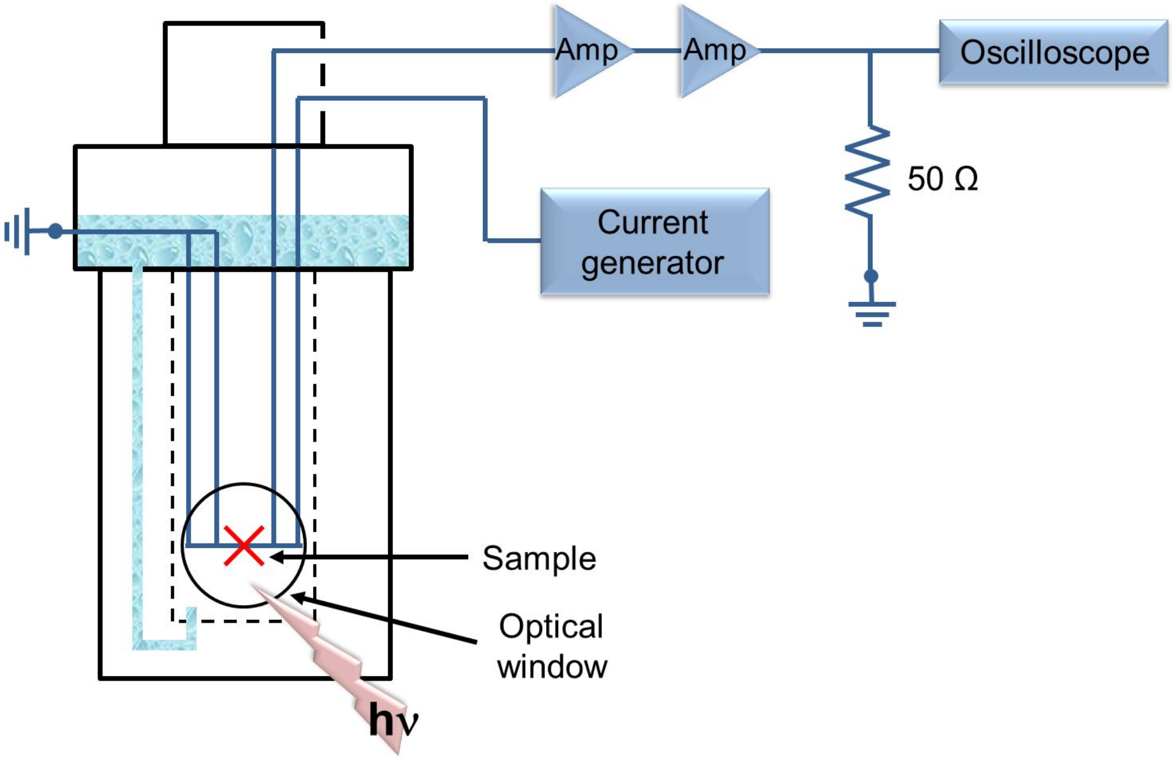

Figure B.2: A schematic diagram of the experimental apparatus used for the photoresponse experiments.

Acknowledgments

First of all, I want to thank my supervisors: Floriana Lombardi, for the contagious joy and enthusiasm she put in her job, for our stimulating discussions, for her never-ending support, and for surviving to the ocean of words I've been forcing her to read since more than five years; Thilo Bauch, for the strong support in the lab, for his brilliant comments and suggestions and for his constructive criticism.

Many thanks go to all my present and past coworkers: David Gustafsson, Domenico Montemurro, Edoardo Trabaldo, Eric Andersson, Evgeny Stepantsov, Gunta Kunakova, Luca Galletti, Maria Ekström, Ranko Toskovic, Reza Baghdadi, Shahid Nawaz and Sophie Charpentier, who directly or indirectly contributed to my work. You have been a source of friendship as well as good advice and collaboration, making hard for me to realize that what I do every day is actually a job!

I am really grateful to Alexei Kalaboukhov, for his help and assistance with XRD, AFM and PLD. A sincere acknowledgment is dedicated to our great clean room staff; in particular I would like to thank Henrik Frederiksen, Mats Hagberg and Bengt Nilsson: our group would have hard time surviving without your technical support!

I would also like to acknowledge all the team in Napoli, from "Federico II" University and CNR/SPIN Institute: Francesco Tafuri, for his guidance in the early beginning of my PhD, and for his silent and never-intrusive presence at my side; Giampiero Pepe, Loredana Parlato, Mikkel Ejrnaes and Roberto Cristiano, for letting me use their equipment and cryostat for the photoresponse measurements and for their contribution to the experiments.

A tremendous boost to our understanding of experimental results came from interaction with the theoreticians. Thanks in particular to Dmitry Golubev, from Aalto University, for his extensive calculations, fruitful discussions about the outcomes and patiently answering all my questions; to Roman Sobolewski, from the University of Rochester, for his support in the understanding of the photoresponse data; to Jonatan Wårdh and Mats Granath, who recently started this new fascinating adventure with us, riding on the crest of the (PD) wave...

Special thanks go to Regina Ciancio and Pasquale Orgiani, from CNR/IOM TASC Laboratory in Trieste, for their TEM studies of our YBCO thin films on MgO (110) substrates.

I gratefully acknowledge Giacomo Ghiringhelli, from Politecnico di Milano, for opening new horizons to my samples, through the investigation with synchrotron based X-ray scattering techniques he has just started.

A special acknowledgment goes to Niclas Lindvall, my living handbook of Sweden: sharing the office with you for so many years has been a pleasure, and it made every single day more pleasant. More in general, my thanks go to all the people working in the Quantum Device Physics Laboratory, for creating such a nice environment to work in.

Marco, I haven't forgotten your name before. Simply, being sort of a younger (forever 27) brother for me during these years, you deserve to be mentioned few lines below...

Finally, I thank my family and my girlfriend (still for a few weeks) Flavia, for all their love and encouragement. Grazie!

Bibliography

[1] J. Zaanen, S. Chakravarty, T. Senthil, P. Anderson, P. Lee, J. Schmalian, M. Imada, D. Pines, M. Randeria, C. M. Varma, M. Vojta, and M. Rice, "Towards a complete theory of High-T_C," *Nat. Phys.* **2**, 138 (2006).

[2] G. Ghiringhelli, M. Le Tacon, M. Minola, S. Blanco-Canosa, C. Mazzoli, N. B. Brookes, G. M. De Luca, A. Frano, D. G. Hawthorn, F. He, T. Loew, M. M. Sala, D. C. Peets, M. Salluzzo, E. Schierle, R. Sutarto, G. A. Sawatzky, E. Weschke, B. Keimer, and L. Braicovich, "Long-range incommensurate charge fluctuations in (Y, Nd)$Ba_2Cu_3O_{6+x}$," *Science* **337**, 821 (2012).

[3] E. H. da Silva Neto *et al.*, "Ubiquitous interplay between charge ordering and high-temperature superconductivity in cuprates," *Science* **343**, 393 (2014).

[4] E. H. da Silva Neto, R. Comin, F. He, R. Sutarto, Y. Jiang, R. L. Greene, G. A. Sawatzky, and A. Damascelli, "Charge ordering in the electron-doped superconductor $Nd_{2-x}Ce_xCuO_4$," *Science* **347**, 282 (2015).

[5] J. M. Tranquada, G. D. Gu, M. Hücker, Q. Jie, H.-J. Kang, R. Klingeler, Q. Li, N. Tristan, J. S. Wen, G. Y. Xu, Z. J. Xu, J. Zhou, and M. v. Zimmermann, "Evidence for unusual superconducting correlations coexisting with stripe order in $La_{1.875}Ba_{0.125}CuO_4$," *Phys. Rev. B* **78**, 174529 (2008).

[6] C. V. Parker, P. Aynajian, E. H. d. Silva Neto, A. Pushp, S. Ono, J. Wen, Z. Xu, G. Gu, and A. Yazdani, "Fluctuating stripes at the onset of the pseudogap in the high-T_c superconductor $Bi_2Sr_2CaCu_2O_{8+x}$," *Nature* **468**, 677 (2010).

[7] J. Chang, E. Blackburn, A. Holmes, N. Christensen, J. Larsen, J. Mesot, R. Liang, D. Bonn, W. Hardy, A. Watenphul, M. v. Zimmermann, E. M. Forgan, and S. M. Hayden, "Direct observation of competition between superconductivity and charge density wave order in $YBa_2Cu_3O_{6.67}$," *Nat. Phys.* **8**, 871 (2012).

[8] C. Castellani, C. Di Castro, and M. Grilli, "Singular quasiparticle scattering in the proximity of charge instabilities," *Phys. Rev. Lett.* **75**, 4650 (1995).

[9] R. Comin, R. Sutarto, E. da Silva Neto, L. Chauviere, R. Liang, W. Hardy, D. Bonn, F. He, G. Sawatzky, and A. Damascelli, "Broken translational and rotational symmetry via charge stripe order in underdoped $YBa_2Cu_3O_{6+y}$," *Science* **347**, 1335 (2015).

[10] G. Campi *et al.*, "Inhomogeneity of charge-density-wave order and quenched disorder in a high-T_C superconductor," *Nature* **525**, 359 (2015).

[11] M. Zgirski, K.-P. Riikonen, V. Touboltsev, and K. Arutyunov, "Size Dependent Breakdown of Superconductivity in Ultranarrow Nanowires," *Nano Lett.* **5**, 1029 (2005).

[12] O. V. Astafiev, L. B. Ioffe, S. Kafanov, Y. A. Pashkin, K. Arutyunov, D. Shahar, O. Cohen, and J. S. Tsai, "Coherent quantum phase slip," *Nature* **484**, 355 (2012).

[13] J. E. Mooij and Y. V. Nazarov, "Superconducting nanowires as quantum phase-slip junctions," *Nat. Phys.* **2**, 169 (2006).

[14] A. A. Shanenko, M. D. Croitoru, M. Zgirski, F. M. Peeters, and K. Arutyunov, "Size-dependent enhancement of superconductivity in Al and Sn nanowires: shape-resonance effect," *Phys. Rev. B* **74**, 052502 (2006).

[15] F. M. Peeters, M. D. Croitoru, and A. A. Shanenko, "Nanowires and nanofilms: Superconductivity in quantum-size regime," *Physica C* **468**, 326 (2008).

[16] S. Bose, A. M. Garcia-Garcia, M. M. Ugeda, J. D. Urbina, C. H. Michaelis, I. Brihuega, and K. Kern, "Observation of shell effects in superconducting nanoparticles of Sn," *Nat. Mater.* **9**, 550 (2010).

[17] A. M. Garcia-Garcia, J. D. Urbina, E. A. Yuzbashyan, K. Richter, and B. L. Altshuler, "Bardeen-Cooper-Schrieffer Theory of Finite-Size Superconducting Metallic Grains," *Phys. Rev. Lett.* **100**, 187001 (2008).

[18] C. M. Natarajan, M. G. Tanner, and R. H. Hadfield, "Superconducting nanowire single-photon detectors: physics and applications," *Supercond. Sci. Technol.* **25**, 063001 (2012).

[19] A. Engel, J. Renema, K. Il'in, and A. Semenov, "Detection mechanism of superconducting nanowire single-photon detectors," *Supercond. Sci. Technol.* **28**, 114003 (2015).

[20] D. Koelle, R. Kleiner, F. Ludwig, E. Dantsker, and J. Clarke, "High-transition-temperature superconducting quantum interference devices," *Rev. Mod. Phys.* **71**, 631 (1999).

[21] C. Granata and A. Vettoliere, "Nano Superconducting Quantum Interference device: A powerful tool for nanoscale investigations," *Phys. Rep.* **614**, 1 (2016).

[22] K. K. Likharev, "Vortex motion and Josephson effect in superconducting thin bridges," *Sov. Phys. JETP* **34**, 906 (1972).

[23] L. G. Aslamazov and S. V. Lempitskii, "Resistive state in broad superconducting films," *Sov. Phys. JETP* **57**, 1291 (1983).

[24] H. Assink, A. J. M. Harg, C. M. Schep, N. Y. Chen, D. Marel, P. Hadley, E. W. J. M. Drift, and J. E. Mooij, "Critical Currents in submicron YBCO lines," *IEEE Trans. Appl. Supercond.* **3**, 2983 (1993).

[25] J. Schneider, H. Kohlstedt, and R. Wordenweber, "Nanobridges of optimized YBCO thin films for superconducting flux-flow type devices," *Appl. Phys. Lett.* **63**, 2426 (1993).

[26] P. Larsson, B. Nilsson, and Z. G. Ivanov, "Fabrication and Transport Measurements of YBCO nanostructures," *J. Vac. Sci. Technol. B* **18**, 25 (2000).

[27] J. A. Bonetti, D. S. Caplan, D. J. Van Harlingen, and M. B. Weissman, "Electronic Transport in Underdoped YBCO Nanowires: Evidence for Fluctuating Domain Structures," *Phys. Rev. Lett.* **93**, 087002 (2008).

[28] G. Papari, F. Carillo, D. Stornaiuolo, L. Longobardi, F. Beltram, and F. Tafuri, "High critical-current density and scaling of phase-slip processes in YBCO nanowires," *Supercond. Sci. Technol.* **25**, 035011 (2012).

[29] M. Lyatti, A. Savenko, U. Poppe, and R. Dunin-Borkowski, "High-quality $YBa_2Cu_3O_{7-x}$ nanobridges fabricated by FIB etching," *arXiv preprint arXiv:1603.03459* (2016).

[30] S. K. H. Lam and D. L. Tilbrook, "Development of a niobium nanosuperconducting quantum interference device for the detection of small spin populations," *Appl. Phys. Lett.* **82**, 1078 (2003).

[31] L. Hao, J. C. Macfarlane, J. C. Gallop, D. Cox, J. Beyer, D. Drung, and T. Schurig, "Measurement and noise performance of nano-superconducting-quantum-interference devices fabricated by focused ion beam," *Appl. Phys. Lett.* **92**, 192507 (2008).

[32] J. Gallop, "SQUIDs: some limits to measurement," *Supercond. Sci. Technol.* **16**, 1575 (2003).

[33] C. P. Foley and H. Hilgenkamp, "Why NanoSQUIDs are important: an introduction to the focus issue," *Supercond. Sci. Technol.* **22**, 064001 (2009).

[34] J. Schneider, M. Muck, and R. Wordenweber, "dc SQUIDs based upon $YBa_2Cu_3O_7$ nanobridges," *Appl. Phys. Lett.* **65**, 2475 (1994).

[35] M. V. Pedyash, D. H. A. Blank, and H. Rogalla, "Superconducting quantum interference devices based on YBaCuO nanobridges," *Appl. Phys. Lett.* **68**, 1156 (1996).

[36] H. Kamerlingh Onnes, "The resistance of pure mercury at helium temperatures," *Commun. Phys. Lab. Univ. Leiden* **12**, 120 (1911).

[37] W. Meissner and R. Ochsenfeld, "Ein neuer Effekt bei Eintritt der Supraleitfähigkeit," *Naturwissenschaften* **21**, 787 (1933).

[38] F. London and H. London, "The Electromagnetic Equations of the Supraconductor," *Proceedings of the Royal Society A: Mathematical, Physical and Engineering Sciences* **149**, 71 (1935).

[39] V. L. Ginzburg and L. D. Landau, *Zh. Eksp. Teor. Fiz.* **20**, 1064 (1950).

[40] M. Tinkham, *Introduction to Superconductivity* (Dover Publications, 2004).

[41] K. F. Herzfeld, E. Maxwell, and R. B. Scott, "Isotope Effect and Lattice Properties in Superconductivity," *Phys. Rev.* **79**, 911 (1950).

[42] J. Bardeen, L. N. Cooper, and J. R. Schrieffer, *Phys. Rev.* **108**, 1175 (1957).

[43] J. Orenstein and A. J. Millis, "Advances in the physics of high temperature superconductivity," *Science* **288**, 468 (2000).

[44] J. Bednorz and K. Müller, "Possible high-Tc superconductivity in the Ba-La-Cu-O system," *Zeitschrift für Physik B Condensed Matter* **64**, 189 (1986).

[45] M. K. Wu, J. R. Ashburn, C. J. Torng, P. H. Hor, R. L. Meng, L. Gao, Z. J. Huang, Y. Q. Wang, and C. W. Chu, "Superconductivity at 93 K in a new mixed-phase Y-Ba-Cu-O compound system at ambient pressure," *Phys. Rev. Lett.* **58**, 908 (1987).

[46] A. Schilling, M. Cantoni, J. D. Guo, and H. R. Ott, "Superconductivity above 130 K in the Hg-Ba-Ca-Cu-O system," *Nature* **363**, 56 (1993).

[47] Y. Tokura and T. Arima, "New Classification Method for Layered Copper Oxide Compounds and Its Application to Design of New High T_c Superconductors," *Jpn. J. Appl. Phys.* **29**, 2388 (1990).

[48] Y. Sassa, "ARPES investigations on in situ PLD grown $YBa_2Cu_3O_{7-\delta}$," *PhD thesis* (2011).

[49] T. A. Zaleski and T. K. Kopeć, "Possible origin of 60-K plateau in the $YBa_2Cu_3O_{6+y}$ phase diagram," *Phys. Rev. B* **74**, 014504 (2006).

[50] W. E. Pickett, "Electronic structure of the high-temperature oxide superconductors," *Rev. Mod. Phys.* **61**, 433 (1989).

[51] J. Brooks and J. Schrieffer, *Handbook of High -Temperature Superconductivity: Theory and Experiment* (Springer, 2007).

[52] M. D. Vázquez-Navarro, A. Kursumovic, and J. E. Evetts, "Study and modelling of oxygen diffusion in YBCO under isothermal conditions," *Supercond. Sci. Technol.* **12**, 1117 (1999).

[53] R. Cava, A. Hewat, E. Hewat, B. Batlogg, M. Marezio, K. Rabe, J. Krajewski, W. Peck Jr, and L. Rupp Jr, "Structural anomalies, oxygen ordering and superconductivity in oxygen deficient $Ba_2YCu_3O_x$," *Physica C* **165**, 419 (1990).

[54] J. M. Tranquada, D. E. Cox, W. Kunnmann, H. Moudden, G. Shirane, M. Suenaga, P. Zolliker, D. Vaknin, S. K. Sinha, M. S. Alvarez, A. J. Jacobson, and D. C. Johnston, "Neutron-Diffraction Determination of Antiferromagnetic Structure of Cu Ions in $YBa_2Cu_3O_{6+x}$ with $x = 0.0$ and 0.15," *Phys. Rev. Lett.* **60**, 156 (1988).

[55] S. Nakamae, K. Behnia, N. Mangkorntong, M. Nohara, H. Takagi, S. J. C. Yates, and N. E. Hussey, "Electronic ground state of heavily overdoped nonsuperconducting $La_{2-x}Sr_xCuO_4$," *Phys. Rev. B* **68**, 100502 (2003).

[56] J. Chang, M. Månsson, S. Pailhès, T. Claesson, O. J. Lipscombe, S. M. Hayden, L. Patthey, O. Tjernberg, and J. Mesot, "Anisotropic breakdown of Fermi liquid quasiparticle excitations in overdoped $La_{2-x}Sr_xCuO_4$," *Nat. Commun.* **4**, 2559 (2013).

[57] C. M. Varma, P. B. Littlewood, S. Schmitt-Rink, E. Abrahams, and A. E. Ruckenstein, "Phenomenology of the normal state of Cu-O high-temperature superconductors," *Phys. Rev. Lett.* **63**, 1996 (1989).

[58] T. Timusk and B. Statt, “The pseudogap in high-temperature superconductors: an experimental survey,” *Reports on Progress in Physics* **62**, 61 (1999).

[59] J. C. Campuzano, H. Ding, M. R. Norman, H. M. Fretwell, M. Randeria, A. Kaminski, J. Mesot, T. Takeuchi, T. Sato, T. Yokoya, T. Takahashi, T. Mochiku, K. Kadowaki, P. Guptasarma, D. G. Hinks, Z. Konstantinovic, Z. Z. Li, and H. Raffy, “Electronic Spectra and Their Relation to the $\pi-\pi$ Collective Mode in High- T_C Superconductors,” *Phys. Rev. Lett.* **83**, 3709 (1999).

[60] S. Chakravarty, H.-Y. Kee, and V “An explanation for a universality of transition temperatures in families of copper oxide superconductors,” *Nature* **428**, 53 (2004).

[61] R. Khasanov, T. Kondo, S. Strässle, D. O. G. Heron, A. Kaminski, H. Keller, S. L. Lee, and T. Takeuchi, “Evidence for a Competition between the Superconducting State and the Pseudogap State of $(BiPb)_2(SrLa)_2CuO_{6+\delta}$ from Muon Spin Rotation Experiments,” *Phys. Rev. Lett.* **101**, 227002 (2008).

[62] V. J. Emery and S. A. Kivelson, “Importance of phase fluctuations in superconductors with small superfluid density,” *Nature* **374**, 434 (1994).

[63] Y. Kohsaka, T. Hanaguri, M. Azuma, M. Takano, J. C. Davis, and H. Takagi, “Visualization of the emergence of the pseudogap state and the evolution to superconductivity in a lightly hole-doped Mott insulator,” *Nat. Phys.* **8**, 534 (2012).

[64] K. Segawa and Y. Ando, “Transport Anomalies and the Role of Pseudogap in the 60-K Phase of $YBa_2Cu_3O_{7-\delta}$,” *Phys. Rev. Lett.* **86**, 4907 (2001).

[65] R. Beyers, B. Ahn, G. Gorman, V. Lee, S. Parkin, M. Ramirez, K. Roche, J. Vazquez, T. Gür, and R. Huggins, “Oxygen ordering, phase separation and the 60-K and 90-K plateaus in $YBa_2Cu_3O_x$,” *Nature* **340**, 619 (1989).

[66] C. Chaillout, M. A. Alario-Franco, J. J. Capponi, J. Chenavas, J. L. Hodeau, and M. Marezio, “Oxygen-vacancy ordering in the $Ba_2YCu_3O_{7-x}$ $(0 \leq x \leq 1)$ superconducting system,” *Phys. Rev. B* **36**, 7118 (1987).

[67] J. M. Tranquada, B. J. Sternlieb, J. D. Axe, Y. Nakamura, and S. Uchida, “Evidence for stripe correlations of spins and holes in copper oxide superconductors,” *Nature* **375**, 561 (1995).

[68] J. Tallon, G. Williams, N. Flower, and C. Bernhard, “Phase separation, pseudogap and impurity scattering in the HTS cuprates,” *Physica C* **282**, 236 (1997).

[69] D. N. Basov, R. Liang, D. A. Bonn, W. N. Hardy, B. Dabrowski, M. Quijada, D. B. Tanner, J. P. Rice, D. M. Ginsberg, and T. Timusk, “In-Plane Anisotropy of the Penetration Depth in $YBa_2Cu_3O_{7-x}$ and $YBa_2Cu_4O_8$ Superconductors,” *Phys. Rev. Lett.* **74**, 598 (1995).

[70] S. T. Johnson, E. M. Forgan, S. H. Lloyd, C. M. Aegerter, S. L. Lee, R. Cubitt, P. G. Kealey, C. Ager, S. Tajima, A. Rykov, and D. M. Paul, “Flux-Line Lattice Structures in Untwinned $YBa_2Cu_3O_{7-\delta}$,” *Phys. Rev. Lett.* **82**, 2792 (1999).

[71] C. Villard, G. Koren, D. Cohen, E. Polturak, B. Thrane, and D. Chateignier, “*ab*-Plane Anisotropy of Transport Properties in Unidirectionally Twinned $YBa_2Cu_3O_{7-\delta}$ Films,” *Phys. Rev. Lett.* **77**, 3913 (1996).

[72] H. J. H. Smilde, A. A. Golubov, Ariando, G. Rijnders, J. M. Dekkers, S. Harkema, D. H. A. Blank, H. Rogalla, and H. Hilgenkamp, "Admixtures to d-Wave Gap Symmetry in Untwinned $YBa_2Cu_3O_7$ Superconducting Films Measured by Angle-Resolved Electron Tunneling," *Phys. Rev. Lett.* **95**, 257001 (2005).

[73] D. H. Lu, D. L. Feng, N. P. Armitage, K. M. Shen, A. Damascelli, C. Kim, F. Ronning, Z.-X. Shen, D. A. Bonn, R. Liang, W. N. Hardy, A. I. Rykov, and S. Tajima, "Superconducting Gap and Strong In-Plane Anisotropy in Untwinned $YBa_2Cu_3O_{7-\delta}$," *Phys. Rev. Lett.* **86**, 4370 (2001).

[74] J. Waldram, *Superconductivity of Metals and Cuprates* (Taylor & Francis, 1996).

[75] T. Sekitani, N. Miura, S. Ikeda, Y. Matsuda, and Y. Shiohara, "Upper critical field for optimally-doped $YBa_2Cu_3O_{7-\delta}$," *Phys. B: Condens. Matter* **346**, 319 (2004).

[76] D. J. Van Harlingen, "Phase-sensitive tests of the symmetry of the pairing state in the high-temperature superconductors - Evidence for $d_{x^2-y^2}$ symmetry," *Rev. Mod. Phys.* **67**, 515 (1995).

[77] D. Gustafsson, D. Golubev, M. Fogelström, T. Claeson, S. Kubatkin, T. Bauch, and F. Lombardi, "Fully gapped superconductivity in a nanometre-size $YBa_2Cu3O_{7-\delta}$ island enhanced by a magnetic field," *Nat. Nanotechnol.* **8**, 25 (2013).

[78] A. V. Chubukov and D. K. Morr, "Electronic structure of underdoped cuprates," *Phys. Rep.* **288**, 355 (1997).

[79] *https://www.mpg.de/6000540/supraconductivity-electron-phonon-coupling* .

[80] S. Blanco-Canosa, A. Frano, E. Schierle, J. Porras, T. Loew, M. Minola, M. Bluschke, E. Weschke, B. Keimer, and M. Le Tacon, "Resonant x-ray scattering study of charge-density wave correlations in $YBa_2Cu_3O_{6+x}$," *Phys. Rev. B* **90**, 054513 (2014).

[81] E. Berg, E. Fradkin, and S. A. Kivelson, "Charge-4e superconductivity from pair-density-wave order in certain high-temperature superconductors," *Nat. Phys.* **5**, 830 (2009).

[82] R. Doll and M. Näbauer, "Experimental Proof of Magnetic Flux Quantization in a Superconducting Ring," *Phys. Rev. Lett.* **7**, 51 (1961).

[83] B. S. Deaver and W. M. Fairbank, "Experimental Evidence for Quantized Flux in Superconducting Cylinders," *Phys. Rev. Lett.* **7**, 43 (1961).

[84] A. A. Abrikosov, "On the magnetic properties of the superconductors of the second group," *Sov. Phys. JETP* **5**, 1174 (1957).

[85] B. Josephson, "Possible new effects in superconductive tunnelling," *Physics Letters* **1**, 251 (1962).

[86] P. W. Anderson and J. M. Rowell, "Probable Observation of the Josephson Superconducting Tunneling Effect," *Phys. Rev. Lett.* **10**, 230 (1963).

[87] K. K. Likharev and L. A. Yakobson, "Steady state properties of superconducting bridges," *Sov. Phys. Tech. Phys.* **20**, 950 (1976).

[88] K. K. Likharev, “Superconducting weak links,” *Rev. Mod. Phys.* **51**, 101 (1979).

[89] D. Y. Vodolazov, I. Maksimov, and E. Brandt, “Modulation instability of the order parameter in thin-film superconductors with edge barrier,” *Europhys. Lett.* **48**, 313 (1999).

[90] L. N. Bulaevskii, M. J. Graf, C. D. Batista, and V. G. Kogan, “Vortex-induced dissipation in narrow current-biased thin-film superconducting strips,” *Phys. Rev. B* **83**, 144526 (2011).

[91] W. A. Little, “Decay of Persistent Currents in Small Superconductors,” *Phys. Rev.* **156**, 396 (1967).

[92] J. S. Langer and V. Ambegaokar, “Intrinsic Resistive Transition in Narrow Superconducting Channels,” *Phys. Rev.* **164**, 498 (1967).

[93] D. E. McCumber and B. I. Halperin, “Time Scale of Intrinsic Resistive Fluctuations in Thin Superconducting Wires,” *Phys. Rev. B* **1**, 1054 (1970).

[94] M. Bell, A. Sergeev, V. Mitin, J. Bird, A. Verevkin, and G. Gol’tsman, “One-dimensional resistive states in quasi-two-dimensional superconductors: Experiment and theory,” *Phys. Rev. B* **76**, 094521 (2007).

[95] N. Giordano, “Evidence for Macroscopic Quantum Tunneling in One-Dimensional Superconductors,” *Phys. Rev. Lett.* **61**, 2137 (1988).

[96] A. Bezryadin, “Quantum suppression of superconductivity in nanowires,” *J. Phys.: Condens. Matter* **20**, 043202 (2008).

[97] K. Arutyunov, D. Golubev, and A. Zaikin, “Superconductivity in one dimension,” *Physics Reports* **464**, 1 (2008).

[98] D. S. Golubev and A. D. Zaikin, “Thermally activated phase slips in superconducting nanowires,” *Phys. Rev. B* **78**, 144502 (2008).

[99] R. Arpaia, D. Golubev, R. Baghdadi, M. Arzeo, G. Kunakova, S. Charpentier, S. Nawaz, F. Lombardi, and T. Bauch, “Resistive state triggered by vortex entry in $YBa_2Cu_3O_{7-\delta}$ nanostructures,” *Physica C* **506**, 165 (2014).

[100] G. N. Gol’tsman, O. Okunev, G. Chulkova, A. Lipatov, A. Semenov, K. Smirnov, B. Voronov, A. Dzardanov, C. Williams, and R. Sobolewski, “Picosecond superconducting single-photon optical detector,” *Appl. Phys. Lett.* **79**, 705 (2001).

[101] H. Weinstock, *SQUID sensors: fundamentals, fabrication, and applications* (Springer, 1996).

[102] K. Hasselbach, D. Mailly, and J. R. Kirtley, “Micro-superconducting quantum interference device characteristics,” *J. Appl. Phys.* **91** (2002).

[103] C. D. Tesche and J. Clarke, “dc SQUID: Noise and optimization,” *J. Low Temp. Phys.* **29**, 301 (1977).

[104] T. Steinborn, G. Miehe, J. Wiesner, E. Brecht, H. Fuess, G. Wirth, B. Schulte, M. Speckmann, H. Adrian, M. Maul, K. Petersen, W. Blau, and M. McConnel, "Twinning of $YBa_2Cu_3O_7$ thin films on different substrates and modification by irradiation," *Physica C* **220**, 219 (1994).

[105] D. Schweitzer, T. Bollmeier, B. Stritzker, and B. Rauschenbach, "Twinning of $YBa_2Cu_3O_7$ thin films on different substrates," *Thin Solid Films* **280**, 147 (1996).

[106] W. K. Kwok, U. Welp, V. M. Vinokur, S. Fleshler, J. Downey, and G. W. Crabtree, "Direct observation of intrinsic pinning by layered structure in single-crystal $YBa_2Cu_3O_{7-\delta}$," *Phys. Rev. Lett.* **67**, 390 (1991).

[107] J. M. Dekkers, G. Rijnders, S. Harkema, H. J. H. Smilde, H. Hilgenkamp, H. Rogalla, and D. H. A. Blank, "Monocrystalline $YBa_2Cu_3O_{7-x}$ thin films on vicinal $SrTiO_3$ (001) substrates," *Appl. Phys. Lett.* **83**, 5199 (2003).

[108] S. Hoon Lee, J.-H. Choi, and S.-G. Lee, "Transition properties of a $YBa_2Cu_3O_7$ nanobridge patterned across a twin boundary of a $LaAlO_3$ substrate," *J. Appl. Phys.* **111**, 063914 (2012).

[109] A. P. Zhuravel, S. M. Anlage, S. K. Remillard, A. V. Lukashenko, and A. V. Ustinov, "Effect of $LaAlO_3$ twin-domain topology on local dc and microwave properties of cuprate films," *J. Appl. Phys.* **108**, 033920 (2010).

[110] J. Mazierska, D. Ledenyov, M. V. Jacob, and J. Krupka, "Precise microwave characterization of MgO substrates for HTS circuits with superconducting post dielectric resonator," *Supercond. Sci. Technol.* **18**, 18 (2005).

[111] V. E. Henrich, "Thermal faceting of (110) and (111) surfaces of MgO," *Surf. Sci.* **57**, 385 (1976).

[112] G. Chern, J. Huang, and T. Leung, "Atomic force microscopy study of the faceting on MgO (110) surface," *J. Vac. Sci. Technol. A* **16**, 964 (1998).

[113] D. Giese, F. Lamelas, H. Owen, R. Plass, and M. Gajdardziska-Josifovska, "Atomic force microscopy and scanning electron microscopy study of MgO (110) surface faceting," *Surf. Sci.* **457**, 326 (2000).

[114] A. Di Chiara, F. Lombardi, F. M. Granozio, U. S. di Uccio, M. Valentino, F. Tafuri, A. Del Vecchio, M. De Riccardis, and L. Tapfer, "Structure and morphology of MgO/YBCO bilayers for biepitaxial junctions," *Physica C* **273**, 30 (1996).

[115] E. Talantsev, N. Strickland, S. Wimbush, J. Storey, J. Tallon, and N. Long, "Hole doping dependence of critical current density in $YBa_2Cu_3O_{7-\delta}$ conductors," *Appl. Phys. Lett.* **104**, 242601 (2014).

[116] Z. Mori, T. Doi, and Y. Hakuraku, "Oxygen diffusion in c-axis oriented $YBa_2Cu_3O_{7-\delta}$ thin films," *J. of Appl. Phys.* **110**, 033915 (2011).

[117] R. Baghdadi, R. Arpaia, T. Bauch, and F. Lombardi, "Toward $YBa_2Cu_3O_{7-\delta}$ Nanoscale Structures for Hybrid Devices," *IEEE Trans. Appl. Supercond.* **25**, 1 (2015).

[118] N. Hussey, "Phenomenology of the normal state in-plane transport properties of high-Tc cuprates," *J. Phys. Condens. Matter* **20**, 123201 (2008).

[119] T. Manako, Y. Kubo, and Y. Shimakawa, “Transport and structural study of $Tl_2Ba_2CuO_{6+\delta}$ single crystals prepared by the KCl flux method,” *Phys. Rev. B* **46**, 11019 (1992).

[120] A. Mackenzie, S. Julian, D. Sinclair, and C. Lin, “Normal-state magnetotransport in superconducting $Tl_2Ba_2CuO_{6+\delta}$ to millikelvin temperatures,” *Phys. Rev. B* **53**, 5848 (1996).

[121] J. Zegenhagen, T. Haage, and Q. Jiang, “Microscopic structure and structuring of perovskite surfaces and interfaces: $SrTiO_3$, $RBa_2Cu_3O_{7-\delta}$,” *Appl. Phys. A* **67**, 711 (1998).

[122] J. Brötz and H. Fuess, “Detwinning in $YBa_2Cu_3O_{7-\delta}$ films on vicinal $SrTiO_3$ (001) due to anisotropic strain at the interface,” *Physica C* **339**, 75 (2000).

[123] T. Haage, H.-U. Habermeier, and J. Zegenhagen, “Periodic step structure of clean and $YBa_2Cu_3O_{7-\delta}$-covered vicinal $SrTiO_3$ (001) surfaces,” *Surf. Sci.* **370**, L158 (1997).

[124] J.-M. Triscone, M. Karkut, L. Antognazza, O. Brunner, and Ø. Fischer, “Y-Ba-Cu-O/Dy-Ba-Cu-O superlattices: A first step towards the artificial construction of high-T_C superconductors,” *Phys. Rev. Lett.* **63**, 1016 (1989).

[125] Q. Li, X. Xi, X. Wu, A. Inam, S. Vadlamannati, W. McLean, T. Venkatesan, R. Ramesh, D. Hwang, J. Martinez, and L. Nazar, “Interlayer coupling effect in high-T c superconductors probed by $YBa_2Cu_3O_{7-x}$ /$PrBa_2Cu_3O_{7-x}$ superlattices,” *Phys. Rev. Lett.* **64**, 3086 (1990).

[126] T. Terashima, K. Shimura, Y. Bando, Y. Matsuda, A. Fujiyama, and S. Komiyama, “Superconductivity of one-unit-cell thick $YBa_2Cu_3O_7$ thin film,” *Phys. Rev. Lett.* **67**, 1362 (1991).

[127] M. Z. Cieplak, S. Guha, S. Vadlamannati, T. Giebultowicz, and P. Lindenfeld, “Origin of the T_C depression and the role of charge transfer and dimensionality in ultrathin $YBa_2Cu_3O_{7-\delta}$,” *Phys. Rev. B* **50**, 12876 (1994).

[128] G. Balestrino and A. Tebano, “Superconductivity in cuprate artificial structures,” *Supercond. Sci. Technol.* **16**, R29 (2003).

[129] I. Chan, D. Vier, O. Nakamura, J. Hasen, J. Guimpel, S. Schultz, and I. K. Schuller, “Thickness dependence of the superconducting transition temperature of YBCO,” *Phys. Lett. A* **175**, 241 (1993).

[130] N. Savvides and A. Katsaros, “Growth and evolution of microstructure of epitaxial $YBa_2Cu_3O_{7-x}$ ultrathin and thin films on MgO,” *Physica C* **226**, 23 (1994).

[131] P. Probst, K. Il’in, A. Engel, A. Semenov, H.-W. Hübers, J. Hänisch, B. Holzapfel, and M. Siegel, “Magnetoresistivity of thin $YBa_2Cu_3O_{7-\delta}$ films on sapphire substrate,” *Physica C* **479**, 173 (2012).

[132] Y. Matsuda, S. Komiyama, T. Onogi, T. Terashima, K. Shimura, and Y. Bando, “Thickness dependence of the Kosterlitz-Thouless transition in ultrathin $YBa_2Cu_3O_{7-\delta}$ films,” *Phys. Rev. B* **48**, 10498 (1993).

[133] W. Tang, C. Ng, C. Yau, and J. Gao, “Thickness dependence of superconductivity for $YBa_2Cu_3O_y$ ultra-thin films,” *Supercond. Sci. Technol.* **13**, 580 (2000).

[134] P. Probst, A. Semenov, M. Ries, A. Hoehl, P. Rieger, A. Scheuring, V. Judin, S. Wünsch, K. Il’in, N. Smale, Y.-L. Mathis, R. Müller, G. Ulm, G. Wüstefeld, H.-W. Hübers, J. Hänisch, B. Holzapfel, M. Siegel, and A.-S. Müller, “Nonthermal response of $YBa_2Cu_3O_{7-\delta}$ thin films to picosecond THz pulses,” *Phys. Rev. B* **85**, 174511 (2012).

[135] M. Varela, Z. Sefrioui, D. Arias, M. Navacerrada, M. Lucía, M. L. de La Torre, C. León, G. Loos, F. Sánchez-Quesada, and J. Santamaría, “Intracell changes in epitaxially strained $YBa_2Cu_3O_{7-x}$ ultrathin layers in $YBa_2Cu_3O_{7-x}$ /$PrBa_2Cu_3O_7-$ superlattices,” *Phys. Rev. Lett.* **83**, 3936 (1999).

[136] J. Garcia-Barriocanal, A. M. Perez-Muñoz, Z. Sefrioui, D. Arias, M. Varela, C. Leon, S. J. Pennycook, and J. Santamaria, “Disorder-controlled superconductivity at $YBa_2Cu_3O_7$ /$SrTiO_3$ interfaces,” *Phys. Rev. B* **87**, 245105 (2013).

[137] M. Cieplak, S. Vadlamannati, S. Guha, C. Nien, and P. Lindenfeld, “From submonolayers to bulk in $YBa_2Cu_3O_{7-\delta}$,” *Physica C* **209**, 31 (1993).

[138] J. Hasen, D. Lederman, and I. K. Schuller, “Comment on ”Refelection high-energy diffraction oscillations during epitaxial growth of high-temperature superconducting oxides”,” *Phys. Rev. Lett.* **70**, 1731 (1993).

[139] T. Terashima and Y. Bando, “Terashima and Bando reply,” *Phys. Rev. Lett.* **70**, 1732 (1993).

[140] M. R. Beasley, J. E. Mooij, and T. P. Orlando, “Possibility of Vortex-Antivortex Pair Dissociation in Two-Dimensional Superconductors,” *Phys. Rev. Lett.* **42**, 1165 (1979).

[141] J. Repaci, C. Kwon, Q. Li, X. Jiang, T. Venkatessan, R. Glover III, C. Lobb, and R. Newrock, “Absence of a Kosterlitz-Thouless transition in ultrathin $YBa_2Cu_3O_{7-\delta}$ films,” *Phys. Rev. B* **54**, R9674 (1996).

[142] Y. Ando, S. Komiya, K. Segawa, S. Ono, and Y. Kurita, “Electronic phase diagram of high-T_C cuprate superconductors from a mapping of the in-plane resistivity curvature,” *Phys. Rev. Lett.* **93**, 267001 (2004).

[143] N. Barišić, M. K. Chan, Y. Li, G. Yu, X. Zhao, M. Dressel, A. Smontara, and M. Greven, “Universal sheet resistance and revised phase diagram of the cuprate high-temperature superconductors,” *Proc. Natl. Acad. Sci.* **110**, 12235 (2013).

[144] M. Hücker *et al.*, “Competing charge, spin, and superconducting orders in underdoped YBa_2Cu_3 O_y,” *Phys. Rev. B* **90**, 054514 (2014).

[145] H. Sato, A. Tsukada, M. Naito, and A. Matsuda, “$La_{2-x}Sr_xCuO_y$ epitaxial thin films (x= 0 to 2): Structure, strain, and superconductivity,” *Phys. Rev. B* **61**, 12447 (2000).

[146] H. Sato, A. Tsukada, M. Naito, and A. Matsuda, “Absence of 1/8 anomaly in strained thin films of $La_{2-x}Sr_xCuO_{4+\delta}$,” *Phys. Rev. B* **62**, R799 (2000).

[147] H. Sato, M. Naito, A. Tsukada, S. Karimoto, and A. Matsuda, “Influence of substrates on epitaxial thin films of high-temperature superconductors,” *Physica C* **362**, 186 (2001).

[148] E. Osquiguil, M. Maenhoudt, B. Wuyts, and Y. Bruynseraede, "Controlled preparation of oxygen deficient $YBa_2Cu_3O_x$ films," *Appl. Phys. Lett.* **60**, 1627 (1992).

[149] S. K. Tolpygo, J.-Y. Lin, M. Gurvitch, S. Hou, and J. M. Phillips, "Universal T_C suppression by in-plane defects in high-temperature superconductors: Implications for pairing symmetry," *Phys. Rev. B* **53**, 12454 (1996).

[150] G. Farnan, M. McCurry, and D. Walmsley, "Fabrication and characterisation of underdoped $YBa_2Cu_3O_{7-\delta}$ thin films," *Physica C* **341**, 2335 (2000).

[151] B. Wuyts, V. Moshchalkov, and Y. Bruynseraede, "Resistivity and Hall effect of metallic oxygen-deficient $YBa_2Cu_3O_x$ films in the normal state," *Phys. Rev. B* **53**, 9418 (1996).

[152] B. Veal and A. Paulikas, "Dependence of hole concentration on oxygen vacancy order in $YBa_2Cu_3O_{7-\delta}$: A chemical valence model," *Physica C* **184**, 321 (1991).

[153] Y. Liu, J. Qu, M. Zhu, S. Zhang, S. Feng, and X. Li, "Stripe characterization in $La_{1.6-x}Nd_{0.4}Sr_xCuO_4$ thin films," *Phys. Rev. B* **70**, 224512 (2004).

[154] J. Cooper and J. Loram, "Some Correlations Between the Thermodynamic and Transport Properties of High T_C Oxides in the Normal State," *J. Physique I* **6**, 2237 (1996).

[155] A. Kapitulnik, J. Xia, E. Schemm, and A. Palevski, "Polar Kerr effect as probe for time-reversal symmetry breaking in unconventional superconductors," *New J. Phys.* **11**, 055060 (2009).

[156] O. Cyr-Choinière, G. Grissonnanche, S. Badoux, J. Day, D. Bonn, W. Hardy, R. Liang, N. Doiron-Leyraud, and L. Taillefer, "Two types of nematicity in the phase diagram of the cuprate superconductor $YBa_2Cu_3O_y$," *Phys. Rev. B* **92**, 224502 (2015).

[157] M. S. Grbić, M. Požek, D. Paar, V. Hinkov, M. Raichle, D. Haug, B. Keimer, N. Barišić, and A. Dulčić, "Temperature range of superconducting fluctuations above T_C in $YBa_2Cu_3O_{7-\delta}$ single crystals," *Phys. Rev. B* **83**, 144508 (2011).

[158] C. Namgung, J. Irvine, J. Binks, and A. West, "Orthorhombic-tetragonal transition in YBa_2Cu_3Ox," *Supercond. Sci. Technol.* **1**, 169 (1988).

[159] J. Ye and K. Nakamura, "Quantitative structure analyses of $YBa_2Cu_3O_{7-\delta}$ thin films: Determination of oxygen content from x-ray-diffraction patterns," *Phys. Rev. B* **48**, 7554 (1993).

[160] H. Takagi, T. Ido, S. Ishibashi, M. Uota, S. Uchida, and Y. Tokura, "Superconductor-to-nonsuperconductor transition in $(La_{1-x}Sr_x)_2CuO_4$ as investigated by transport and magnetic measurements," *Phys. Rev. B* **40**, 2254 (1989).

[161] M. Presland, J. Tallon, R. Buckley, R. Liu, and N. Flower, "General trends in oxygen stoichiometry effects on T_C in Bi and Tl superconductors," *Physica C* **176**, 95 (1991).

[162] R. Liang, D. Bonn, and W. Hardy, "Evaluation of CuO_2 plane hole doping in $YBa_2Cu_3O_{6+x}$ single crystals," *Phys. Rev. B* **73**, 180505 (2006).

[163] C. H. Wu, Y. T. Chou, W. C. Kuo, J. H. Chen, L. M. Wang, J. C. Chen, K. L. Chen, U. C. Sou, H. C. Yang, and J. T. Jeng, "Fabrication and characterization of high-T_C $YBa_2Cu_3O_{7-x}$ nanoSQUIDs made by focused ion beam milling," *Nanotechnology* **19**, 315304 (2008).

[164] N. Curtz, E. Koller, H. Zbinden, M. Decroux, L. Antognazza, Ø. Fischer, and N. Gisin, “Patterning of ultrathin YBCO nanowires using a new focused-ion-beam process,” *Supercond. Sci. Technol.* **23**, 045015 (2010).

[165] G. Zhang, X. Lu, T. Zhang, J. Qu, W. Wang, X. Li, and S. Yu, “Microstructure and superconductivity of highly ordered $YBa_2Cu_3O_{7-\delta}$ nanowire arrays,” *Nanotechnology* **17**, 4252 (2006).

[166] A. I. Mansour, K. H. Chow, and J. Jung, “Persistent critical current of $YBa_2Cu_3O_{7-\delta}$ nanowires,” *J. Appl. Phys.* **110**, 063909 (2011).

[167] P. Morales, M. DiCiano, and J. Y. T. Wei, “Selective epitaxial growth of submicron complex oxide structures by amorphous $SrTiO_3$,” *Appl. Phys. Lett.* **86**, 192509 (2005).

[168] A. A. O. Elkaseh, W. J. Perold, and V. V. Srinivasu, “Josephson nanoconstrictions made by AFM plowing of $YBa_2Cu_3O_{7-x}$ films,” *J. Appl. Phys.* **108**, 053914 (2010).

[169] K. Xu and J. R. Heath, “Long, Highly-Ordered High-Temperature Superconductor Nanowire Arrays,” *Nano Lett.* **8**, 3845 (2008).

[170] K. Kajino, T. Kimura, Y. Horii, M. Watanabe, M. Inoue, and A. Fujimaki, “Preparation of Narrowed $YBa_2Cu_3O_{7-\mathrm{x}}$ Nanobridges Down to 30 nm With Reduced Degradation,” *IEEE Trans. Appl. Supercond.* **19**, 178 (2009).

[171] G. Papari, F. Carillo, D. Born, L. Bartoloni, E. Gambale, D. Stornaiuolo, P. Pingue, F. Beltram, and F. Tafuri, “YBCO Nanobridges: Simplified Fabrication Process by Using a Ti Hard Mask,” *IEEE Trans. Appl. Supercond.* **19**, 183 (2009).

[172] R. Arpaia, S. Nawaz, F. Lombardi, and T. Bauch, “Improved Nanopatterning for YBCO Nanowires Approaching the Depairing Current,” *IEEE Trans. Appl. Supercond.* **23**, 1101505 (2013).

[173] S. Nawaz, R. Arpaia, F. Lombardi, and T. Bauch, “Microwave Response of Superconducting $YBa_2Cu_3O_{7-\delta}$ Nanowire Bridges Sustaining the Critical Depairing Current: Evidence of Josephson-like Behavior,” *Phys. Rev. Lett.* **110**, 167004 (2013).

[174] S. Nawaz, R. Arpaia, T. Bauch, and F. Lombardi, “Approaching the theoretical depairing current in $YBa_2Cu_3O_{7-x}$ nanowires,” *Physica C* **495**, 33 (2013).

[175] S. Tahara, S. M. Anlage, J. Halbritter, C.-B. Eom, D. K. Fork, T. H. Geballe, and M. R. Beasley, “Critical currents, pinning, and edge barriers in narrow $YBa_2Cu_3O_{7-\delta}$ thin films,” *Phys. Rev. B* **41**, 11203 (1990).

[176] M. Flik and C. Tien, “Size effect on the thermal conductivity of high-Tc thin-film superconductors,” *J. Heat Transfer* **112**, 872 (1990).

[177] P. Mikheenko, X. Deng, S. Gildert, M. S. Colclough, R. A. Smith, C. M. Muirhead, P. D. Prewett, and J. Teng, “Phase slips in submicrometer $YBa_2Cu_3O_{7-\delta}$ bridges,” *Phys. Rev. B* **72**, 174506 (2005).

[178] M. Pedyash, G. Gerritsma, D. Blank, and H. Rogalla, “Coherent vortex motion in superconducting nanobridges based on YBaCuO thin films,” *IEEE Trans. Appl. Supercond.* **5**, 1387 (1995).

[179] J. Bardeen, "Critical Fields and Currents in Superconductors," *Rev. Mod. Phys.* **34**, 667 (1962).

[180] A. G. Zaitsev, R. Schneider, G. Linker, F. Ratzel, R. Smithey, P. Schweiss, J. Geerk, R. Schwab, and R. Heidinger, "Microwave measurements of the absolute London penetration depth in double-sided $YBa_2Cu_3O_{7-x}$ thin films on sapphire," *Rev. Sci. Instrum.* **73**, 335 (2002).

[181] *http://www.ceraco.de/* .

[182] M. Y. Kupriyanov and V. F. Lukichev, *Fiz. Nizk. Temp.* **6**, 445 (1980).

[183] M. W. Brenner, S. Gopalakrishnan, J. Ku, T. J. McArdle, J. N. Eckstein, N. Shah, P. M. Goldbart, and A. Bezryadin, "Cratered Lorentzian response of driven microwave superconducting nanowire-bridged resonators: Oscillatory and magnetic-field induced stochastic states," *Phys. Rev. B* **83**, 184503 (2011).

[184] M. W. Brenner, D. Roy, N. Shah, and A. Bezryadin, "Dynamics of superconducting nanowires shunted with an external resistor," *Phys. Rev. B* **85**, 224507 (2012).

[185] G. Papari, F. Carillo, D. Stornaiuolo, D. Massarotti, L. Longobardi, F. Beltram, and F. Tafuri, "Dynamics of vortex matter in YBCO sub-micron bridges," *Physica C* **506**, 188 (2014).

[186] R. Baghdadi, R. Arpaia, S. Charpentier, D. Golubev, T. Bauch, and F. Lombardi, "Fabricating Nanogaps in $YBa_2Cu_3O_{7-\delta}$ for Hybrid Proximity-Based Josephson Junctions," *Phys. Rev. Applied* **4**, 014022 (2015).

[187] R. Arpaia, S. Charpentier, R. Toskovic, T. Bauch, and F. Lombardi, "$YBa_2Cu_3O_{7-\delta}$ nanorings to probe fluxoid quantization in High Critical Temperature Superconductors," *Physica C* **506**, 184 (2014).

[188] I. Sochnikov, A. Shaulov, Y. Yeshurun, G. Logvenov, and I. Bozovic, "Large oscillations of the magnetoresistance in nanopatterned high-temperature superconducting films," *Nat. Nanotechnol.* **5**, 516 (2010).

[189] F. Carillo, G. Papari, D. Stornaiuolo, D. Born, D. Montemurro, P. Pingue, F. Beltram, and F. Tafuri, "Little-Parks effect in single nanoscale YBCO rings," *Phys. Rev. B* **81**, 054505 (2010).

[190] V. Juričić, I. F. Herbut, and Z. Tešanović, "Restoration of the Magnetic hc/e Periodicity in Unconventional Superconductors," *Phys. Rev. Lett.* **100**, 187006 (2008).

[191] F. Loder, A. P. Kampf, T. Kopp, J. Mannhart, C. W. Schneider, and Y. S. Barash, "Magnetic flux periodicity of h/e in superconducting loops," *Nat. Phys.* **4**, 112 (2008).

[192] V. Vakaryuk, "Universal Mechanism for Breaking the hc/2e Periodicity of Flux-Induced Oscillations in Small Superconducting Rings," *Phys. Rev. Lett.* **101**, 167002 (2008).

[193] T.-C. Wei and P. M. Goldbart, "Emergence of h/e-period oscillations in the critical temperature of small superconducting rings threaded by magnetic flux," *Phys. Rev. B* **77**, 224512 (2008).

[194] J.-X. Zhu and H. T. Quan, “Magnetic flux periodicity in a hollow *d*-wave superconducting cylinder,” *Phys. Rev. B* **81**, 054521 (2010).

[195] W. A. Little and R. D. Parks, “Observation of Quantum Periodicity in the Transition Temperature of a Superconducting Cylinder,” *Phys. Rev. Lett.* **9**, 9 (1962).

[196] R. D. Parks and W. A. Little, “Fluxoid Quantization in a Multiply-Connected Superconductor,” *Phys. Rev.* **133**, A97 (1964).

[197] J. R. Clem and K. K. Berggren, “Geometry-dependent critical currents in superconducting nanocircuits,” *Phys. Rev. B* **84**, 174510 (2011).

[198] F. Carillo, G. M. De Luca, D. Montemurro, G. Papari, M. Salluzzo, D. Stornaiuolo, F. Tafuri, and F. Beltram, “Coherent transport in extremely underdoped $Nd_{1.2}Ba_{1.8}Cu_3O_z$ nanostructures,” *New J. Phys.* **14**, 083025 (2012).

[199] T. Pereg-Barnea, P. Turner, R. Harris, G. Mullins, J. Bobowski, M. Raudsepp, R. Liang, D. Bonn, and W. Hardy, “Absolute values of the London penetration depth in $YBa_2Cu_3O_{6+y}$ measured by zero field ESR spectroscopy on Gd doped single crystals,” *Phys. Rev. B* **69**, 184513 (2004).

[200] B. Ramshaw, J. Day, B. Vignolle, D. LeBoeuf, P. Dosanjh, C. Proust, L. Taillefer, R. Liang, W. Hardy, and D. Bonn, “Vortex lattice melting and H_{C2} in underdoped $YBa_2Cu_3O_y$,” *Phys. Rev. B* **86**, 174501 (2012).

[201] D. Gustafsson, F. Lombardi, and T. Bauch, “Noise properties of nanoscale $YBa_2Cu_3O_{7-\delta}$ Josephson junctions,” *Phys. Rev. B* **84**, 184526 (2011).

[202] D. S. Hopkins, D. Pekker, P. M. Goldbart, and A. Bezryadin, “Quantum Interference Device Made by DNA Templating of Superconducting Nanowires,” *Science* **308**, 1762 (2005).

[203] C. Granata, E. Esposito, A. Vettoliere, L. Petti, and M. Russo, “An integrated superconductive magnetic nanosensor for high-sensitivity nanoscale applications,” *Nanotechnology* **19**, 275501 (2008).

[204] R. Vijay, E. M. Levenson-Falk, D. H. Slichter, and I. Siddiqi, “Approaching ideal weak link behavior with three dimensional aluminum nanobridges,” *Appl. Phys. Lett.* **96**, 223112 (2010).

[205] M. V. Pedyash, D. H. Blank, J. De Muijnck, and H. Rogalla, “Properties of YBaCuO nanobridges and dc-SQUIDs,” *IEEE Trans. Appl. Supercond.* **7**, 2764 (1997).

[206] R. Arpaia, M. Arzeo, S. Nawaz, S. Charpentier, F. Lombardi, and T. Bauch, “Ultra low noise $YBa_2Cu_3O_{7-\delta}$ nano superconducting quantum interference devices implementing nanowires,” *Appl. Phys. Lett.* **104**, 072603 (2014).

[207] G. J. Podd, G. D. Hutchinson, D. A. Williams, and D. G. Hasko, “Micro-SQUIDs with controllable asymmetry via hot-phonon controlled junctions,” *Phys. Rev. B* **75**, 134501 (2007).

[208] M. M. J. Khapaev, “Extraction of inductances of plane thin film superconducting circuits,” *Supercond. Sci. Technol.* **10**, 389 (1997).

[209] P. A. Rosenthal, M. R. Beasley, K. Char, M. S. Colclough, and G. Zaharchuk, "Flux focusing effects in planar thin film grain boundary Josephson junctions," *Appl. Phys. Lett.* **59**, 3482 (1991).

[210] J. R. Clem and E. H. Brandt, "Response of thin-film SQUIDs to applied fields and vortex fields: Linear SQUIDs," *Phys. Rev. B* **72**, 174511 (2005).

[211] M. Sampietro, L. Fasoli, and G. Ferrari, "Spectrum analyzer with noise reduction by cross-correlation technique on two channels," *Rev. Sci. Instrum.* **70**, 2520 (1999).

[212] T. Schwarz, J. Nagel, R. Wölbing, M. Kemmler, R. Kleiner, and D. Koelle, "Low-Noise Nano Superconducting Quantum Interference Device Operating in Tesla Magnetic Fields," *ACS Nano* **7**, 844 (2013).

[213] J. Nagel, K. B. Konovalenko, M. Kemmler, M. Turad, R. Werner, E. Kleisz, S. Menzel, R. Klingeler, B. Büchner, R. Kleiner, and D. Koelle, "Resistively shunted $YBa_2Cu_3O_7$ grain boundary junctions and low-noise SQUIDs patterned by a focused ion beam down to 80 nm linewidth," *Supercond. Sci. Technol.* **24**, 015015 (2011).

[214] D. Drung, "High-T_c and low-T_c dc SQUID electronics," *Supercond. Sci. Technol.* **16**, 1320 (2003).

[215] D. Drung, "Low frequency noise in low Tc multiloop magnetometers with additional positive feedback," *Appl. Phys. Lett.* **67**, 1474 (1995).

[216] N. Bluzer, "Temporal relaxation of nonequilibrium in Y-Ba-Cu-O measured from transient photoimpedance response," *Phys. Rev. B* **44**, 10222 (1991).

[217] A. D. Semenov, G. N. Gol'tsman, I. G. Gogidze, A. V. Sergeev, E. M. Gershenzon, P. T. Lang, and K. F. Renk, "Subnanosecond photoresponse of a YBaCuO thin film to infrared and visible radiation by quasiparticle induced suppression of superconductivity," *Appl. Phys. Lett.* **60**, 903 (1992).

[218] M. Lindgren, M. Zorin, V. Trifonov, M. Danerud, D. Winkler, B. Karasik, G. Gol'tsman, and E. Gershenzon, "Optical mixing in a patterned $YBa_2Cu_3O_{7-\delta}$ thin film," *Appl. Phys. Lett.* **65**, 3398 (1994).

[219] M. Leung, P. R. Broussard, J. H. Claassen, M. Osofsky, S. A. Wolf, and U. Strom, "Optical detection in thin granular films of YBCO at temperatures between 4.2 and 100 K," *Appl. Phys. Lett.* **51**, 2046 (1987).

[220] N. Bluzer, "Biexponential decay and delay artifact in the photoresponse of superconductors," *IEEE Trans. Appl. Supercond.* **3**, 2869 (1993).

[221] A. Frenkerl, "High temperature superconducting thin films as broadband optical detectors," *Physica C* **180**, 251 (1991).

[222] J. M. Chwalek, C. Uher, J. F. Whitaker, G. A. Mourou, J. Agostinelli, and M. Lelental, "Femtosecond optical absorption studies of nonequilibrium electronic processes in high Tc superconductors," *Appl. Phys. Lett.* **57**, 1696 (1990).

[223] S. N. Dorenbos, E. M. Reiger, U. Perinetti, V. Zwiller, T. Zijlstra, and T. M. Klapwijk, "Low noise superconducting single photon detectors on silicon," *Appl. Phys. Lett.* **93**, 131101 (2008).

[224] F. Marsili, V. B. Verma, J. A. Stern, S. Harrington, A. E. Lita, T. Gerrits, I. Vayshenker, B. Baek, M. D. Shaw, R. P. Mirin, and S. W. Nam, "Detecting single infrared photons with 93% system efficiency," *Nature Photon* **7**, 210 (2013).

[225] R. Arpaia, M. Ejrnaes, L. Parlato, R. Cristiano, M. Arzeo, T. Bauch, S. Nawaz, F. Tafuri, G. P. Pepe, and F. Lombardi, "Highly homogeneous YBCO/LSMO nanowires for photoresponse experiments," *Supercond. Sci. Technol.* **27**, 044027 (2014).

[226] A. V. Gurevich and R. G. Mints, "Self-heating in normal metals and superconductors," *Rev. Mod. Phys.* **59**, 941 (1987).

[227] M. Ejrnaes, A. Casaburi, O. Quaranta, S. Marchetti, A. Gaggero, F. Mattioli, R. Leoni, S. Pagano, and R. Cristiano, "Characterization of parallel superconducting nanowire single photon detectors," *Supercond. Sci. Technol.* **22**, 055006 (2009).

[228] F. Mattioli, M. Ejrnaes, A. Gaggero, A. Casaburi, R. Cristiano, S. Pagano, and R. Leoni, "Large area single photon detectors based on parallel configuration NbN nanowires," *J. Vac. Sci. Technol., B* **30**, 031204 (2012).

[229] R. Arpaia, M. Ejrnaes, L. Parlato, F. Tafuri, R. Cristiano, D. Golubev, R. Sobolewski, T. Bauch, F. Lombardi, and G. Pepe, "High-temperature superconducting nanowires for photon detection," *Physica C* **509**, 16 (2015).

[230] N. Marrocco, G. P. Pepe, A. Capretti, L. Parlato, V. Pagliarulo, G. Peluso, A. Barone, R. Cristiano, M. Ejrnaes, A. Casaburi, N. Kashiwazaki, T. Taino, H. Myoren, and R. Sobolewski, "Strong critical current density enhancement in NiCu/NbN superconducting nanostripes for optical detection," *Appl. Phys. Lett.* **97**, 092504 (2010).

[231] P. Przyslupski, I. Komissarov, W. Paszkowicz, P. Dluzewski, R. Minikayev, and M. Sawicki, "Magnetic properties of $La_{0.67}Sr_{0.33}MnO_3$-$YBa_2Cu_3O_7$ superlattices," *Phys. Rev. B* **69**, 134428 (2004).

[232] L. Parlato, R. Arpaia, C. De Lisio, F. Miletto Granozio, G. P. Pepe, P. Perna, V. Pagliarulo, C. Bonavolontà, M. Radovic, Y. Wang, R. Sobolewski, and U. Scotti di Uccio, "Time-resolved optical response of all-oxide $YBa_2Cu_3O_7/La_{0.7}Sr_{0.3}MnO_3$ proximitized bilayers," *Phys. Rev. B* **87**, 134514 (2013).

[233] J. T. Petrisor, M. S. Gabor, C. Tiusan, V. Galluzzi, G. Celentano, S. Popa, A. Boulle, and T. Petrisor, "Magnetic pinning effects of epitaxial $La_xSr_{1-x}MnO_3$ nanostructured thin films on $YBa_2Cu_3O_{7-\delta}$ layers," *J. Appl. Phys.* **112**, 053919 (2012).

[234] T. Aytug, M. Paranthaman, B. W. Kang, S. Sathyamurthy, A. Goyal, and D. K. Christen, "$La_{0.7}Sr_{0.3}MnO_3$: A single, conductive-oxide buffer layer for the development of $YBa_2Cu_3O_{7-\delta}$ coated conductors," *Appl. Phys. Lett.* **79**, 2205 (2001).

[235] M. Sutherland, D. G. Hawthorn, R. W. Hill, F. Ronning, S. Wakimoto, H. Zhang, C. Proust, E. Boaknin, C. Lupien, L. Taillefer, R. Liang, D. A. Bonn, W. N. Hardy, R. Gagnon, N. E. Hussey, T. Kimura, M. Nohara, and H. Takagi, "Thermal conductivity across the phase diagram of cuprates: Low-energy quasiparticles and doping dependence of the superconducting gap," *Phys. Rev. B* **67**, 174520 (2003).

[236] A. K. Elmurodov, F. M. Peeters, D. Y. Vodolazov, S. Michotte, S. Adam, F. d. M. de Horne, L. Piraux, D. Lucot, and D. Mailly, "Phase-slip phenomena in NbN superconducting nanowires with leads," *Phys. Rev. B* **78**, 214519 (2008).

[237] A. Stockhausen, K. Il'in, M. Siegel, U. Södervall, P. Jedrasik, A. Semenov, and H.-W. Hübers, "Adjustment of self-heating in long superconducting thin film NbN microbridges," *Supercond. Sci. Technol.* **25**, 035012 (2012).

[238] W. C. Stewart, "Current-Voltage Characteristics of Josephson Junctions," *Appl. Phys. Lett.* **12**, 277 (1968).

[239] D. E. McCumber, "Effect of ac Impedance on dc Voltage-Current Characteristics of Superconductor Weak-Link Junctions," *J. Appl. Phys.* **39**, 3113 (1968).

[240] V. Ambegaokar and B. I. Halperin, "Voltage Due to Thermal Noise in the dc Josephson Effect," *Phys. Rev. Lett.* **22**, 1364 (1969).

[241] P. Thoma, J. Raasch, A. Scheuring, M. Hofherr, K. Il'in, S. Wunsch, A. Semenov, H.-W. Hubers, V. Judin, A.-S. Muller, N. Smale, J. Hanisch, B. Holzapfel, and M. Siegel, "Highly Responsive Y-Ba-Cu-O Thin Film THz Detectors With Picosecond Time Resolution," *IEEE Trans. Appl. Supercond.* **23**, 2400206 (2013).

[242] A. D. Semenov, P. Haas, H.-W. Hübers, K. Ilin, M. Siegel, A. Kirste, T. Schurig, and A. Engel, "Vortex-based single-photon response in nanostructured superconducting detectors," *Physica C* **468**, 627 (2008).

[243] L. N. Bulaevskii, M. J. Graf, and V. G. Kogan, "Vortex-assisted photon counts and their magnetic field dependence in single-photon superconducting detectors," *Phys. Rev. B* **85**, 014505 (2012).

[244] A. V. Gurevich and R. Mints, "Self-heating in normal metals and superconductors," *Rev. Mod. Phys.* **59**, 941 (1987).

[245] H. Courtois, M. Meschke, J. Peltonen, and J. P. Pekola, "Origin of hysteresis in a proximity Josephson junction," *Phys. Rev. Lett.* **101**, 067002 (2008).

[246] M. Tinkham, J. Free, C. Lau, and N. Markovic, "Hysteretic I-V curves of superconducting nanowires," *Phys. Rev. B* **68**, 134515 (2003).

[247] S. Charpentier, D. Golubev, R. Arpaia, R. Baghdadi, P. Fournier, T. Bauch, and F. Lombardi, "Hot spot formation in electron doped PCCO nanobridges," *to be submitted* (2016).

[248] S. Nakamae, K. Behnia, N. Mangkorntong, M. Nohara, H. Takagi, S. Yates, and N. Hussey, "Electronic ground state of heavily overdoped nonsuperconducting $La_{2-x}Sr_xCuO_4$," *Phys. Rev. B* **68**, 100502 (2003).

[249] M. Smith, J. Paglione, M. Walker, and L. Taillefer, "Origin of anomalous low-temperature downturns in the thermal conductivity of cuprates," *Phys. Rev. B* **71**, 014506 (2005).

[250] S. Soltan, J. Albrecht, and H.-U. Habermeier, "Ferromagnetic/superconducting bilayer structure: A model system for spin diffusion length estimation," *Phys. Rev. B* **70**, 144517 (2004).

[251] P. Fulde and R. A. Ferrell, "Superconductivity in a strong spin-exchange field," *Phys. Rev.* **135**, A550 (1964).

[252] A. Larkin and I. Ovchinnikov, "Inhomogeneous state of superconductors," *Sov. Phys. JETP* **20**, 762 (1965).

[253] M. Hamidian *et al.*, "Detection of a Pair Density Wave State in $Bi_2Sr_2CaCu_2O_{8+x}$ Using Scanned Josephson Tunneling," *arXiv preprint arXiv:1511.08124* (2015).

[254] J. Johansson, K. Cedergren, T. Bauch, and F. Lombardi, "Properties of inductance and magnetic penetration depth in (103)-oriented $YBa_2Cu_3O_{7-\delta}$ thin films," *Phys. Rev. B* **79**, 214513 (2009).

[255] Y. Wang and A. V. Chubukov, "Interplay between unidirectional and bidirectional charge-density-wave orders in underdoped cuprates," *Phys. Rev. B* **92**, 245140 (2015).

[256] P. A. Lee, "Amperean pairing and the pseudogap phase of cuprate superconductors," *Phys. Rev. X* **4**, 031017 (2014).

[257] T. Schwarz, R. Wölbing, C. F. Reiche, B. Müller, M.-J. Martínez-Pérez, T. Mühl, B. Büchner, R. Kleiner, and D. Koelle, "Low-Noise $YBa_2Cu_3O_7$ Nano-SQUIDs for Performing Magnetization-Reversal Measurements on Magnetic Nanoparticles," *Phys. Rev. Applied* **3**, 044011 (2015).